UNIVERSITÀ DEGLI STUDI DI TRIESTE
e
UNIVERSITÀ CA' FOSCARI DI VENEZIA

XXXI CICLO DEL DOTTORATO DI RICERCA IN

_____CHIMICA_____

DEVELOPMENT OF NANOMATERIALS TO OPTIMIZE DRUG THERAPY IN CANCER PATIENTS:
Synthesis and characterization of different nanocomposites

Settore scientifico-disciplinare: **__CHIM02__**

DOTTORANDA
ANNA DEL TEDESCO

COORDINATORE
PROF. BARBARA MILANI

SUPERVISORE DI TESI
PROF. PIETRO RIELLO

CO-SUPERVISORE DI TESI
DOTT. GIUSEPPE TOFFOLI

ANNO ACCADEMICO 2017/2018

Summary

Abstract

In this thesis, several types of nanocomposites have been developed. Starting from mesoporous zirconia nanoparticle (MZN) and its functionalization, and using it as common denominator, different systems for theranostic and orthopaedic applications have been produced. MZN has been functionalized with phospho-derivates to avoid organosilanes, usually employed in modification of several types of nanoparticles.

To obtain a theranostic system, a nanocomposite of zirconia and cobalt ferrites, obtained by wet impregnation and thermal treatments, has been linked, through bis-phosphonic acids with tio-ending group, to gold nanoparticles to obtain a system which is potentially able to perform magnetic and plasmonic hyperthermia, SERS and medical imaging. A deep study on physical-chemical properties of this composite was performed, varying quantities of cobalt ferrites introduced, doping only with iron, and modifying the surface with different phosphonic acids. Trials to obtain a porous structure with good magnetic properties for theranostic applications have been done: first the procedure of wet impregnation and thermal treatments has been modified with lower temperature, after results obtained with MCX line at Elettra Synchrotron of Trieste, then single-domain magnetic seeds used as nuclei for the synthesis of mesoporous zirconia nanoparticles have been made. Further improvement of the magnetic system was investigated by synthetizing bi-magnetic core-shell structures, doping cobalt ferrites with zinc and nickel, and trying to obtain dielectric shell made of zirconia on core nanoparticles to further improve the possibility of embedding in MZN.

Moreover, starting from evidences of layer organization of modified MZN on different surfaces, a systematic study has been performed. Several solvents and surfaces have been tested with drop casting and dip coating protocols. Then, to improve the linking, a covalent bond, employing EDC/S-NHS carbamide bonds, has been obtained on modified titanium in different ways. Tests on biofilms growth have been conducted on the best surface. To improve the system for orthopaedic applications, silver nanoparticles have been synthetized inside pores channels of MZN (MZN@Ag), to obtain long and short time drug delivery. Several protocols have been tried to have silver only inside pores or strictly linked to MZN. Tests on the activity of silver modified zirconia have been performed on *E. coli*.

Then, preliminary tests of linking of nanoparticles with biological molecules, such as antibodies, have been performed in order to evaluate if it was possible to work only with phosphonates instead of organosilanes as functionalizing moieties.

These results represent the necessary preliminary study for the applications of several nanocomposites to biomedical field, and need further investigation for practical uses in daily treatments. Indeed, the application of these systems to cancer or orthopaedics patients needs more and more studies due to the complexity of human body and diseases and this thesis could represents a good starting point for the study for practical applications.

List of Abbreviations

- Ab: Antibody
- AgNP: Silver Nanoparticle
- APTES: 3-aminorpopyltriethoxysilane
- AuNP: gold nanoparticle
- BE: Benzylether
- BPMG: N,N-bis(phosphonomethyl)glycine
- BPODE: (2-((8-sulfanyloctyl)sulfanyl)ethane-1,1-diyl)bis(phosphonic acid)
- BPPhE: 2-phenylethene-1,1-dyilphosphonic
- CAPS: N-cyclohexyl-3-aminopropanesulfonic acid
- CEST: Carboxyethylsilanetriol, sodium salt
- CMC: critical micelles concentration
- $Co(acac)_2$: Cobalt(II) acetylacetonate
- CP-MAS: Cross-Polarization - Magic Angle Spinning
- CTAB: Hexadecyltrimethylammonium bromide
- DC: direct current
- DCD: direct current demagnetization
- DE: Direct Excitation
- EBP: ethylenbisphosphonate
- EDC: N-3-dimethylaminopropyl-N'-ethylcarbodiimide hydrochloride
- EDS: Energy-Dispersive Spectrometry
- EDX: Energy-Dispersive X-Ray analysis
- ELISA: enzyme-linked immunosorbent assay
- EtOH: ethanol
- FC: field-cooled
- $Fe(acac)_3$: Iron(III) acetylacetonate
- FEG-SEM or FE-SEM: Field Emission Scanning Electron Microscope
- HA: hydroxyapatite
- H_c: coercivity field
- HDA: hexadecylamine
- HDD: 1,2-hexadecanediol
- HEPES: 4-(2-Hydroxyethyl)piperazine-1-ethanesulfonic acid
- HRP: horseradish peroxidase
- IRM: isothermal remanent magnetization
- MAS: Magic Angle Spinning
- MBP: Methylenbisphosphonate
- MES: 2-(N-morpholino)ethanesulfonic acid
- MG-SH: thiolated-Malachite-green
- MMA: Methyl methacrylate
- mMZN: nanocomposites made of ZrO_2 and $CoFe_2O_4$
- MNP: Magnetic nanoparticles
- M_r: remanent magnetization
- MRI: magnetic resonance imaging

- M_S: saturation magnetization
- MSN: Mesoporous Silica Nanoparticles
- MZN: Mesoporous Zirconia Nanoparticles
- m-ZrO_2: monoclinic zirconia
- $Ni(acac)_2$: Nickel(II) acetylacetonate
- NMR: Nuclear Magnetic Resonance
- NP: nanoparticle
- OA: Oleic Acid
- OAm: Oleylamine
- PAA: 2-phospho-L-ascorbic acid trisodium salt
- PBS: phosphate buffer solution
- PCOOH: 3-phosphonopropionic acid
- PEA: 2-aminoethyl dihydrogen phosphate
- PMIDA: N-(phosphonomethyl)iminodiacetic acid
- PMMA: polymethylmethacrylate
- PNH2: 3-aminoethylphosphonic acid
- PSER: O-Phospho-DL-serine
- PTyr: O-Phospho-L-tyrosine
- S(T)EM: Scanning (Transmission) Electron Microscopy
- SERS: surface enhancement Raman Spectroscopy
- SFD: switching field distributions
- S-NHS: N-hydroxysulfosuccinimide
- T_b: blocking temperature
- TEG: Triethylen glycol
- TEM: Transmission Electron Microscopy
- TEOS: Tetraethyl orthosilicate
- TMB: 3,3',5,5'-Tetramethylbenzidine
- TPR: temperature programmed reduction
- TRIS: tris(hydroxymethyl)aminomethane hydrochloride
- TRM: thermoremanent magnetization
- TR-SH: thiolated-Texas-Red
- t-ZrO_2: tetragonal zirconia
- ZB: Zirconium(IV) butoxide
- ZFC: zero-field-cooled
- $Zn(acac)_2$: Zinc acetylacetonate hydrate
- ZP: Zirconium(IV) propoxide
- $Zr(acac)_4$: Zirconium(IV) acetylacetonate

1. INTRODUCTION

Motivation and brief state of the art:

Nanomaterials gained increasing interest during these years, due to their wide feasibility in different fields. Particularly, for biomedical applications they obtain higher consideration thanks to the large contribution to personalized therapy, early detection of diseases and point of care devices [1-5]. As a matter of fact, these strategies for improving patients therapy need complex structures to reach different response in one time but need also the easiest and the faster way of application for the worker. The coupling of different materials in one nanocomposite could enlarge the applicability of the system and bring into being a theranostic system, which means the combination of a therapeutic part with a diagnostic one, in a single object.

During this work, several nanostructures have been developed for many biomedical applications. Zirconia was chosen as common denominator for all the made systems due to its high biocompatibility, stability and easy way of synthesis, and investigated as valid alternative to systems made by silica [6-8]. Indeed, silica nanoparticles are the common particles used for nanomedicine to couple, cover, convey and stabilize other interesting, but potentially toxic, materials. This widely application comes also from the easy way of surface modifications of these systems by commercially available organosilane, allowing subsequent modifications [7-11]. Zirconia particles are relatively new and poorly studied, for example compared to silica particles, although this oxide is already widely used in medical applications [6, 12-16]. On the other hand, a system which exploits different properties from silica is needed, to completely cover the applicability of mesoporous nanoparticles, particularly in biomedical field. However, due to the lack of studies on this kind of systems, zirconia is usually coupled to silica [16-18], employing the widely available organosilane for functionalizations. Thus, we focus our study on MZNs, obtaining theranostic, biosensing and orthopaedic devices, totally avoiding the employment of silica or organosilanes, and deeply studied both for functionalizations and structural modifications.

Brief explanation of the work:

In our study we explored the coupling of zirconia with other different phases such as magnetic oxides, gold or silver particles, both loading the porosity of the MZN, synthetizing magnetic core-shell nanostructures or linking nanoparticles to the surface. Moreover, different ways of surface functionalization have been investigated, to avoid the use of organosilanes.

First of all, a magnetic phase has been introduced in pores of MZNs, making a magnetic nanocomposite, which has been modified superficially. Coupling with other materials, gold nanoparticles in particular, has been performed, in order to obtain a theranostic system which could exploit both magnetic and plasmonic properties. In this way, a nanotool which is potentially able to perform magnetic and plasmonic hyperthermia and act also as biosensor, employing Surface Enhancement Raman Spectroscopy (SERS) and magnetic sorting, has been produced. Then improvement of the system has been tried: tests for maintain porosity of MZN, modifying the previously employed protocol with lower thermal treatment, and for the synthesis of $CoFe_2O_4$@MZN, without thermal

treatment, have been performed. Later, improvements of magnetic properties of feasible magnetic seeds for the synthesis of zirconia have been studied, using a thermal decomposition method to produce single-domain bi-magnetic core-shell nanoparticles, in collaboration with Davide Peddis at CNR-ISM in Roma and Gurvinder Singh at NTNU of Trondheim.

In parallel, after evidences on the spontaneous affinity of modified MZNs with several surfaces, modifications of bulky surfaces for orthopaedical applications have been investigated. Moreover, to improve the construction, silver nanoparticles have been synthetized inside pores of zirconia, to obtain antimicrobial activity and to maintain residual porosity for the loading of other molecules.

At the end, few tests for the linking of antibodies to nanoparticles, avoiding the use of organosilane molecules have been conducted to understand if an improvement of the system with biological moieties should be obtained.

Outline of the organization of the manuscript:

After a brief introduction of the topics, methods and discussion are divided in main groups related also on the possible application:

- Synthesis and surface modification of MZNs to improve their applications.
- Theranostic applications
    - Modifications of MZNs with magnetic phase, via wet impregnation.
    - Modifications of the system to obtain theranostic nanoparticles or biosensors.
    - Obtaining a porous structure coupling $CoFe_2O_4$ with MZNs.
    - Synthesis of core-shell structure of different spinel ferrites.
- Orthopaedic applications
    - Modification of bulk surfaces.
    - Modification of MZNs with silver.
    - Preliminary biological tests.
- Preliminary tests of coupling with antibodies.

The conclusions and future perspective will follow these sections.

As one can deduct from this outline, the aim of the thesis is to develop a nanotool that should be able to improve patients cure both in orthopaedic and in oncological applications as biosensor or for theranostic or drug delivery. As a matter of fact, this work is the preliminary study of the synthesis and of the physico-chemical properties of such systems, that needs further investigation for a practical application.

1.1. Nanomaterials in Medicine

Nanomaterial is a system with at least one dimension in the range of nanometres, which exploits different properties in opposition to its bulk counterpart, making it suitable for various applications.

Particularly, several types of nanomaterials could be used in medicine, both organic and inorganic ones, taking advantage of their different properties. They could be made of polymers, surfactants, metals or metal oxides. Polymeric nanoparticles are mostly used as drug delivery systems, thanks to their biocompatibility, as micelles and liposomes [5, 19]. Inorganic nanoparticles, instead, are more used as theranostic systems, thanks to their ability to load/be imaging probes or load/bind drugs or recognition moieties, as proteins or nucleic acids [20-23].

Widely used are mesoporous silica nanoparticles (MSN), thanks to their easy way of synthesis and surface modifications, high surface area and high biocompatibility [8, 10, 20, 23-24]. Moreover, MSNs are usually used to increase biocompatibility of other nanoparticles, as magnetic nanoparticles, and to couple properties between different materials [10, 25-26]. The same applications of silica nanoparticles have also other mesoporous materials, such as TiO_2 [27] or ZrO_2 [6] nanoparticles.

Magnetic nanoparticles (MNP), mostly made of metals oxides, are another system commonly used in biomedicine. MNPs, due to their physico-chemical properties, are applied in many fields. Theranostic systems could be created, especially for easy localization in the body with magnetic resonance imaging (MRI) and hyperthermia capability. Also, detection devices could be made with MNPs, using their magnetic properties as signal or to concentrate analytes [21, 28-33].

Gold nanostructures are one more object that is commonly used in biomedicine. Small dimensions and particular shapes give them characteristic properties that are exploited in theranostic and sensing [2, 34-35].

Quantum Dots, Carbon Dots or Nanotubes are other systems widely used in medicine. Their very small size (typically of only a few nanometres), their optical properties and surface chemistry make them suitable for multimodal imaging and drug delivery [36].

Moreover, nanoparticles made by other material are used for tissue engineering, such as hydroxyapatite (HA) that is fully used to increase mesenchymal cells growth and delivery drugs [37-38]. Furthermore, it has been seen that ceramic nanostructures in bone scaffold could promote adhesion of osteoblast cells and prevent bacterial contamination [39-40].

1.1.1. Theranostic applications

Theranostic is an emerging way to treat disease in which therapy and diagnosis are matched, improving efficacy and timing of curing. Indeed, being able to see and treat sickness conditions in the faster way as possible, should be more effective than in normal ways of treatments. Moreover, it's strictly related to nanoscience due to the capability of nanostructure to bind different materials with diverse applications. Usually, indeed, is not possible to achieve various characteristics with only one substance, because each one has a specific ability in a determine field, for instance imaging or therapy. An imaging probe is needed to be coupled to a drug to follow the release of it and to see the behaviour of the disease to the treatment. Common imaging probe are magnetic nanoparticles or paramagnetic ions for MRI, fluorescent dyes, noble metals nanoparticles for computed tomography (CT) or photoacoustic imaging (PAI). These systems are then coupled to a

drug using different ways, which could be physical adsorption or direct bond (covalent, ionic or H-bond). These materials, unfortunately, are usually toxic, they suffer from leaching from the body and they have low bioavailability due to their surface properties or hydrophobic characters. On the other hand, it is not easy to directly couple materials suitable for imaging or drug delivery and such systems could increase toxicity and decrease inert properties in fluids. So, a coupling material is usually needed to obtain a whole theranostic system. Nowadays, the most used system to couple various materials to obtain a multimodal structure is silica (SiO_2), which is incline to bind or host other molecules or materials and this is a perfect linker between inorganic and organic worlds. The easy way of synthesis of different types of nanostructure increases the interest on this material. Indeed, the shape of silica nanoparticles could highly vary, like mesoporous (MSN), hollow, rods or act as a full core. Moreover, it is highly biocompatible and could prevent the toxicity and the elimination of other materials from the body, thanks to the easy way of surface functionalizations, increasing also the stability of the system [7, 9]. On the other hand, many drugs need a vehicle to increase their efficacy and decrease side effects. With these considerations, one can see the necessity of a system that could couple all these tools and be as safe as possible. Moreover, it can be seen how mesoporous materials could be a good linking agent that can be doped with imaging components (or linked to them) and load drugs, thanks to high surface area. A lot of example can be given for the magnetic core system, coupled with a mesoporous silica shell and linked to proteins, polymers or other nanoparticles to achieve theranostic goal [7, 9-10, 20, 23-25, 41-45]. Other mesoporous and/or inert materials can be used as linking agent, such as titania or zirconia, due to the same easy way of synthesis of silica. These other substances are more inert and resistant to corrosive or external agents than the silica ones and can be used as a complementary system to cover also the part of application that silica can't reach. Moreover, they can be used as active material in the treatment due to their physico-chemical properties [6, 46-49]. Another system that could be used to couple different moieties are polymers, thanks to their good biocompatibility and easy way of synthesis [50] but unfortunately, the difficulties in reproducibility avoid a larger use in this field.

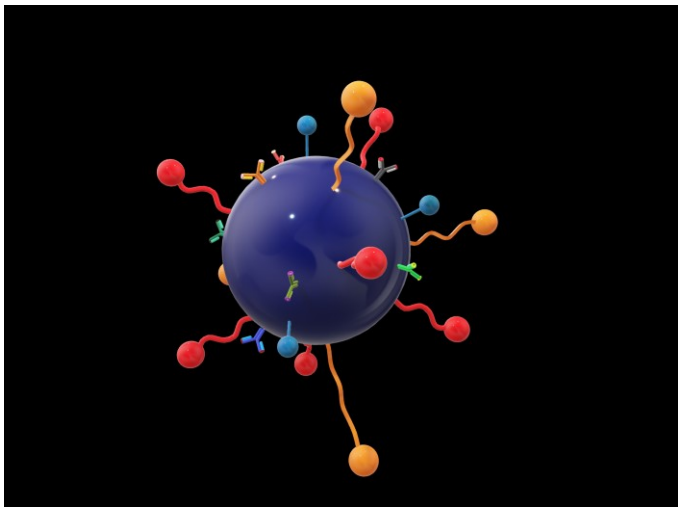

Figure 1: Schematic representation of multifunctional nanoparticle for theranostic and biosensing applications. Differently coloured objects should represent drugs, or imaging probes or growth factors.

1.1.2. Biosensing applications

Another field of interest in nanomedicine is the analytical part of it. The early detection of disease and the state of the therapy (i.e. the metabolism of drugs from a specific patients) are crucial points that must be improved for a better response of cure in cancer patients. Point of care devices and tools (biosensing, bioanalytical and bio-detection ones) for the diagnosis, which are easy to use and fast, are ever more needed and nowadays possible. Indeed, common care following of the patients' needs time consuming and expensive techniques that clinics try to avoid. Moreover, personalised therapy must be increased, due to the so different response to a therapy of diverse patients. In this view, a lot of systems are in developing to catch as early as possible disease and to see how drugs have been metabolised by the body [2]. Usually, a recognition moiety is bond to nanostructure to assure active recognition binding of the analytes. These systems are typically biological molecules which can be antibodies and other proteins, aptamers (particularly designed DNA strand) or molecular imprinted polymers [51]. In this way the analyte, that could be a protein, a small molecule, a cell a virus, a gen, a bacterium or an exosome, is strictly bond to the recognition system and makes its analysis easier.

The most common test used for early detection is enzyme-linked immunosorbent assay (ELISA) that uses antibody-antigen recognition binding and could be modified with nanoparticle to produce ELISA-sandwich assay [52-53]. Other systems can be made coupling different nanoparticles to obtain a multiresponse analysis. An example is magnetic nanoparticle coupled with gold or silver nanoparticle that could exploit magnetic properties both for detection [54] and purification of samples, and gold (or silver) for its plasmonic properties and surface capability to enhance signal in Raman spectroscopy (SERS) [55-58]. In this view, specific design must be done to obtain the so-called hot spots to enhance the signal. Hot spots exist in all those nanoparticle arrangements in which the local electromagnetic field can be increased by several orders of magnitude, making possible the enhancements of the Raman signal up to 10 to 14 orders of magnitude. In this case even the single molecule detection [59-60] becomes possible, especially if they are coupled with magnetic nanoparticle to purify and concentrate samples.

1.1.3. Orthopaedic applications

Concerning bone tissue engineering, there is a continuous demand for products that are more biocompatible and comparable to natural and healthy bone. Different causes are responsible for bone defects due to particular diseases, such as tumour, or specific trauma. Each cause of defects needs a certain treatment like each type of bone damaged. In this perspective, nanotechnology offers materials that are able to mimic the hierarchical structures of native bone tissue that directly interacts with cells. The same occurs with drug delivery systems that are able to release drugs and target to the desired site. Indeed, nanostructured materials have shown the enhance of osteoblast functions and osteointegration and, together with a scaffold, they could release drugs or growth factor for a better osteointegration [5, 40, 61-66]. Designing even better material for implantation or bone regeneration is crucial to obtain less immune response with a good integration in the body. Moreover, orthopaedic implantations and surgical procedures can

suffer from the possibility of infections and need an easy and effective way to treat them [39-40].

For bone scaffolds and implantations, the most used material are the ones which provide structural supports, such as titanium alloys, stainless steel alloys, hydroxyapatite (HA), alumina, zirconia, polymethylmethacrylate (PMMA), poly(lactic acid) (PLA) and mixture of carbon fibres with polymers. Nanocomposites or nanostructured surfaces are new techniques used to improve osseointegration that are reaching increasing interest in research and clinical fields. Moreover, all the materials described above could be coupled together to increase the properties of the system. For example, nanoparticles of TiO_2 or ZrO_2 could cover titanium implants or HA could be mixed with PMMA to improve cell adhesion or deliver growth factors. Furthermore, implants could be designed to prevent cancer growth using drugs or particular metals which are, on the other hand, ineffective for healthy cells [40, 63].

Another use of nanotechnology in orthopaedics is in the prevention or struggle bacterial infection occurring during surgery, that is the main reason for implantation failure. Nanomaterials can help with the local long-term release of antibiotics drugs, also avoiding multidrug resistance developed by bacteria. Silver nanoparticles could be embedded in the implantation and release Ag^+ ions as antibacterial agents during long periods. Furthermore, antibiotic drugs could be loaded inside nanoparticles to tackle infections [39-40, 67-68].

1.2. Synthesis of nanoparticles

Different nanostructures can be synthetized with many approaches. Mesoporous structures are defined as a material with pores having a diameter between 2 and 50 nm, usually produced via sol-gel synthesis. On the other hand, room temperature superparamagnetic nanostructures can be more frequently made with thermal decomposition method or via polyol-assisted template method, that can provide spherical single-domain nanoparticles with narrow distribution of diameters and with good colloidal stability.

1.2.1. Mesoporous nanoparticles

Mesoporous nanoparticles are made with sol-gel process from almost a century [6, 23, 27, 69-80]. It involves hydrolysis and condensation of the precursors, leading to a branched system between the element of interest and oxygen. For transition metals, especially for d^0 (as Zr(IV)), the main precursor used to obtain nanoparticles is the alkoxylate complex, thanks to the capability to stabilize the highest oxidation state. Indeed, -OR are hard-π donor ligands, but makes the complex more unstable to nucleophilic reaction, thanks to the possibility of expansion of the unsaturated coordination sphere and the high speed of hydrolysis. During hydrolysis, metals are solvated from water, giving three types of complexes:

$$[M(OH_2)]^{z+} \rightleftharpoons [MOH]^{(z-1)} + H^+ \rightleftharpoons [M=O]^{(z-2)} + 2H^+$$

Aquo *Hydroxo* *Oxo*

The nature of the complex derives from the charge, the coordination number and electronegativity of the metal and from pH of the solution and the stabilisation of the field of ligands. Moreover, M^{4+} metals could do all types of complexes, and usually, Zr(IV) makes oxo-hydroxo complexes.

The mechanism of hydrolysis generally involves nucleophilic addition (A_N), subsequent H^+ transfer, phase transition and elimination of the protonated species (Figure 2).

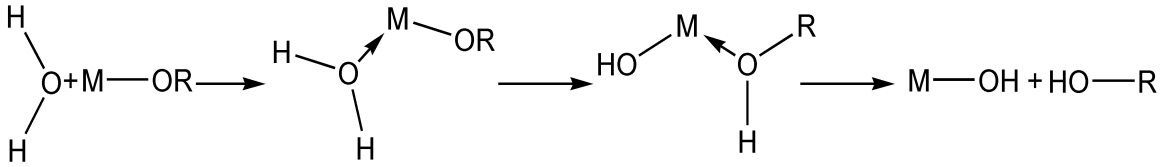

Figure 2: Hydrolysis of metal alkoxide precursor

Condensation follows hydrolysis and can occur with two different mechanism: nucleophilic substitution (S_N) or A_N. S_N happens if preferred coordination is satisfied, while the other one take place if is not satisfied. Due to the bad character of oxo and aquo ligands as leaving group, is usually needed a catalyst to promote condensation reaction and could be an acid or a base compound. In both mechanism oxygen improves its coordination sphere thanks to the presence of unshared electronic doublet (Figure 3).

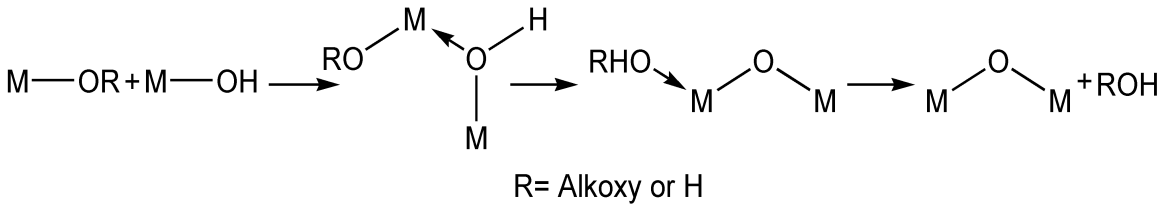

Figure 3: Mechanism of condensation reaction

Moreover, it has been seen that longer chain in the alkoxy group can stabilize the reaction due to steric factor. Based on what is the final product that could be obtained, acid or base catalyst can be used as previous reported. Indeed, acids lead to a more linear way of condensation, while base carry to a more branched one.

Interparticle interaction during synthesis is a crucial point to make monodisperse and separated nanoparticles. Indeed, the stability of the sol is important and London and van der Waals forces have to be taken into account due to their involvement in aggregation. To avoid this problem with metal precursor, a double layer of charge is needed. To obtain it, salts of alkali halides are usually employed that surround the nuclei and direct the growth. The selection of these salts is crucial, because their charge and radii dimensions could affect the shape of nanoparticles [6, 69-71, 73].

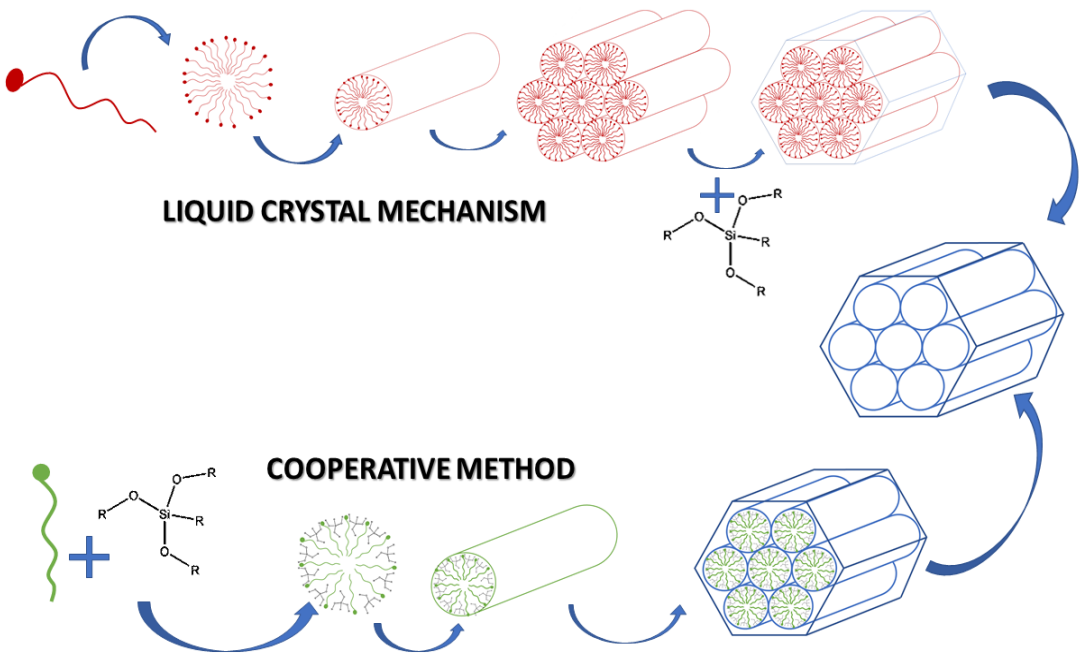

Figure 4: Mechanisms of soft template synthesis: example of liquid crystals (top) and cooperative (down) methods to obtain a porous structure, starting from surfactants and alkoxylated precursors of the desired oxide.

To obtain mesoporous structure, template synthesis methods are used (Figure 4) [6, 23, 71, 73, 79-80]. Template agents could be both soft, as surfactant molecules that can arrange in 3D structures, and hard, as other inorganic materials with different properties from the desired one. Soft templates, the most used ones, can be amphiphilic molecules, such as surfactants, or polymers that can produce supramolecular structures, due to hydrophilic-hydrophobic interactions. They can be classified as cationic, anionic or neutral, depending on the nature of the polar head (surfactants), or the intrinsic charge of the structure (polymers). The synthesis can occur with two main mechanisms: liquid crystal template or cooperative method (Figure 4). With the first, template molecules arrange in a 3D structure before the introduction of the desired inorganic precursor. For this process, a certain concentration of the molecules, critical micelles concentration (CMC), is needed. Moreover, different types of structures (sphere, rods, exc.) can be achieved increasing the quantities of the surfactants which can arrange in many structures. For the cooperative mechanism, inorganic molecules are necessary and cooperate with other molecules for the construction of the 3D scaffold. In this way, channels can be created also below the CMC. As already said, different structures could be achieved changing concentration and the dimension also depends on the length of the hydrophobic chain. Furthermore, using hydrophobic molecules, swelling of the pore can be made. Indeed, organic molecules preferentially go inside the structure, trying to avoid any contact with hydrophilic environment. After the synthesis of the inorganic structure, the template agent is removed to obtain the porous structure. The removal of the directing agent can be done with thermal treatment, in order to burn up the organic moieties leaving unchanged the inorganic ones, or with vacuum extraction or solvent extraction, if the desired structure is sensitive to temperature changing [71-73, 81].

On the other hand, the use of hard template can be different. In this approach a hard material is synthetized around another hard material that present a particular 3D structure. Usually silica and metal oxide are coupled together, due to their different

response at etching condition. This nanocasting approach is widely used to produce metal oxide mesostructures thanks to the stability of the scaffold at high temperature, sometimes necessary to stabilize the material. Indeed, MxOy are really sensitive to high temperature usually needed for the removal of soft template, but also to crystallize and stabilize them [72, 81].

1.2.2. Magnetic nanoparticles

To obtain spherical shaped nanoparticles, with narrow distribution of diameters, high crystallinity, specific magnetic properties and good reproducibility, many ways of synthesis are generally used. The most used, indeed, are co-precipitation method, thermal decomposition, hydrothermal method, microemulsion, sol-gel and polyol methods [21, 28-31, 34, 57, 82-106]. Here we will focus on thermal decomposition and polyol ones, that are used in this thesis.

Thermal decomposition method involves organometallic compounds, like acetylacetonate, carbonyl, acetate, exc., of the desired metal precursor and surfactant molecules to stabilise the so formed nanoparticles. Common used surfactant agents are oleic acids, oleylamine, or other long chain acids or amines that are needed to prevent aggregation. Generally, solvents with high boiling point are used, and reactions are conducted between 200 and 300 °C, in order to decompose organometallic precursors. Metals and metal oxides nanoparticles can be done with this procedure and, usually, also reducing agents is needed to preserve the desired oxidation states of the metals (i.e. polyols). Morphology, size and magnetic properties can be tuned changing ratio between precursors and precursors/surfactants, concentrations of reagents, temperature and timing of the reaction. Changing these parameters is also possible to obtain core-shell structures of different compositions, especially using seed-mediated growth method. In this way, already formed nuclei can be used to further growing on the surface other materials to produce an object differently composed and with other properties respect to the starting one [82, 86-91, 107].

On the other hand, polyol technique consists in the use of metals salts as precursor and polyols both as solvent and reducing agents. In this way, ethylene, diethylene, triethylene or tetraethylene glycols are used near their boiling point to obtain the reduction of the desired metals. Moreover, over the aforementioned uses of the polyol, it can serve also as capping agent for the so formed nanoparticles, avoiding aggregation. Oxides nanoparticles are obtained introducing water to the reaction mixture, to obtain a system that acts more like the sol-gel process [82-85].

Moreover, these methods can be integrated on the sol-gel one, without the presence of water, but involving the same reactions, called nonhydrolytic sol-gel process [73, 108].

1.3. Physico-Chemical properties of nanoparticles

As previously reported, nanometric dimensions provoke changes in physico-chemical properties of the material. Decreasing length, indeed, make changes in how atoms affect each other, with consequences in energy behaviour.

1.3.1. Magnetic properties

In condensed matter, atomic moments could be isolated or mutually act together, leading to non-cooperative or cooperative magnetisms, respectively. Paramagnetism and diamagnetism are the main forms of non-cooperative ones. Paramagnets are materials where exist identical, but uncoupled, atomic moments in an isotropic environment which can partially align as a response to an external magnetic field. On the other hand, diamagnetism is when the magnetic moments of the material react to an external magnetic field by aligning antiparallel to it. However, ferromagnetism arises from the reciprocally interaction of atomic magnetic moments that determine magnetic order in the system. These interactions can arise from direct exchange, where wave functions are superimposed, or indirect one, where a coupling exist through relatively big distances, sometimes also through a non-magnetic ion (superexchange). The exchange interaction is quantitatively described by Heisenberg spin Hamiltonian:

$$H_{exc} = -2\sum_{i<j} J_{ij}\vec{S}_i \cdot \vec{S}_j$$

Where J_{ij} is the exchange integral describing the degree of coupling between the spins S_i and S_j. If J_{ij} has positive value, ferromagnetism (FM) is favoured and below a critical temperature (Curie temperature, T_c) magnetic moments are aligned. If J_{ij} has negative value, spins are oriented antiparallel and under a critical temperature (Néel temperature, T_N) antiferromagnetism (AFM) (if magnetic moment are compensated) or ferrimagnetism (FiM) (if magnetic moments are not compensated) can be seen [108-110].

Ordered solid magnetic materials have preferred orientations, easy axes, where energy has a minimum and depends on crystalline structure and chemical composition. The work needed to move the magnetization from the easy axis to the hard axis is called magnetic anisotropy energy, and is stored in the material as potential energy. It is strictly related to microscopic and macroscopic properties of the material. Different forms of anisotropy energy can be defined on the basis of the properties that regulate it. Magnetocrystalline anisotropy is an intrinsic characteristic of the material and it depends on crystal symmetry and atomic arrangement in the lattice. The main symmetries for this anisotropy are uniaxial and cubic. Shape anisotropy, on the other hand, is due to the magnetization of the sample body, that produces a magnetic field inside it that opposes to the magnetization. The demagnetizing field depends on shape and size of the magnet, and modifying them is the best way to tune this type of anisotropy. Surface anisotropy depends on the lack of crystalline symmetry on surface atoms respect to the core ones, so it increases with higher surface/volume ratio and is deeply related to the interaction with the surrounding atoms and molecules [111].

A bulk cooperative magnetic system, to minimize its energy, will organize itself in a certain number of small regions, with different sizes and shapes, called domains, (i.e. uniformly magnetized regions having atomic magnetic moments oriented in the same direction). Two adjacent domains are separated by transition regions, called domain walls, in which the spins gradually rotate (coherently or incoherently) from one domain to the other. In an demagnetized FM or FiM material, magnetic domains have random directions so that

the sum of the overall domain moments is approximately zero [111-112]. Going to the nanometre scale, below the critical radius (r_c), single magnetic domains are energetically favoured. Single domain particles usually have uniform magnetization at any field and can be considered as a large magnetic unit (i.e. superspin) with a magnetic moment (μ_p) proportional to the volume of the particle (V_p).

$$r_c \propto \frac{\sqrt{AK}}{\mu_0 M_S^2}$$ A = exchange stiffness, K = anisotropy constant, μ_0 = vacuum permeability

$$\mu_p = M_S V_p$$ M_S = saturation magnetization of the material

Generally, the energies required to reverse the spin orientation within a single magnetic domain particle are larger than those needed to induce domain wall movement, yielding coercivities larger than those of the bulk (Figure 5). This increase of coercivity is due to the transition from multi- to single- domain particles [110].

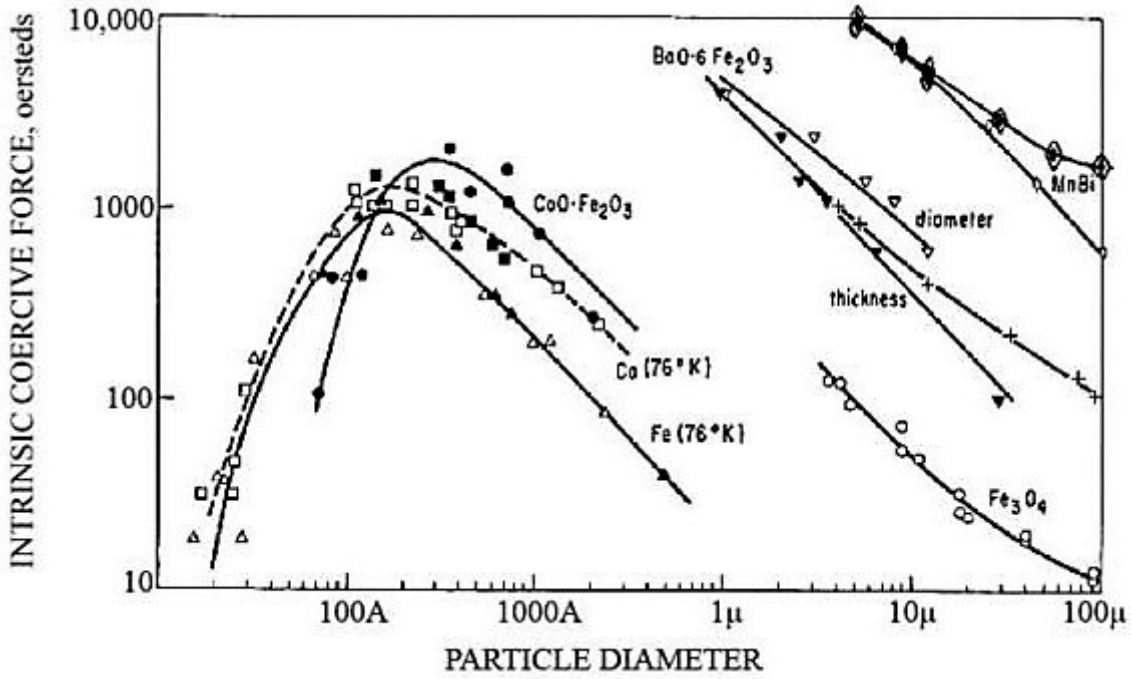

Figure 5: Experimental relation between coercivity and diameter for particles deriving their coercive force principally from crystal anisotropy energy, recorded at room temperature, except for Fe and Co [113].

Under certain dimension, the previously introduced r_c, the energy barrier is easily overcome by thermal excitations ($k_BT>K_AV$) and the particles are able to rotate, resulting in demagnetizations of the particles. Under such conditions, the behaviour of an assembly of nanoparticles in absence of magnetic field is similar to a paramagnetic material, so it is called superparamagnetism, but the saturation magnetization is much larger and easier to reach.[1]

[1] We must point out that the critical dimension for the monodomain condition is different from the one for superparamagnetism, which is usually smaller.

Relaxation times of superspins follow the Arrhenius law:

$$\tau = \tau_0 exp \frac{K_A V}{k_B T}$$

with τ_0 as constant value for the material, related to the characteristic reversal time for spins, k_B as the Boltzmann constant and T as the absolute temperature. Another characteristic of superparamagnetic nanoparticles is the lower value of coercivity respect to their larger counterpart, as is seen in Figure 5, in which below the critical dimension it decreases.

The dynamic magnetic properties of an ensemble of superspin are strictly related to the experimental measuring times (τ_m) of the technique used to follow the relaxation. If τ is smaller than τ_m the relaxation is faster than the measurement and the superparamagnetic state is observed, while if τ is bigger than τ_m only static properties can be seen. In this condition, the blocked state, the isothermal field dependence of magnetization show irreversible behaviour (i.e. hysteresis of magnetization). When the relaxation time is equal to the experimental measuring time, the blocking temperature (T_B) is defined as a modification of the latter equation:

$$\tau_m = \tau_0 \exp\left(\frac{\Delta E_A}{k_B T_B}\right)$$

So, in typical experiment τ_m ranges from 10-10^2 s of direct current (DC) magnetization measurements, up to 10^{-10}-10^{-12} s for neutron diffraction [108, 111, 114].

Magnetic metal oxides

Metal oxides material, magnetic or not, are the most common and studied ones due to their easy way of synthesis, low toxicity and good stability, as previously reported. Among the magnetic one, spinel structured materials are almost the most important due to their crystal structure that permit the tuning of magnetic properties in an easy way. They have $Me^{II}Me^{III}_2O_4$ and face-centred cubic structure (fcc) with oxygen as cubic close-packed. The two interstitial sites are occupied by cations coordinated to oxygen: the tetrahedral (A) and the octahedral (B) sites. Normal spinels have Me^{II} in the A-sites, while Me^{III} in the B-sites (Figure 6). On the other hand, if A-sites are occupied by Me^{III} and the B ones randomly by Me^{II} and Me^{III}, the structure is the one of invers spinel. The degree of inversion (γ) is given by the fraction of divalent ions in octahedral sites, and quantify the cationic distribution between the sites A and B. Sometimes it could be easier to find the ratio of Me^{III} in A and B sites (α), given by Mössbauer measurement as an example [108].

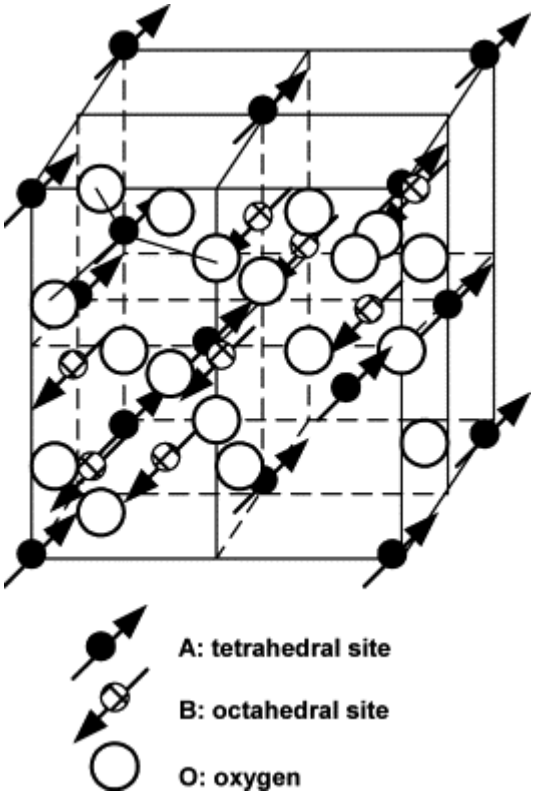

Figure 6: Spinel structure [115]

Superexchange interactions between atomic magnetic moments in A (J_{AA}) and B (J_{BB}) interstices cause ferromagnetic order through ions of the two sites, up to two magnetic sublattices. On the other hand, interactions among A and B sites (J_{AB}) introduce antiferromagnetic or ferrimagnetic order between the sites that are 10 times higher than J_{AA} and J_{BB}. Furthermore, the intralattice interaction that is dominant is the J_{AB} and induce uncompensated order between the sublattice of A and B. The net magnetization can be then considered as directly proportional to the difference between the sublattices magnetizations. Therefore, spinel's magnetic properties can be controlled through magnetic coupling and is related to the chemical composition and crystal structure. Moreover, big changes on magnetic properties can be done by substitution or change on the distribution of both cations [108, 115].

Hard and soft magnetic material

Magnetic materials are classified on the basis of their capability of magnetizing and demagnetizing in hard and soft ones, but they can also be classified by the strength of the coercivity field. A soft magnetic material is the one with an easy way of magnetization and narrow hysteresis loop, which means that it has high saturation magnetization, low coercivity and anisotropy, and an example could be nickel ferrite. On the other hand, hard magnetic material is characterized by high saturation magnetization, high coercivity and anisotropy, such as cobalt ferrites [115]. For these differences in magnetic properties they could be applied in different fields. In biomedical applications, hard materials are suitable for hyperthermia application, while soft materials are more appropriate as contrast agents.

2. MATERIALS AND METHODS

2.1. General

2.1.1. Materials

Sodium Acetate (Aldrich), 2-aminoethyl dihydrogen phosphate (PEA, Aldrich), 2-phospho-L-ascorbic acid trisodium salt (PAA, Aldrich, 95%), O-Phospho-DL-serine (PSER, Aldrich, 98%), O-Phospho-L-tyrosine (PTyr, Aldrich), 3-aminoethylphosphonic acid (PNH2, Aldrich, 99%), 3-phosphonopropionic acid (PCOOH, Aldrich, 94%), N-(phosphonomethyl)iminodiacetic acid (PMIDA, Aldrich, 95%), N,N-bis(phosphonomethyl)glycine (BPMG, Aldrich, 98%), Zirconium(IV) propoxide (ZP, Aldrich or Fluka, 70%wt in propanol), Zirconium(IV) butoxide (ZB, Aldrich, 80%wt in 1-butanol), 2-(N-morpholino)ethanesulfonic acid (MES, Aldrich), tris(hydroxymethyl)aminomethane hydrochloride (TRIS, MB Grade, Aldrich), Sodium tetraborate decahydrate ($Na_2B_4O_7*10H_2O$, Aldrich), Sodium hydrogencarbonate ($NaHCO_3$, Aldrich), N-cyclohexyl-3-aminopropanesulfonic acid (CAPS, Ultrapure, Usb), Methyl methacrylate (MMA, Aldrich), 3-aminorpopyltriethoxysilane (APTES, Aldrich), Sulfuric acid (Carlo Erba, 96%), Hydrogen peroxide (Aldrich, 30% vol), Acetic acid (>99.8%, Aldrich), Ninhydrin (Fluka), Glycine (Aldrich), N-3-dimethylaminopropyl-N'-ethylcarbodiimide hydrochloride (EDC, Aldrich), N-hydroxysulfosuccinimide (S-NHS, Aldrich), Silver nitrate ($AgNO_3$, Aldrich), Formaldehyde solution (Aldrich, 37 wt% in water), Sodium chloride (NaCl, Fluka), Sodium hydroxide (NaOH, Aldrich), D-(+)-Glucose (Aldrich), di-sodium hydrogen phosphate (Aldrich), Hexadecyltrimethylammonium bromide (CTAB, Aldrich), n-hexane (Aldrich), Tetraethyl orthosilicate (TEOS, Aldrich), cobalt nitrate hexahydrate ($Co(NO_3)_2*6H_2O$, Janssen Chimica 99.99%), iron nitrate nonahydrate ($Fe(NO_3)_3$, Aldrich 99.99%), Carboxyethylsilanetriol, sodium salt (CEST, ABCR, 25% in water), Ethanol amine (≥98%, Aldrich), 4-(2-Hydroxyethyl)piperazine-1-ethanesulfonic acid (HEPES, Aldrich), HBS-EP+ buffer (0.1 M HEPES, 1.5M NaCl, 0.03 M EDTA, 0.5% v/v Surfactant P20, pH 7.4, GE Healthcare Bio-Science AB), Oleic Acid (OA, Aldrich, 90%), Oleylamine (OAm, Aldrich, 70%), 1,2-hexadecanediol (HDD, Aldrich, 90%), Cobalt(II) acetylacetonate ($Co(acac)_2$, Aldrich, 97%), Iron(III) acetylacetonate ($Fe(acac)_3$, Aldrich), Nickel(II) acetylacetonate ($Ni(acac)_2$, Aldrich, 95%), Zinc acetylacetonate hydrate ($Zn(acac)_2$, Aldrich) , Zirconium(IV) acetylacetonate ($Zr(acac)_4$, Aldrich, 97%), hexadecylamine (HDA, Alfa Aesar 90%), sodium fluoride (NaF, Eurobio 99%), Herceptin 150 mg (Trastuzumab (21 mg/ml), L-histidine hydrochloride, L-histidine, α,α-trehalose dihydrate, polysorbate20, Roche), Perjeta 420 mg/14 ml (Pertuzumab (30 mg/ml), L-histidine glacial acetic acid, polysorbate20, Roche), Recombinant HER2-ECD protein (code 10004-RP04, Sino Biological Inc.), 3,3',5,5'-Tetramethylbenzidine (TMB, code ES001, Merck Millipore), Streptavidin-HRP (code DY998, R&D Systems), Goat anti-rabbit IgG-HRP conjugate (Ab-HRP, code 401353, 1 mg/ml, Merck Millipore), EZ-Link Sulfo-NHS-LC-Biotinylation Kit (code 21435, Thermo Scientific), Triethylen glycol (TEG, Aldrich), Benzylether (BE, Aldrich, 98%), Ethanol (EtOH, Aldrich 99.8%), Methanol (Aldrich), Iso-propanol (Carlo Erba), Acetone (VWR, technical grade), Toluene (Aldrich) and ultrapure water. Reagents were used as received, except drugs (Antibodies) for patients use that were purified as described later. Methylenbisphosphonate (MBP), ethylenbisphosphonate (EBP), (2-((8-sulfanyloctyl)sulfanyl)ethane-1,1-diyl)bis(phosphonic acid) (BPODE) and 2-phenylethene-

1,1-dyilphosphonic (BPPhE) acid were provided by Prof A. Scarso from Università Ca' Foscari of Venezia.

2.1.2. Characterization methods

Size and shape of the nanoparticles were studied by electron microscopy using a Zeiss Sigma VP Field Emission Scanning Electron Microscope (FE-SEM or FEG-SEM), equipped with a Bruker Quantax Energy-Dispersive Spectrometry (EDS) microanalysis detector. Mean and standard deviation of the FE-SEM micrographs were determined measuring at least 100 nanoparticles for each sample. The diameters were measured using the image analysis software ImageJ [116-117].

Transmission Electron Microscopy (TEM) images were taken with a JEOL 3010, operating at 300 kV, equipped with a GATAN (Warrendale, PA, USA) multiscan CCD camera, TEM specimens were prepared by ultrasonically dispersing the powdered samples in ethanol (approximately 1 mg mL^{-1}) and depositing several drops of the suspension on a holey carbon film grid.

Scanning (Transmission) Electron Microscopy S(T)EM images were taken with Hitachi S-5500 S(T)EM in NanoLab at NTNU in Trondheim, operating between 0.5 and 30 kV and a maximum beam current of 20 µA, equipped with detector for secondary and low- and high-angle back scattered electrons, bright-field and dark-field transmission measurements, Bruker XFlash EDX Detector. S(T)EM specimens were prepared as for TEM measurements. ImageJ software was used to determine morphological parameters as for FEG-SEM images.

A Philips X'Pert goniometer working in Bragg–Brentano geometry was used for the X-ray Powder Diffraction (XRPD) measurements. A focusing graphite monochromator and a proportional counter with a pulse-height discriminator were used. Nickel-filtered Cu Kα radiation (λ=1.54056 Å) and a step-by-step technique were employed (steps: 0.05° 2θ, collection times: of 30 s/ step). The size of the crystallites was evaluated by Line Broadening Analysis (LBA) [118].

SAXS measurements were performed using a Kratky (PAAR) camera with an entrance slit of 25 µm. Nickel-filtered Cu Kα radiation, a pulse-height discriminator, and a proportional counter were used. Sample holder scattering and absorption effects were treated, as usual.

The nitrogen adsorption–desorption isotherms were measured at liquid nitrogen temperature (-196 °C) using a Micromeritics ASAP 2010 volumetric adsorption analyzer. The Brunauer-Emmett-Teller (BET) equation [119] was used to calculate the specific surface area from adsorption data and the pore size distributions were calculated from the adsorption branches of the isotherms based on the Barrett-Joyner-Halenda (BJH) model [120].

DRIFT-IR spectra were recorded with a Nexus FT-IR using Nicolet AVATAR Diffuse Reflectance accessorize.

UV-Vis Agilent 8453 was used to record UV-Vis spectra.

Perkin Elmer Victor 3V 1420 multilabel counter was used as plate reader.

NanoDrop 2000c Spectrophotometer from Thermo Scientific was used to quantify proteins in solution. A 2µl drop of the solution was deposited on sample holder and analysed.

DLS and ζ-potential measurements were recorded with a Malvern Zetasizer Nanosampler instrument equipped with a 633 nm He−Ne Laser. Colloidal solution of nanoparticles in buffers solutions at different pH values were prepared with concentration of nanoparticles around 0.1 mg/ml.

X-ray photoelectron spectroscopy (XPS) was performed using a Perkin Elmer Φ 5600ci spectrometer using nonmonochromatic Al K_α radiation (1486.6 eV) in the 10^{-7} Pa pressure range. All the binding energy (BE) values are referred to the Fermi level. The correct calibration of the BE scale was verified during analysis by checking the position of both $Au4f_{7/2}$ and $Cu2p_{3/2}$ bands (from pure metal targets), falling at 84.0 and 932.6 eV, respectively [121]. After a Shirley-type background subtraction, the raw spectra were fitted using a nonlinear least-squares fitting program adopting Gaussian−Lorentzian peak shapes for all the peaks. Because of surface charging, samples presented a shift of the bands toward higher BEs: the charging effect was corrected by using an internal reference ($Zr3d_{5/2}$ band centred at 182.4 eV in ZrO_2 compound). The uncertainty of all the determined BEs was lower than 0.2 eV. The atomic composition was evaluated using sensitivity factors as provided by Θ V5.4A software. The relative uncertainty of the reported atomic fraction of the different elements is lower than 5−10%.

^{31}P solid state NMR (SS-NMR) spectra were recorded on a Varian Infinity Plus 400 spectrometer working at Larmor frequencies of 400.34 and 162.06 MHz for ^{1}H and ^{31}P nuclei, respectively, using a CPMAS probe head accommodating rotors with outer diameters of 3.2 mm. The spectra were recorded under Magic Angle Spinning (MAS) at a spinning frequency of 20 kHz, using a Direct Excitation (DE) pulse sequence with high-power decoupling from ^{1}H nuclei. The 90° pulse duration was 2 µs for ^{31}P nuclei and a relaxation delay of 5 s between consecutive transients was used. About 1000 scans were accumulated for each sample. The signal of H_3PO_4 (80%) at 0 ppm was used as reference for ^{31}P chemical shift scale.

Magnetophoretic characterization was performed by recording the decreasing UV-Vis extinction of a solution of the magnetic nanosystems under a magnetic gradient obtained with a small magnet [122]. The solution was inserted in the UV-Vis spectrometer in a cuvette of 3x10x10 mm^3 (optical path 10 mm) where the magnet (Supermagnete, S-10-20-N, D=10 mm diameter, h=20 mm height), was inserted perpendicular to the optical path and in contact with the solution.

DC magnetization measurements were performed with a Quantum Design SQUID magnetometer, equipped with a superconducting coil which produces magnetic fields in the range from −5 T to +5 T. Powders have been immobilized in an epoxy resin to prevent any movement of the nanoparticles during the measurements. Magnetization versus temperature measurements were performed using the zero-field-cooled (ZFC), field-cooled (FC), and thermoremanent magnetization (TRM) protocols. Zero- field-cooled and field-cooled magnetization measurements were carried out by cooling the sample from room temperature to 5 K in zero magnetic field; then a static magnetic field of 2.5 mT was applied. M_{ZFC} was measured during warming up from 5 to 300 K, whereas M_{FC} was recorded during the subsequent cooling. In the TRM measurements, the sample was cooled from 300 to 5 K in an external magnetic field of 2.5 mT; the field was then turned off and the magnetization was measured on warming up. The field dependence of remanent magnetization was measured using the IRM (isothermal remanent magnetization) and DCD (direct current demagnetization) protocols. The initial state for an IRM measurement is a totally demagnetized sample cooled in a zero magnetic field. In the present case, an external field was applied for 10 s, then it was switched off and the remanence was measured (M_{IRM}). The process was repeated, increasing the field up to 5T. In a DCD measurement the initial state is the magnetically saturated one. An external field of −5T was applied for 10 s, and then a small external field in the direction opposite to magnetization was applied; after 10 s, it was switched off and the remanent magnetization (M_{DCD}) was measured. This was repeated increasing the field up to +5T [109, 123]. Samples of spinel ferrites obtained by thermal decomposition method were analysed with Quantum Design PPMS Dynacool, working with a temperature range between 1.8 K and 400 K, magnetic field range from -9 T to +9 T and sensitivity: 1e-06 emu (VSM) or 5e-06 emu (DC magnetization with ACMS II option). Protocols and sample preparations were the same used with SQUID magnetometer, but using different ranges.

A ^{57}Fe Mössbauer spectrum was recorded using a ^{57}Co/Rh γ-ray source mounted on an electromagnetic transducer with a triangular velocity form. For the analysis of Mössbauer spectra the program 'Mosfit' has been used. The isomer shift values were referred to α-Fe at 300 K. The samples consist of a thin layer of about 40 mg of the powdered compound located in a sample holder.

2.2. Synthesis and functionalization of Mesoporous Zirconia Nanoparticles

2.2.1. Synthesis of Mesoporous Zirconia Nanoparticles

Mesoporous zirconia nanoparticles were synthetized by a previously reported protocol, developed by our laboratory [6, 124]. It involves a template sol-gel process for the synthesis of nanoparticles of metal alkoxide precursor, with alkali salts to produce double layer of charges around the particles to avoid aggregation. The extraction of the surfactant was performed by vacuum extraction to avoid crystallization of the nanoparticles [27]. After some problem with reagent as we received, we modified the protocols changing alkoxide from propoxide to butoxide (see Results and Discussions section).

Protocol

In a round bottom flask of the desired dimension (on the bases of mg produced use the flask with the same amount of ml), HDA, sodium fluoride solution, water and ethanol are mixed and put under vigorous stirring. In the meanwhile, prepare a solution of the desired zirconium alkoxide in ethanol. After the complete dissolution of HDA in the first solution and the disappearance of the two phases in the second one, the latter is added very slowly to the first one drop by drop. After the addition the solution was left under vigorous stirring overnight. The molar ratio between reagents in this first step, respect to moles of Zr(IV) alkoxide, is the one reported in Table 1.

Table 1: Ratio between reagents of the first step of MZN's synthesis

Solution 1	MW (uma)	Density (g/ml)	Purity (%)	Ratio (mol/mol)
EtOH	46.07	0.79	0.95	724.13
H_2O	18.00	1.00	1.00	17.04
NaF (0.1 M)	41.99			1.79E-2
HDA	241.46	1.00	0.98	1.82
Solution 2				
$Zr(alkoxide)_4$	383.68	1.05	0.70/0.80	1.00
EtOH	46.07	0.79	1.00	9.65

For the scalability of the system is necessary to adjust the content of water, to decrease the rate of hydrolysis and condensations, and to produce one or more grams, half of the solution of salt is used. Moreover, to avoid hydrolysis during the addition when high amount of Zr precursor is needed, nitrogen gas pression was used to transfer the second solution, into the first one, through a needle.

After a night of stirring, the nanoparticles were recovered with centrifugation (9000 rpm for 15 minutes) and washed three times with ethanol. After the drying of the powder under air, it was put in a Teflon autoclave for hydrothermal treatment, with 12.5 ml of EtOH and 6.25 ml of water for gram of powder, at 170 °C for 16 hours. Then, the powder was filtered with a Millipore filtration system, using paper with porosity between 1 and 11 µm, to avoid cross-contamination. Therefore, the powder is put in a big enough round bottom flask, with reduced

pression around $5*10^{-2}$ mbar and heated at 120 °C for more than 16 hours to extract the surfactant used. This procedure of extraction is used to avoid crystallization of the structure of zirconia and maintain the porosity of the system.

MZNs are then characterized with FEG-SEM, nitrogen physisorption, TEM and DLS, to determine shape, porosity and surface charge. Images obtained with FEG-SEM were then analysed with ImageJ to obtain diameters distributions [116-117].

2.2.2. Functionalization of MZNs

In order to avoid silica layer usually used for surface modifications [17, 76, 125] of many kind of nanoparticles, other solutions were investigated. Starting from the evidence of the affinity between M(IV) centre, especially zirconium, and organic acids, such as phosphonic acids [18, 126-134], we screened a lot of possibility. We started from the commercially available phosphate molecules, such as O-Phospho-DL-Serine or 2-Phospho-L-Ascorbic Acid, with a simple protocol in water solution. After a first screening, with another research group in our University, that commonly synthetized bisphosphonate molecules, we developed an easy way of functionalization, finding the best condition of attachment.

First protocol

A water dispersion of MZNs, 10 mg/ml, was made, using also ultrasonication tips. After that, phosphate molecules were added, in order to reach the final concentration of 10-15 mM. The dispersion was left under vigorous stirring overnight. Nanoparticles are recovered via centrifugation, 12000rpm for 10 minutes, and washed with water at least three times. If the recovering was not enough after centrifugation, a Millipore filter with 0.2 µm porosity paper was used.

Final protocol

A 10 mg/ml dispersion of nanoparticle in acetate buffer at pH 4.00 was made. The right amount of phosphonic acid was added, for having a 10 mM solution of it. The dispersion was left stirring for 1 hour, to allow the complete functionalization. Nanoparticles are recovered through centrifugation as for the previous protocol and washed several times.

With these protocols many functionalized zirconia nanoparticles have been product, the phospho-derivates used are represented in Scheme 1.

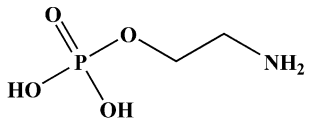

2-aminoethyl dihydrogen phosphate

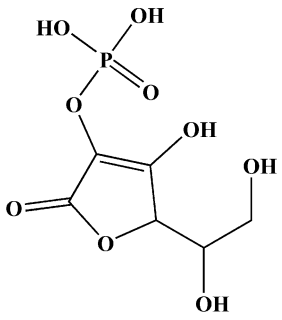

2-phospho-L-ascorbic acid

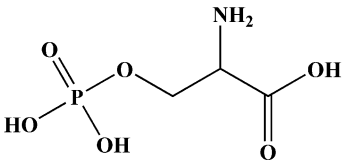

L-phosphoserine

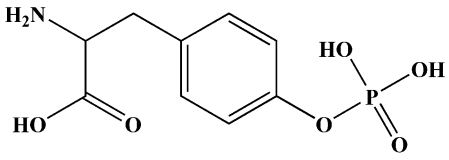

O-phosphotyrosine

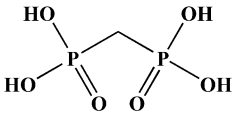

metilenbisphosphonate

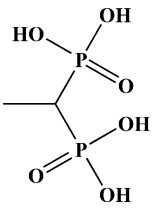

etilenbisphosphonate

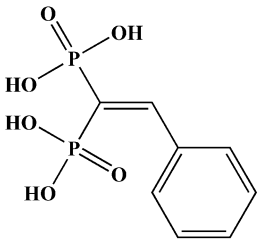

2-phenylethene-1,1-dyilphosphonic acid

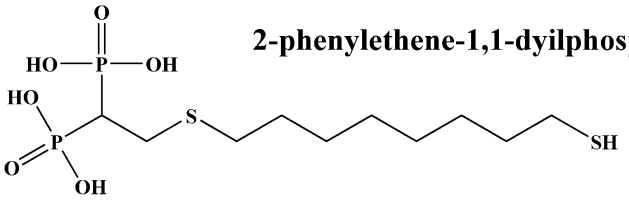

(2-((8-sulfanyloctyl)sulfanyl)ethane-1,1-diyl)bis(phosphonic acid)

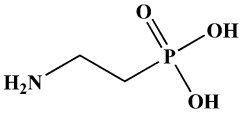

2-aminoethylphosphonic acid

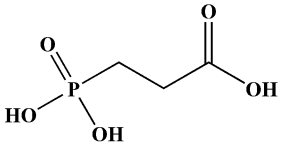

3-phosponopropionic acid

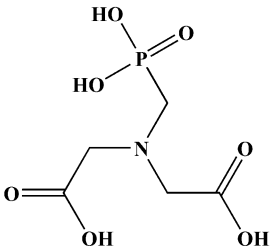

N-(phosphonomethyl)iminodiacetic acid

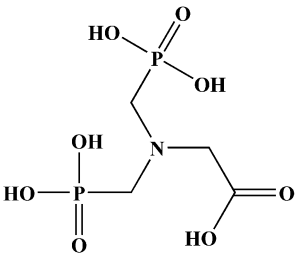

N,N-Bis(phosphonomethyl)glycine

Scheme 1: Phosphate and phosphonate used for the modification of MZNs

2.3. Theranostic applications

To produce a biosensor or a theranostic system, different magnetic nanoparticles have been developed, to find the best properties for our purposes.

2.3.1. Modifications of MZNs with magnetic phase

Starting from a procedure already studied from our research group [135], MZN with cobalt ferrite inside pores has been made. Comparison with silica was also done: mesoporous silica nanoparticles (MSN) were prepared with template sol-gel method already reported elsewhere [136] and cobalt ferrite was introduced inside the pores with procedure of A. Parma *et al*. [135].

MSNs protocol

In a beaker big enough, CTAB was dissolved in water and sodium hydroxide. N-hexane was then added and left stirring for at least 15 minutes to make an emulsion. Then, the stirring was stopped to allow phase separation, and TEOS was added dropping on the walls of the container. Stirring was turn on again and a vortex was made from the top to the bottom of the solution, being careful that the top surface was uniform. The reaction carries on for five hours at room temperature. In Table 2 molar ratio has been reported. The product was filtered with gooch and washed alternatively with water and methanol for three times. The powder was left drying overnight in an oven at 60 °C and then calcined with the following launching steps: 90 °C, 1 °C/min, 2 hours hold; 550 °C, 2 °C/min, 5 hours hold.

Table 2: Molar ratio of precursors for MSNs synthesis

	MW (uma)	Density (g/ml)	Purity (%)	Molar Ratio
n-hexane	86.18	0.66	95.00	25.10
H_2O	18.00	1.00	100.00	1268.00
NaOH (2M)	40.00	/	/	0.32
CTAB	364.45	1.00	98.00	0.12
TEOS	208.33	0.93	98.00	1.00

MSN@$CoFe_2O_4$ protocol

Mesoporous SiO_2 nanoparticles (0.3 g) were impregnated with an aqueous solution (4 mL) of $Co(NO_3)_2$*$6H_2O$ (0.061 g, 0.21 mmol) and of $Fe(NO_3)_3$*$9H_2O$ (0.168 g, 0.42 mmol) salts in accord with the stoichiometric ratio of Co and Fe required to give the desired nominal fraction of cobalt-iron oxide ($CoFe_2O_4$). This weight fraction of $CoFe_2O_4$ was fixed to 14% of the total composite weight ($CoFe_2O_4$@SiO_2) (4% mol/mol). After stirring the suspension overnight, the sample was dried by removing the solvent under reduced pressure. The impregnated material was annealed at 700 °C for 12 hours in air, with launching steps as follow: 10 °C/min, 200°C; 5°C/min, 500°C; 2.5°C/min, 700°C.

MZN@$CoFe_2O_4$ protocol

10 mg/ml of mesoporous zirconia nanoparticles (MZNs) are dispersed in ultrapure water and are impregnated using nitrate salts of the desired metal (Co and Fe) in the required amount. After stirring overnight, the impregnated materials are dried in vacuum and then annealed at 700 °C for 12 h in air with launching steps as follow: 10 °C/min, 200°C; 5°C/min, 500°C; 2.5°C/min, 700°C. Three samples with different nominal content of cobalt ferrite ($CoFe_2O_4$ moles/ZrO_2 moles)× 100 have been obtained: 4%, 8% and 12,5%.

To study the possible solid solution made between ZrO_2 and Fe_xO_y and its behaviour, samples with only iron were made. Indeed, it is shown in literature that iron can goes inside the crystal structure of zirconia, stabilizing unfavoured crystal phases [47, 137-138].

MZN@Fe_xO_y protocol (MZN@Fe)

10 mg/ml of mesoporous zirconia nanoparticles (MZNs) were dispersed in ultrapure water and are impregnated using nitrate salts of Fe in the required amount. After stirring overnight, the impregnated materials are dried in vacuum and then annealed at 700 °C for 12 h in air with launching steps as follow: 10 °C/min, 200°C; 5°C/min, 500°C; 2.5°C/min, 700°C. Two samples with different nominal content of iron (Fe moles/ZrO_2 moles)× 100 have been obtained: 4% and 6%.

The system was characterized with several techniques: SEM, TEM, XRPD, SAXS, SQUID, DLS, Mössbauer and at MCX line in Elettra Synchrotron in Trieste.

2.3.2. Modifications of the system to obtain a biosensor

To apply these nanosystems in biomedical field, MZN@$CoFe_2O_4$ at 8% have been modified superficially, with previously reported protocols (in Functionalization of MZN). Molecules used for the functionalizations of this system are: 3-phosphonopropionic acid, 2-aminoetilphosphonopropionic acid and (2-((8-sulfanyloctyl)sulfanyl)ethane-1,1-diyl)bis(phosphonic acid).

The so modified nanoparticles were then linked to probe or targeting moieties via different ways.

The system modified with BPODE was used to link gold nanoparticles obtained by laser ablation from the research group of Prof M. Meneghetti from Università degli Studi of Padova.

Protocol for the synthesis of AuNP

Gold nanoparticles (AuNP) were synthesized using the laser ablation synthesis in solution (LASiS) method (7). LASiS was conducted by focusing pulses (9 ns, 1064 nm, 10 Hz) of a Nd:YAG (Quantel YG981E) laser on a pure (99.999%) gold target under water at room temperature and pressure. The colloidal solution of AuNP was stable without surfactants or other stabilizing molecules because of the native negative charges present on the NP after the ablation. AuNP were obtained with

average dimensions of 25 nm and ζ-potential of -30 mV. Nanoparticles can be easily functionalized because of their naked surface.

Synthesis of MZN@$CoFe_2O_4$@AuNP protocol

0.7 mg of MZN@$CoFe_2O_4$ nanoparticles, functionalized with (2-((8-sulfanyloctyl)sulfanyl)ethane-1,1-diyl)bis(phosphonic acid) were dispersed in 1 ml of distilled water. The solution was centrifuged at 800 rcf for 3 minutes to eliminate aggregates. After magnetic separation, the zirconia based nanoparticles were dispersed in 1 ml of AuNP water colloidal solution (3 10^{-9} M), synthesized with Laser Ablation assisted Synthesis in Solution (LASiS) (see above) [139]. Modification of the MZN@$CoFe_2O_4$ nanoparticles with the AuNP (MZN@$CoFe_2O_4$@AuNP) was obtained after sonicating for two hours and with the addition of a NaCl solution to a final concentration of 20 mM. Cleaning from free AuNP was obtained by magnetic sorting. Finally, the SERS reporter, Malachite-green functionalized with a thiol function [140] (20 µl at 30 µM), was added to MZN@$CoFe_2O_4$@AuNP dispersed in 1 ml of distilled water. After sonicating for 45 minutes MZN@$CoFe_2O_4$@AuNP were cleaned three times by magnetic sorting.

To compare the system with a non-magnetic one, the same construction was made with bare MZNs.

Synthesis of MZN@AuNP protocol

0.7 mg of MZN nanoparticles, functionalized with BPODE molecule, were centrifuged at 650 rcf for 8 minutes to eliminate aggregates. Then the supernatant was centrifuged at 25000 rcf for 10 minutes and after elimination of the supernatant, 1 ml of AuNP water colloidal solution (3 10^{-9} M), synthesized with laser ablation assisted synthesis in solution (LASiS) [139] were added. Sonication and the solution of NaCl were used as in the case of MZN@$CoFe_2O_4$@AuNP. Cleaning from free AuNP was obtained by centrifugation at 810 rcf for 6 minutes since denser AuNP were precipitated whereas MZN@AuNP nanostructures were recovered from the supernatant. Texas red functionalized with two thiols [140-141] (20 µl at 30 µM), was added, as a SERS reporter, to 1 ml of MZN@AuNP in water. After sonicating for 45 min the nanostructures were cleaned three times from the reporter, by centrifugation.

The system was then tested and characterized with SEM, TEM, DLS, magnetophoretic measurements and SERS.

2.3.3. Obtaining a porous structure coupling $CoFe_2O_4$ and MZNs

A theranostic system, which could be the one just described, can be improved by porosity of it, making the loading of molecules, such as drugs, growth factors or proteins, possible. So, test was performed to obtain a porous nanocomposite using wet impregnation methods previously reported on already synthetized MZNs, but with thermal treatment at lower temperature.

MZN@$CoFe_2O_4$ protocol

10 mg/ml of mesoporous zirconia nanoparticles (MZNs) are dispersed in ultrapure water and are impregnated using nitrate salts of the desired metal (Co and Fe) in the required amount (for the 8% mol/mol). After stirring overnight, the impregnated materials are dried in vacuum and then annealed at 450 °C for 4 h in air with launching steps as follow: 10 °C/min, 200°C; 5°C/min, 450°C.

To improve the magnetic properties and make a coupled system with MZNs and maintain porosity, single-domain magnetic seeds were used as core. Polyol synthesis for cobalt ferrites has been initially chosen for this purpose.

Protocol for polyol

$Fe(NO_3)_3$*$9H_2O$ (2 mmol) and $Co(NO_3)_2$*$6H_2O$ (1 mmol) were dissolved in 1 ml of water and added to 100 ml of TEG in a 250ml round bottom flask. The solution was heated until the boiling point (around 280 °C) and kept in reflux for 2 hours with magnetic stirring. The product was then recovered through magnetic separation and washed twice with 10 ml of acetone.

The seeds obtained in this way were then used to growth MZN.

$CoFe_2O_4$@MZN protocol

The synthesis occurs as in the "Synthesis of Mesoporous Zirconia Nanoparticles", with two variations. The desired amount of $CoFe_2O_4$ seeds are dispersed in the solution of ethanol, water, salts and surfactant through sonication, then the solution of zirconium precursor was added under mechanical stirring at high speed (>700 rpm), instead of the magnetic ones. Weight ratio between seeds and expected zirconia tested is 1:2.

2.3.4. Synthesis of core-shell structure of different spinel ferrites

In order to further improve the system for biomedical application, in particular magnetic properties, core-shell structure of single-domain magnetic nanoparticles have been developed, in collaboration with the research group of D. Peddis of CNR-ISM of Roma and G. Singh of NTNU of Trondheim.

The typical procedure used was developed optimizing the one from S. Sun *et al*. [107]. It consists in the thermal decomposition of acetylacetonate precursors of the desired metals and proceed with a seed mediated growth of the core-shell system.

Core protocol

In a typical procedure, $M(acac)_2$ and $Me(acac)_3$ in molar ratio 1:2 were placed in a two-neck round bottom flask (100 ml) with 20 ml Benzylether (BE). To this solution, 6 mmol of Oleic Acid (OA), 6 mmol of Oleylamine (OAm) and 10 mmol of 1,2-hexadecanediol (HDD) were added. The solution was mixed under N_2 or Ar flux and undergoes a heating process with a first step at 200 °C (heating rate 5 °C/min) kept for 2h and a second step up to 300 °C (heating rate 5 °C/min) keeping for 1h. After cooling down to room temperature, the sample was purified from excess reactants

with several washings in ethanol, acetone and toluene in centrifuge at 4000 rpm for 10 minutes each or through magnetic separation.

Core-shell protocol

Once the core is formed, another synthetic step was required to obtain the shell. In a typical procedure, around 20 mg of core NPs were placed in a two-neck round bottom flask (100 ml) with 5 ml of BE and 0.6 ml of OA to create a homogeneous dispersion. Then, an appropriate amount (0.33 mmol) of $M(acac)_2$ and $Me(acac)_3$ were added. Finally, 15 ml of BE and 0.6 ml of OA were added and left to mix. After a vacuum cycle to eliminate oxygen from the reaction flask, the reaction proceeded under Argon for 30 minutes at 290 °C (heating rate 5 °C/min). After cooling down to room temperature, the sample was magnetically washed overnight in toluene and isopropanol and washed three times with the same solvents to eliminate by-products or excess of reagents.

Many core-shell structures have been synthetized, changing the content of M and Me, both of the core and the shell. In particular, cobalt ferrite was doped with nickel and zinc to change hard and soft character of the material in the system. In Table 3 synthetized systems are summarised.

Table 3: Core-Shell systems synthetized

	Core	Shell	
	$CoFe_2O_4$	$CoFe_2O_4$	Zn doped shell
		$Zn_{0.25}Co_{0.75}Fe_2O_4$	
		$Zn_{0.5}Co_{0.5}Fe_2O_4$	
		$Zn_{0.75}Co_{0.25}Fe_2O_4$	
		$ZnFe_2O_4$	
		$CoFe_2O_4$	Ni doped shell
		$Ni_{0.25}Co_{0.75}Fe_2O_4$	
		$Ni_{0.5}Co_{0.5}Fe_2O_4$	
		$Ni_{0.75}Co_{0.25}Fe_2O_4$	
		$NiFe_2O_4$	
Zn doped core	$Zn_{0.25}Co_{0.75}Fe_2O_4$	$CoFe_2O_4$	Ni doped shell
		$Ni_{0.25}Co_{0.75}Fe_2O_4$	
		$Ni_{0.5}Co_{0.5}Fe_2O_4$	
		$Ni_{0.75}Co_{0.25}Fe_2O_4$	
	$Zn_{0.5}Co_{0.5}Fe_2O_4$	$CoFe_2O_4$	
		$Ni_{0.25}Co_{0.75}Fe_2O_4$	
		$Ni_{0.5}Co_{0.5}Fe_2O_4$	
		$Ni_{0.75}Co_{0.25}Fe_2O_4$	
	$Zn_{0.75}Co_{0.25}Fe_2O_4$	$CoFe_2O_4$	
		$Ni_{0.25}Co_{0.75}Fe_2O_4$	
		$Ni_{0.5}Co_{0.5}Fe_2O_4$	
		$Ni_{0.75}Co_{0.25}Fe_2O_4$	
Ni doped core	$Ni_{0.25}Co_{0.75}Fe_2O_4$	$CoFe_2O_4$	Zn doped shell
		$Zn_{0.25}Co_{0.75}Fe_2O_4$	
		$Zn_{0.5}Co_{0.5}Fe_2O_4$	
		$Zn_{0.75}Co_{0.25}Fe_2O_4$	
	$Ni_{0.5}Co_{0.5}Fe_2O_4$	$CoFe_2O_4$	
		$Zn_{0.25}Co_{0.75}Fe_2O_4$	
		$Zn_{0.5}Co_{0.5}Fe_2O_4$	
		$Zn_{0.75}Co_{0.25}Fe_2O_4$	
	$Ni_{0.75}Co_{0.25}Fe_2O_4$	$CoFe_2O_4$	
		$Zn_{0.25}Co_{0.75}Fe_2O_4$	
		$Zn_{0.5}Co_{0.5}Fe_2O_4$	
		$Zn_{0.75}Co_{0.25}Fe_2O_4$	
	$NiFe_2O_4$	$CoFe_2O_4$	
	Fe_3O_4		

Moreover, protocols were used to try to introduce a dielectric shell. Zirconium oxide has been chosen as dielectric material and Fe_3O_4 as magnetic core, due to possible further employment in the coupling with MZN and the affinity between the two materials.

ZrO_2 shell protocol

For the synthesis of ZrO_2 shell on Fe_3O_4 cores the classical procedure was used, with $Zr(acac)_4$ as zirconium source. Around 20 mg of core NPs were placed in a two-neck round bottom flask (100 ml) with 5 ml of BE and 0.6 ml of OA to create a homogeneous dispersion. Then, an appropriate amount (0.33 mmol) of $Zr(acac)_4$ was added. Finally, 15 ml of BE and 0.6 ml of OA were added and left to mix. After a vacuum cycle to eliminate oxygen from the reaction flask, the reaction proceeded under Argon for 30 minutes at 290 °C (heating rate 5 °C/min). After cooling down to room temperature, the sample was magnetically washed overnight in toluene and isopropanol and washed three times with the same solvents to eliminate by-products or excess of reagents.

Furthermore, for trying to have hydrophilic core-shell particles, ligand exchanges are performed. N,N-(bisphosphonometyl) glycine and N-(phosphonomethyl)-iminodiacetic acid are used. Some protocols were tested: first the one of X. Wang *et al*. [142] was tested, then basic conditions were applied.

First protocol

10 mg of NPs ($CoFe_2O_4$) with hydrophobic ligands were put with 100 mg of the new ligand (N-(Phosphonomethyl)iminodiacetic acid hydrate) in 4 ml of EtOH and sonicated for 10 minutes. Stirring for 20 minutes was performed, and hexane was added to be sure of the exchange happening and wash the particles with ethanol and hexane several times. If the ligand precipitate as a white solid, wash it with water and recover nanoparticles with a magnet.

Basification protocol

Nanoparticles were suspended in CAPS buffer at pH 10, 25 mM, with the new ligand with 1:2 weight ratio. The dispersion was sonicated for half an hour and put in mechanical agitation for 2 hours. The product was washed first with water, to remove the excess of ligand, then with NaOH solution, 0.5 M, to stop the acidification from the new ligand.

The same could be done in THF instead of buffer solution to allow a better dispersion in the solvent without aggregates.

2.4. Orthopaedic applications

2.4.1. Surface modifications of bulk material

After the modification with phospho-derivate molecules, it has been seen that MZNs deposit on different surface spontaneously. Starting from this point, it has been decided to try to modify bulky surfaces in the strongest way as possible to avoid the leakage of nanoparticles, with different technique and exploiting different kind of bonds.

Layer by layer technique is usually used to modify surfaces with organic molecules, polymer or silane, using also the sol-gel chemistry [143]. Different kind of interaction can be used, such as electrostatic bond, covalent bond, hydrophobic interaction and so on. All these kinds of links are affected by environmental conditions, that determine the successful of covering and the stability of the layer. Nanoparticle layer deposition is a technique that is in development and, nowadays, not widely used due to the lack of protocols to make a reproducible cover of surfaces [144].

Many techniques are used to modify the surface of a solid: sputtering, dip coating, spin coating, spray-coating, plasma coating, drop casting, electrochemical deposition and electromagnetic deposition [70, 73, 145-146]. The drop casting consists on the deposition of a drop on a flat surface, that evaporating deposits nanoparticles. The thickness of the layer depends on the concentration of nanoparticles in the colloidal solution and can be tuned also varying ionic force, pH and volatility of the solvents. On the other hand, dip coating is the removal of the substrate from a solution in a controlled way, with particular care on speed and contact angle with the solution. Viscosity and capillary effects govern the deposition and is crucial to avoid drastic effect during evaporation of the solvent to allow the formation of a homogeneous layer. Also in this case, physical-chemical properties of the solvent are crucial for the deposition, also because they can affect the affinity with the surface [147].

Therefore, starting from the evidence of layer organization during solvent evaporation of modified nanoparticles, a methodological study has been conducted.

Different modifications of nanoparticles have been used, moreover, some surfaces have been modified to improve affinity with MZNs. Some of the used surfaces were modified, using atmospheric plasma device, by NADIR srl.

Drop casting protocol

A colloidal solution of modified MZNs, with a concentration of 5 mg/ml, was made using also ultrasonication tips to remove aggregates. With a micropipette, a drop of 4 µl was deposited on the surface and left drying at air condition.

MZN-L-phosphoserine (MZN-PSER) was used as modified nanoparticles. Amino-modified glass and aluminium with different roughness degree were used as testing surfaces. Solvents used were listed in Table 4.

Table 4: List of solvents used for the drop casting deposition method

Solvent	**Concentration (mM)**	**pH**
Ultrapure Water	/	/
Methanol	/	/
Ethanol	/	/
Iso-propanol	/	/
Acetone	/	/
Sodium acetate buffer	25	4
Sodium acetate buffer	25	4.8
MES buffer	25	5
MES buffer	25	6.3
TRIS buffer	25	7
TRIS buffer	25	7.5
Sodium borate buffer	25	8.2
Sodium carbonate buffer	25	8.7
CAPS buffer	25	9.6

Dip coating protocol

A colloidal solution of modified MZNs, with a concentration of 10 mg/ml, was made using also ultrasonication tools to remove aggregates. The substrate was immersed in the suspension and removed with controlled speed fixed at 0.01 mm/s.

MZNs used for dip coating procedure were modified with: L-phosphoserine, 2-phenylethene-1,1-dyilphosphonic acid, 3-phosphonopropionic acid and 2-aminoethyl dihydrogen phosphate. Glass, amino-modified glass, silicon wafer, aminated silicon wafer, carboxy-modified silicon wafer, copper, aluminium, bare and aminated titanium were used as testing surfaces. Solvents used were listed in Table 5.

Table 5: Solvent used for dip coating protocol

Solvent	**Concentration (mM)**	**pH**
Ultrapure water	/	
Ethanol	/	
Acetone	/	
Sodium acetate buffer	5	4
MES buffer	5	6.3
TRIZMA buffer	5	7
Sodium carbonate buffer	5	8.7

Surface modification

As mentioned above, modified surfaces have been used to improve affinity with nanoparticles. Physical and chemical method have been employed to obtain such target. Bare surfaces were used for plasma deposition method, while the oxidation is needed for chemical methods to produce anchoring sites.

Plasma deposition method

The desired surface was put at 3 mm from plasma nozzle and a first activation step was done. To avoid boundary effects, the surface was surrounded with inert material. After this step, Ar gas was gurgled in a monomer solution of the wanted modification agent, with different flux depending on the reagent, to allow the vaporization of the precursor and the transfer through the plasma nozzle. The torch was moved with constant speed of 10 mm/s, and the deposition could be done with continuous or pulsed mode. MMA and APTES were used to modify glass, silicon or titanium with this protocol.

Titanium oxidation

Titanium was left in a piranha solution (sulfuric acid and hydrogen peroxide 5:1) for three hours. After that time, the solid was removed from the solution and washed with water and ethanol [61]. The surface can be removed from the reacting environment with dip coating tools or manually.

Sol-gel amination

A solution with 5% vol/vol of water in ethanol was made and the pH was adjusted around 5 with acetic acid. 5 % vol/vol of APTES was added under vigorous stirring and it was left hydrolysing for at least 5 minutes at room temperature. Then the substrate was added and left reacting for 2 hours. The solid was removed and washed with ethanol to remove the excess of APTES. To complete the condensation, it was put in oven at 120 °C for half an hour [148]. The surface can be removed from the reacting environment with dip coating tools or manually.

Phosphonate modification

After the oxidation of titanium sheet, a modification with 2-aminoethyl phosphonic acid was done. The substrate was put in a 25 mM solution of the phosphonic acid in ultrapure water and left under stirring for 2 hours. Then the slab was removed and washed with water to remove unbonded molecules. The surface can be removed from the reacting environment with dip coating tools or manually.

Ninhydrin assay

To prove the presence of primary amine on the modified surfaces, the ninhydrin assay was done, only to prove the presence of it and not to quantify, with the appearance of violet-blue colour.

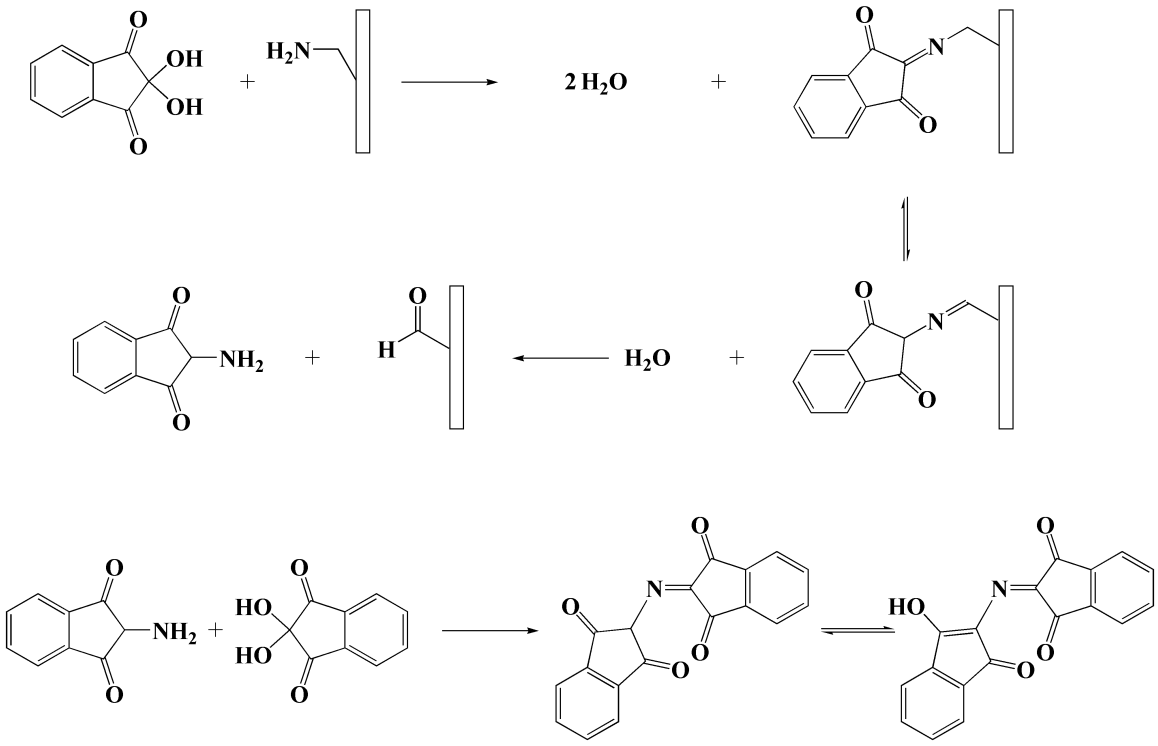

Scheme 2: Ninhydrin test reaction scheme

Protocol

800 µL of a 20 mM solution of ninhydrin in ethanol was added to 1 mL of water. The sheet was put in this solution and left reacting for 15 minutes at 90 °C to increase the kinetic of the reaction. The control solutions were made with a glycine solution 5.5 mM for the positive and of ultrapure water for the negative one.

Coupling with nanoparticles

Carboxylic modified MZNs (protocols previously reported) are linked through EDC/S-NHS (1-ethyl-3-(3-dimethylaminopropyl)carbodiimide hydrochloride/sulfo-N-hydroxysulfosuccinimide) protocol. Carbamide bond formation is the most common way used to couple an amine with a carboxylic group for biological purpose. Due to low toxicity and good knowledge of the process, EDC/S-NHS protocol was used [148].

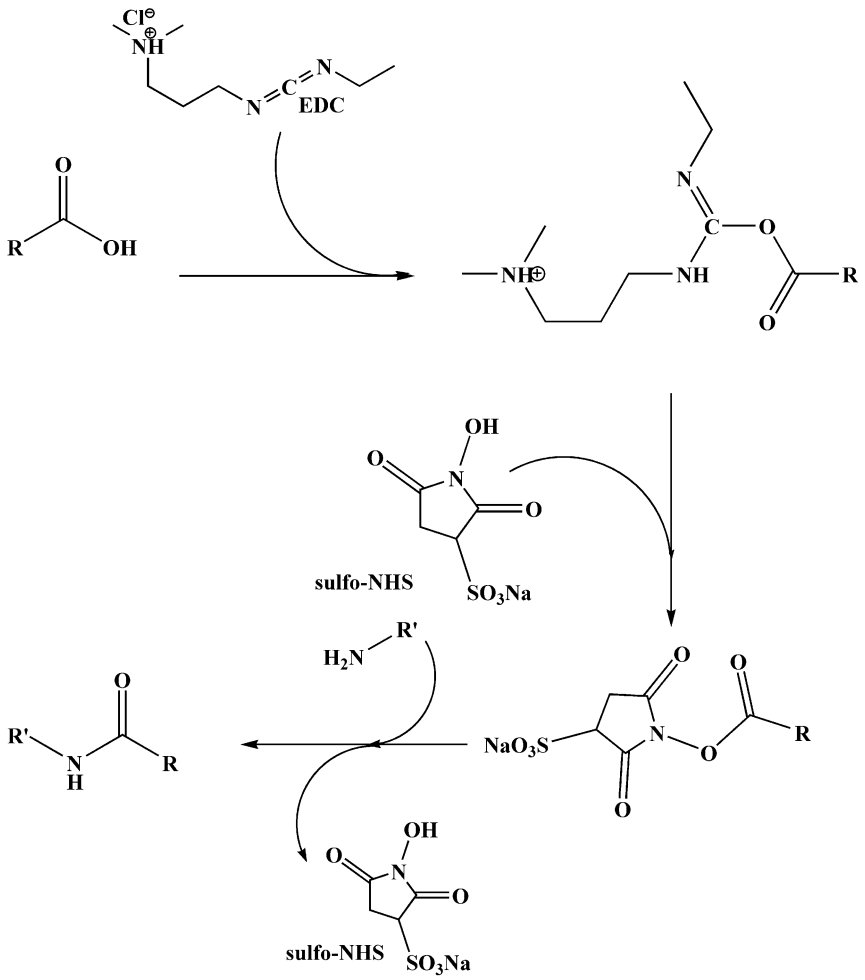

Scheme 3: Reaction mechanism of EDC/S-NHS coupling

Protocol

MZNs modified with a phosphonic acid having a carboxylic terminal group were suspended in MES buffer (20mM) at pH 5, with a concentration of nanoparticles of 10 mg/ml. EDC and S-NHS were added for having a final concentration of 4 mM and 8 mM, respectively. Suspension was left reacting for one hour at room temperature to activate the carboxylic group. Then MES buffer at pH 7.5 was added to increase the pH of the solution up to 7 and dilute nanoparticles to 5 mg/ml. Amino-modified surface was added to the solution and left reacting overnight. To stop the reaction, glycine was added for having a concentration of 5 mM, and left stirring for 30 minutes. The sample was removed and washed with a water bath under stirring for 30 minutes. The surface can be removed from the reacting environment with dip coating tools or manually.

Alternatively, carboxylated surfaces can be activated with EDC/S-NHS and aminated nanoparticles can be linked.

2.4.2. Silver modification of MZNs

In order to introduce silver nanoparticles inside pores of zirconia, several methods have been tried to produce a stable and antibacterial heterostructure. First the procedure of Tian *et al*. [149] has been adapted for our system, without the use of silane molecules.

Protocol

A solution of 2-aminoethyl dihydrogen phosphate (11 mM) and $AgNO_3$ (8 mM) was made with ultrapure water, to leave the formation of the complex with amino group and silver ion. Then MZN are added to the solution (final concentration of 10 mg/ml) and left stirring overnight. Formaldehyde solution (final concentration 1 mM) is added to reduce Ag^+ and left reacting for 3.5 hours under stirring. The product was recovered with centrifugation and washed three times with water.

To improve the system, a classical wet impregnation procedure was performed, taking into account to fill up half of the pore volume of MZNs with silver nitrate.

Protocol

MZNs were dispersed in water, 10 mg/ml, and $AgNO_3$ was added with a final concentration of 36.5 mM and left stirring overnight. The solvent is removed with depression using rotary evaporator. The silver in MZN@Ag^+ (25 mg) was reduced with 1.3 ml of formaldehyde solution (37% vol) and the powder turned to black color. After 1.5 hours of reaction, the product is filtered and washed with water.

For a creation of silver nanoparticles deeper inside pores of zirconia, procedures that involves insoluble Ag-derivates were studied. A method to produce AgCl was tried and tested with temperature programmed reduction (TPR) to see if a thermal treatment could be used to produce AgNP, maintaining porous MZNs. On the other hand, ways through Ag_2O were tried.

Protocol AgCl

An excess of NaCl was introduced inside pores of MZNs via wet impregnation method. The desired amount of NaCl was dissolved in water and MZNs were added for having 10 mg/ml concentration and left stirring overnight. After drying with rotary evaporator, 25% mol of $AgNO_3$ was added with a water solution and left stirring overnight as well. The dried powder was tested with TPR: a quartz tubular reactor, 4.84% H_2/Ar with gas flow of 40 ml/min as reducing agents, temperature range between 30 and 850 °C with 10 °C/min rating steps, anhydrone desiccant trap and thermo-conductibility detector at 100 °C were used.

Protocol Ag_2O

A solution of MZNs (10 mg/ml) and $AgNO_3$ (18 mM) was made with water and stirred for 2 hours. The solution was dried with rotary evaporator, then, 3M solution of NaOH was added in order to have at least the same moles of Ag and stirred for one hour. Dry the powder again and add a 33 mM glucose solution in excess to reduce Ag^+ to Ag^0, left reacting under stirring for an hour, then filter the product and wash with water. Glucose was used instead of formaldehyde to avoid toxicity of reagents that could misrepresent biological tests.

To increase the penetration inside the pores and the retention of Ag^+ ions on zirconia, a modified procedure of synthesis of MZNs was used to directly obtain modified nanoparticles with phosphate groups (MZN-PO_4) [150].

Protocol MZN-PO_4

The procedure described before for the synthesis of MZNs was modified using a solution of Na_2HPO_4 0.1 M instead of the one of NaF. All other parameters were left the same.

Protocol MZN-PO_4@Ag

A solution of MZN-PO_4 (10 mg/ml) and $AgNO_3$ (18 mM) was made with water and stirred overnight. The solution was dried with rotary evaporator, then, 3M solution of NaOH was added in order to have at least the same moles of Ag and stirred for one hour. Dry the powder again and add a 33 mM glucose solution in excess to reduce Ag^+ to Ag^0, left reacting under stirring for an hour, then filter the product and wash with water.

In order to prove the possibility of wet impregnation of $AgNO_3$ and calcination under reducing atmosphere, without destroying the porous structure of zirconia, three samples with different amount of silver (3, 25, 50% mol) were analysed with synchrotron radiation. MCX line at Elettra synchrotron in Trieste was used to analyse the behaviour of the particles with increasing temperature from 25 to 600 °C, with a temperature rate of 10 °C/min, and follow crystal phases transition of the system with X-ray diffraction.

2.4.3. Preliminary biological tests

Nanoparticle-modified surfaces and MZN@Ag were tested with bacteria to preliminary see the efficacy of these modifications.

Protocol for tests on bacteria

OD600 of overnight *E. coli* inoculum in NB was measured and serial dilutions were made into 5 ml of NB, in order to plate 400 CFUs. The experiments were conducted preparing NA with different concentrations of Ag@MZN and bare MZNs. Pictures of plates were then analysed with ImageJ.

2.5. Preliminary tests of coupling with antibodies

Carboxylic modified mMZN-8% (protocols previously reported) are linked through EDC/S-NHS protocol with antibodies [148]. The conjugation with antibodies was slightly different to be sure of maintaining the 3D structure of the protein: the procedure reported from Thermo Fisher (Dynabeads® MyOne™ Carboxylic Acid) was used.

Protocol for Abs conjugation

2.5 mg of nanoparticles were suspended in MES 25 mM at pH6 for having a concentration of 30 mg/ml. 2.5 mg of EDC and sulfo-NHS were added and the suspension was put in agitation with rotation at 40 rpm for 30 minutes at RT. The activated nanoparticles were washed three times with MES. Then, 125 µg of Ab were added, the solution was diluted for having 10 mg/ml concentration of nanoparticles and left in agitation with the same conditions as before. Ethanol amine 10 mM was used to stop the reaction. The precipitate was washed at least three times with MES or TRIS (pH7.4) or HEPES buffers and resuspended in a buffer suitable for protein conservation. Three types of Abs were used for the modification: Ab-HRP, transtuzumab and pertuzumab. The quantification of Ab-

HRP on the NPs was performed with the TMB modification, classical for ELISA tests. In particular, in a 96-wells plate, the sample for the calibration curves was put, with serial dilution from number 1 to 12, in the wells, and the right amount of TMB solution was added. The same was done with the unknown sample. After 10 minutes of reaction, TMB was stopped with the same amount of H_2SO_4 0.18 M solution and read at 450 nm using a plate reader with UV-Vis light.

3. RESULTS AND DISCUSSION

3.1. Synthesis of Mesoporous Zirconia Nanoparticles

Mesoporous zirconia nanoparticles were synthetized by a previous reported protocol, developed by our laboratory [6, 124]. It involves template sol-gel process for the synthesis of nanoparticles from metal alkoxide precursor, with alkali salts to produce double layer of charges around the particles to avoid aggregation. The extraction of the surfactant was performed with vacuum extraction to avoid crystallization and collapse of the nanoparticles [27]. The obtained nanoparticles are spherical with a good homogeneity in diameters, as one can see from Figure 7 and are also characterized by high surface area (ranging from 120 to 450 m^2/g) and high pores volume and pore diameters (~0.3 cm^3/g and 2.5-8 nm respectively) (Figure 8).

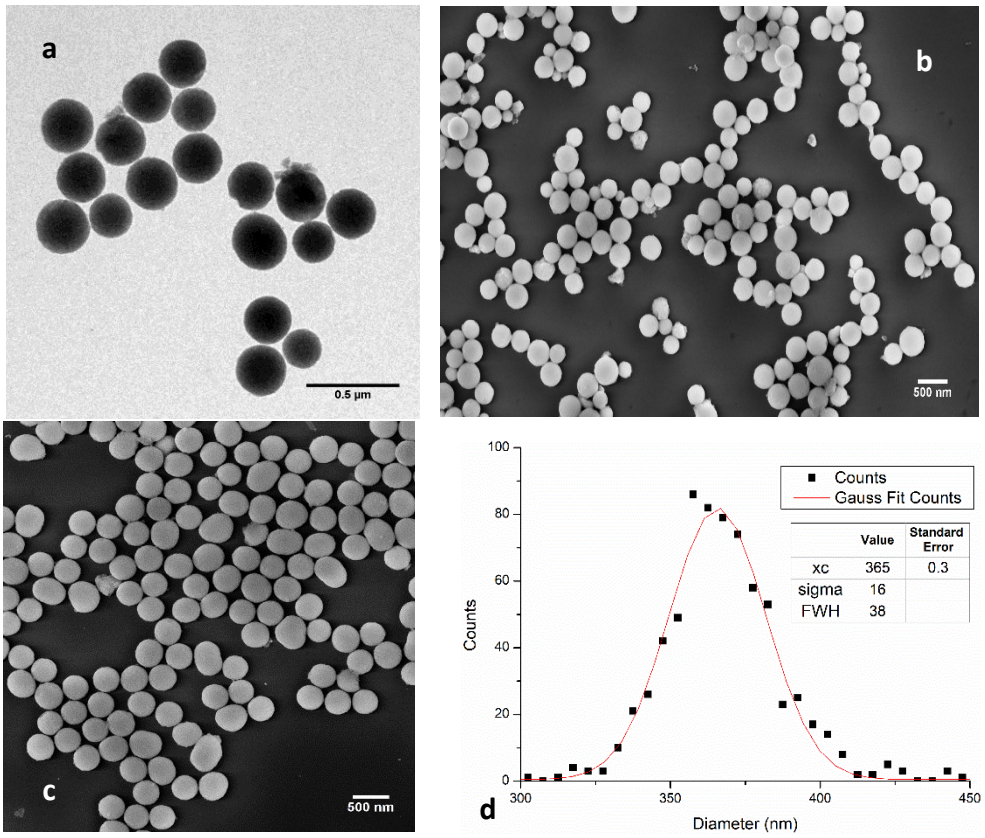

Figure 7: TEM (a) and FEG-SEM images of different batches of MZNs (b, c) and diameters distribution of nanoparticles (in c) fitted with Gaussian function (d)

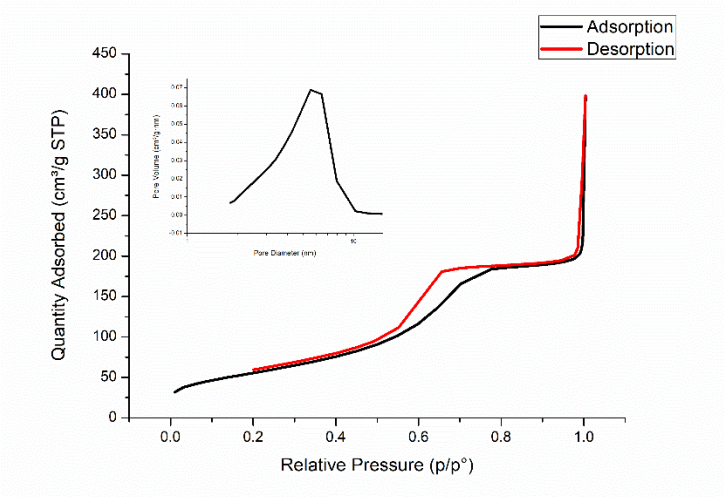

Figure 8: Nitrogen physisorption of MZN, with pore diameter distribution in the inlet

Amorphous or partially crystalline nanoparticles could be obtained with this synthesis even if no thermal treatment, except the hydrothermal one at 170 °C, were done. Figure 9 shows the XRD patterns of an amorphous and a semi-crystalline batch. Small and mainly tetragonal crystal nuclei, stabilized by the smallness of the crystallites sizes, can be found in some samples (Figure 9 red line).

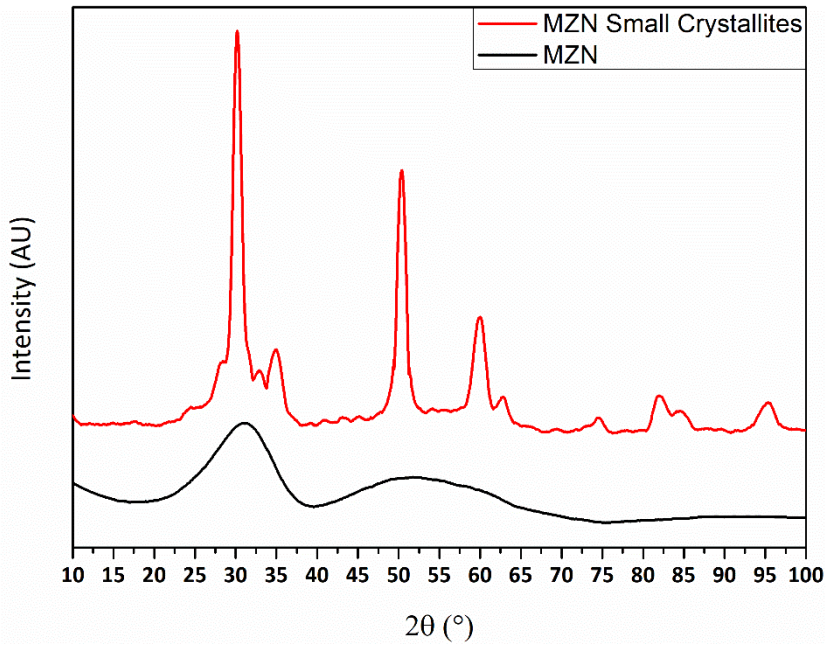

Figure 9: Comparison of XRPD on MZNs totally amorphous and with very small crystallites

Due to the fact that the syntheses were done at room temperature, seasoning influences shape and porosity of nanoparticles. Indeed, higher temperature produce higher diameter, larger pore and lower surface area. In Figure 10 season trend for surface areas and pores diameter is depicted. As one can see from this tendency, big changing happens in a laboratory with poorly controlled atmospheric conditions (temperature and humidity). For this reason, controlled conditions were tested (pointed in Figure 10),

performing the reaction in a closed thermostated round bottom jacket reactor where the temperature was fixed at 37 °C. In this way, smaller surface area and bigger pores were obtained.

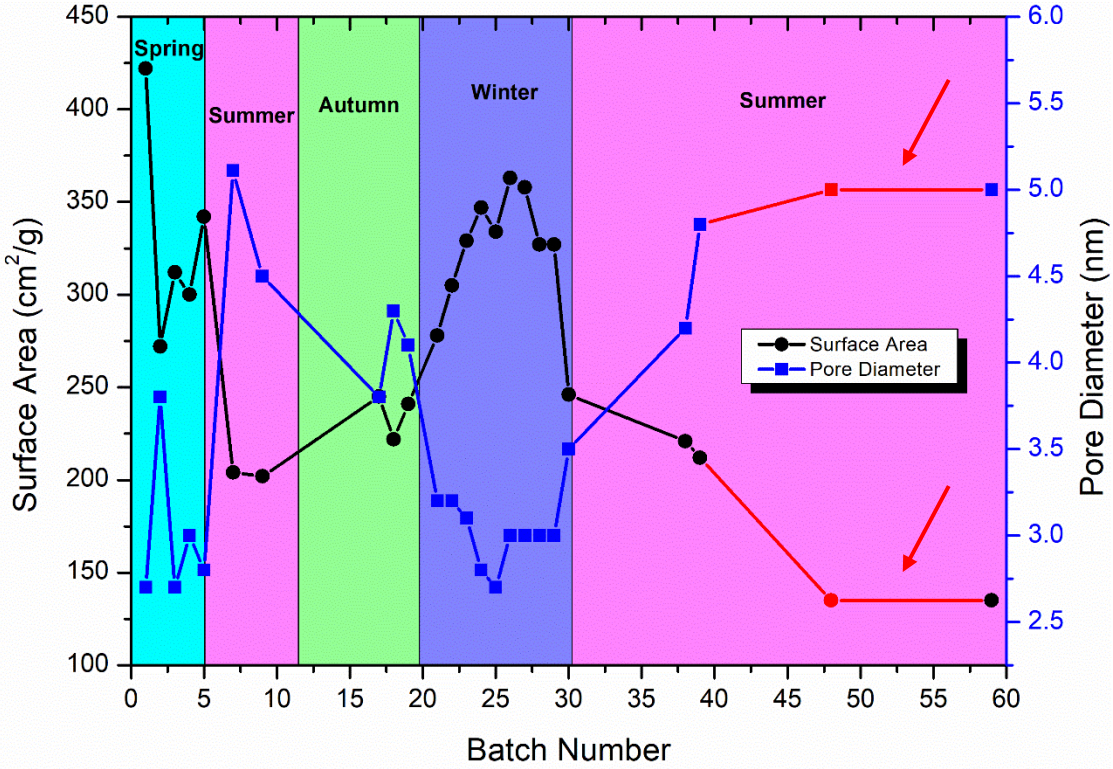

Figure 10: Seasoning trend of surface area (dots) and pore diameter (squares)

During these years, however, issue with zirconium precursor has been found. New Zirconium(IV) propoxide from Sigma Aldrich didn't lead to separate and spherical nanoparticles, conversely from what was obtained until that moment with the old Fluka ones. Before changing supplier to solve this problem, many ways have been tried: changing quantities of water and salts, diluting the system or aging precursor etc... (see Table 6). However, no solution and no explanation of the problem was found, and the study of the precursor did not show any differences between the two suppliers.

As one can see from Figure 11, precursor from Sigma Aldrich ever produce aggregates, while with the Fluka one nanoparticles appear well separated, spherical and monodispersed. A solution was found changing supplier for the precursors (Acros Chemicals) or changing alkoxide (Zirconium(IV) butoxide) but no clear explanation was given to the observed behaviour. Finally, with the control of the temperature, we were able to tune the pores and surface areas, with stable diameters and shapes for the appropriate application.

Table 6: List of modifications on the MZNs synthesis tested with Sigma Aldrich precursor

Batch name	*Change done*
MZN10	Normal condition
MZN11	Half ZP
MZN12	2/3 ZP
MZN13	3/4 ZP
MZN21	1/3 ZP
MZN20	1/2 ZP, controlled T
MZN22	Controlled T
MZN23	Aging
MZN25	Aging
MZN26	Aging
MZN27	Aging
MZN28	Double H_2O
MZN29	3/2 H_2O
MZN30	5/4 H_2O
MZN31	9/8 H_2O
MZN32	[NaF] 0.2M
MZN33	Tested each ½ hour
MZN34	1/2 H_2O
MZN35	3/4 H_2O
MZN36	Only salt solution
MZN37	1-Propanol

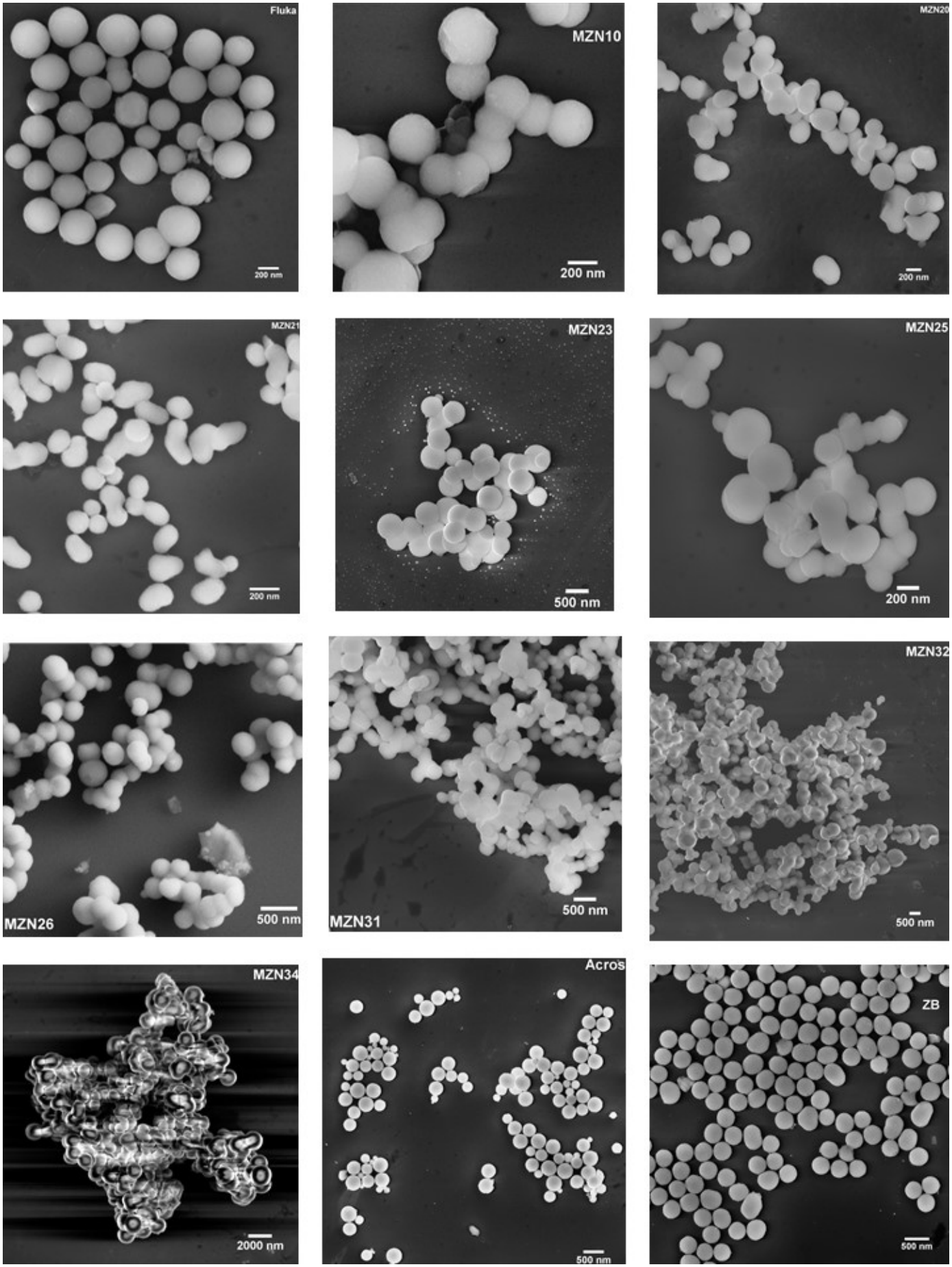

Figure 11:FEG-SEM images of different batches of MZN obtained with different conditions, name of batches or type/company of the precursor are put in each image.

3.2. Functionalization of MZNs

It is known from literature that Zr^{4+} has a certain affinity for phospho-derivates molecules [18, 127-128, 131, 151] and a surface modifications for MZN was developed, avoiding the use of a silica layer, usually employed in literature [17, 76], with a totally new library of molecules and way of functionalization. The firsts studies of the affinity of our zirconia nanoparticles were done with commercially available phosphate-molecules, such as 2-aminoethyl dihydrogen phosphate (PEA), 2-phospho-L-ascorbic acid trisodium salt (PAA), O-Phospho-DL-serine (PSer) and O-Phospho-L-tyrosine (PTyr) (Scheme 4) and synthetized 2-phenylethene-1,1-dyilphosphonic acid (BPPhE) (Scheme 5).

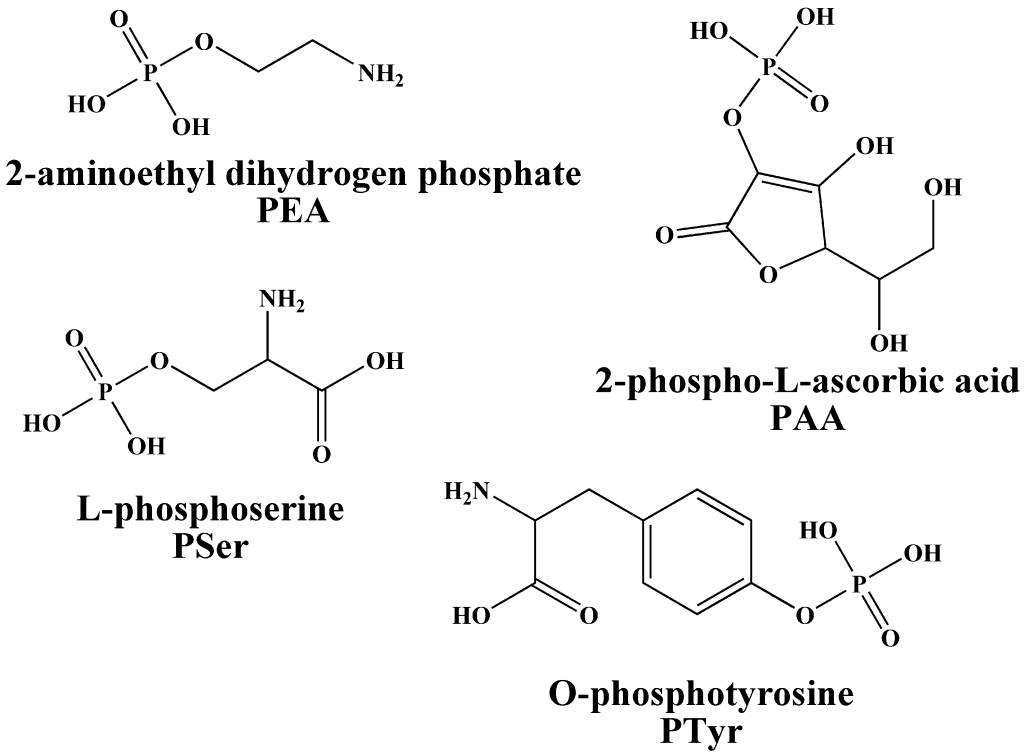

Scheme 4: Organo-phosphate molecules used for functionalizations

First preliminary tests included a long exposure (overnight) of the MZNs with a high concentration of commercial phospho-derivates molecules. ζ-potential and XPS measurements were used to study the modification of the surface of the nanoparticles.

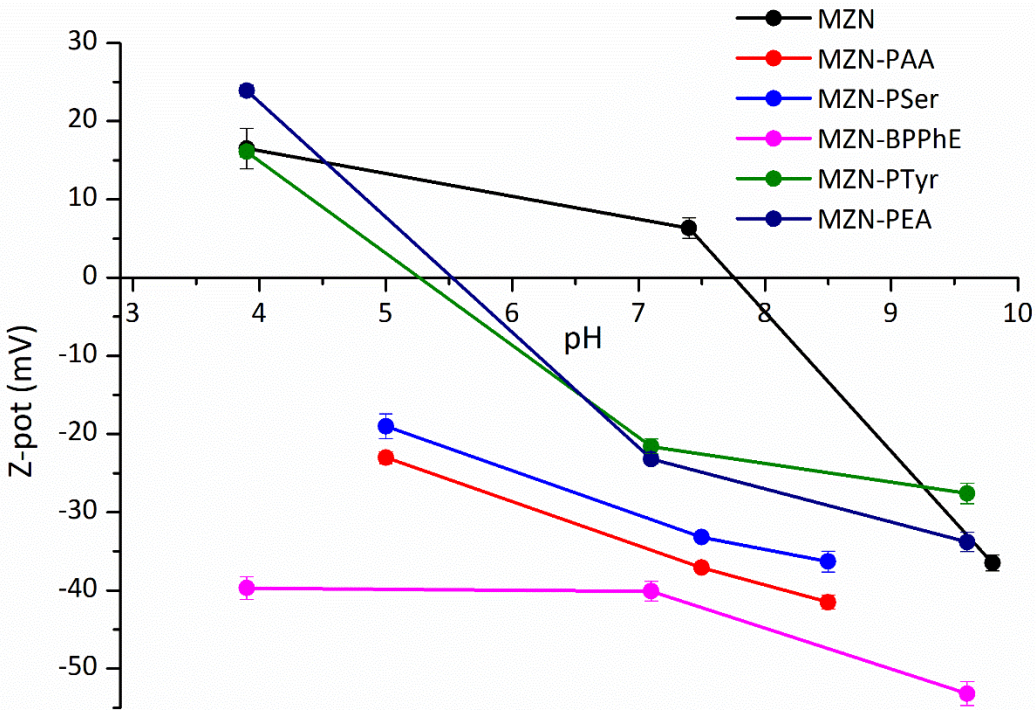

Figure 12: ζ-potential of firsts tests of functionalizations of MZNs

From ζ-potential measurements (Figure 12) it is clear how more acidic compounds change MZNs surface charges. Indeed, PSer and PAA modifications alter surface properties, giving to MZNs charges under -20 mV at all the tested pH values, that improves colloidal stability of nanoparticles. As a matter of fact, unmodified zirconia presents a sigmoid behaviour on titration with changing pH values, with an isoelectric point around pH 7.5, which means that under neutral conditions, aggregation of nanoparticles is favourite, and with more basic compounds, probably due to the compensation from the amino-group to the totally charge of the molecules, show an isoelectric point around pH 5.5. Moreover, from preliminary attempts, it was seen that bisphosphonic acid (BPPhE) largely improves the colloidal stability, providing higher surface charge in MZNs, as is visible in Figure 12.

XPS analyses were performed on these samples to further confirm the presence of phosphate and phosphonate on the surface of nanoparticles. Indeed, the XPS sampling depth is typically around 5-10 nm, and makes this technique able to evidence the presence, at the surface of the nanoparticles, of chemical elements belonging to the molecules of interest. From these analyses, presence of phosphor is confirmed both for the tested phosphate and phosphonate (Figure 13 and Table 7 and Table 8). However, nitrogen presence confirmation is difficult, due to its light elementary character, and for some of the examined species the amount of phosphor and nitrogen should be equal but for two samples the amount of nitrogen results lower than the phosphorous one, and with P-Tyr, no N was found (Figure 13b, blue line, Table 8). This could be due to the labile structure of the modifying molecule that can decompose during functionalization. The hypothesis of this lack of signal is the action of zirconia as a catalyst for the hydrolysis of the phosphoric ester bond, but further investigations should be necessary to confirm the hypothesis.

In Figure 13 bands related to P2p signal recorded with XPS are reported for the modified samples. As one can see, a small shift for the peak related to the bis-phosphonic acid (BPPhE) is present if compared to peaks related to phosphate molecules, that can be ascribed to the different nature of chemical environment of P atoms for phosphonic ones (one less O). The detected values are compatible with the chemical environment of the elements considered in the different functionalizing groups. In particular, the P2p BE values detected in all the P-containing samples (see Table 7) are slightly lower than those reported for the single phosphonate molecules [86]: this is ascribed to a chemical environment of the phosphorus atoms less electronegative, i.e. consistent with oxygen atoms not only bonded to phosphorus but also to NPs atoms (Zr in our case) as observed in similar systems [86, 134].

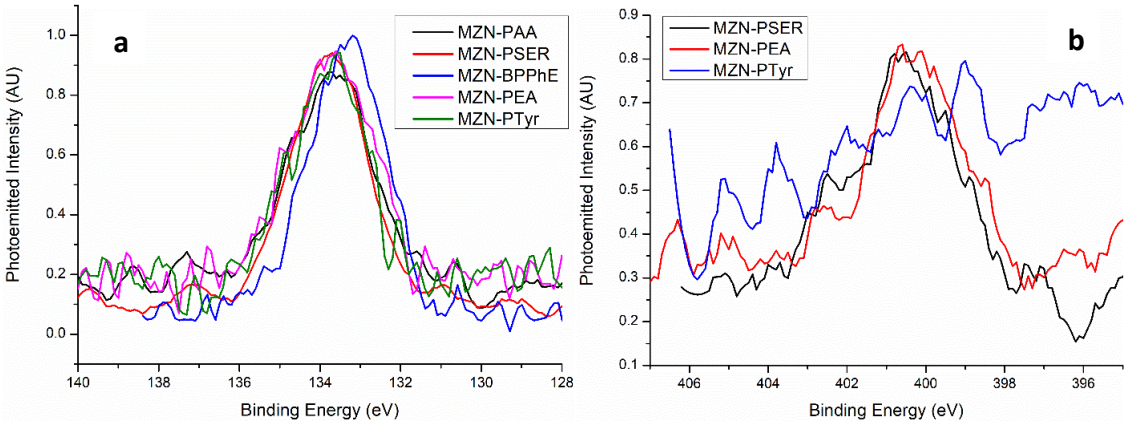

Figure 13: XPS P2p bands (a) recorded for MZN-PAA (black), MZN-PSER (red), MZN-BPPhE (blue), MZN-PEA (pink), MZN-PTyr (green) and XPS N1s bands (b) recorded for MZN-PSER (black), MZN-PEA (red) and MZN-PTyr (blue)

Table 7: Binding energy values of P2p and N1s bands as detected in the functionalized nanoparticles.

	P2p (eV)	**N1s (eV)**
MZN-PAA	133.7	-
MZN-PSER	133.8	400.6
MZN-BPPhE	133.3	-
MZN-PEA	133.7	400.3
MZN-PTyr	133.8	-

Table 8: C, O, Zr, P, S, and N atomic fraction as obtained by XPS data in MZN, MZN-PAA, MZN-PSER, MZN-PEA, MZN-PTyr, MZN-BPPhE samples

Sample	C%	O%	Zr%	P%	N%
MZN	26	52	22	-	-
MZN-PAA	21	60	17	~1.7	-
MZN-PSER	21	59	15	~3.4	~1.5
MZN-PEA	24	54	19	~1.7	~1.2
MZN-PTyr	32	52	14	~1.5	-
MZN-BPPhE	34	49	13	~4	-

Because of these preliminary results bisphosphonic acids with different terminal functional groups were developed in collaboration with Prof A. Scarso of Università Ca' Foscari of Venezia [152-154] and used to modify MZNs. The collaboration with Prof A. Scarso was also helpful for the develop of the better protocol of MZNs functionalizations, using Solution-NMR to follow the kinetics of coupling reactions (studies in best buffer solution and times of reaction). Methylenbisphosphonate (MBP), ethylenbisphosphonate (EBP) and (2-((8-sulfanyloctyl)sulfanyl)ethane-1,1-diyl)bis(phosphonic acid) (BPODE) have been used after first tests with 2-phenylethene-1,1-dyilphosphonic acid (Scheme 5).

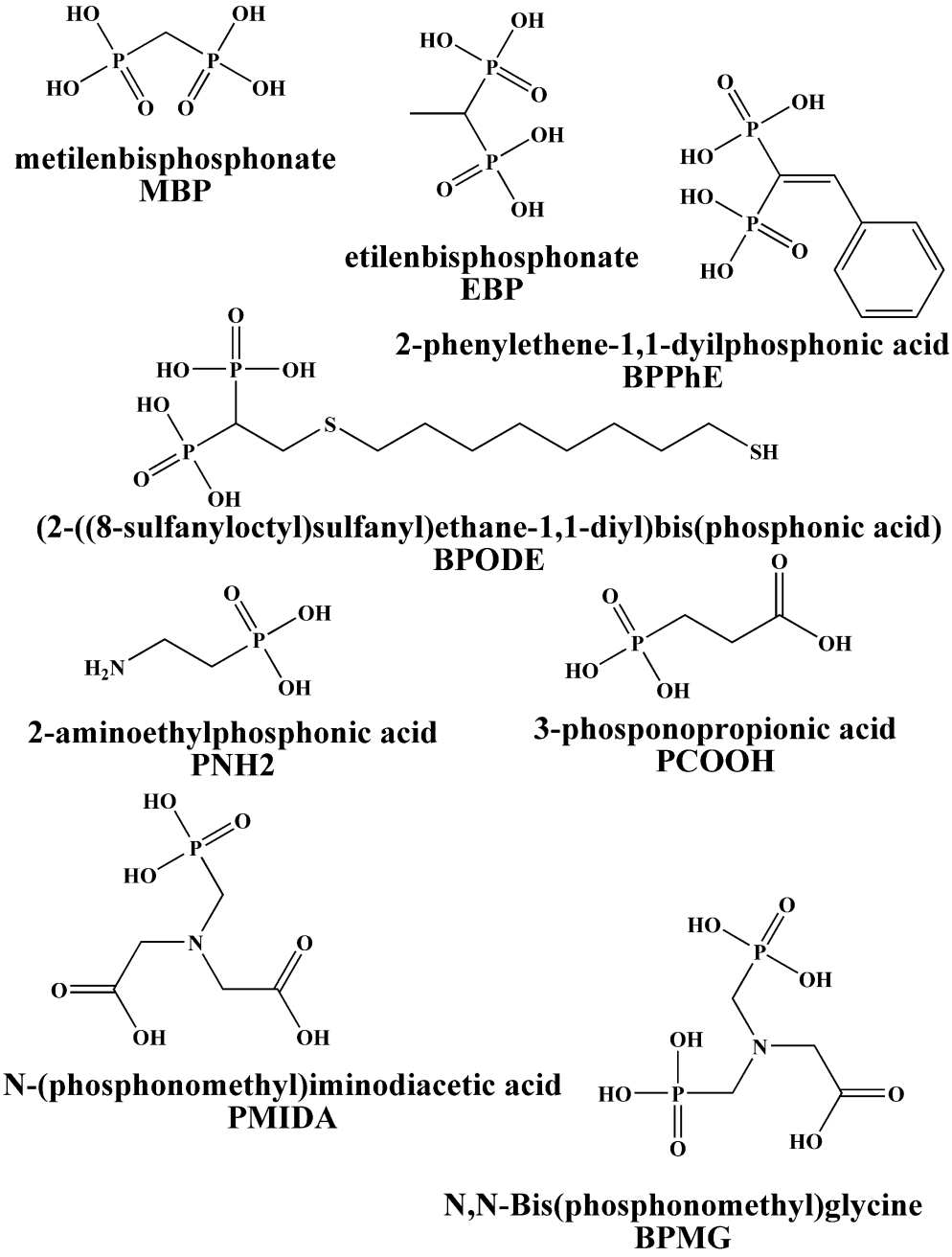

Scheme 5: Phosphonate molecules used for MZNs modifications

In Figure 14 trends of ζ-potential after modification with bisphosphonic acids at different pH are reported. As one can see, bisphosphonic acid give, also in this case, value of charges

ever lower than zero, so no isoelectric point is present for modified nanoparticles in the studied range. Lower values are the ones of MZN-BPODE, where, probably, -SH terminal group increases the negative charge.

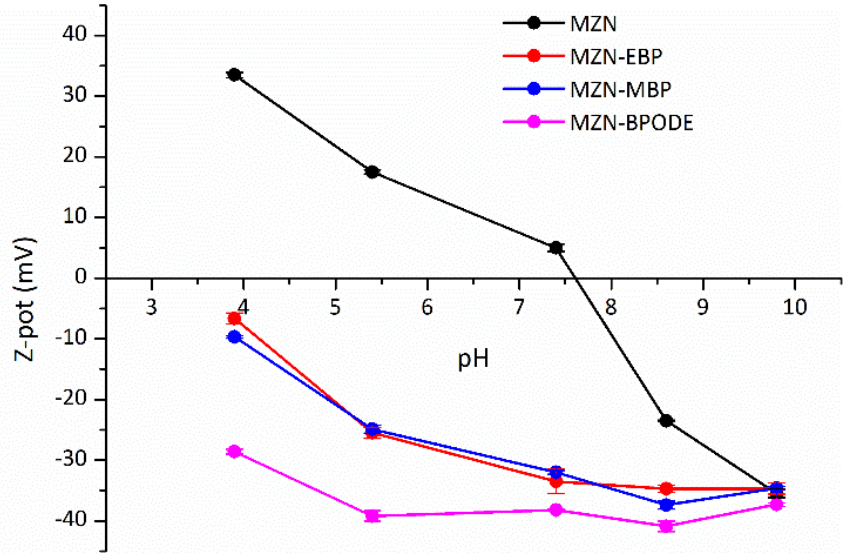

Figure 14: ζ-potential behaviour of MZN and modified MZNs with bisphosphonic acids

Even if bisphosphonic acids seems to be the best choice for MZNs modifications, also monophosphonic acids have been used, especially for the difficulties on synthesis of specific ending groups. For this reason, 2-aminoethylphosphonic acid (PNH_2), and 3-phosponopropionic acid (PCOOH), commercially available, have been employed to modify MZNs. In Figure 15 comparison of ζ-potential values from monophosphonic (PCOOH and PNH2) and bisphosphonic acids (MBP and EBP) are reported.

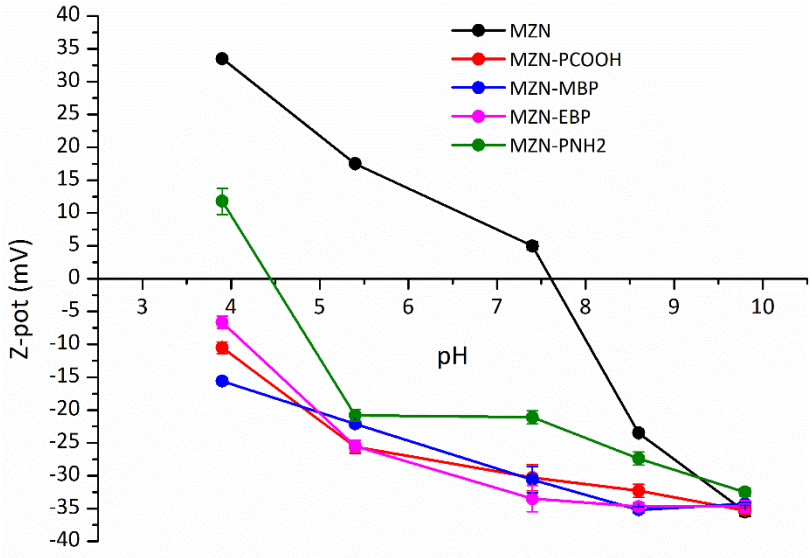

Figure 15: Comparison of ζ-potential between MZN, MZN-PCOOH, MZN-PNH2, MZN-EBP and MZN-MBP

From this comparison is clear that no differences are present with bis- or monophosphonic acids, for what concerns charge on surfaces, except for PNH2 where the amino group produces positive values at lower pH, due to compensation during protonation.

FT-IR characterizations have been also performed on bisphosphonate-modified MZNs. In Figure 16a, FTIR-DRIFT spectra of MZN and MZN-MBP and ATR-FTIR spectrum of pure MBP are compared. Significant changes in the P-O region (900-1250 cm^{-1}) were analysed. The stretching vibration of the P-OH at 906 cm^{-1} disappears in the infrared spectra of modified nanoparticles, while other peaks became a broad band after conjugation. These spectrum modifications are associated with covalent bonding of phosphonic acid to the surface, probably via condensation reactions [132-133]. The broadening and shifting of all peaks corresponding to P-OH vibrations were found in all modified samples (examples are reported in Figure 16), and these could demonstrate the MZN modification. The modifications in P-OH vibrations are also highlighted in the inlet of Figure 16c. Moreover, with complex molecules, other peaks related to other residues are present, as shown in Figure 16b and c, where vibration of C-H bond is highlighted.

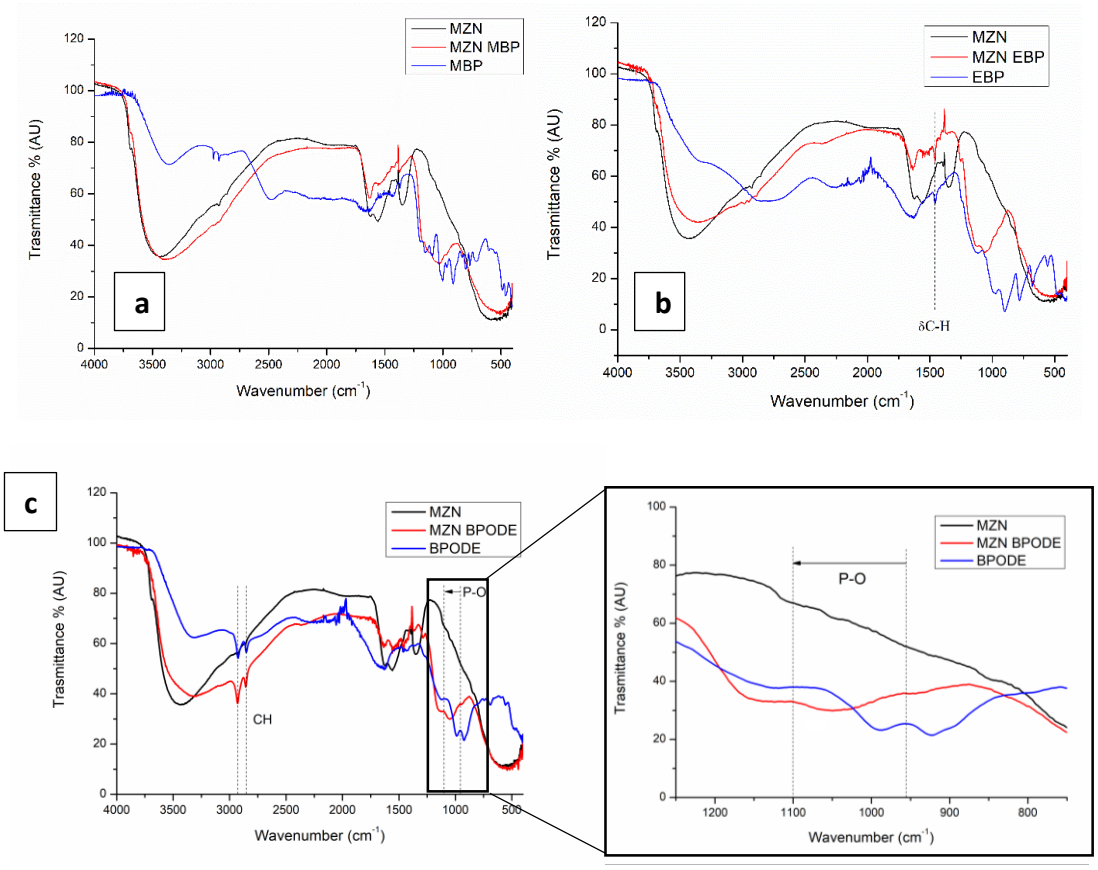

Figure 16:FT-IR spectra of comparison between bare MZN, bare modifying molecules and modified MZN for MZN-MBP (a), MZN-EBP (b) and MZN-BPODE (c)

Even in this case, XPS measurements were performed on MZN-MBP and MZN-EBP, and results confirms the previously obtained ones, with BE for P2p of 133.4 eV for both samples, in agreement with the results of MZN-BPPhE (133.3 eV).

To deeply understand the mechanism of modification and the bond between with, solid state NMR analyses have been performed on some modified samples, thanks to the collaboration with Prof M. Geppi and Dr S. Borsacchi. The ^{31}P DE-MAS spectra of the samples PCOOH, MZN-PCOOH, MZN-MBP, MZN-EBP are reported in Figure 17.

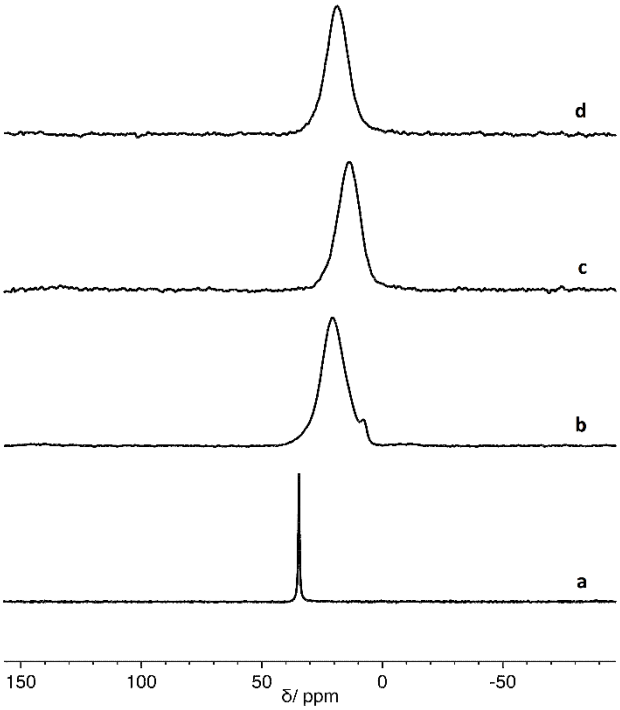

Figure 17: ^{31}P DE-MAS spectra of PCOOH (a), MZN-PCOOH (b), MZN-MBP (c), MZN-EBP (d)

The spectrum of PCOOH (Figure 17 a) is characterized by a single narrow peak resonating at about 35 ppm, characteristic of a crystalline solid. On the contrary the spectrum of MZN-PCOOH shows a very broad signal centred at a chemical shift of 20 ppm, with a minor component at about 8 ppm (Figure 17 b). Based on the literature [155-161] the 15 ppm decrease of the chemical shift in passing from the pure acid to the modified zirconia can be ascribed to a bi-dentate anchoring of PCOOH on the zirconia surface, involving the reaction of two P-OH groups. The large breadth of this peak indicates a remarkable loss of structural order for PCOOH, and it is compatible with a distribution of slightly different geometrical environments for ^{31}P nuclei, as for instance P-O-Zr angles. The small signal at 8 ppm can be tentatively ascribed to a minor fraction of molecules forming a tri-dentate anchoring also involving the P=O group or to a small amount of bulk metal phosphonate.

As far as bisphosphonates are concerned, the ^{31}P DE-MAS spectra of their hybrids with zirconia show a single broad peak centred at about 14 and 19 ppm for MZN-MBP and MZN-EBP, respectively (Figure 17 c and d). These values are shifted by about -10 ppm with respect to the isotropic chemical shifts of the corresponding pure bisphosphonates [162]. Based on both the literature [155-161] and other experimental data, it is reasonable to interpret these spectra with the reaction of all P-OH groups with the zirconia surface. As in the case of the monophosphonate, the breadth of the peaks indicates the presence of a distribution of geometries around ^{31}P nuclei and, on the whole, the amorphous nature of the organic layer.

Another time, characterization data confirms the strong character of bonds between phosphonate molecules and MZNs and could be defined as a covalent bond between

them. So, this shows how this class of molecules represents an interesting alternative to the employment of organosilanes to functionalize ZrO_2.

However, their use presents some problems in the presence phosphate buffers, where the detachment of functionalizing molecules was observed, even if other experimental evidences outlined a strong bond between the two systems. Indeed, for antibodies (Abs) conjugations is usually needed to use phosphate buffers (PBS) and the leakage of the biological moieties is observed. These results, presented later in this work, were investigated deeply by the research group of Prof Scarso, elsewhere, and evidenced how monophosphonic acids are detached more easily than bisphosphonic ones by phosphate buffer. This confirmed the better choice in using bisphosphonate instead of mono-ones, but difficulties on synthesis limited it.

3.3. Theranostic applications

3.3.1. Modifications of MZNs with magnetic phase

Nowadays, nanoparticles are reaching increasing interest in medicine due to their capability to be tuned for having the desired properties and to be used as theranostic system. Indeed, coupling together different materials can expand the field of applications due to different physical-chemical properties of such components, reaching the goal of personalized therapy of patients [21, 44, 49, 163-165]. So, to develop a system that can unroll these functions, we think about starting from magnetic nanoparticles as core of the tools. To do so, an already studied protocol has been adapted for our zirconia system [135]. With this method, which employs the wet impregnation of nitrate salts of desired metals and thermal treatments at high temperature, MSN with $CoFe_2O_4$ were previously made in our laboratory. Then, the procedure has been modified to produce MZN with cobalt ferrite as magnetic phase (MZN@$CoFe_2O_4$ or mMZN). Three different concentrations of cobalt-iron oxides have been tested (4, 8, 12.5 % mol/mol) to find the best amount of doping agents and to try to avoid the failure of zirconia structure. Indeed, it has been known from literature and from our previous works that amorphous zirconia crystallizes at temperature above 300 °C, sometimes destroying the structure [6, 16, 18, 46-47, 125, 166]. So, there was grounds to fear that our nanoparticles, treated at 700 °C for 12 hours, can collapse during the synthesis. Fortunately, although the high temperature of treatment, the NPs impregnated with cobalt and iron salts did not aggregate and the general shape of the NPs is maintained for low quantities of metals oxides loaded (Figure 18a and b). However, SEM images (Figure 18c) show a large amount of iron and cobalt oxide particles outside the ZrO_2 nanospheres for the 12.5% sample, that undergoes also a very strong change in morphology and microstructure. Comparison with silica system was performed to understand the differences between them. MSN before and after impregnation of 14% wt/wt (4% mol/mol) of cobalt ferrites, the same weight percentage of the 8% mol/mol in MZN, are presented in Figure 19. As one can see, with MSN no morphological changes are present as no cobalt iron oxides outside nanoparticles.

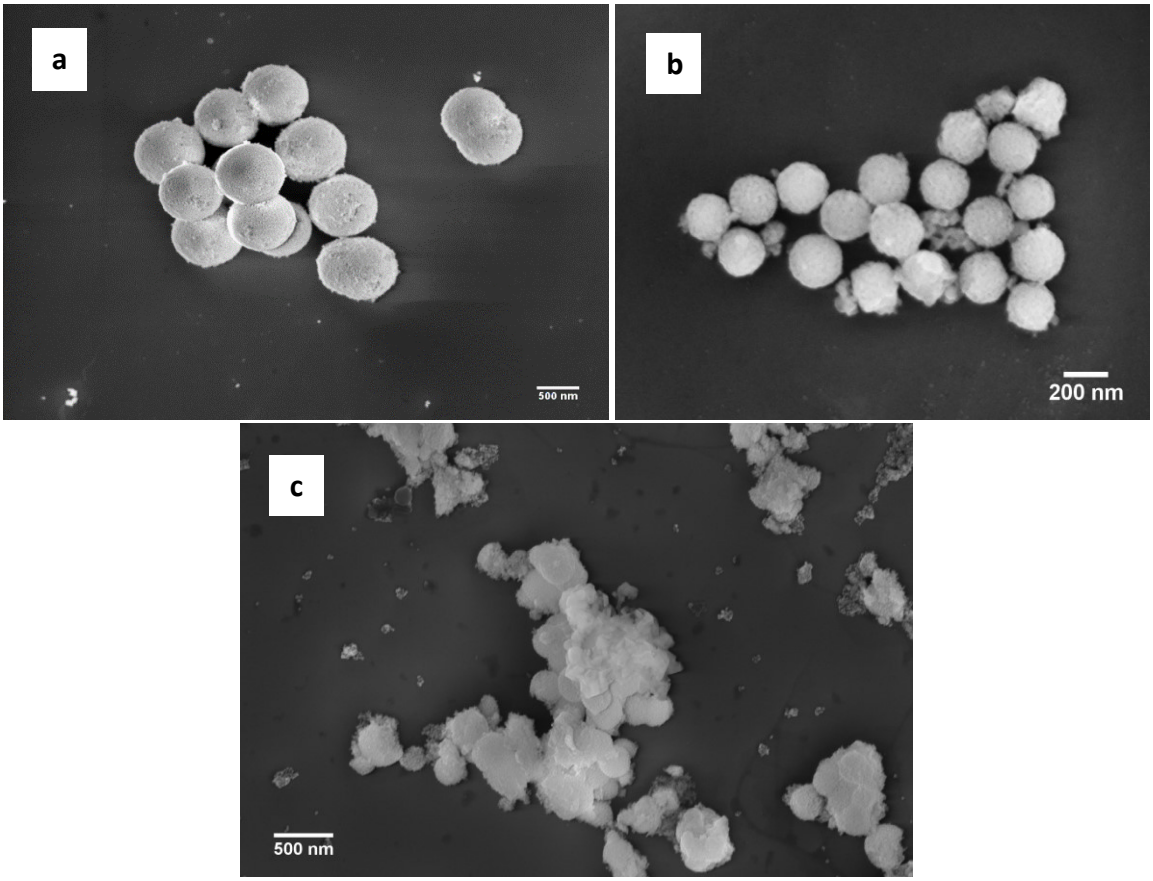

Figure 18: SEM images of sample mMZN-4 (a), mMZN-8(b) and mMZN-12(c)

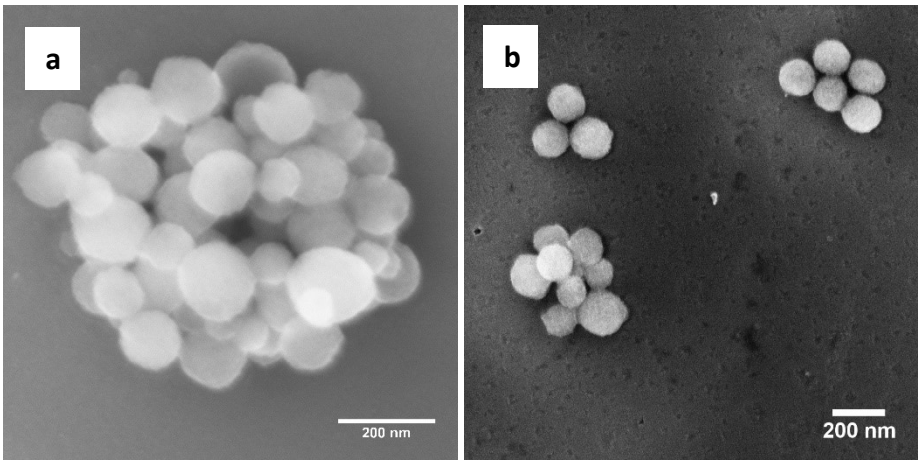

Figure 19: FEG-SEM images of MSN (a) and MSN@$CoFe_2O_4$ (b)

All the samples with MZNs, after thermal treatment, have a surface area around 20 m^2/g (nitrogen physisorption analysis) (Figure 20a) (8% respect to the bare MZNs), and close to the surface area of full density ZrO_2 NPs of similar size: pores are now filled up with metal oxides and/or shrunk because of the crystallization of zirconium oxide. This behaviour appears very different from what obtained with MSN, where porous structure did not collapse (Figure 20b) and the surface area is the 87% of the untreated ones. It can be ascribed to the amorphous character of silica also after high temperature thermal treatment and the higher pore volume compared to MZNs (circa 1 cm^3/g).

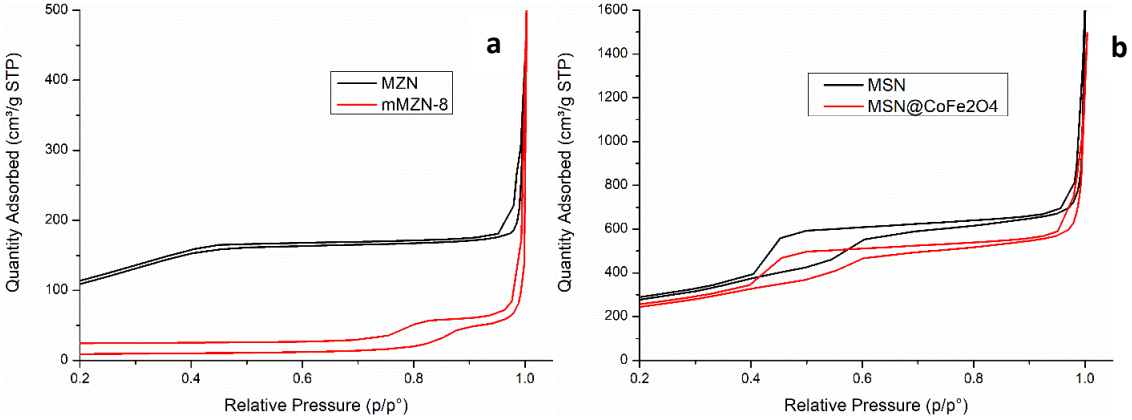

Figure 20:Comparison of N_2 physisorption analysis of MZN and mMZN-8 (a) and of MSN and MSN after introduction of cobalt ferrites (b)

On the respect of all said before, MZNs were chosen for further investigation due to the faster recovering of these systems when exposed to a common magnet, compared to the ones based on MSNs. Indeed, with zirconia, magnetic sorting is usually performed within few minutes, as described later on, while with silica, hours are sometimes needed to fully recover them.

TEM images of the mMZN-8% confirm that shape and size of the nanoparticles are maintained and show that they have a crystalline microstructure (Figure 21) with a size in between 15-30 nm (confirmed by SAXS and WAXS measurements Table 9).

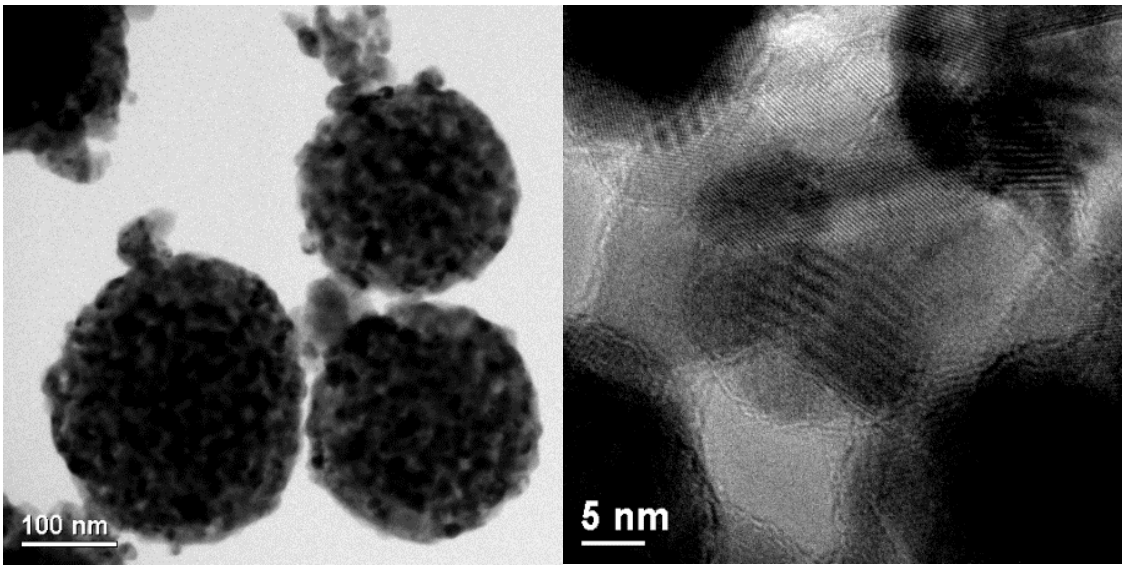

Figure 21: TEM and HR-TEM images of sample mMZN-8

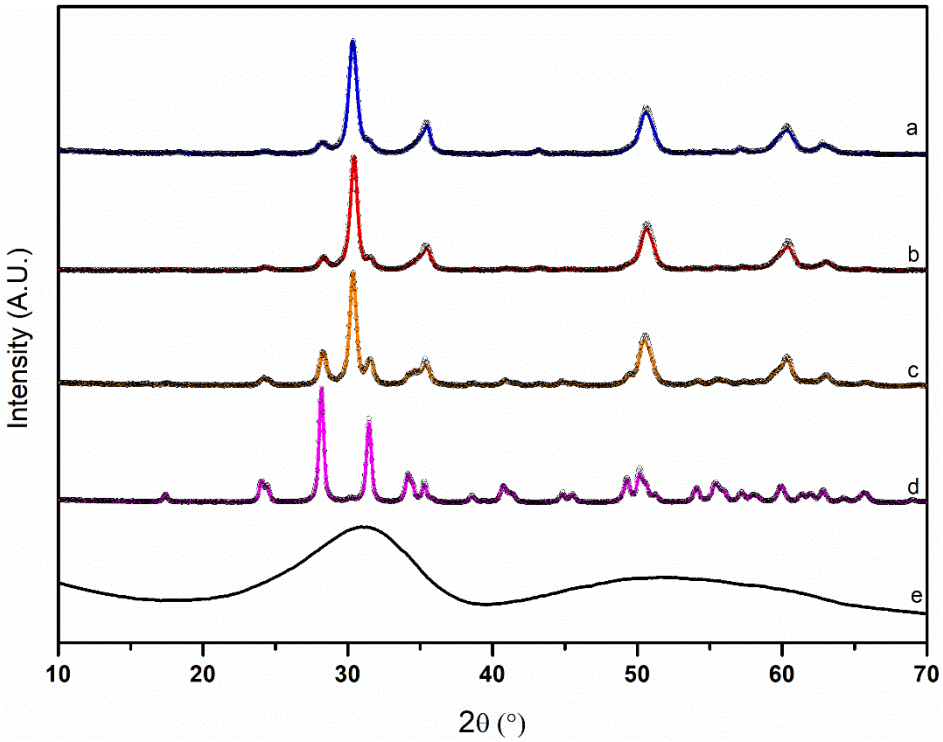

Figure 22: XRPD pattern of sample a) mMZN-12, b) mMZN-8, c) mMZN-4, d) MZN@700°C, e) MZN, solid line for fits, circles for experimental data, data fitted with ICSD # 417639 for m-ZrO_2 and ICSD # 164862 for t-ZrO_2.

The XRPD (Figure 22) plots show both the MZN patterns before (amorphous) and after the heat treatment and its effect on mMZN. The crystallization of the MZN gives mainly the thermodynamically stable monoclinic ZrO_2 with a very low content of tetragonal ZrO_2 probably stabilized by the small size of the crystallites (Table 10). On the other hand, the crystallization of all the mMZN samples produce both tetragonal and monoclinic ZrO_2. The stabilization of the most symmetric tetragonal phase is probably due to the formation of a solid solution between the Zr and Fe or Co oxides [47, 167-169]. The weigh fraction of the tetragonal phase of the zirconium oxide increases with the amount of Co and Fe ions until 70% ca. for the 8% and 12.5% samples. Furthermore, the crystalline $CoFe_2O_4$ fraction, determined by Rietveld analysis, is always lower than the loaded one in accordance with the hypothesis that part of the Fe-Co oxides forms solid solutions with the Zr oxide stabilizing the tetragonal zirconia fraction. We can also observe that the missing fraction of Co-Fe oxide saturated at about 3.5 mol%.

Table 9: Crystallites and particles sizes, uncertainty is in the order of 10%.

Units: nm	**XRPD <L>vol (nm)**	**XRPD <L>vol (nm)**	**XRPD <L>vol (nm)**	**SAXS Sphere Diam. (nm)**
Sample Name	**t-ZrO_2**	**m-ZrO_2**	**$CoFe_2O_4$**	**$CoFe_2O_4$**
MZN@700 °C	10	21	/	/
mMZN-4	14	13	6	22
mMZN-8	11	7	18	31
mMZN-12.5	9	7	17	17

Table 10: XRPD quantities of different phases of the different samples, uncertainty is in the order of 10%.

Sample Name	t-ZrO_2 %wt	m-ZrO_2 %wt	$CoFe_2O_4$ %wt	$CoFe_2O_4$ %mol
MZN@700 °C	2	98	/	/
mMZN-4	56	38	6	3.2
mMZN-8	73	19	8	4.4
mMZN-12.5	68	17	15	8.5

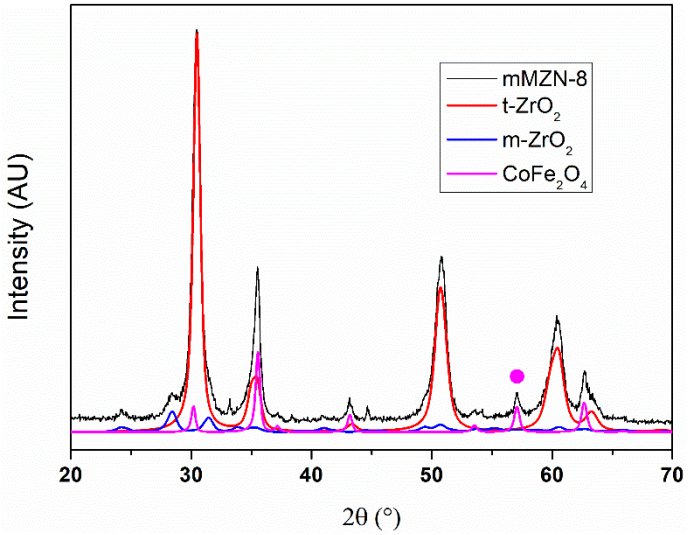

Figure 23:XRPD pattern of mMZN-8 compared to the ones related to t-ZrO_2 (ICSD # 164862), m-ZrO_2 (ICSD # 417639) and $CoFe_2O_4$ (ICSD # 41257), highlighted with pink dot the only peak related to cobalt ferrite not covered by the ones of zirconia.

However, the quantification of $CoFe_2O_4$ ever appears very difficult, due to the superposition of the XRD reflections related to this phase, with the ones ascribable to zirconia (Figure 23). As is visible from Figure 23, the only peak attributable uniquely to cobalt ferrites is the one pointed with the pink dot, and this situation makes the quantification of the magnetic phase difficult and the expected error is high.

SAXS analyses (see Figure 24 a,b), allows measuring the size of the $CoFe_2O_4$ oxide particles that have an electron density lower than the electron density of the ZrO_2 oxide matrix. The size of the large spheres (200 nm) is higher than the resolution of the employed Kratky camera so only the asymptotic h^{-3} behaviour (Porod asymptotic law for a slit smeared camera) is visible as background.

SAXS data are fitted assuming a distribution of spherical $CoFe_2O_3$ inclusion: Figure 24 a and b show the fit and the size distribution obtained for the 8% sample. All the results agree with the size obtained with XRPD pattern analyses (Table 9): the $CoFe_2O_4$ crystallites sizes are smaller or equal to the sizes of the particles. Only the 12.5% sample show a different behaviour that could be explained by the large fraction of small magnetic nanocrystal grown outside the pores.

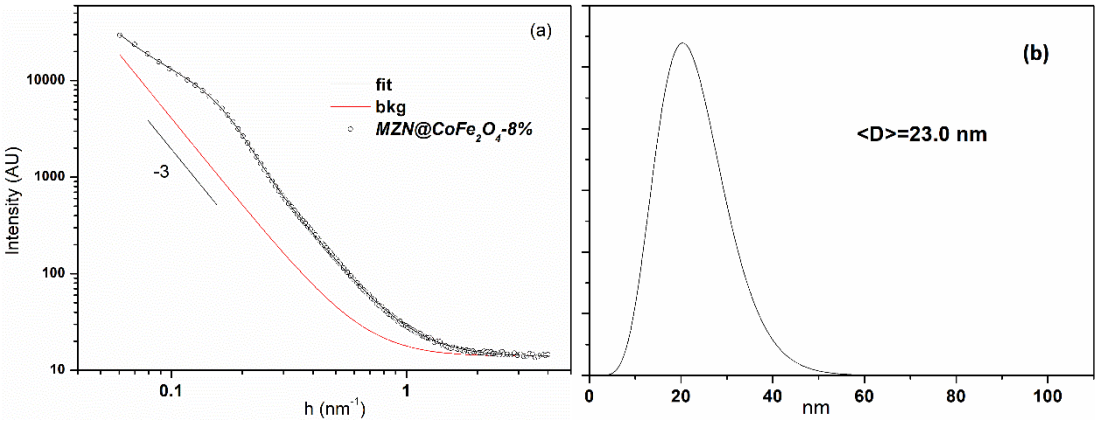

Figure 24: (a)Fit of SAXS data with a distribution of spherical particles. (b) Fitted size distribution of $CoFe_2O_4$ nanoparticles.

For a better understanding of the behaviour of zirconia with doping agents, two samples with only iron nitrate were produced, with 4 and 6% mol/mol, with the same procedure of samples with cobalt and iron. As one can see from Figure 25, shapes of nanoparticles are similar to the one loaded with $CoFe_2O_4$, with maintained roundness and low aggregation. Moreover, the stabilization of the tetragonal phase of zirconia with increasing quantities of iron is confirmed one more time, as one can see from XRPD analyses in Figure 26 and Table 11. Indeed, the quantity of t-ZrO_2 raise up to 80% wt, for the Fe 6%, higher than those obtained with Co and Fe. In addition, these samples did not present any crystal phase that could be traced back to Fe_xO_y confirming the possibility of a solid solution with iron and zirconium oxides.

Table 11: XRPD quantities of different phases of the different samples, uncertainty is in the order of 10%.

Sample Name	t-ZrO_2 %wt	m-ZrO_2 %wt
MZN@700 °C	2	98
MZN@Fe-4%	66	34
MZN@Fe-6%	80	20

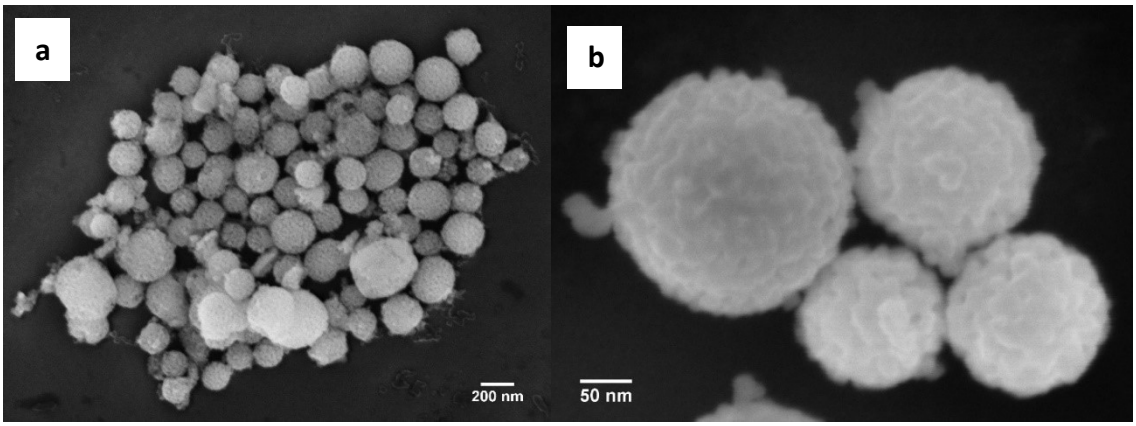

Figure 25: FEG-SEM images of MZN@Fe-4% (a) and MZN@Fe-6% (b)

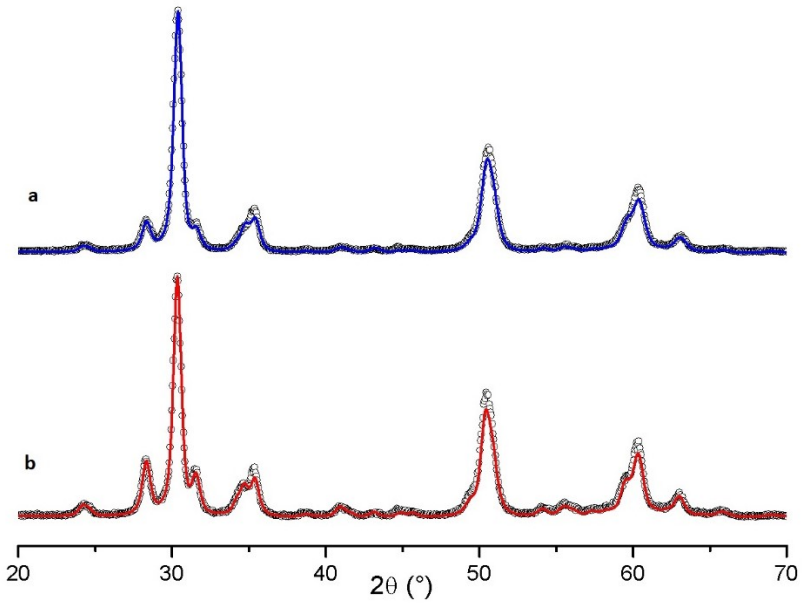

Figure 26: XRPD pattern of MZN@Fe6% (a) and MZN@Fe4% (b), dotted curves as observed diffractogram and solid one as fitted diffrattogram.

Further investigations of this behaviour were performed with Mössbauer spectroscopy at 77K, thanks to the collaboration with Prof N. Yaacoub of Université du Maine. As is visible in Figure 27, sextet and doublet are present and shifting values are reported in Table 12. From <δ> values obtained and the presence of the doublet, it seems that also this technique provides a confirmation on the fact that iron dopes zirconia, subtracting to cobalt ferrites. The isomer shift of the doublets (paramagnetic behaviour) correspond to the Fe^{3+} in solid solution with zirconia, and the asymmetrical shape of the doublet shows the presence of iron in different crystallographic sites. Indeed, it has been found in literature [170] that this shifting is associated to the presence of iron in the crystal structure of tetragonal or cubic zirconia. On the other hand, sextet could be attributable to the presence of cobalt ferrites, as already reported in literature [171-172]. Spectra of sample loaded only with iron seems showing that, also in this case, only solid solution is formed, and no iron oxides are present, due to the absence of the sextet.

Moreover, these results confirm again the saturation behaviour of iron quantity that could goes in solid solution with zirconia. Ratios between sextet and doublet, indeed, give us the possibility of quantification of the fraction of Fe^{3+} which goes in solid solution. In Table 13 molar percentage are reported for samples doped with $CoFe_2O_4$, taking into account the nominal quantity of loaded salts. Moreover, the atomic fraction of iron which went in solid solution with zirconia, is labelled with x as $Fe_x^{3+}Zr_{(1-x)}^{4+}O_{(2-\frac{x}{2})}^{-2}$. From Mössbauer measurements, the missing fraction of Co-Fe saturate around 2 mol%. Again, difficulties in quantification with XRPD data due to superpositions of peaks could explain differences between the two techniques, and the one obtained with Mössbauer spectroscopy seems the most reliable.

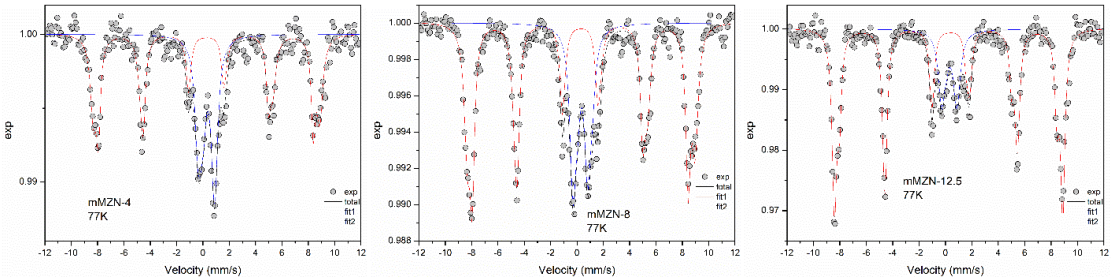

Figure 27:Mössbauer spectra of mMZN-4, mMZN-8 and mMZN-12.5 recorded at 77 K.

Table 12: Value of shifting <δ> obtained with Mössbauer spectroscopy at 77 K and ratio percentage between phases

		<δ>	%
mMZN-4	Sextets Fe^{3+}(A/B)	0.43	63
	Doublets	0.47	37
mMZN-8	Sextets Fe^{3+}(A/B)	0.45	72
	Doublets	0.48	28
mMZN-12.5	Sextets Fe^{3+}(A/B)	0.46	82
	Doublets	0.46	18
MZN@Fe6%	Doublets	0.44	100

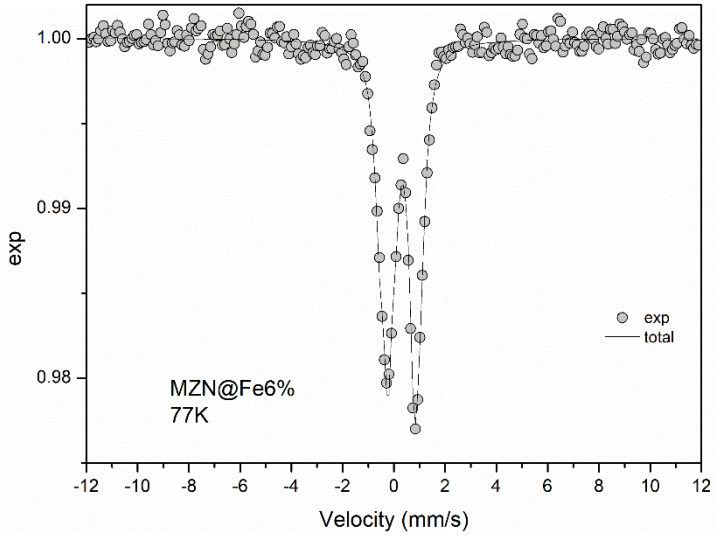

Figure 28: Mössbauer spectra of MZN@Fe6% recorded at 77 K.

Table 13: Quantification of molar percentage content of $CoFe_2O_4$ obtained with Mössbauer spectroscopy and XRPD and atomic fraction of iron in solid solution.

	$CoFe_2O_4$ %mol (Mössbauer)	$CoFe_2O_4$ %mol (XRPD)	x (Fe^{3+}) (atomic fraction)
mMZN-4	2.6	3.2	0.03
mMZN-8	5.9	4.4	0.046
mMZN-12.5	10.5	8.5	0.049

DC magnetization measurements with SQUID magnetometer were also performed on samples with cobalt and iron. As expected, at low temperature the samples with $CoFe_2O_4$

show a hysteretic behaviour. mMZN-4 shows an evident kink around zero field, together with strong not saturating character at high field. This feature can be associated to the presence of a soft magnetic phase, probably due to the separation of Co_3O_4, as already observed in literature [173], inducing an off stoichiometry in $CoFe_2O_4$ nanoparticles. Due to the strong not-saturating character at high field the extrapolation of saturation magnetization by fitting can bring to unphysical values. Then as a rough estimation of magnetization at high field the value at 5T will be considered. The presence of soft magnetic phase mMZN-4 sample affects the value of coercivity field (H_c) and, especially the value of saturation magnetization (M_s) at 300 K that is extremely low, with respect to the other samples confirming the presence of some impurities (e.g. Co_3O_4). Due to the particular behaviour of this sample, it seems to be unphysical to determine a value of reduced remanence magnetization (M_r/M_{5T}), where M_r is the remanent magnetization. On the other hand, samples with 8% and 12.5% of cobalt ferrite show quite high coercivity, compatible with the presence of stoichiometric nanostructured $CoFe_2O_4$. At low temperature a strong non-saturating tendency is observed probably due high surface anisotropy [87]. The M_s value was obtained by fitting the high-field part of the hysteresis curve, recorded at 300 K, using the relation:

$$M = M_S \times \left(1 - \frac{a}{H} - \frac{b}{H^2}\right)$$

Where H is the field strength, and a and b are parameters determined by the fitting procedure [174].

Anyway, values of magnetization measured at 5 T (M_{5T}) are also compatible with the presence of $CoFe_2O_4$ nanoparticles with M_{5T} for mMZN-8 that is very close to the bulk value (93 A m^2 Kg^{-1}) [171] indicating the good quality of the particles in this sample. The lowering of M_{5T} with respect of bulk value observed in mMZN-12.5 can be ascribed to the complex interplay between surface spin disorder (i.e. spin canting) and cationic distribution [111]. All the samples show non-zero coercivity and remanence magnetization at 300 K (Figure 29), clearly indicating that at this temperature nanoparticles in "blocked state" are still present. Value of saturation magnetization and at 5 T confirms again the bettered performance of mMZN-8 sample showing the highest saturation magnetization.

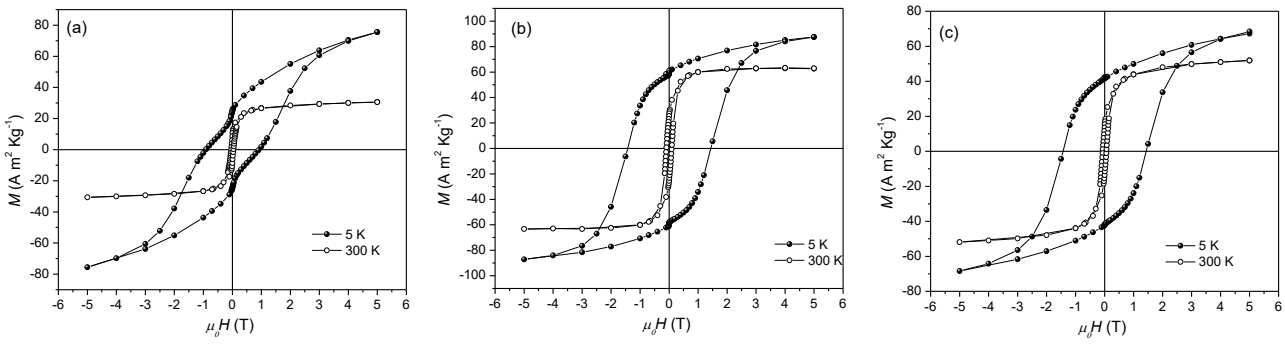

Figure 29: Hysteresis loops recorded at 5 K (full circles) and 300 K (empty circles) for mMZN-4(a) mMZN-8(b) and mMZN-12.5(c)

Table 14: Coercive Field ($\mu_0 H_c$), magnetization recorded at 5 T (M_{5T}, 5K), reduced remanent magnetization (M_r/M_{5T}), Saturation Magnetization recorded at 300 K (M_S 300K). Uncertainties on the last digit are given in parentheses.

Sample	$\mu_0 H_c$_5K (T)	M_{5T} (5K) (A m^2 Kg^{-1})	M_r/M_{5T}	M_s (300 K) (A m^2 Kg^{-1})
mMZN-4	0.91(5)	--	-	29.4 (4)
mMZN-8	1.44(6)	82(4)	0.67	57.0 (8)
mMZN-12.5	1.43(6)	68 (5)	0.6	54.6 (3)

In these cases, however, M_r/M_s is not evaluable due to the unsaturated character of samples measured at 5 K around 5T, so M_r/M_{5T} has been calculated.

The analysis of remanent magnetization curves measured by IRM and DCD protocols (Figure 30) allowed also to investigate the interaction regime among particles. For an assembly of noninteracting single-domain particles with uniaxial anisotropy and magnetization reversal by coherent rotation, the two remanence curves are related via the Wohlfarth equation:

$$m_{DCD}(H) = 1 - 2m_{IRM}(H)$$

where m_{DCD}(H) and m_{IRM}(H) represent the reduced terms M_{DCD}(H)/M_{DCD}(5T) and M_{IRM}(H)/M_{IRM}(5T) and M_{DCD}(5T) and M_{IRM}(5T) are the remanence values for the DCD and IRM curves at 5 T, respectively. Following this equation, the two irreversible susceptibilities (χirr = dm/dH) are related as:

$$\left|\frac{dm_{DCD}}{dH}\right| = 2\frac{dm_{IRM}}{dH}$$

with a maximum at the same reverse field. Deviations from such behaviour are due to the presence of interactions which can be quantified in terms of the so-called interaction field:

$$H_{int} = \frac{(H'_r - H_r)}{2}$$

H'_r and H_r correspond to the position of the maxima of the field derivative of m_{DCD}(H) and m_{IRM}(H) curves respectively (i.e., maxima in the irreversible susceptibility which maps the switching field distribution). In the case of mMZN-8% the value obtained for H_{int} (-26 mT) suggests very weak demagnetizing interactions.

Kelly *et al.* [175] rewrote the Wohlfarth relation to explicitly reveal deviations from a noninteracting case:

$$\delta m = m_{DCD} - (1 - 2m_{IRM})$$

In particular, a negative deviation from the linearity condition is an evidence of the predominance of dipole−dipole interactions, while a positive deviation can be attributed to the predominance of exchange interactions. A different method to provide information on the nature of interactions, consist in plotting $m_r^{DCD}(H)$ against $m_r^{IRM}(H)$ (Henkel plot), where a negative curvature indicates a demagnetizing interaction, while a positive curvature can be attributed to a promotion of the magnetized state.

In this case, δm plot (Figure 30c) indicates that dipolar interactions are predominant. Moreover, the presence of two magnetic phases is evident due to the double peak in the plot, which confirms the hypothesis of a second soft magnetic material derived from the removal of cations from stoichiometric cobalt ferrites. From Henkel plot (Figure 30d), it seems that also in this case demagnetizing interaction are predominant, but the low curvature did not give a certain interpretation, leaving open the possibility of the coexistence of both interactions [114, 176].

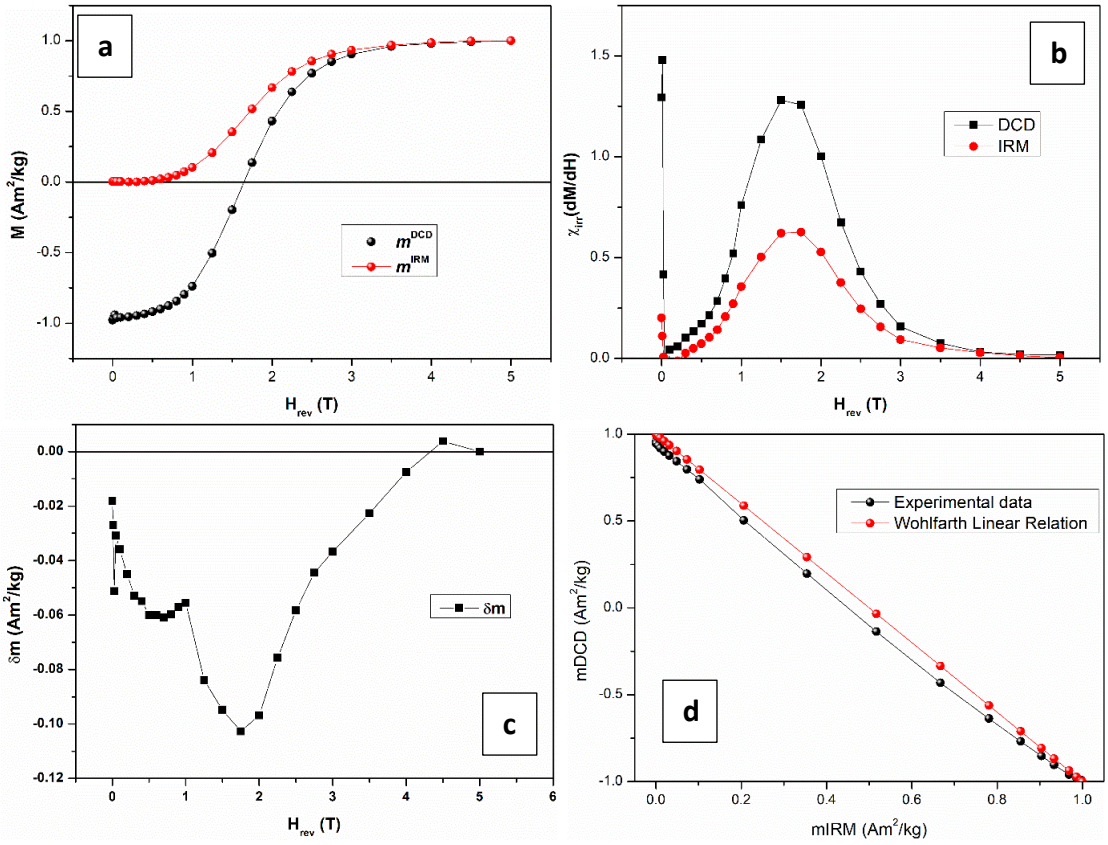

Figure 30: Sample mMZN-8%: DCD and IRM curves (a), Irreversible susceptibility (χ_{irr} = dM/dH) derived by DCD (black) and IRM (red) (b), δm plot (c) and Henkel plot (d)

ZFC-FC (Zero Field Cooling-Field Cooling) analyses have been performed but did not show any superposition in the evaluated temperature range. So, as is also visible in hysteresis loops at 300 K (Figure 29) where non-zero coercivity is present, it was impossible to define a blocking temperature (T_B) for the systems, meaning that at room temperature there are blocked particles, yet, and the system is not in a superparamagnetic state.

Surface modification of mMZN-8%

Once established that mMZN-8% was the best sample for our purposes of applications, it has been modified with different phosphonic acids, which present the desired terminal groups, for further modifications. The presence of the modifying molecules is given as previously reported, with ζ-potential and FTIR measurements (see Results and Discussion, Functionalization of MZN) and later on in the next chapter. Moreover, DC magnetization measurements were performed to establish if there were any modification of the

magnetic properties of the samples after modifications. Figure 31 shows the hysteretic behaviour of samples when modified, taking into account the theoretical mass of the magnetic phase. As one can see, the evolution of the loops substantially changes with different phosphonic acids introduced, particularly with bis-phosphonic ones, which means that there is an interaction also between cobalt ferrite and the organic molecules. Particularly, saturation and remanent magnetization decrease for the sample with BPODE, while seems to increase with PCOOH molecules. However, the impossibility to perform thermogravimetric analyses on these samples with our instrument, due to the presence of sulphur in the organic molecule, did not allow us to establish the real amount of modifying molecules to adjust the weight of the magnetic phase in a more accurate way. So, the significant data from these measurements are the values related to reduced remanent magnetization and coercivity, that change with samples as is visible in Table 15, showing a different behaviour. Moreover, if the weight of the sample is correct respect only to the nominal amount of magnetic phase, without taking into account the weight of modifying molecules, a systematic error has to be found and the magnetization has to be lower than the bare mMZN-8 if the molecules did not affect it, due to underestimation of the magnetic part. However, the behaviour was not the one expected and the sample modified with PCOOH shows in any case higher value than the bare ones, meaning that both modifications have effects on the magnetic behaviours of our samples in different ways.

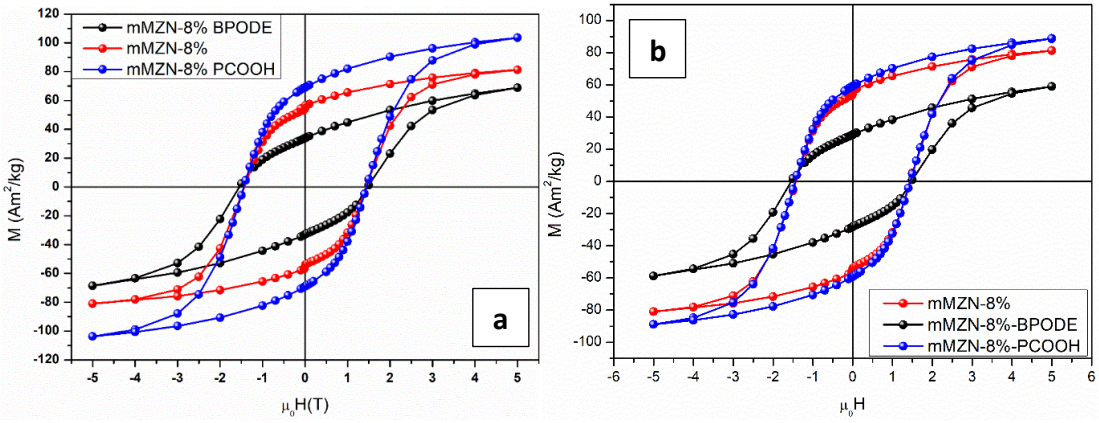

Figure 31: Hysteresis loops of mMZN-8% modified with different phosphonic acids, recorded at 5 K, with theoretical weight correction with functionalization amount (a) and without (b)

Table 15: Coercive Field ($\mu_0 H_c$), magnetization recorded at 5 T (M_{5T}, 5K) for data corrected taking into account of nominal weight of functionalizing molecules, reduced remanent magnetization (M_r/M_{5T}). Uncertainties on the last digit are given in parentheses.

Sample	$\mu_0 H_c$_5K (T)	M_{5T} (5K) (A m^2 Kg^{-1})	M_r/M_{5T}
mMZN-8 PCOOH	1.44(5)	104(4)	0.7
mMZN-8 BPODE	1.49(9)	69(4)	0.5
mMZN-8	1.44(6)	82(4)	0.7

The higher grade of modifications in the magnetic properties with bis-phosphonic acids compared to mono-phosphonic ones could be ascribed to the higher acidity which can stronger interact with the external surface of the nanocomposites.

The measurements of the magnetization of these nanoparticles are a proof of the successful functionalization of the particles even after loading of magnetic phases [87, 176].

3.3.2. Modifications of the system to obtain theranostic nanoparticles or biosensors

Linking with gold nanoparticles to obtain a SERS-based biosensor or tools for hyperthermia treatment

For SERS application, the thiolated mMZN-8 are modified with gold nanoparticles obtained with laser ablation (see Materials and Methods), thanks to the collaboration with the research group of Prof M. Meneghetti at Università degli Studi of Padova. TEM and FEG-SEM images, reported in Figure 32, clearly show the presence of the AuNP on the surface of the mMZN-8 nanoparticles.

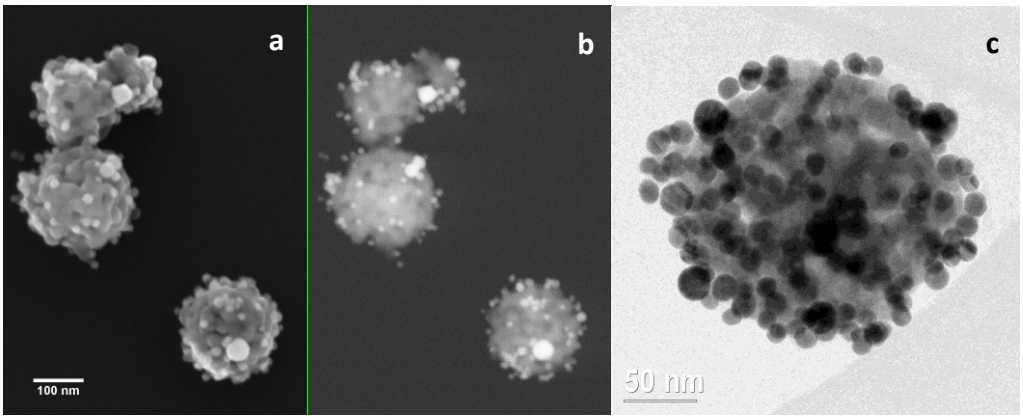

Figure 32:FEG-SEM images (InLens a and AsB b) and TEM (c) of mMZN8@Au.

An important property of magnetic nanoparticles is their mobility in a magnetic gradient, which can be exploited for applications in different research fields like enhancing the detection sensitivity by pre-concentration of the analyte or cells, bacteria or exosomes separation [35].

So, particles migration, under a magnetic gradient, was followed by the UV-Vis extinction changes of their colloidal solution [122]. Changes of the recorded extinction spectrum is fitted considering the attraction force generated by the magnetic gradient and the viscosity of the solvent which counterbalanced the accelerated motion of the particles toward the magnet [177]. The fitting of the extinction changes recorded with the magnetophoretic experiment can be obtained considering the distribution of the nanoparticles diameters recorded with SEM images (R_{SEM}).

The extinction spectrum of the colloidal solution of mMZN and its comparison with MZN is reported in Figure 33.

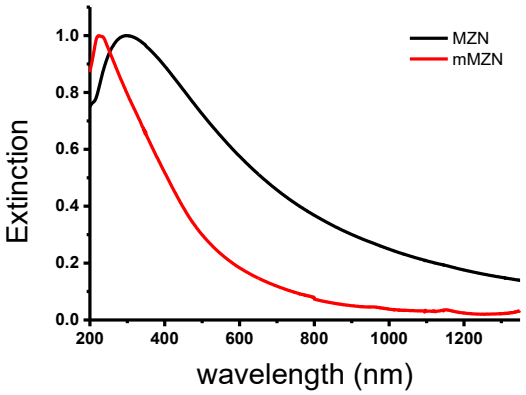

Figure 33: Extinction spectra of MZN (black line) and mMZN (red line)

Figure 34a shows the variation of the extinction for mMZN recorded at 370 nm (dotted curve) as a function of time and normalized at 0 min. The fitting (continuous blue line) is obtained with the parameters reported in Table 16. A parameter of the fitting is the percentage of the magnetic phase and one can see that the fitting suggests a value very similar to that obtained with the XRD measurements (see Table 10). The nanoparticles show a good response to the magnetic gradient since in 6 minutes more than 90 % were recovered within 3 mm from the magnet and almost 100% after 10 min.

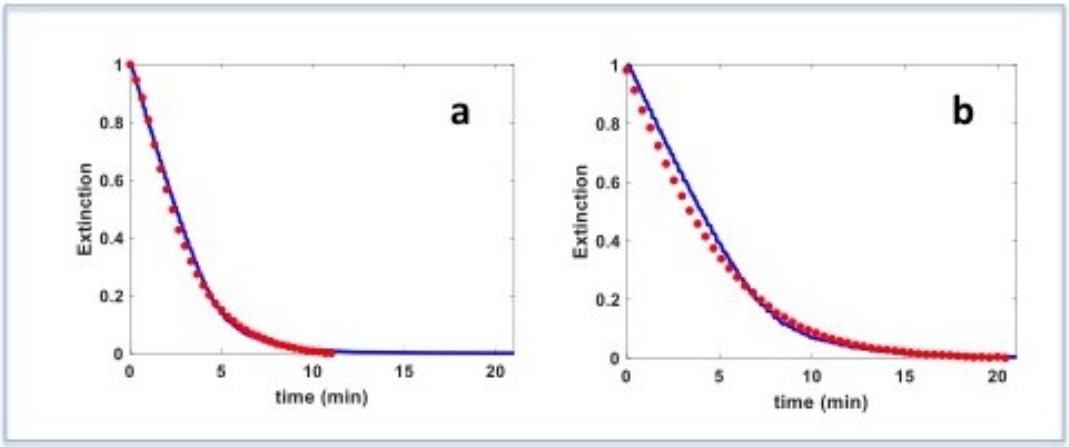

Figure 34: (a) Fitting of magnetophoretic curves for mMZN and (b) for mMZN@AuNPs with parameters values reported in Table 16.

The same experiment was performed with the mMZN-8@AuNP nanostructures (see the "Materials and Methods" section for the synthesis and below for their extinction spectrum). The data and their fitting (parameters values in Table 16) are reported in Figure 34b. The hydrodynamic diameter is now larger than in the previous case, probably because of the different hydrodynamic of the particles with the AuNP on their surface. The magnetic response of mMZN-8@AuNP is always good since almost 100% of the particles were recovered within 18 min.

Table 16: Parameters for the fitting of the magnetophoretic curves reported in Figure 34 (a) and (b) for mMZN and mMZN@AuNPs, respectively.

	mMZN	mMZN@AuNPs
Saturation magnetization (300 K)	~$200 \cdot 10^3$ A/m (34.2 A·m^2/kg)	
Magnetic % (molar)	5.8%	
Zirconia density	5895 kg/m^3	
Cobalt ferrite density	5290 kg/m^3	
Hydrodynamic radius	$1.0 \cdot R_{SEM}$	$1.6 \cdot R_{SEM}$
Water viscosity (T=20°C)	0.001 Pa·s	

Figure 35 reports the extinction spectra of MZN@AuNP and mMZN-8@AuNP. Insets show the spectra obtained by subtracting the broad baseline, which derives mainly from the scattering of the zirconia nanoparticles (see below). In the insets, one can see the characteristic bands of aggregated nanoparticles, namely a plasmonic band around 520-550 nm, also observed for isolated AuNP, and other plasmonic bands at longer wavelengths (600 to 800 nm), characteristic of aggregated AuNP. The aggregation of the nanoparticles is very important because hot spots, where SERS is particularly enhanced, are created between nanoparticles (see below).

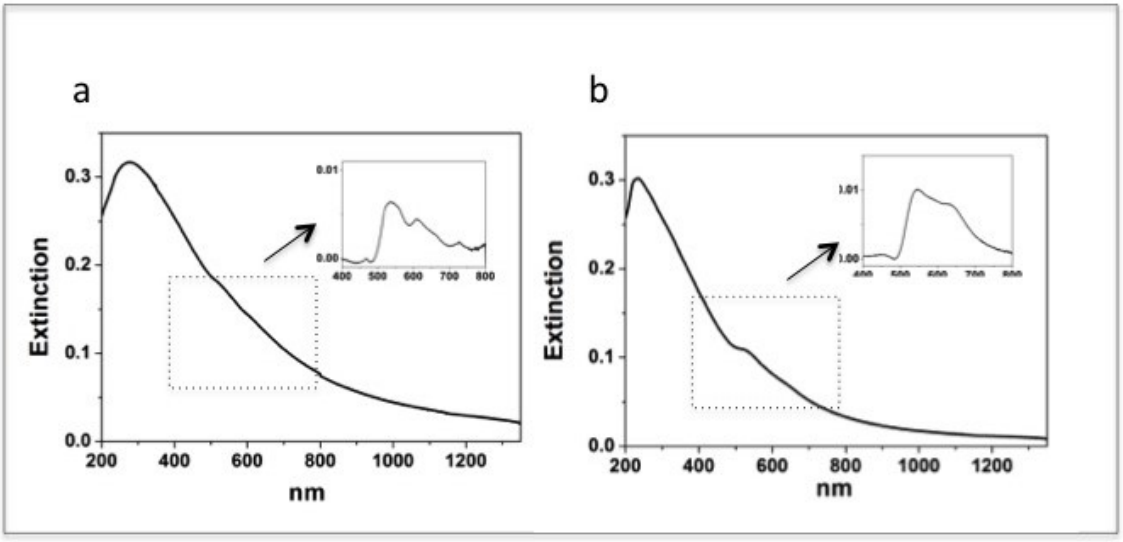

Figure 35: UV-Vis-NIR extinction spectra of (a) MZN@AuNP and (b) mMZN-8@AuNP. Insets show the spectral region from 400 to 800 nm after baseline subtraction.

MZN@AuNP were functionalized with the SERS reporter thiolated-Texas-Red (TR-SH) and Figure 36a reports the SERS spectrum of these nanoparticles with the characteristic bands of TR-SH [35, 141] at 1504 and 1650 cm^{-1}. mMZN@AuNP were functionalized with thiolated-Malachite-green (MG-SH) and Figure 36b shows the characteristic band at 1617 cm^{-1} [178]. Both spectra are very intense, as expected for SERS spectra determined by hot spots. These spectra show that these nanocomposites can be used as efficient SERS tags for applications in which their presence is monitored, like in targeting of tumor cells [35, 140].

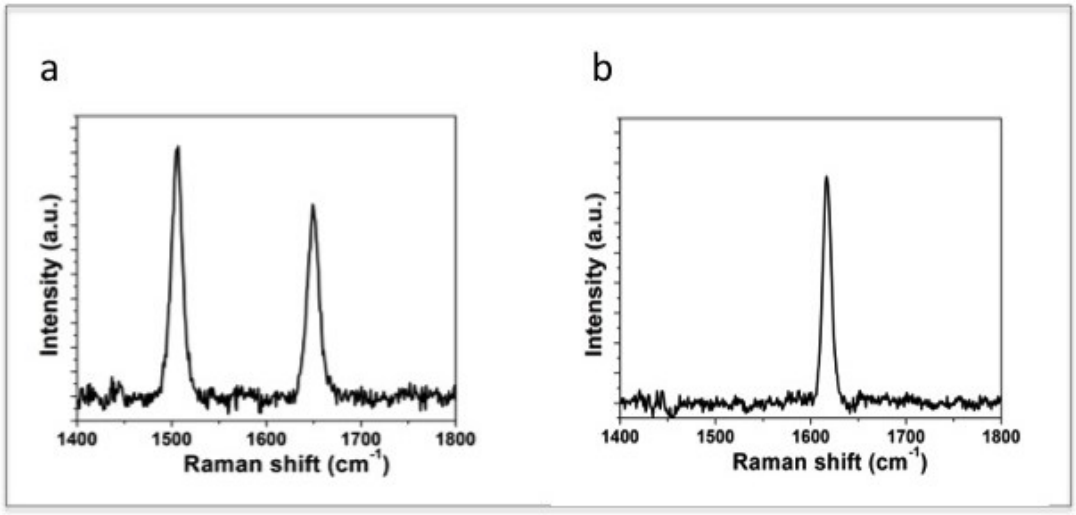

Figure 36: SERS spectra of (a) MZN@AuNP functionalized with TR-SH and (b) mMZN@AuNP functionalized with MG-SH.

The extinction spectrum of gold nanoparticles aggregated on the surface of the zirconia particles (MZN@AuNP) and the SERS enhancement in the hot spots of these aggregates can be calculated with a BEM calculation [179-180]. A model structure for the calculation is reported in Figure 37 with a zirconia sphere of diameter 200 nm and seven gold nanoparticles of 25 nm, organized, at the distance of 0.5 nm from each other, in a 'flower' (Figure 37b) on the surface of the zirconia sphere. Figure 38a reports the calculated spectra for this structure, which show that the scattering component due to the zirconia particles is the most important contribution to the extinction spectrum. The calculations also show (Figure 38b) that the small absorbance component of MZN@AuNP is mostly due to the AuNP 'flower'.

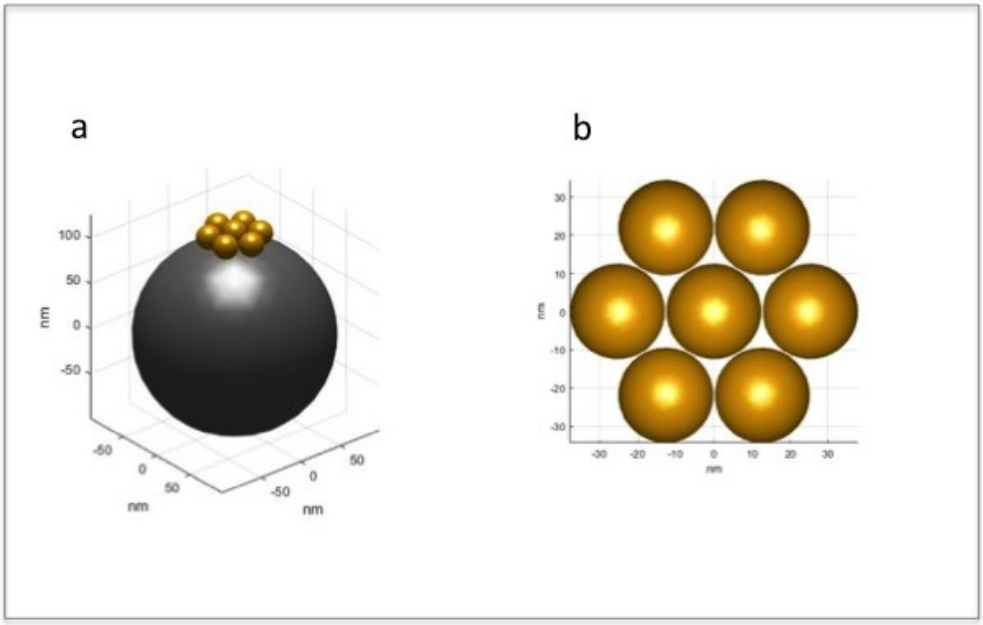

Figure 37: Model for the calculation of the extinction, scattering and absorption spectra of MZN@AuNP with a zirconia sphere of 200 nm of diameter and a 'flower' of seven AuNP of 20 nm (a). Organization of AuNP in the 'flower' (b).

The same BEM calculations allow evaluating the enhancement of the SERS spectrum. The largest enhancement is found, as expected, within the gaps between the AuNP (the so-called hot spots). With an exciting line at 633 nm, one calculates, for the AuNP 'flower' on the zirconia sphere, a SERS enhancement value of 4.0 10^{10}. The calculated enhancement is characteristic of the cluster of AuNP, (for the isolated flower one calculates a maximum enhancement of 5.8 10^{10}) and show that the presence of the zirconia sphere has a very small influence on the SERS enhancement.

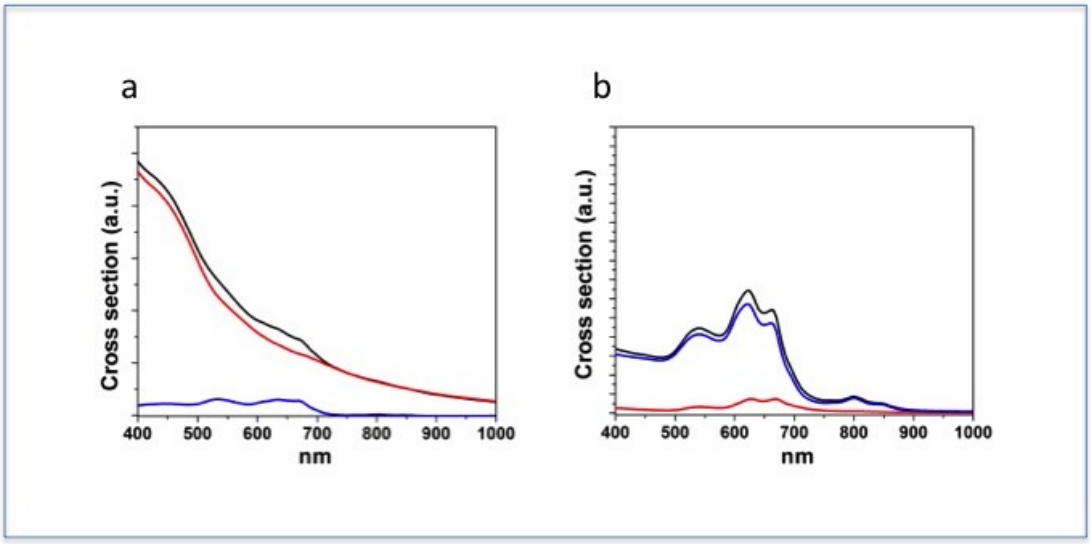

Figure 38: BEM calculation of the extinction (black lines), scattering (red lines) and absorption spectra (blue lines) of the model structure (a) and of AuNP 'flower' only (b).

A proof of concept experiment for exploiting the magnetic properties of mMZN@AuNP is conducted mixing these nanostructures with MZN@AuNP and then operating a magnetic sorting. The efficiency of the separation can be monitored with the signals of the SERS reporter MG-SH, which functionalizes mMZN@AuNP, and those of TR-SH used for MZN@AuNP.

Figure 39 reports the SERS spectrum of the solution obtained with a mixing of an equal volume of mMZN@AuNP and of MZN@AuNP in which both the SERS signals of TR-SH and MG-SH can be observed. In particular the bands at 1504 and 1650 cm^{-1} can be recognized as signals of TR-SH and that at 1617 cm^{-1} as that of MG-SH.

The magnetic separation is performed with four magnets (Supermagnete, S-5-25-N, D=5 mm diameter, h=25 mm height) on the side of a small vial containing the colloidal solution, for 1h. Then, the solution was separated from the nanostructures attracted by the magnets. The SERS spectrum of the solution is reported in Figure 40a, whereas the spectrum of the nanostructures attracted by the magnets and dispersed again in water is reported in Figure 40b.

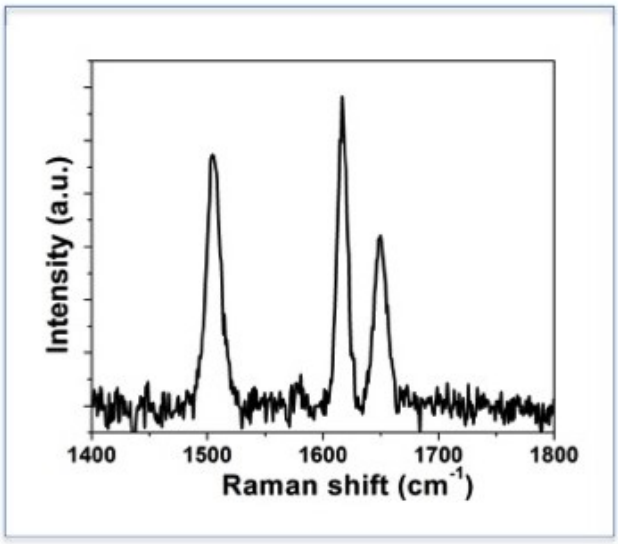

Figure 39: SERS spectrum, excited at 633 nm, of the solution with mMZN@AuNP and MZN@AuNP mixing.

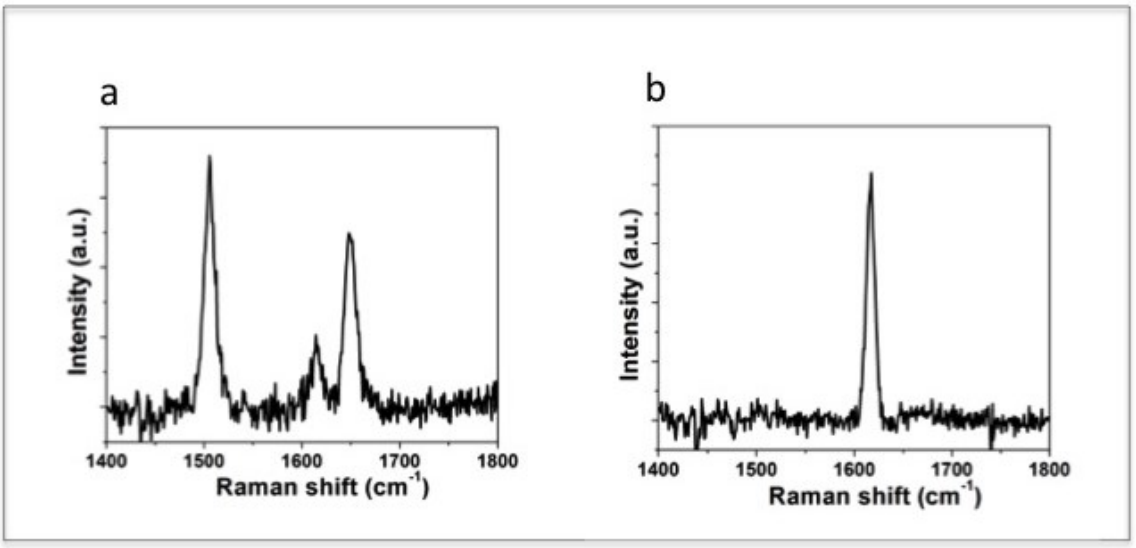

Figure 40: SERS spectra, excited at 633 nm, of the solution with the nanostructures not attracted (a) and attracted (b) by the magnets.

One can see that the spectrum of the nanostructures presents in solution (Figure 40a) shows the SERS signals of TR-SH at 1504 and 1650 cm^{-1} and only a small signal of MG-SH at 1617 cm^{-1}. The residual signal of MG-SH derives from the difficulty of pipetting the solution without perturbing the nanoparticles attracted by the magnet. The nanostructures attracted by the magnets (Figure 40b) show, on the other hand, only the spectrum of MG-SH at 1617 cm^{-1}.

The separation of the nanostructures can be considered quite satisfactory considering the high efficiency of the SERS spectra to the presence of a very small quantity of SERS reporters.

3.3.3. Obtaining a porous structure coupling $CoFe_2O_4$ and MZNs

Strategy #1:

Due to the previously obtained results on mMZNs, a deeper investigation of the system was performed to understand if it was possible to obtain porous structure with thermal treatment at lower temperature. Indeed, the goal is to obtain a magnetic structure that could be able to load drugs for an improved theranostic system. Therefore, further XRD measurements were performed at Elettra Synchrotron in Trieste on samples loaded with cobalt and iron and only with iron, using an oven [181], to follow the crystallization with increasing temperature. The investigation was carried out between 25 and 800 °C, taking a diffractogram each 100 °C. As is visible in Figure 41a, bare MZN shows prevalently monoclinic crystal phase after thermal treatment, the more thermodynamically stable, even if it was prevalently tetragonal before the treatment. Although, for the sample loaded with cobalt and iron (the 8% mol/mol), tetragonal phase seems more abundant, even if the monoclinic one is still present (Figure 41b).

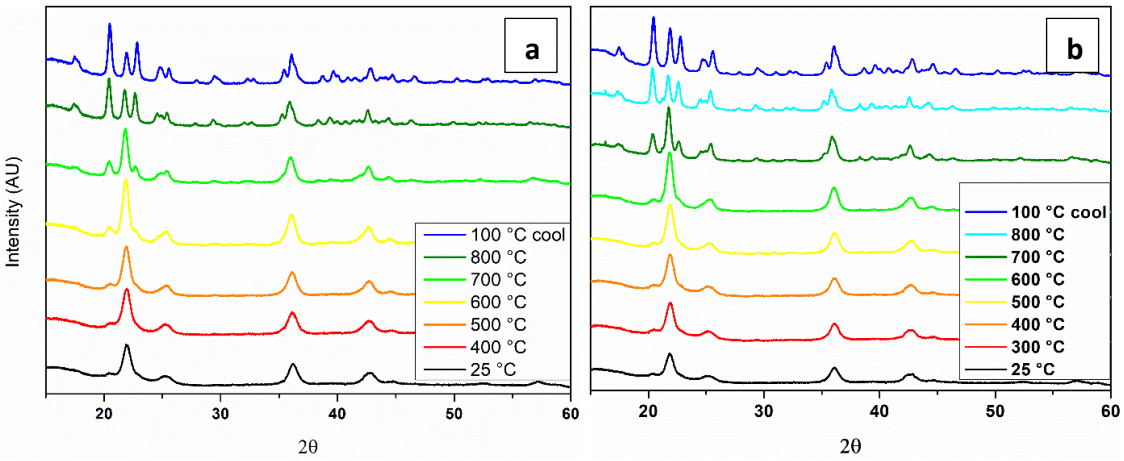

Figure 41: XRD patterns with increasing temperature of MZN (a) and mMZN-8% (b) (λ = 1.12576 Å)

To confirm the stabilization of the tetragonal phase by the formation of solid solution between iron and zirconia, synchrotron experiments were performed also on MZN@Fe4% and MZN@Fe6%. Figure 42a shows how tetragonal phase increase with increasing quantity of doping agents, and confirms the presence of solid solution, due to the absence of any peaks related to iron oxides. Figure 42b shows the behaviour during crystallization of MZN@Fe6% sample with increasing temperature.

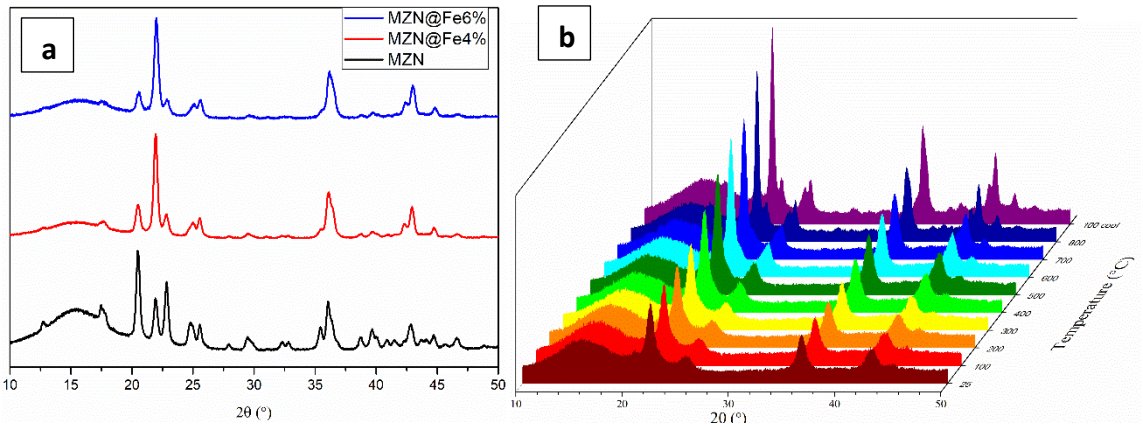

Figure 42: X-ray diffraction spectra of sample loaded with iron after thermal treatment at 800 °C (a) and the behaviour with temperature of MZN@Fe-6% (b) recorded at Elettra Synchrotron (acquired with λ = 1.12576 Å)

After these results, trials to obtain a magnetic phase with residual porosity, employing thermal treatment with lower temperature, were performed. From XRD diffractograms in Figure 43, one can see that crystal growth starts above 500 °C when crystallites sizes increase, where also peaks related to monoclinic phase appears. Indeed, fitting the XRD profiles in the range reported in Figure 43 b, it has been seen, using the Scherrer analysis of the XRD peaks, that crystallites sizes start to grow at 500 °C (Figure 43 c), which cause the collapse of the porous structure, and the closure of the pores. TGA-DTA analysis was performed both on the pure MZN and on the mMZN-8 sample (Figure 43d). The pure sample shows two well defined exothermic peaks at approximatively 300 and 450 °C. The first one corresponds to the crystallization of small tetragonal crystallites and the burning of residual organic groups [6, 182], while the second one, at 450 °C, correspond to the monoclinic phase crystallization [182]. The elimination of chemically bound water is responsible of the endothermic peak around 100 °C. The behaviour of the mMZN-8 is more complex and substantially different: the decomposition of the nitrate (endothermic process) increases the endothermic peak of bare MZN and partially overlapped to the first peak of bare zirconia, which appears broadened and smaller, while the second one appears modified by the crystallization of the magnetic phase. Moreover, the second transition of zirconia seems to be moved at higher temperature (550 °C vs 450°C) and this can be explained with the stabilization of the tetragonal phase due to iron ions. (Figure 43 d). Indeed, as is visible from Figure 43 b and c, crystallizations of nanoparticles change drastically above 550 °C, where tetragonal phase start to decrease while monoclinic phase increase, as also crystallites dimensions.

For these considerations the thermal treatment at 450 °C was chosen to promote the formation of the magnetic phase without the collapse of the porous mMZN nanocomposite.

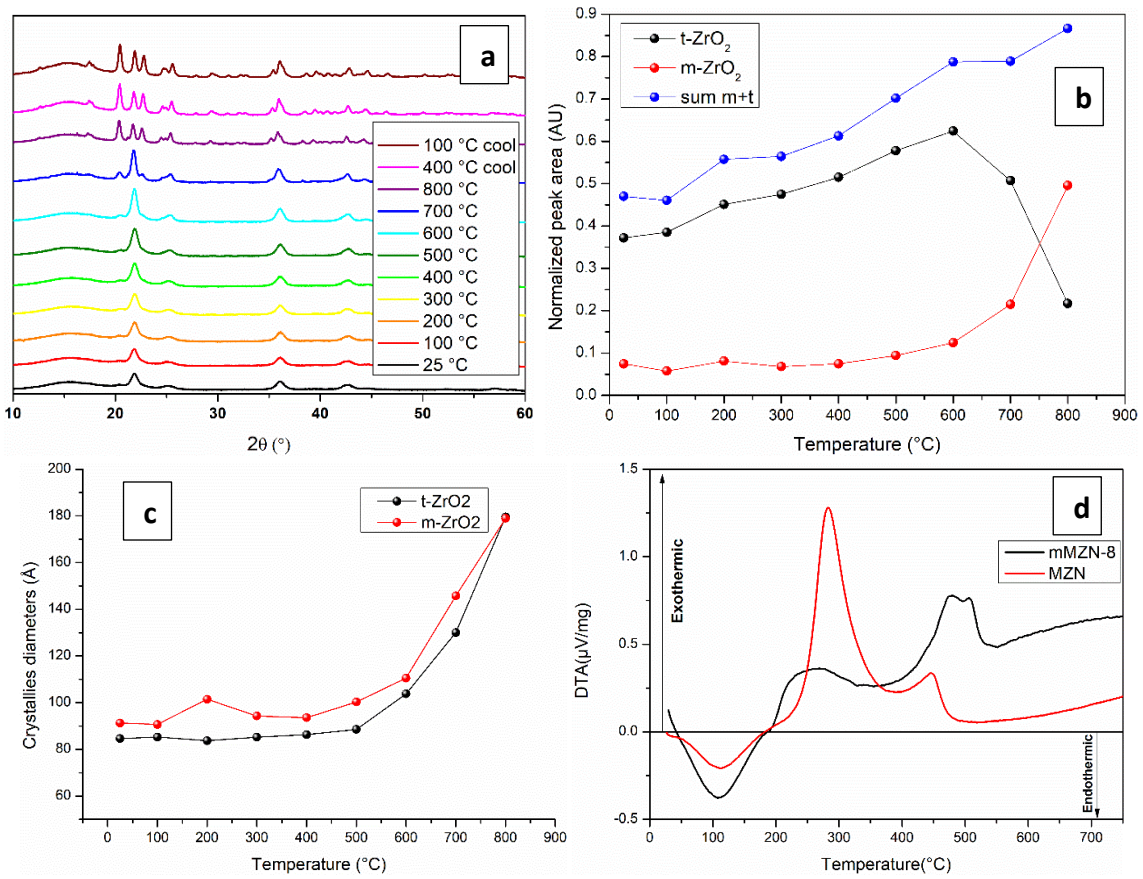

Figure 43: XRD patterns with increasing temperature of mMZN-8% (a), peak area of tetragonal and monoclinic phase, calculated between 20 and 30 2ϑ and normalized using H. Toraya equations [183] (b) crystallites diameters obtained fitting peaks between 20 and 30 2ϑ with increasing temperature of treatment for sample mMZN-8% (λ = 1.12576 Å); DTA curves of MZN (red) and mMZN-8 (black) (d)

So, thermal treatment at 450°C was carried out on the sample loaded with 8% of cobalt and iron for 4 hours. This preliminary attempt shows how is possible to maintain porosity, even if treated with quite high temperature (Figure 44) respect what it is possible with MZN. Sample obtained in this way, indeed, shows surface area of 140.0±0.5 m^2/g and pore volume of 0.19 cm^3/g (usually MZNs have 204±0.5 m^2/g surface area and 0.31 cm^3/g pore volume). However, the response to a magnet is not as good as the one obtained with the treatment at higher temperature. Indeed, in Figure 45 is visible how this system appears slower than the previous reported ones, and neither after one hour of magnetic sorting the system was fully recovered from the magnet, maybe due to poorer saturation magnetization.

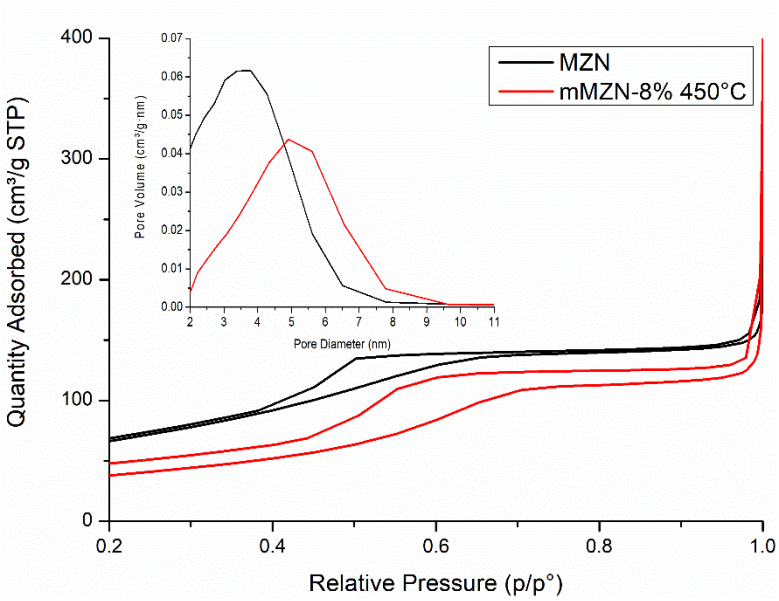

Figure 44: Nitrogen physisorption of MZN and mMZN-8% treated at 450 °C, in the inlet the pore volume distribution.

Moreover, TEM images show the different internal structure of the sample from that obtained with 700 °C thermal treatment, as is visible in Figure 46, and the presence of cobalt and iron inside nanoparticles is confirmed by EDX spectrum recorded in the middle of a single particle. These nanoparticles appear very different from the one obtained with 700 °C treatment, presented in Figure 21 and Figure 46 d. Indeed, here the big crystallites, which composed previous reported samples, are not detectable, and cobalt ferrite particles seems also smaller compared to the classical mMZNs. Unfortunately, neither XRD nor SAXS can give information on crystallite size of the magnetic phase. The XRD peaks of the $CoFe_2O_4$ are very broad and hidden by the peaks of ZrO_2 while the SAXS scattering due to the Co-Fe oxides and to the MZN porosity are overlapped.

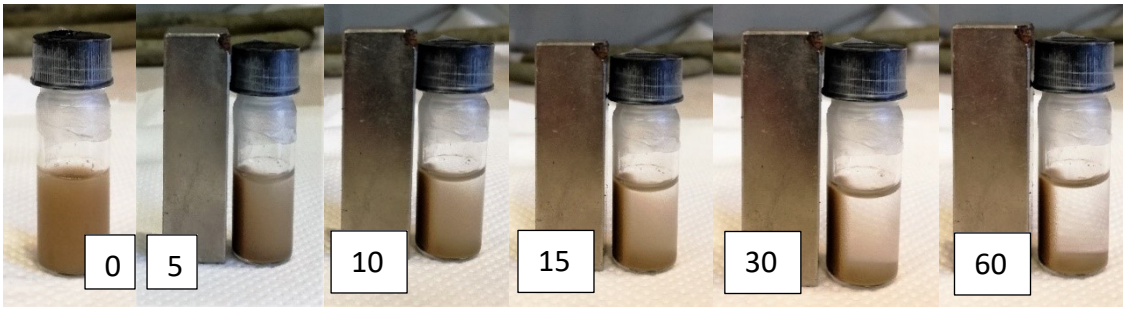

Figure 45: mMZN-8 treated at 450 °C for 4 h, recovered with a magnet at different times: 0, 5, 10, 15, 30, 60 minutes.

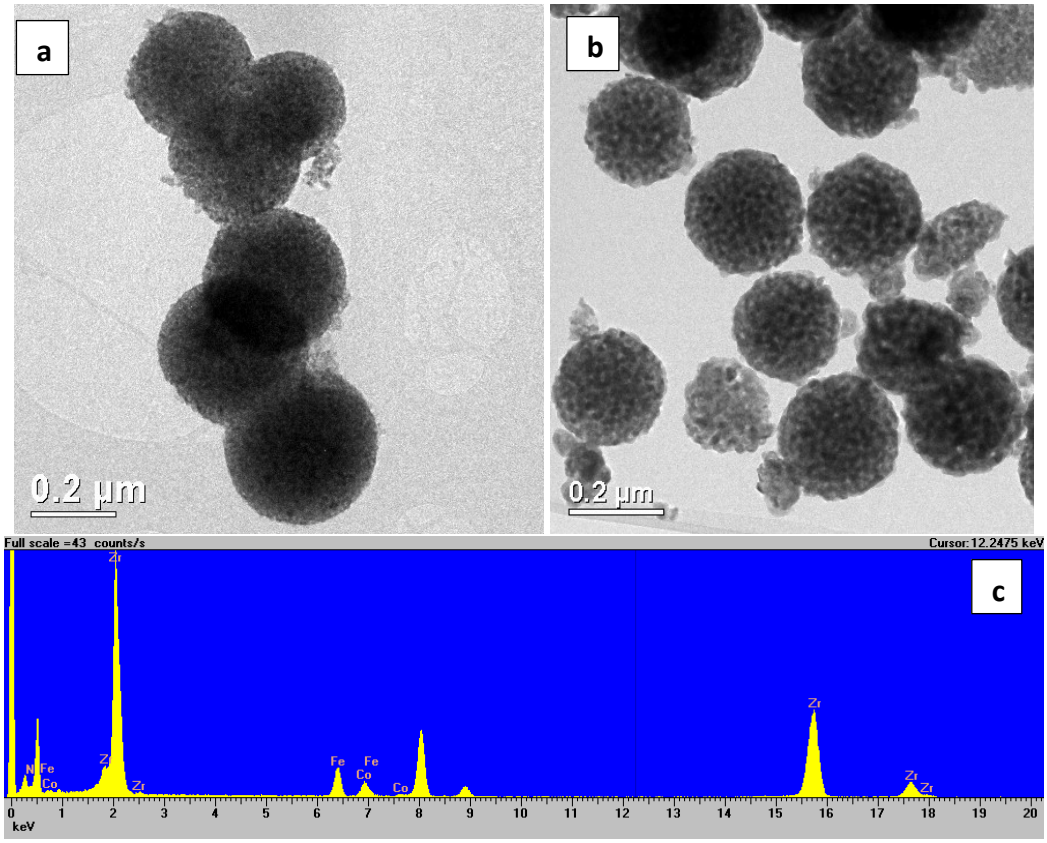

Figure 46: TEM images of mMZN8% treated at 450°C (a) and at 700 °C (b) and EDX spectrum (c) recorded in the middle of a single particle

Certainly, further investigations need to be done to improve magnetic performance and for a better understanding of the structure and magnetic properties of the nanoparticles.

Strategy #2:

Thus, to obtain nanoparticles that couple good magnetic properties and a porous and protecting structure, cobalt ferrites nanoparticles were first synthetized and then used as nuclei for the growth of previously reported mesoporous zirconia nanoparticles. To do so, polyol method, which employ metals nitrate salts precursor and, in our case, triethylenglycol as reducing and capping agents, was employed to obtain single-domain nanoparticles. This protocol produces nanoparticles that are stable enough in polar solvents, such as ethanol, needed for the synthesis of MZN, that allow the use of these particles as seeds in our synthesis method. In this way, no high temperature thermal treatment is required to produce magnetic phase inside zirconia, and a porous structure can be maintained.

$CoFe_2O_4$ nanoparticles obtained with this method are quasi-spherical and with diameters between 3 and 6 nm (Figure 47a) and EDX spectrum obtained with TEM further confirms their composition (Figure 47c) while XRD (Figure 47b) confirms the cubic spinel structures of cobalt ferrites: peaks related to this phase are present (red vertical line in the image) and the Scherrer analysis of the peak broadening confirm a size of 5± 0.5 nm.

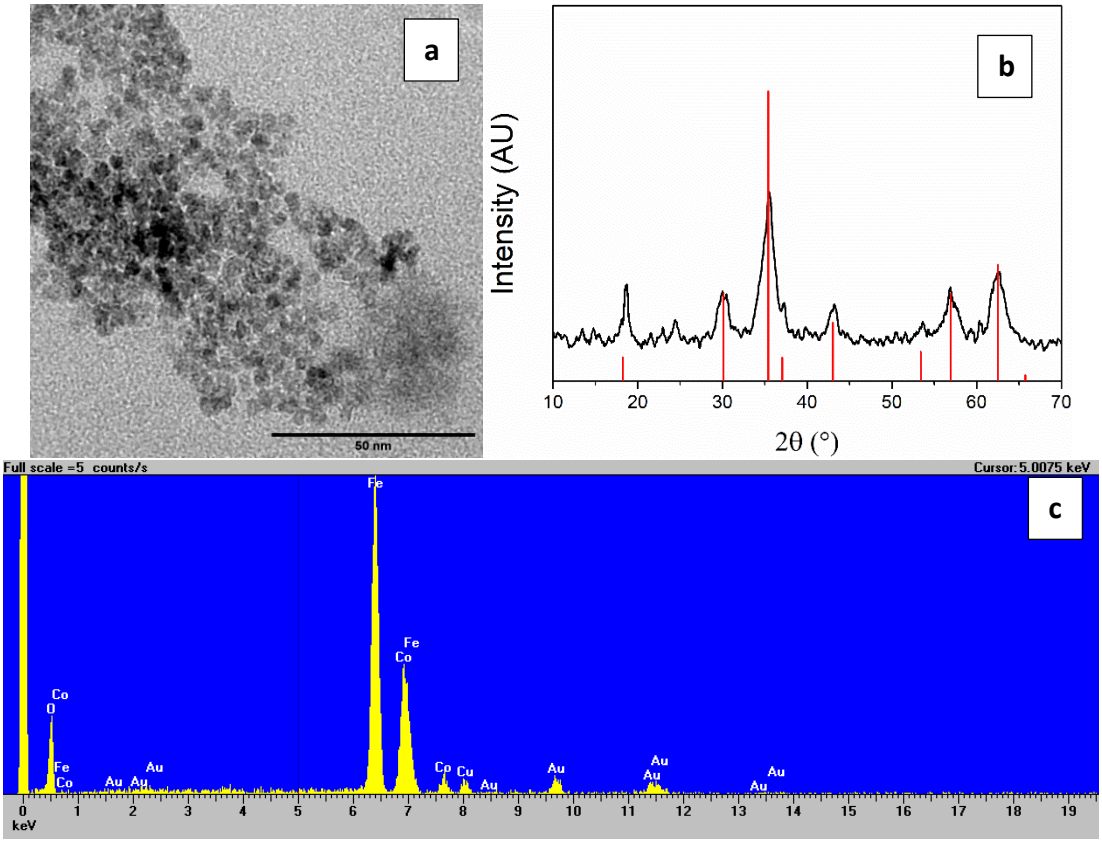

Figure 47: TEM image(a), XRD pattern (red lines correspond to $CoFe_2O_4$ (ICSD # 41257)) (b) of $CoFe_2O_4$ obtained with polyol synthesis and EDX spectrum obtained on TEM image.

These nanoparticles were then used as nuclei for the growth of zirconia, introducing them in the reaction environment before the addition of zirconium precursor. The reaction was conducted as a normal synthesis of MZN, using a mechanical stirring instead of a magnetic one, with a ratio between seeds and final expected zirconia of 50 % wt/wt, which correspond to 33 %wt/wt of the total compound. The so high amount was found as the best one to obtain good response to a magnet, no segregation of two phase (one magnetic and one made of zirconia with low amount of seeds) and good sphericity of the final system.

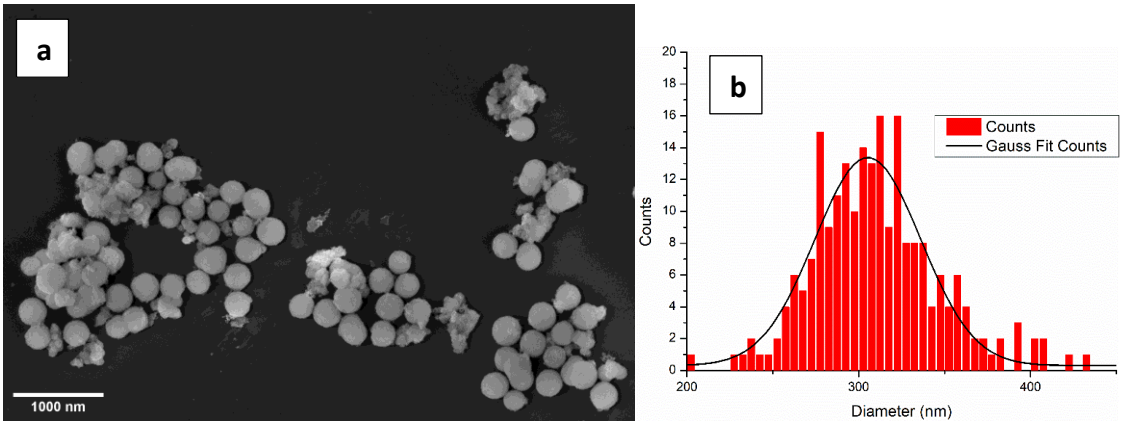

Figure 48: FE-SEM image of MZN obtained with CoFe2O4 seeds (a) and distribution of size obtained treating images with ImageJ software (b) [116-117]

Figure 48 shows magnetic MZNs obtained with this protocol: almost spherical nanoparticles are visible even if some impurities are present. The standard deviation on measured diameters is only the 10%, and the mean diameter obtained is 305±30 nm.

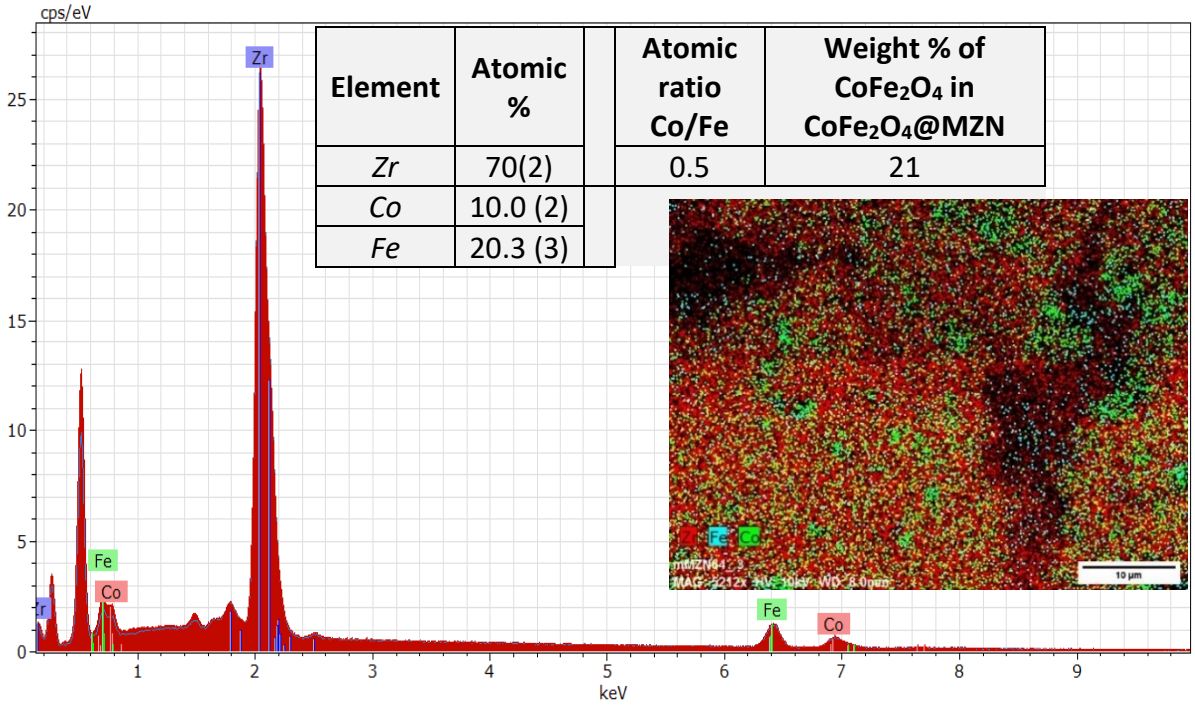

Element	Atomic %		Atomic ratio Co/Fe	Weight % of $CoFe_2O_4$ in $CoFe_2O_4$@MZN
Zr	70(2)		0.5	21
Co	10.0 (2)			
Fe	20.3 (3)			

Figure 49: Spectrum, maps (inset) and quantifications of elements (table in inset) obtained with EDX at FEG-SEM on massive sample of $CoFe_2O_4$@MZN

EDX spectrum obtained on the composite sample (Figure 49) confirmed the presence of iron and cobalt and quantifications was obtained. The nominal weight percentage of the $CoFe_2O_4$ in $CoFe_2O_4$@MZN (33%) seems diverging from the one obtained, but this difference could be ascribed to the weight of capping agent (triethylenglycol), which determines an overestimation of the loaded magnetic phase. Moreover, the map of the elements (Figure 49: inset) shows the homogeneity degree of the $CoFe_2O_4$ distribution and regions with higher amount of cobalt and iron could be found. These situations could be ascribed both to the difficulties in dispersing seeds of magnetic nanoparticles in the reaction environment, and to inhomogeneity of stirring during the synthesis, as previously reported.

XRD patterns of $CoFe_2O_4$ and $CoFe_2O_4$@MZN, reported in Figure 50, show how tetragonal zirconia is predominant. However, in this case peaks at 57 and 62 degrees, related to cobalt ferrite, are visible also in the nanocomposite, due to high quantities of $CoFe_2O_4$. Table 17 compare the size of the $CoFe_2O_4$ obtained by the Scherrer analysis of the XRD peaks.

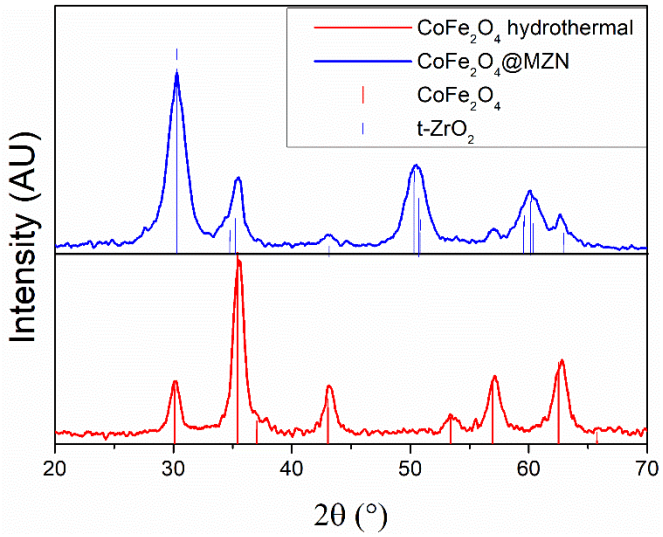

Figure 50: XRD diffractogram of $CoFe_2O_4$ (black line), $CoFe_2O_4$ treated in hydrothermal condition used for synthesis of zirconia (red line) and $CoFe_2O_4$@MZN (blue line) peaks related to spinel cobalt ferrites (ICSD # 41257) and tetragonal zirconia (ICSD # 164862) are highlighted with spikes.

Table 17: XRPD fitted diameter for $CoFe_2O_4$ obtained with polyol method and coupled with MZN; $<L>_{vol}$ is the diameter of crystallites.

Sample	$<L>_{vol}$ (nm)
$CoFe_2O_4$	5.0± 0.5
$CoFe_2O_4$ hydrothermal	5.7±0.6
$CoFe_2O_4$@MZN	4.0±0.5

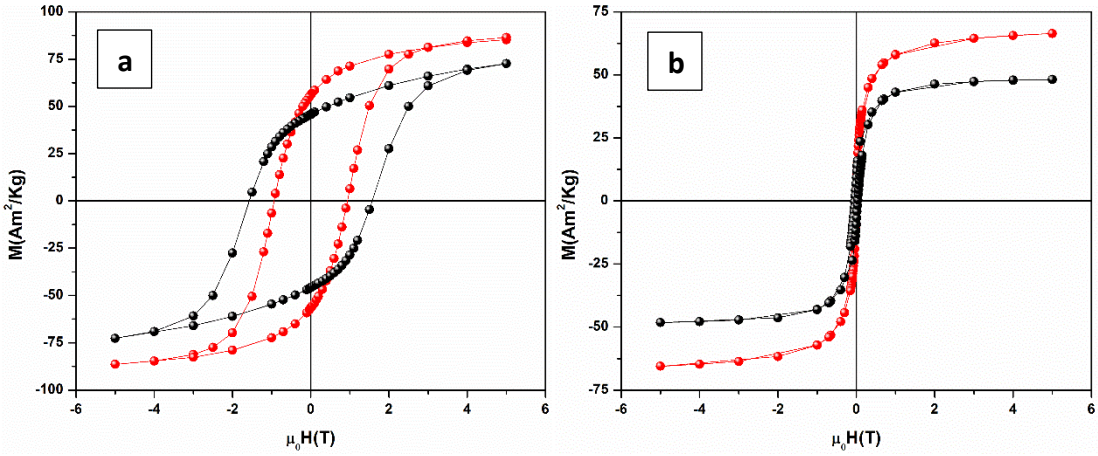

Figure 51: Hysteresis loops of cobalt ferrite NPs (red line and dots), cobalt ferrite in zirconia (black line and dots), measured at 5K (a) and measured at 300K (a).

DC magnetic measurements were performed and at 5 K and all samples show "quasi static behaviour" (i.e. blocked ferrimagnetic nanoparticles) (Figure 51a), showing hysteretic behaviours. The magnetic properties of monodomain nanoparticles are strictly related to their size and morphology, as previously reported. This correlation is well described by the M vs H curves measured at 5 K (Figure 51a). Both samples present quite high values of coercivity, as expected considering the high magneto-crystalline anisotropy of $CoFe_2O_4$

NPs [184]. It is evident that, once the cobalt ferrite nanoparticles are dispersed into zirconia (Figure 51a, black line and dots), a change occurs in the magnetic properties of the material respect to "bared" NPs (Figure 51a, red line and dots), with an increase of H_C and a decrease of M_S, even if only the mass of the magnetic phase was taken into account. In order to dispel any doubt that zirconia was the only one responsible for these changes, it was decided to subject the magnetic particles to the same hydrothermal treatment but without incorporating them into zirconia to see how much the zirconia was responsible for the changes that occurred. The Scherrer analysis of the XRD pattern (Figure 50, red line) shows that the crystal sizes were only slightly increased (see Table 17).

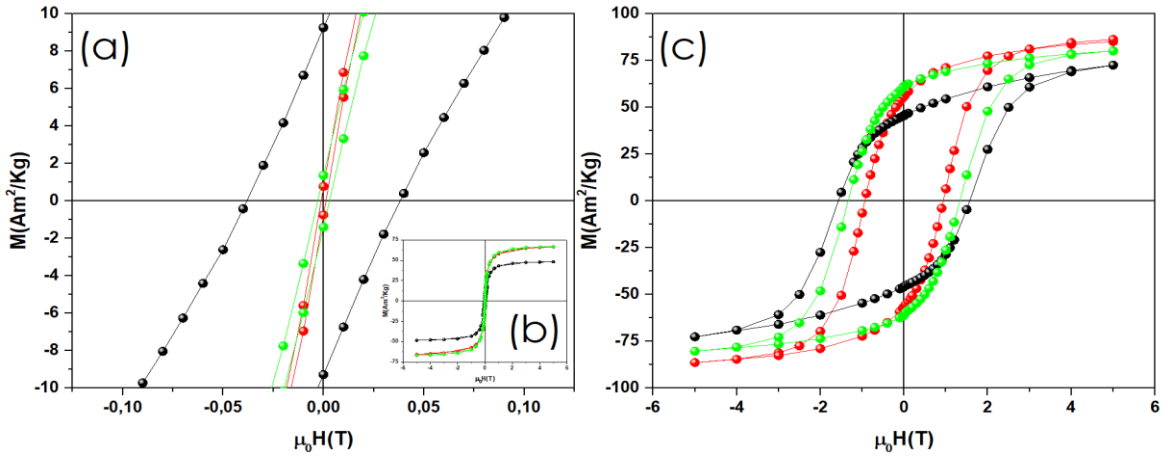

Figure 52: Hysteresis loops of cobalt ferrite NPs (red line and dots), cobalt ferrite in zirconia (black line and dots), cobalt ferrite after hydrothermal procedure (green line and dots); detail of hysteresis measured at 300K (a), full hysteresis measured at 300K (b). and at 5K (c).

The hysteresis loop of the particles thus treated (Figure 52c, green line and dots) shows equally evident differences with respect to the same particles in zirconia: there is an increase in M_S and a decrease in H_C. Therefore, zirconia increases the coercive field of the material produced but dampens the saturation magnetization. The same can be seen from the hysteresis of the same materials at 300K (Figure 52a and b): coercive field of cobalt ferrite dispersed in MZN's magnitude is ten time the samples of bare cobalt ferrite.

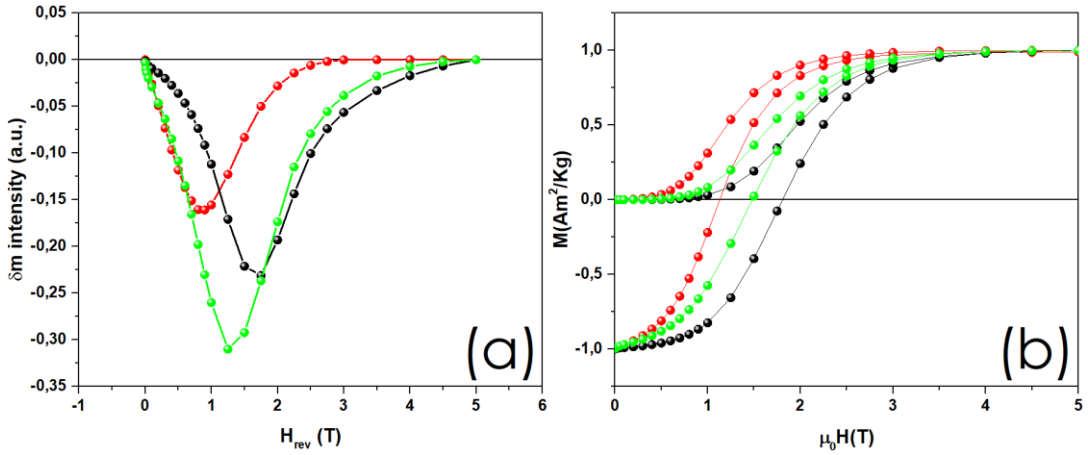

Figure 53: (a) δm parameter of cobalt ferrite NPs (red line and dots), cobalt ferrite in zirconia (black line and dots), cobalt ferrite after hydrothermal procedure (green line and dots); (b) remanent magnetization curves.

Data coming from IRM and DCD (Figure 53b) show that $CoFe_2O_4$ after hydrothermal treatment (Figure 53a, green line and dots) has a greater negative δm value respect to the same NPs incorporated in zirconia (Figure 53a, black line and dots). This proves that zirconia has the capability to decrease the amount of dipole-dipole interactions respect to magnetizing interaction. It is important to underline that by δm analysis is just possible to determine what kind of interactions are predominant and affect the magnetic behaviour of the system. Indeed, magnetizing and demagnetizing interactions, simultaneously present, contribute in an opposite way to the shape of the curve, thus resulting in a balance between the different contributions [175].

Table 18: Saturation magnetization (M_S); reduced remanence magnetization (M_R/M_S); coercive field (H_C) T=5K; coercive field (H_C) T=300K; interaction field (H_{in}); switching field distribution (SFD); difference between H_C measured by hysteresis and DCD (ΔH_C). Uncertainties on the last digit are given in parentheses.

Sample	M_S (Am^2Kg^{-1})	M_R/M_S	5K_H_C (T)	300K_ H_C (T)	H_{in} (T)	SFD (T)	ΔH_C (T)
$CoFe_2O_4$	88,0(8)	0,64(1)	0,94(1)	0,001(1)	0,03(1)	1,15(1)	0,19(1)
$CoFe_2O_4$@MZN	82,4(8)	0,55(1)	1,55(2)	0,038(3)	0,08(1)	1,83(1)	0,24(1)
$CoFe_2O_4$ HT	86,9(8)	0,70(1)	1,33(2)	0,003(3)	0,1(1)	1,50(1)	0,15(1)

Both samples showed M_S values quite close to bulk values (93 Am^2Kg^{-1}), as also reported for highly crystalline cobalt ferrite nanoparticles [185]. In addition, they exhibited values of reduced remanent magnetization (M_R/M_S) close to the one related to bulk cubic symmetry $CoFe_2O_4$, indicating a tendency toward a magnetic anisotropy with cubic symmetry in the cases of "bared" $CoFe_2O_4$ and after hydrothermal procedure [176], but with a decreased value for MZN. The $CoFe_2O_4$ sample shows a slightly lower value of switching field distributions: 1.15(1) vs 1.50(1) and 1,83(1) T, in agreement with the lower H_C, but, most importantly, their switching field distributions (SFD) are narrow, indicating that the sharp particle size distribution is associated with a sharp SFD. This represents a clear advantage, since it corresponds to a sharp reversal of the magnetization of the whole ensemble and to a narrow distribution of superparamagnetic (SPM) blocking temperatures. All the values are reported in Table 18.

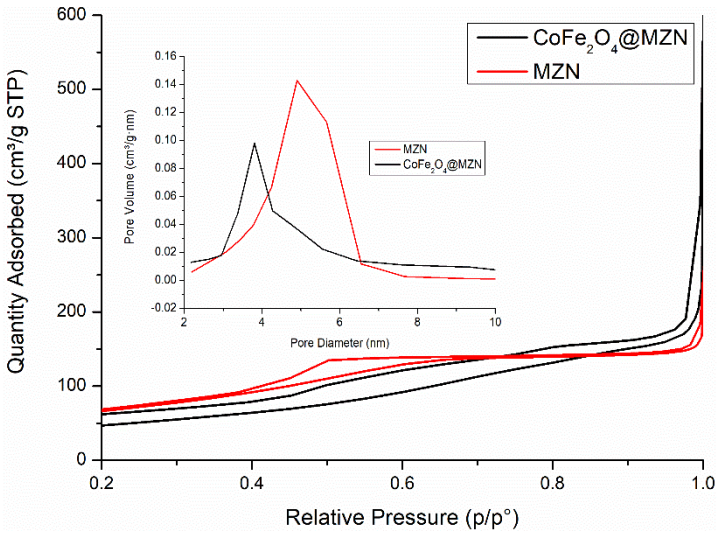

Figure 54: Nitrogen physisorption of bare MZN (red) and $CoFe_2O_4$@MZN (black)

Among all these promising properties, the goal of the synthesis of these structures was to obtain a magnetic nano-tool presenting remain porosity. Figure 54 shows how in this case a porous structure is obtained, reaching a surface area of 182.6±0.4 m^2/g and pore volume of 0.28 cm^3/g and pore diameter between 3.8 and 5 nm, whom compared to "normal" MZN seems in good agreement (i.e. 204±0.5 m^2/g, 0.31 cm^3/g and 5 nm). The broad distribution of pores sizes can be ascribed to the presence of magnetic nanoparticles that can interact during the micelles formation of template agents. This result of porosity confirms the possibility of employing the system for many applications thanks to the high surface area, such as DDS, and shows the needs of further investigations. Moreover, results from EDX specimens show also the needs of investigation on magnetic seeds, tuning both magnetic properties and surface characteristics, to obtain a more homogeneous system.

3.3.4. Synthesis of core-shell structure of different spinel ferrites

Bi-magnetic core-shell particles

To increase the field of applicability of magnetic nanosystems and improve the previously reported objects, bi-magnetic core-shell structures of spinel ferrites have been synthetized. Hard and soft magnetic materials were interchanged in core and shell to tune magnetic properties. Thus, it could be possible to produce a system with coupled magnetic phase where saturation magnetization and coercivity have desired characteristics for the application both as imaging probe and for hyperthermia treatments. Indeed, for MRI applications, high saturation magnetization and low susceptibility are needed, while for hyperthermia treatment high anisotropy and susceptibility are necessaries, so is evident the requirement of coupling two different magnetic phases that could act together in a theranostic system.

Thanks to the collaboration with Gurvinder Singh in NTNU University of Trondheim and the facility of NanoLab, several core-shell structures have been synthetized during the period abroad. Starting from $CoFe_2O_4$ structures, Ni and/or Zn ions have been introduced to modify magnetic properties of such hard-magnetic material. Thermal decomposition method employing acetyl acetonates precursor of metal ions and oleic acids, oleyl amine and hexadecandiol as capping and reducing agents were used to obtain such systems, following an optimized procedure derived from the work of Sun *et al.*[107] (see "Materials and Methods, Synthesis of core-shell spinel ferrites" for details). In this way, several core nanoparticles with doping content of 0, 25, 50 and 75% mol of Ni or Zn replacing cobalt in $CoFe_2O_4$ have been synthetized. In Figure 55 core nanoparticles with different stoichiometries are reported. As one can see, very small nanoparticles are obtained with this protocol, with diameters between 6 and 8 nm (reported in Table 19). However, the sphericity is not very high and seems quite polydisperse in diameter, also due to the so small dimension.

Table 19: Dimension of core nanoparticles obtained treating images with ImageJ obtained with S(T)EM [116-117]

Sample	Diameter
$CoFe_2O_4$	8±2
$Co_{0.75}Ni_{0.25}Fe_2O_4$	7±2
$Co_{0.5}Ni_{0.5}Fe_2O_4$	7±2
$Co_{0.25}Ni_{0.75}Fe_2O_4$	8±2
$Co_{0.75}Zn_{0.25}Fe_2O_4$	7±2
$Co_{0.5}Zn_{0.5}Fe_2O_4$	7±2
$Co_{0.25}Zn_{0.75}Fe_2O_4$	7±2

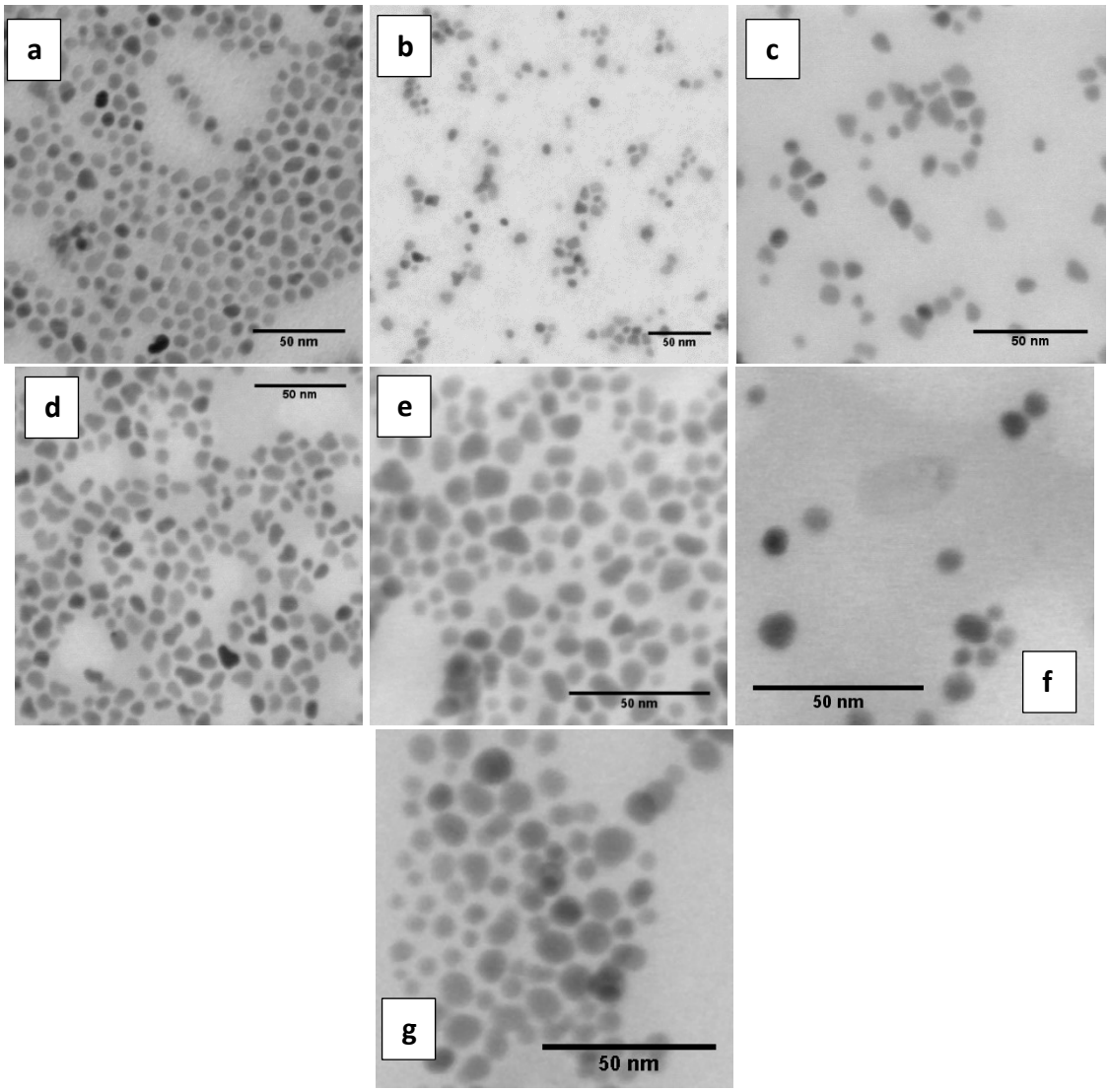

Figure 55: S(T)EM images of core particles: $CoFe_2O_4$ (a), $Co_{0.75}Ni_{0.25}Fe_2O_4$ (b), $Co_{0.5}Ni_{0.5}Fe_2O_4$ (c), $Co_{0.25}Ni_{0.75}Fe_2O_4$ (d), $Co_{0.25}Zn_{0.75}Fe_2O_4$ (e), $Co_{0.5}Zn_{0.5}Fe_2O_4$ (f), $Co_{0.75}Zn_{0.25}Fe_2O_4$ (g)

XRD measurements were performed to confirm spinel crystal structure of these samples. As one can see from Figure 56, doping agents did not affect the spinel structure [186]. Moreover, the high FWHM of diffractogram peaks confirm the small dimension of nanoparticles.

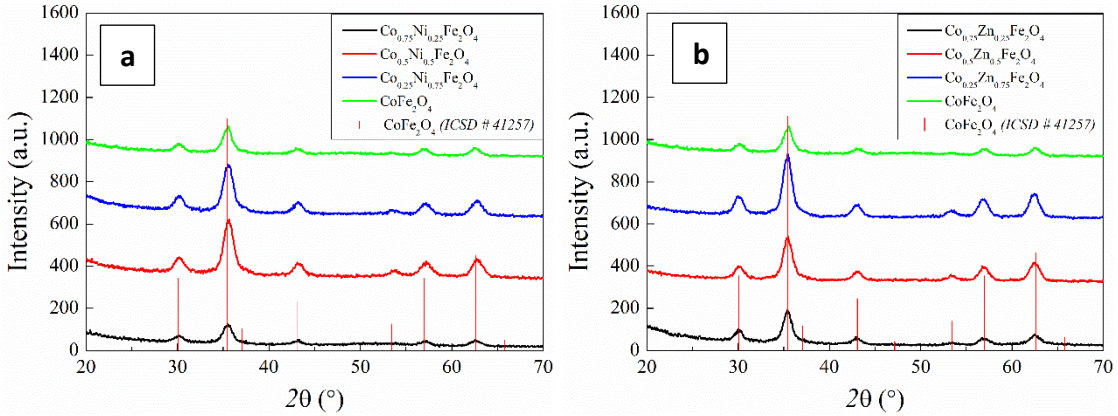

Figure 56: XRD pattern of core of $CoFe_2O_4$ doped with Ni (a) and Zn (b)

DC magnetization measurements were performed on samples doped with Zn, due to the better shape and size distribution, to confirm the single domain both crystalline and magnetic. As expected [172], samples show hysteretic behaviours at 5K (Figure 57a), with increasing saturation magnetization and decreasing coercivity with higher content of Zn (Table 20). On the other hand, M_s measured at 300 K show lower values respect to bare cobalt ferrites for quantities up to 50% of Zn, but come back up with the higher content of this ion (Figure 57b). These results, however, are not in agreement with what reported in literature, where is fount that increasing Zn content more than 50% molar, leads to a decrease in M_s at room temperature, even if a detailed study of the behaviour of nanoparticles of Zn substituted $CoFe_2O_4$ is still not present [95, 97, 101, 187-191].

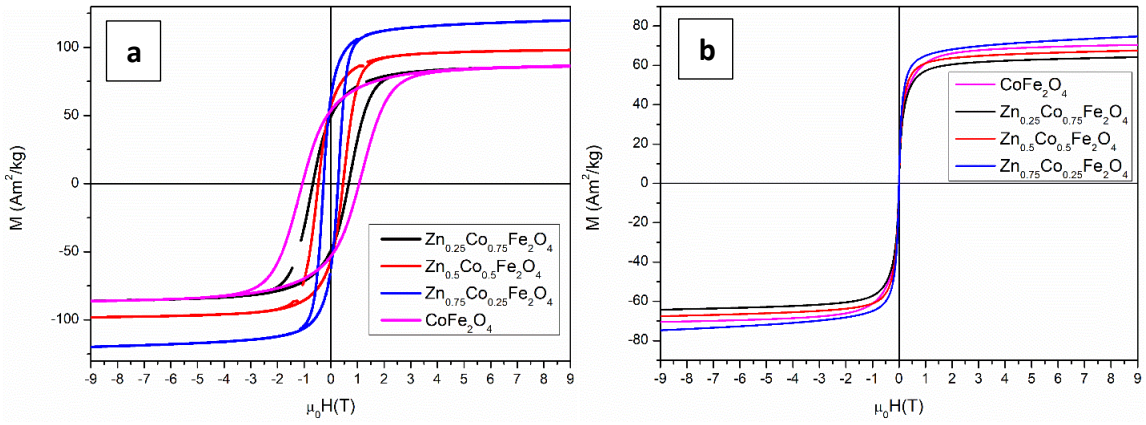

Figure 57: Hysteresis loop of Zn doped core recorded at 5 K (a) and 300 K (b)

Table 20: Coercive field ($\mu_0 H_C$) T=5K; magnetization at 9 T (M_{9T}) T=5K; saturation magnetization (M_S) at 5 and 300 K; reduced remanence magnetization (M_R/M_S); maximum in temperature (T_{max}) obtained by ZFC-FC, temperature of irreversibility (T_{irr}) and blocking temperature (T_b). Uncertainties on the last digit are given in parentheses.

Sample	**$\mu_0 H_c$_5K** (T)	**M_{9T} (5K)** ($A\ m^2\ Kg^{-1}$)	**M_s (5 K)** ($A\ m^2\ Kg^{-1}$)	**M_r/M_s**	**M_s (300 K)** ($A\ m^2\ Kg^{-1}$)	**T_{MAX}** (K)	**T_{Irr} (3%)** (K)	**T_b** (K)
$CoFe_2O_4$	1.06(1)	86.297(4)	89.26 (1)	0.6	73.40(1)	290(3)	323(9)	212.0(2)
$Co_{0.75}Zn_{0.25}Fe_2O_4$	0.672(1)	85.996(6)	88.9 (3)	0.55	67.59(2)	286(3)	330(10)	242(2)
$Co_{0.5}Zn_{0.5}Fe_2O_4$	0.464(2)	98.018(4)	100.50 (2)	0.56	71.33(2)	229(3)	247(9)	197(1)
$Co_{0.25}Zn_{0.75}Fe_2O_4$	0.273(3)	119.739(6)	125.67 (5)	0.5	82.10(3)	192(3)	215(10)	176(1)

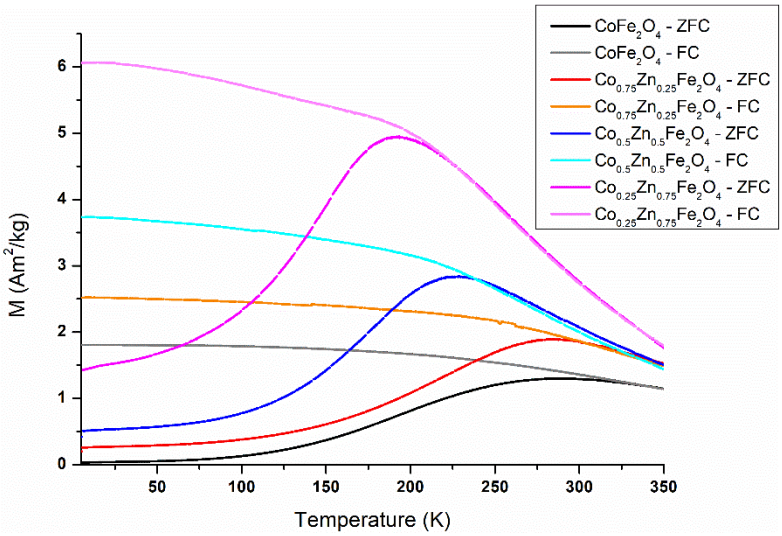

Figure 58: ZFC-FC measurements on cobalt ferrite and zinc substituted cobalt ferrites.

ZFC-FC measurements were performed in core samples and show how T_{max}, T_{irr} and T_b decrease with increasing quantities of Zn (Table 20). Indeed, Zero Field Cooling-Field Cooling measurements are usually employed to study the thermal dependence of magnetization. The ZFC magnetization curves have a maximum at a temperature (T_{max}), which is related to the average blocking temperature through the relation: $T_b \propto \beta T_{max}$; where β is a proportionality constant, depending on the type of size distribution. The temperature below which the ZFC and FC curves show an irreversible behaviour (T_{irr}, in this case fixed at 3%) is associated with the blocking of the biggest particles, assuming that the anisotropy energy barrier is determined by the magneto-crystalline anisotropy. Above this temperature a fully superparamagnetic regime is entered. Indeed, as reported in "Introduction", a superparamagnetic state is reached when all the particles are in the unblocked state and their magnetic moment switches due to thermal vibrations/energy [114].

From these results is clear how the increasing quantity of Zn lead to an increasing superparamagnetic state of the core nanoparticles.

However, further investigations on magnetic properties and structures of the core are needed to deeply understand the system.

Then, shells on doped cobalt ferrite core were introduced varying composition for further tuning properties for biomedical applications. In particular, Zn and Ni doped cobalt ferrites shells were synthetized on $CoFe_2O_4$ core. Nickel doped cores were covered with Zinc doped $CoFe_2O_4$ shell and Zinc doped cores were covered with Nickel doped $CoFe_2O_4$ shells, in order to have each system and its opposite (Table 3).

Better results were obtained with $CoFe_2O_4$ core and Zn or Ni doped $CoFe_2O_4$ shells, where nanoparticles appear more spherical and less polydisperse (Figure 59 for Zn doped and Figure 60 for Ni doped). Moreover, shells thickness, measured as the difference in diameters measured by S(T)EM between core and core-shell, appears more coherent between different samples (Table 21 and Table 22 and Figure 59 e).

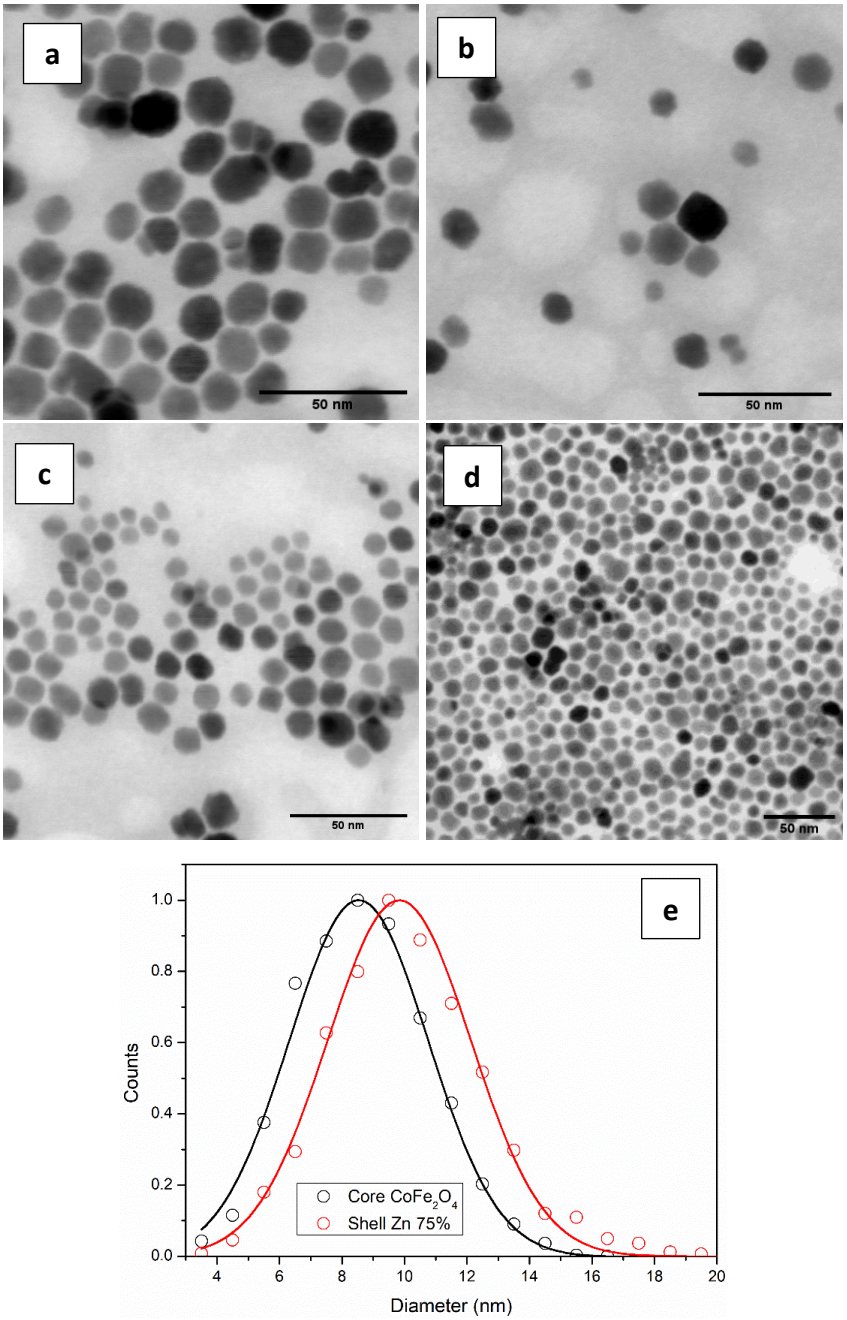

Figure 59: S(T)EM images of $CoFe_2O_4$ with shells of $Zn_{0.25}Co_{0.75}Fe_2O_4$ (a), $Zn_{0.5}Co_{0.5}Fe_2O_4$ (b), $Zn_{0.75}Co_{0.25}Fe_2O_4$ (c), $ZnFe_2O_4$ (d) and comparison of fitted diameters of core and core-shell as example (e)

Table 21: Dimension of nanoparticles obtained with treating images obtained with S(T)EM with ImageJ[116-117]

Samples	Diameter (nm)	Shell Thickness (nm)
$CoFe_2O_4$ (core)	8±2	-
$CoFe_2O_4$@ $Zn_{0.25}Co_{0.75}Fe_2O_4$	14±3	~2.65
$CoFe_2O_4$@ $Zn_{0.5}Co_{0.5}Fe_2O_4$	10±3	~0.7
$CoFe_2O_4$@ $Zn_{0.75}Co_{0.25}Fe_2O_4$	10±2	~0.65
$CoFe_2O_4$@ $ZnFe_2O_4$	10±3	~0.56

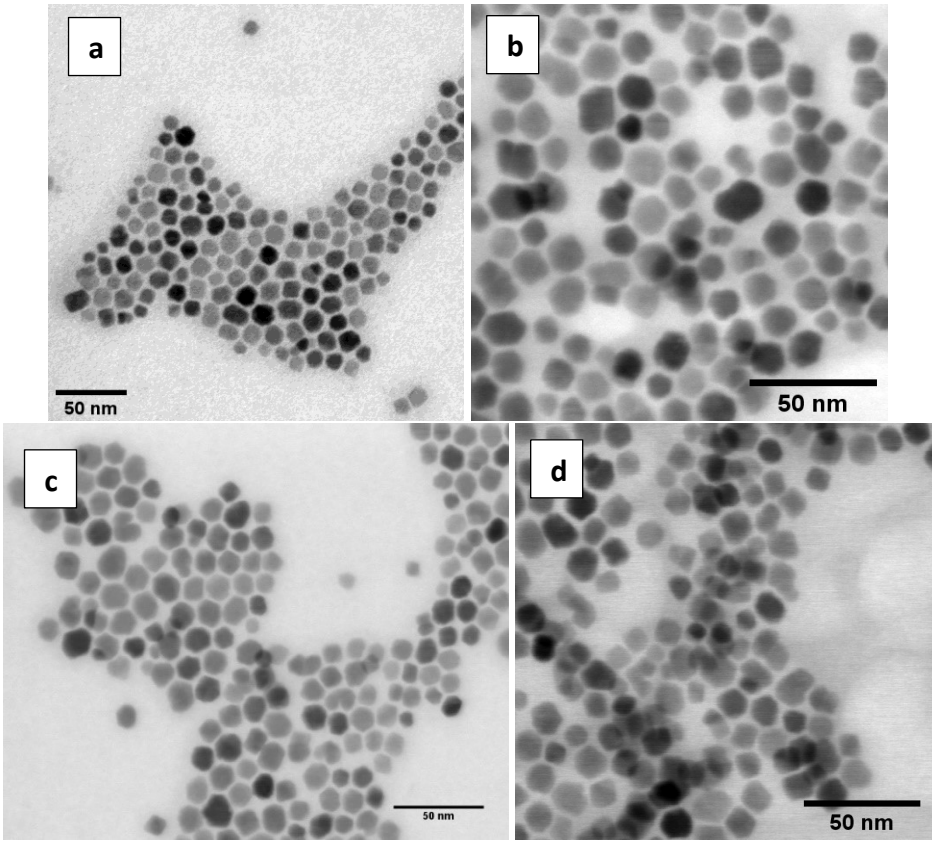

Figure 60: S(T)EM images of $CoFe_2O_4$ with shells of $NiFe_2O_4$ (a), $Ni_{0.25}Co_{0.75}Fe_2O_4$ (b), $Ni_{0.5}Co_{0.5}Fe_2O_4$ (c), $Ni_{0.75}Co_{0.25}Fe_2O_4$ (d)

Table 22: Dimension of nanoparticles obtained with treating images obtained with S(T)EM with ImageJ [116-117]

Samples	Diameter (nm)	Shell Thickness (nm)
$CoFe_2O_4$ (core)	8±2	-
$CoFe_2O_4$@ $Ni_{0.25}Co_{0.75}Fe_2O_4$	12±3	~1.9
$CoFe_2O_4$@ $Ni_{0.5}Co_{0.5}Fe_2O_4$	12±2	~1.25
$CoFe_2O_4$@ $Ni_{0.75}Co_{0.25}Fe_2O_4$	11±3	~1.05
$CoFe_2O_4$@ $NiFe_2O_4$	12±3	~1.65

The introduction of the shell did not affect structurally, size apart, nanoparticles, and XRD patterns did not change upon modification (Figure 61), which is another proof of doping without segregations of other crystal phases.

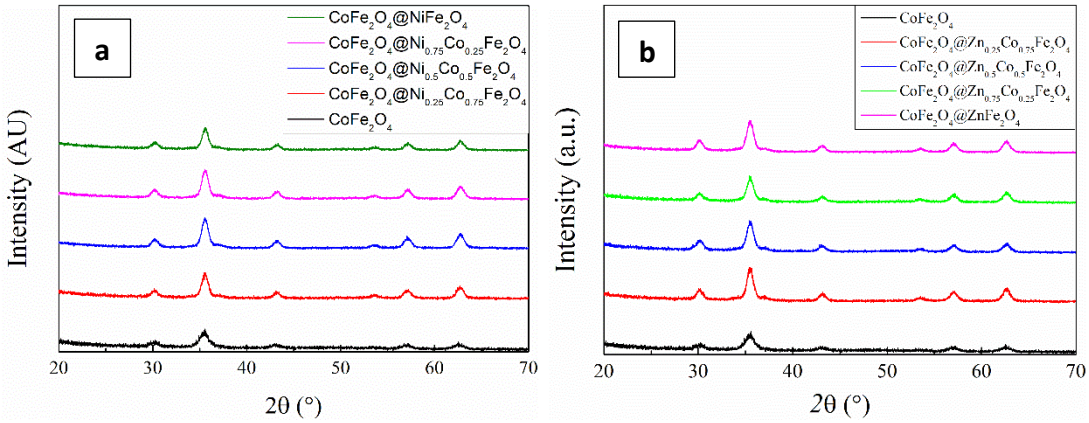

Figure 61: XRD patterns of $CoFe_2O_4$ with Ni (a) or Zn (b) doped $CoFe_2O_4$ shells

The so formed core-shell nanoparticles are then characterized with DC magnetization measurements, in order to see the behaviour through modifications, even in this case Zn doped shell samples have been chosen. Nanoparticles show hysteretic behaviours at 5 K, showing almost the same behaviour of core doped with Zn, with increasing magnetization saturation and decreasing coercivity, augmenting the quantity of Zn, but to a lesser degree than those observed with core. Indeed, after a first increasing in H_c values, due to the addition of the shell and the higher volume of nanoparticles, a decreasing tendency with the increasing amount of zinc is observed, up to the value related to $ZnFe_2O_4$ shell, where H_c appears even lower than that measured for core. As previously reported, these effects could be ascribed to the introduction of the soft magnetic phase of $ZnFe_2O_4$.

The most interesting thing is the absence of kink around zero field, that means that the two magnetic phases, the one from the core and the one from the shell, are coupled and there is no segregation, differently from what appears with mMZNs.

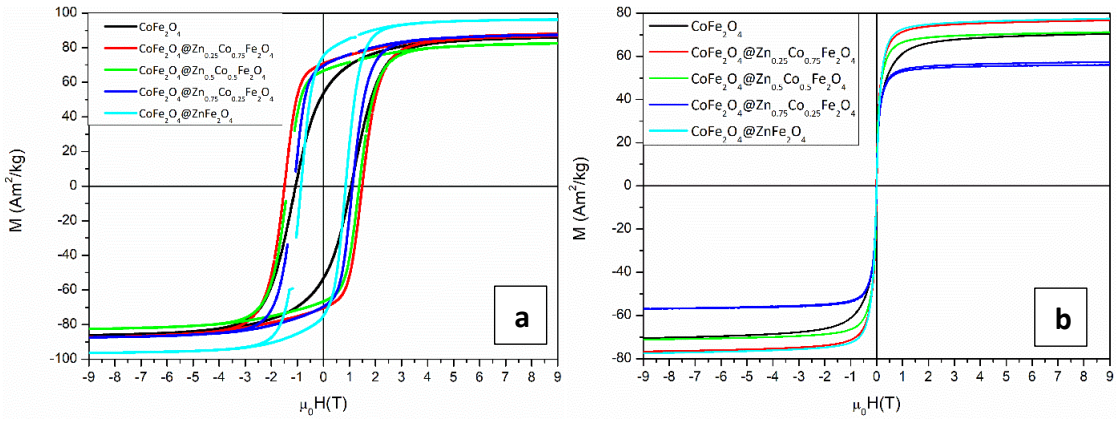

Figure 62:Hysteresis loop of Zn doped shells recorded at 5 K (a) and 300 K (b)

Table 23: Coercive field ($\mu_0 H_C$) T=5K; magnetization at 9 T (M_{9T}) T=5K; reduced remanence magnetization (M_R/M_S); saturation magnetization (M_S) at 5 and 300 K. Uncertainties on the last digit are given in parentheses.

Sample	$\mu_0 H_c$_5K (T)	M_{9T} (5K) (A m^2 Kg^{-1})	M_r/M_s	M_s (5 K) (A m^2 Kg^{-1})	M_s (300 K) (A m^2 Kg^{-1})
$CoFe_2O_4$	1.06(1)	86.297(4)	0.6	89.262 (2)	73.40(1)
$CoFe_2O_4$ @$Co_{0.75}Zn_{0.25}Fe_2O_4$	1.493(6)	87.696(6)	0.78	90.820 (4)	78.76 (3)
$CoFe_2O_4$ @$Co_{0.5}Zn_{0.5}Fe_2O_4$	1.373(7)	82.483(5)	0.79	84.614 (4)	73.01 (2)
$CoFe_2O_4$ @$Co_{0.25}Zn_{0.75}Fe_2O_4$	1.124(6)	87.378(4)	0.78	89.172 (4)	57.4 (2)
$CoFe_2O_4$ @$ZnFe_2O_4$	0.856(5)	96.310(7)	0.77	97.446 (7)	79.92 (2)

Also in this case ZFC-FC measurements were performed, but did not show any superposition in the studied region of temperature. The superparamagntec character of these samples seems not confirmed by these preliminary results, thus further investigations are needed.

Moreover, further investigations of the systesms need to be performed, in order to establish all magnetic and structural properties of all core-shell nanoparticles, for the right application in the biomedical fields.

Magnetic-dielectric core-shell particles

Preliminary results were also obtained trying to couple a magnetic core and a zirconia shell with thermal decomposition methods. A previously synthetized batch of Fe_3O_4 seeds was treated with oleic acid and $Zr(acac)_4$ to obtain a shell on these nanoparticles made of ZrO_2. Iron oxide has been chosen for this test due to the good affinity between iron and zirconium, as previously reported. In Figure 63 a and b, S(T)EM images of core and core shell samples are reported. Small nanoparticles were obtained also in this case, with quite good circularity and not too high polydispersion, which increase with the introduction of the shell. A preliminary proof of the shell formation is the increasing of the diameter of nanoparticles from 7 to 9.7 nm, as is visible in Figure 63c (table in inlet). However, from Figure 63 c, no differences in XRD diffractogram are visible, maybe due to the low amount of ZrO_2 introduced. Further characterization and tests are needed to see if the introduction of the shell was really formed and this sample could be considered as a good starting point to couple superparamagnetic cores obtained with thermal decomposition methods and zirconia.

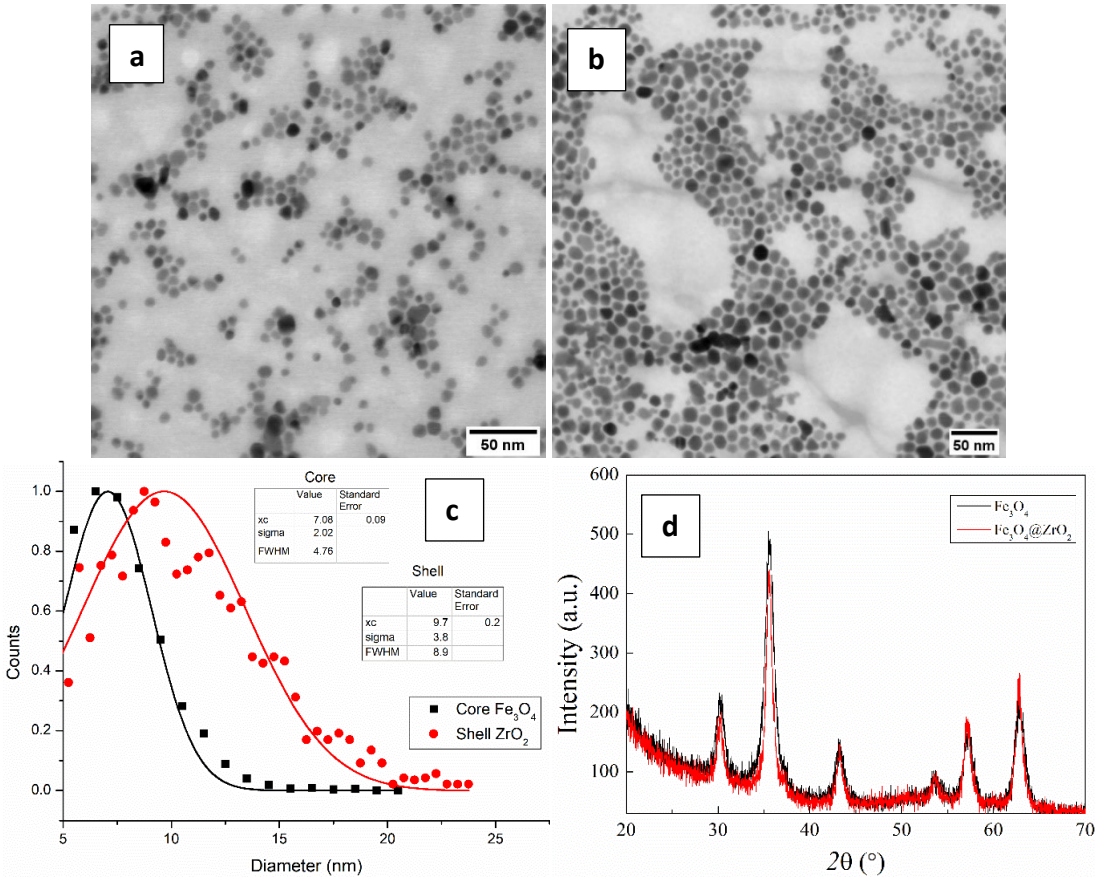

Figure 63: S(T)EM images of Fe3O4 core (a), Fe3O4@ZrO2 core-shell (b), distribution of diameters of core (black) and core-shell (red) (c) and XRD measurements of core (black) and core-shell (red) (d).

Exchange Ligand

The synthesis of these systems, however, produce nanoparticles that are dispesible in apolar solvents, due to the oleic acid as capping agent, which makes impossible the application in biological systems. Thus, to make them suitable for water environments, preliminary tests of exchange ligand were performed. BPMG and PMIDA were used as new legands for nanoparticles, and the protocol from X. Wang et al [142]. was followed, which employed ethanol as solvent. A high amount of exchanging molecules was mixed with as synthetized nanoparticles, in particular $CoFe_2O_4$, in ethanol, with the help of a sonication system. The resulting nanoparticles now seems having good affinity with water. However, TEM images reveal that the phosphono-carboxylic acids partially degraded metal oxides, as is visible in Figure 64, and coupled with EDX spectra seems that the molecules extract metal ions due to their acidity. Indeed, lower quantity of Co appears respect to the one of iron, and the peak related to P is very high. It could be due to the high acidity of new ligand and the capability of it to produce metal-organic framework, especially between cobalt and PMIDA, as founded in literature [192-193]. A proof of this theory is visible in Figure 64b, where a polymer structure appears surrounding nanoparticles, and react under microscope beam. However, it has been found in literature that phosphonic acids could be good capping agents also for these system [194-195], so further investigations were started.

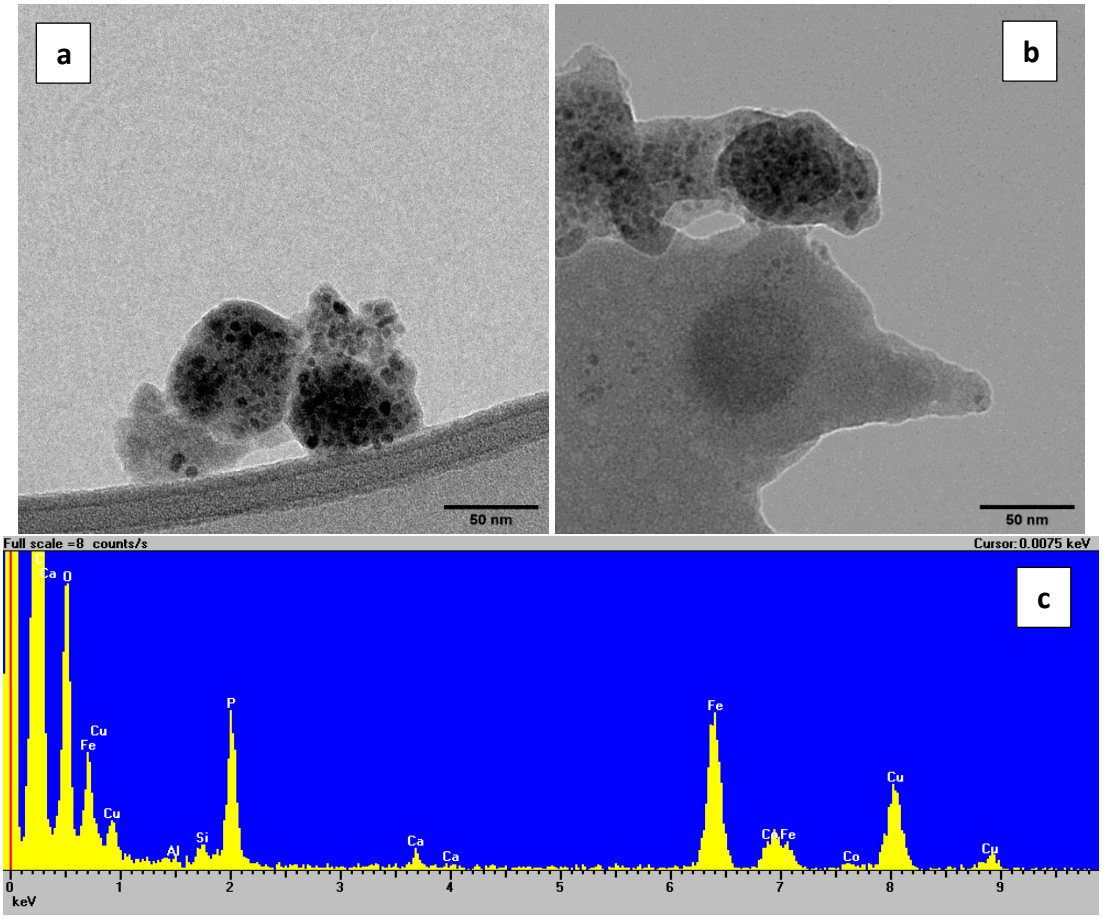

Figure 64:TEM images of CoFe2O4 after exchange ligand with BPMG (a and b) and EDX spectra recorded on it (c).

Basification with buffer solution seems not having good results, but no characterization was performed, due to instrumental problems. However, with tests of dispersion in water, it seems that the system was not the right one, yet.

A good compromise could be found with aprotic solvents, where the acidity and/or protonation-deprotonation are limited.

Further investigations are certainly needed to find the best protocol for exchange ligands to finally couple these seeds with MZN, as the system prepared with core obtained with polyol method.

3.4. Orthopaedic applications

3.4.1. Surface modifications of bulk materials

Layer by layer technique are usually used to modify surfaces with organic molecules, polymer or silane, employing also the sol-gel chemistry [143]. Different kind of interaction can be used, such as electrostatic bond, covalent bond, hydrophobic interaction and so on. Moreover, all these kinds of links are affected by environmental conditions, that determine the successful of covering and the stability of the layer. Nanoparticle layer deposition is a technique that is in development and, nowadays, not widely used due to the lack of protocols to make a reproducible cover of surfaces [144].

Many techniques are used to modify the surface of a solid: sputtering, dip coating, spin coating, spray-coating, plasma coating, drop casting, electrochemical deposition and electromagnetic deposition [70, 73, 145-146]. The drop casting consists on the deposition of a drop on a flat surface, that evaporating deposits nanoparticles. The thickness of the layer depends on the concentration of nanoparticles in the colloidal solution and can be tuned also varying ionic force, pH and volatility of the solvents. In Dip coating the substrate, immersed in the colloidal suspension, is withdrawn at a constant speed to avoid any jitters. Viscosity, capillarity and evaporation speed of the solvent govern the deposition and the formation of the layer. Physical-chemical properties of the solvent are always crucial for the deposition, affecting its affinity with the surface [147].

After the modifications of MZNs with organophosphate, it has been seen that, when the dispersion of nanoparticles was left drying, layers of nanoparticles on the internal surface of the vial, with optical opal like behaviours, were spontaneously formed. Starting from this evidence, analyses with FEG-SEM were done on these ordered multilayers. From these analyses it has been found that neat layers were produced during drying of colloidal solutions of MZNs, as one can see in Figure 65.

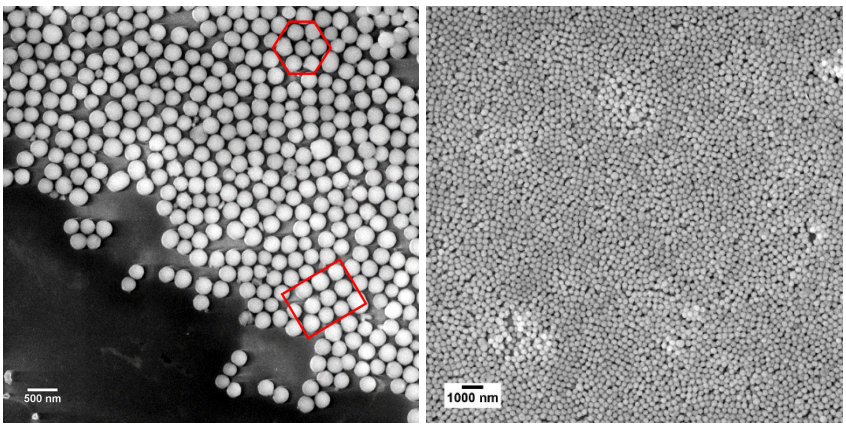

Figure 65: Examples of layers on silicon, obtained with MZN-PSer

Nanoparticles appear very disordered, but small ordered regions with cubic or hexagonal packing can be observed, as one can see in Figure 65 (evidenced in red). A first attempt was made with Drop casting, in order to establish the best conditions for the deposition, but poor results have been obtained because of the low homogeneity and reproducibility

of the formed layers, mainly for the difficulties in controlling the surface tension and vaporization of solvent.

Dip coating, due to higher reproducibility of the technique, was then employed to perform different tests varying the surfaces (with particular care on the smoothest ones) and its functionalization, functionalizations of nanoparticles and solvents of colloidal suspensions.

The best results were obtained at the lower speed (0.01 mm/s) allowed by our dip coater instrument and with MZN-PCOOH and amino-modified surfaces.

The modification of the studied surfaces (glass, silicon and titanium) was firstly obtained using an atmospheric plasma device able to activate and functionalize the surfaces with a single step (scheme of the plasma device is reported in Figure 66, thanks to the collaboration with Nadir srl.).

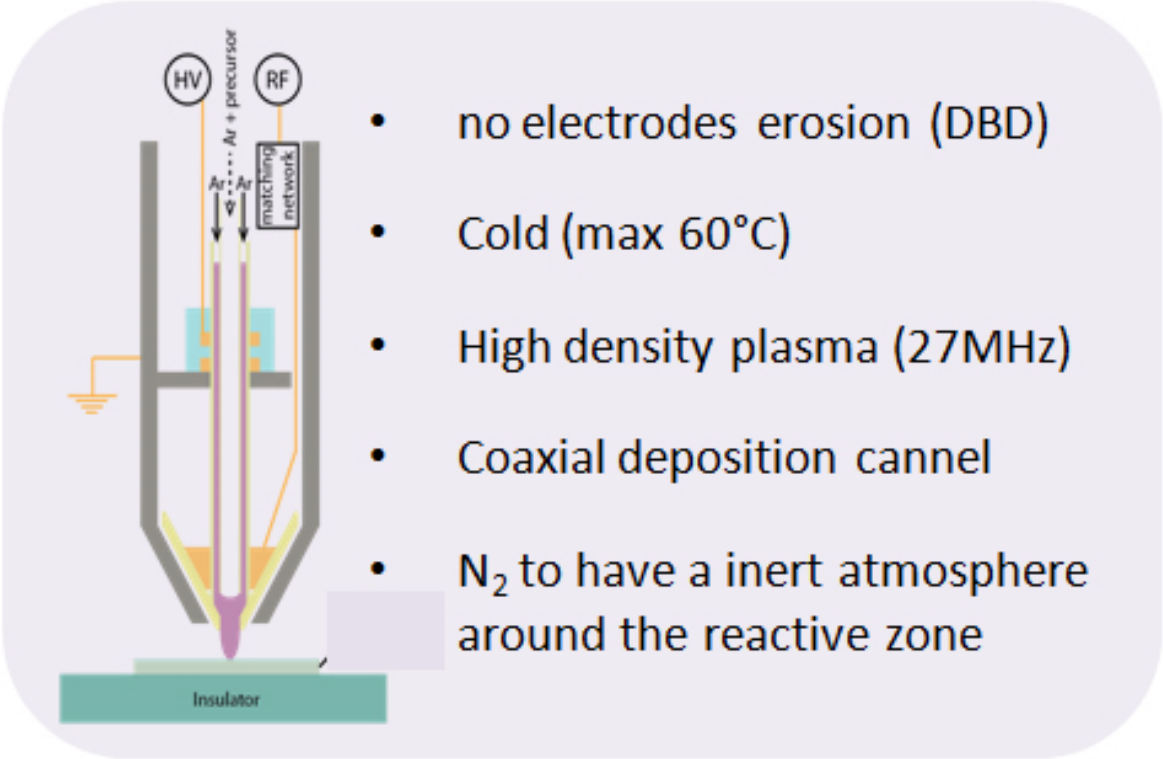

Figure 66: Schematic representation of atmospheric plasma device and main characteristics.

The preliminary tests on amino-functionalized surfaces were carried out on glass and silicon, modified with APTES and with MZN modified with PCOOH. Borosilicate glass slides and Silicon wafers were chosen for the first studies because of their smooth surface and because they can be easily modified with silane precursors. From Figure 67, one can see how polarity of solvents influences the covering of surfaces: organic solvents involve low covering degree and low uniformity respect to the water and water buffer solutions. Moreover, the choice of the right pH value, seems to be crucial for better coatings, as is evident from Figure 67 d, e, f, where a decreasing of bonded nanoparticles to the surface is visible from pH 4 to 9. Indeed, it has been found that the best conditions for the

deposition with this NPs modification on glass were obtained using acidic conditions or water, where surface charges on nanoparticles were less than with basic pH (see ζ-potential in Figure 15). As expected, higher percentages of covering were reached if amino groups were present on the surface and the carboxylic one on the nanoparticles and was able to interact strongly with bulky surface, condition reached in this case with buffer at pH 4 (Figure 67 g, chosen for FEG-SEM analysis after preliminary evidences at optical microscope) due to protonation and deprotonation of both species and from results obtained on bare glass (Figure 67 d-f).

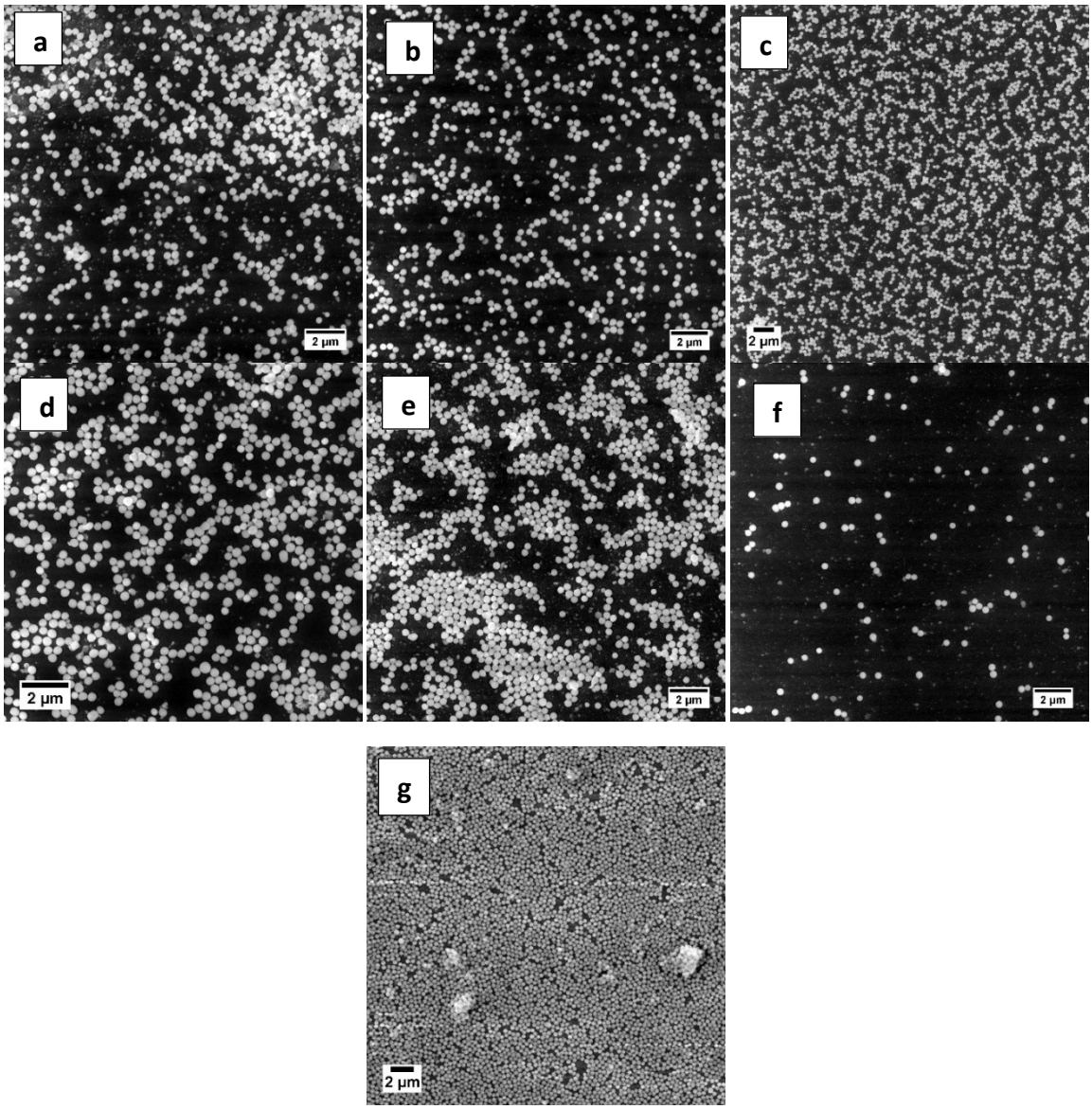

Figure 67: Dip coating deposition of MZN-PCOOH on glass: a) ethanol dispersion, b) acetone dispersion, c) water dispersion, d) acetate buffer at pH4 dispersion, e) MES buffer pH6 dispersion, f) CAPS buffer pH9 dispersion. g) Aminated glass and MZN-PCOOH dispersed in acetate buffer pH4.

Figure 68 shows the effect of the functionalization of the surface of a silicon wafer using a colloidal dispersion of MZN-PCOOH in water or buffer solution: the surfaces were partially functionalized, so the difference between the amino-modified surface behaviour

and the unmodified one is visible. The differences between the degree of covering is also evident and the modified part result highly covered in both samples. Very good layers are obtained with pH7 buffered solution (Figure 68b) chosen because is the optimal pH for possible further modifications of the protocol, discussed later, compared to pH 4, which previously appeared as the best for covering. Moreover, taking into account pKa values of both functionalizing molecules, pH7 allows to have ionic species with opposite charge on the surface and on the MZN [196-197].

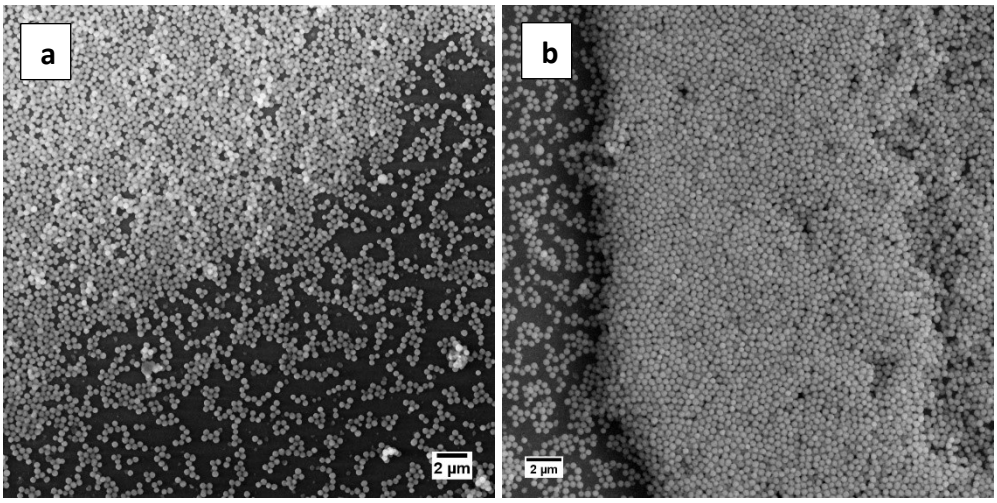

Figure 68: Dip coating technique: MZN-PCOOH on aminated silicon, a) dispersion in water, b) dispersion in TRIS at pH7.

MZN-PCOOH and amino-modified surfaces were preferred to MZN-PNH2 and carboxylic-modified surfaces: atmospheric plasma deposition does not work properly with the carboxylated-silane precursor (sodium salt of carboxyethylsilane triol) because a water solution must be used, while alcoholic solution is employed with APTES.

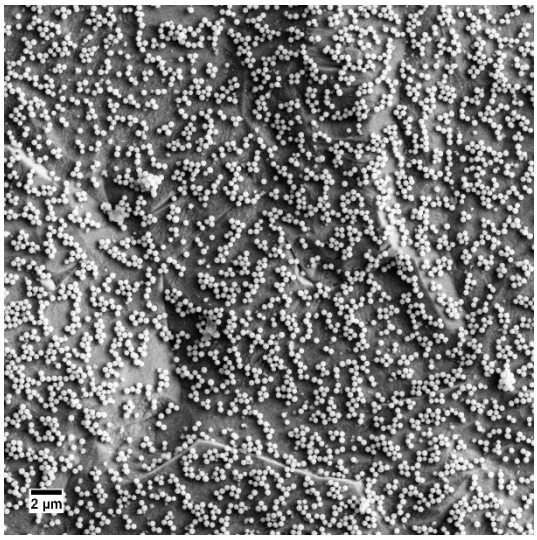

Figure 69: Dip coating deposition on bare titanium alloy: MZN-PCOOH in acetate buffer at pH4.

Tests on titanium were then performed, to confirm the possibility of modifications in titanium implantations. First the affinity of nanoparticles with titanium was tested (Figure 69), with bare metallic surface and acetate buffer dispersion at pH 4, to see electrostatic interaction between MZN-PCOOH and the surface. Ti alloy was then modified using

atmospheric plasma device with APTES, to obtain an -NH_2 group enriched surface, and dip coating technique was employed to obtain the nanoparticles layers.

However, the behaviours of metals to plasma treatments are totally different from the previous surfaces, due to the conductive character of the system, so the quality of covering is very low, especially for our purposes, probably due to polymerizations of APTES also through amine moieties.

So, covalent carbamide coupling has been exploited to promote the linking of nanoparticles in a more permanent way, due to the appeal of this surface in implants applications. In this procedure, carboxylic moieties are usually activated with imide molecules to allow the linking with primary amino groups, producing a carbamide bond.

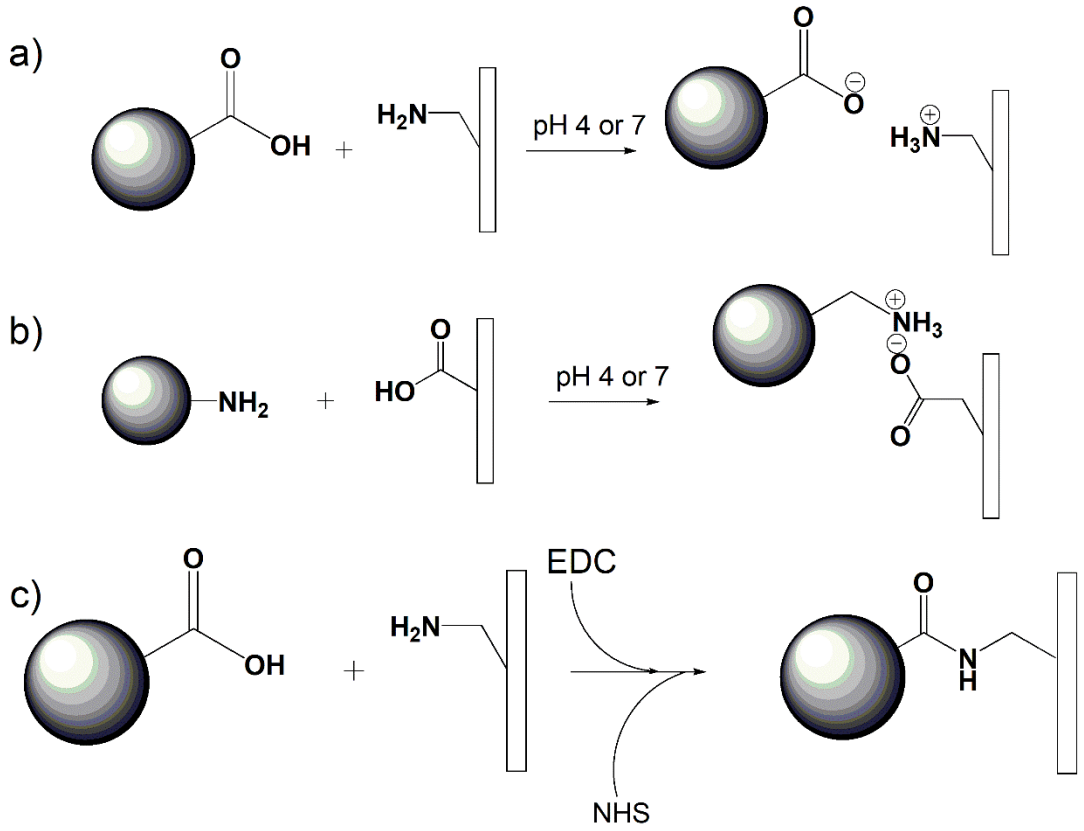

Scheme 6: Schematic representation of possible interaction between modified nanoparticles and surfaces: weak interaction between carboxylated nanoparticles and aminated surfaces (a) and the reverse situation (b) and covalent coupling with carbamide bond between carboxylated nanoparticles and aminated surfaces (c)

Procedure and details of the reaction are reported in “Coupling with nanoparticles” in “Materials and Methods” section. The first trials on the surfaces functionalized by APTES using the plasma promoted process, however, did not give successful results for our purposes (Figure 70), indeed, not uniform coatings were produced. For these amino-modified surfaces, the behaviour was different from the expected one, so tests for the confirmations of the presence of primary amine, needed for carbamide bonds formation, were done. IR spectroscopy did not give us any confirmation of the presence of this group [198], so ninhydrin assay was performed. It consists in a colorimetric assay for the detection and quantification of primary amines in proteins (see Ninhydrin assay in

Materials and Methods). The test done pointed out that no primary amines were present on the surface of the titanium, making impossible the covalent linking with nanoparticles. This absence could be caused by the technique and parameters employed for the modification, indeed, plasma device can induce polymerizations of the precursors randomly or with different degrees, so involving also the amine terminal group of the monomer, that results in a useless surface for our purpose. This behaviour was not pointed out, and a problem, with previous results due to the ability of each types of amine to produce hydrogen or ionic bonds.

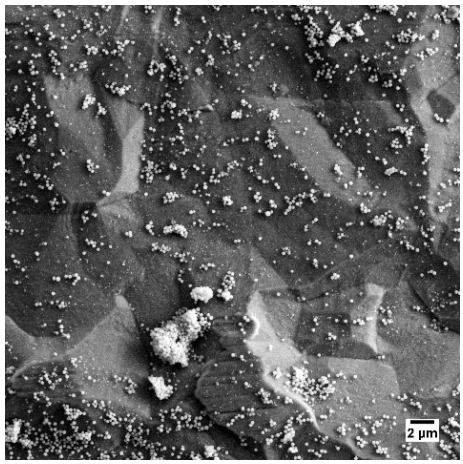

Figure 70: EDC/S-NHS protocol used to couple nanoparticles to modified Ti alloy: MZN-PCOOH on Ti-SiO_2-NH.

So, other trials were not performed due to the behaviour of the modifying agent and of the surface with plasma treatments with the chosen working conditions, but better results can be obtained in the future, setting the best parameters for the covering.

Getting these points, the focus was put in the amino-modified titanium alloy with other ways of modifications, which appear faster and easier for our purposes. Sol-gel chemistry and dip coating protocols were used at the beginning: a film of TiO_2 was produced on the top of the material using Piranha solution for the oxidation, to which it has been grown up a silica layer obtained with APTES as precursor. To be sure of the anchoring and polymerization of the monomer to the surface, a step at 120 °C in oven was done, followed by the ninhydrin assay to confirm the presence of free primary amine. With positive assay results, covalent coupling between surface and nanoparticles was performed. The outcomes of these tests were better than the previous ones, and more uniform surfaces were obtained (Figure 71). Moreover, dip coating was used to produce a “control” sample, using only electrostatic bonds with acetate buffer colloidal solution of MZN-PCOOH at pH 4 (Figure 71 a and c). As one can see from images, the most homogeneous coating is the one obtained with the linking of dip coating technique and covalent bonds. Moreover, this sample is the one with higher degree of covering, almost total, which means that the coupling of chemical bonds with dip coating technique is the best choice for the covering.

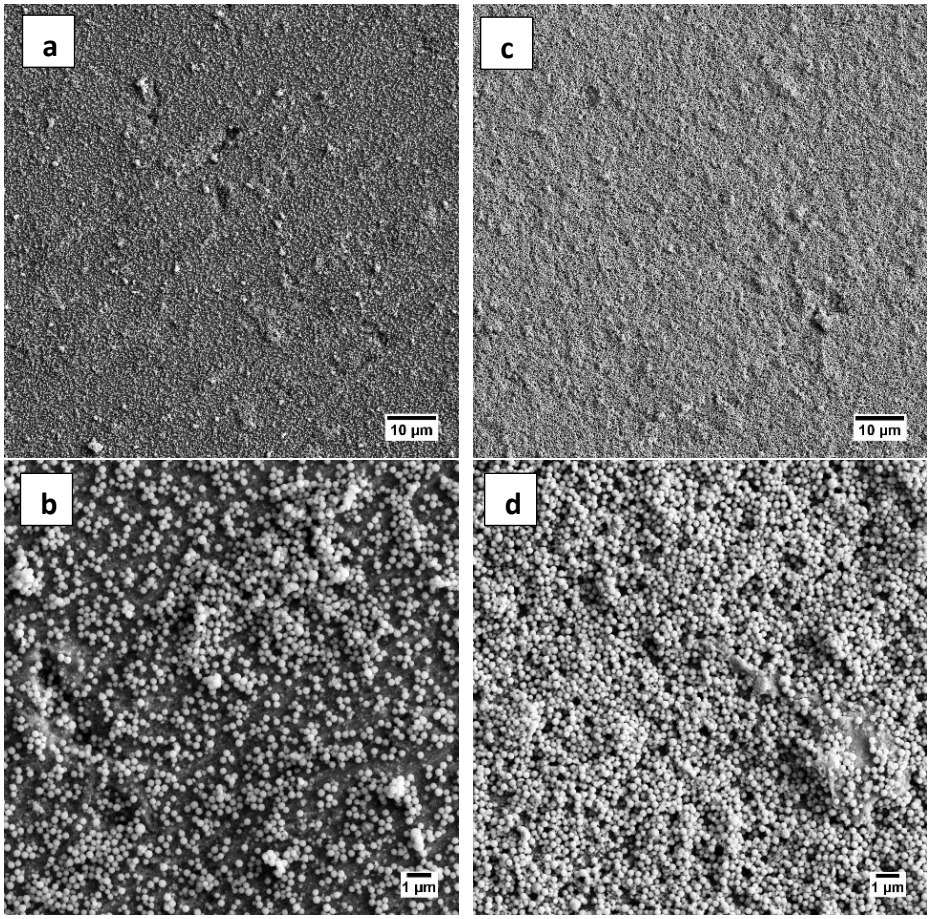

Figure 71: Ti grade 5 alloy superficially modified with APTES: dip coating with MZN-PCOOH in acetate buffer at pH4 (a, b), covalent coupling with MZN-PCOOH and with dip coating (c, d).

After these tests, Ti was modified using oxidation and PNH2, to further improve the linkage of carboxylic-modified nanoparticles and to avoid silica layer, that can be less stable than the bond with phosphonate molecules [132, 134]. This modified surface was then linked to MZN-PCOOH to see how this changes the system.

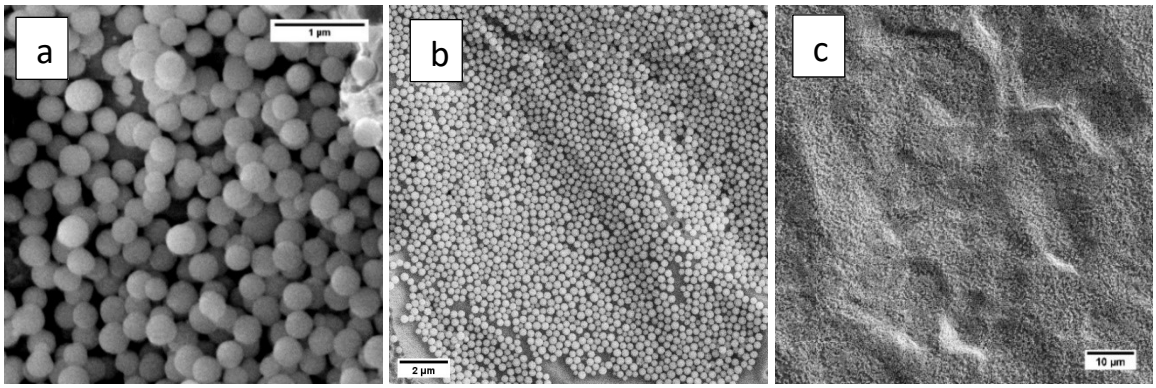

Figure 72: FEG-SEM images of MZN-PCOOH covalently linked to Ti-PNH2 at different magnifications: 25KX (a), 5KX (b), and 2.5KX (c)

Figure 72 shows how it was possible to obtain a good layer of nanoparticles covalently linked to the surface, also in this case. It is clear, however, that roughness of the surface influence the homogeneity of the covering.

At this point, preliminary tests were done for biofilms growth (*Staphylococcus Epidermidis*) on this last sample, to see the growth of bacteria on the surface. As one can see from Figure 73b, small amount of bacteria grow on Ti modified with nanoparticles, while biofilms are highly present on tests performed on bare titanium (Figure 73a), confirming the fact that this system can be employed to improve artificial limbs. Moreover, nanoparticles are still porous, so they can host antibiotic molecules or silver nanoparticles to further improve the opposition on bacterial growth, also with prolonged release of antibacterial Ag^+ ions in the time. Moreover, increasing roughness of the surface of implantation can improve cell adhesion and differentiation, promoting bone regenerations, also thanks to the coupling of these materials [61-63, 68, 199].

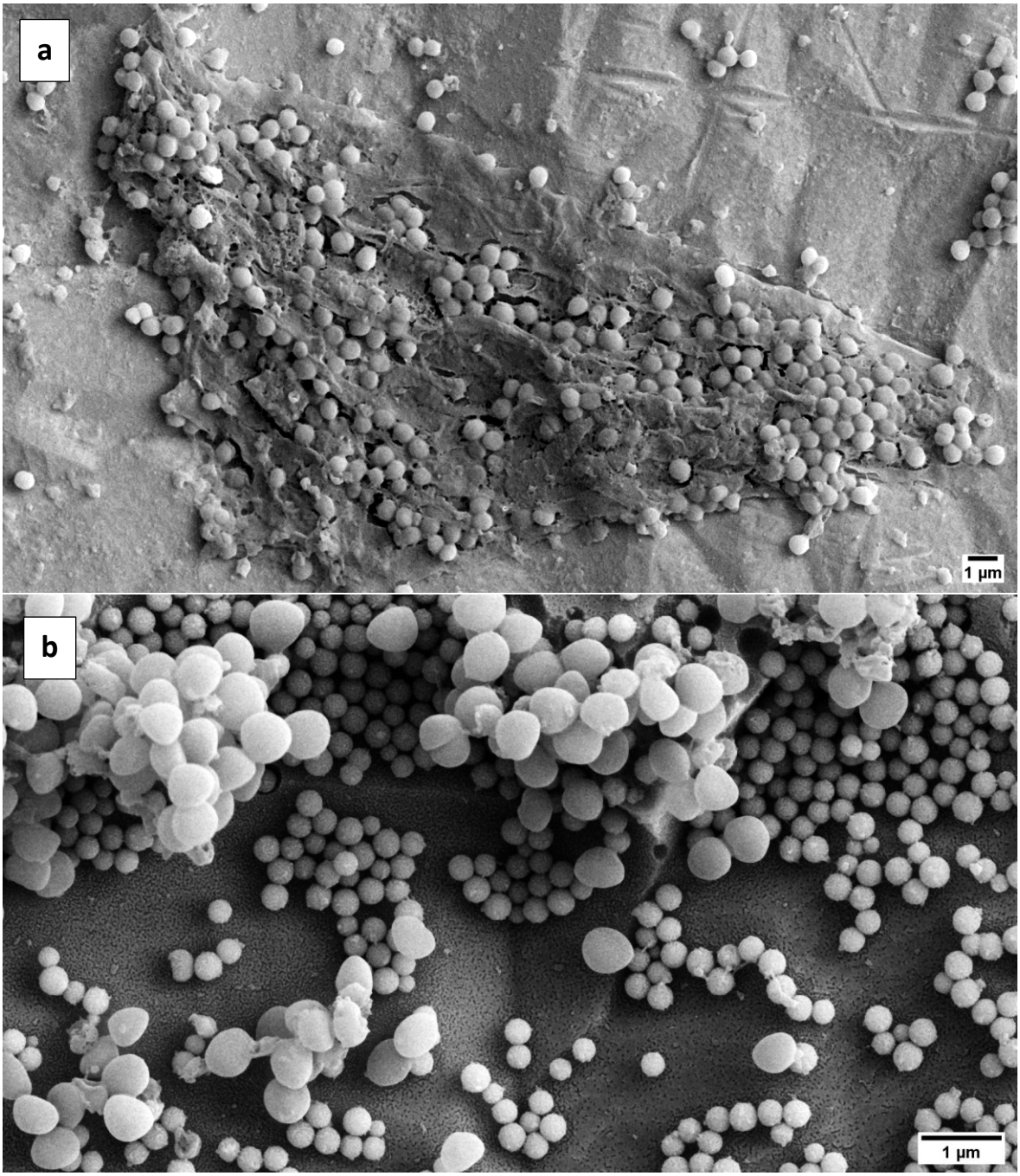

Figure 73: FEG-SEM images of fixed bacteria grown on bare titanium (a) and Ti-PNH2 linked with MZN-COOH (b).

3.4.2. Silver modifications of MZNs

It is known from literature that silver colloidal solutions act as antibacterial agents to contrast several infections [200-204]. Indeed, silver is usually used to treat bacterial infection since XV century [205-206]. Due to these properties, it was thinking to apply silver nanoparticles to our system made of zirconia, to obtain a tool that can be anchored to surfaces, eventually loaded with drugs (i.e. antibiotics) and that possess long term activity against bacteria without circulating agents. The advantage of this solution, compared to the use of free silver nanoparticles, is that the particles, immobilized inside the pores of the MZN, are not able to move into the body and translocate to various tissues [207-209].

So, it has been decided to fill up the 50% of the pore volume of the MZNs with silver nitrate, in order to have 37% w/w nominal of silver, but leaving open the pores to allow the loading with drugs. A classical wet impregnation method was employed, to fill MZN with the salt and then the system was reduced with formaldehyde solution. With this method a system like the one in Figure 74 is usually obtained. As is visible from FEG-SEM images recorded using both backscattered and secondary electrons, brightest spots obtained by backscattered electrons represent silver NPs on the surface of MZNs (Figure 74 a, e, g). It is clear that not all the metals went inside the pores, but particles grow also on the surface of zirconia confirmed also by TEM images (Figure 74 d), where darkest particles represent AgNPs. Figure 74 b shows also very small dark spot on the MZN that could be the evidence of AgNPs inside the pores. High resolution TEM images cannot be collected in the internal part of nanoparticles because of the thickness of the MZN. EDX analysis confirm the presence of Ag in the internal part of zirconia, as shown in Figure 74 c, and quantities are reported in Table 25. Value obtained with EDX quantification show that 14% mass of silver is present inside the single particles reported in Figure 74b, however this quantification is not representative of all the sample, due to sampling problems of the technique (few nm of sampling). Moreover, due to the inhomogeneity, silver grows outside pores, also during the analysis with the microscope, reduced by electrons derived from the microscope. As one can see in Figure 74 a, indeed, a big amount of silver outside pores was formed during the analysis, probably deriving from unreacted salts. A further confirmation of the presence of nanoparticles with the same size of the pore is given by the XRD and SAXS measurements. Two Ag populations with different crystal sizes has been introduced both for XRD and SAXS in order to fit the diffraction patterns. Figure 75 shows the XRD and SAXS fits and Table 24 reports the average volumetric sizes of the fitted populations.

The particles size obtained for the diameters are 3 and 11 nm with SAXS: the volumetric distribution reported in Figure 75c shows that particles with average diameter of 3.2 nm circa, the average value of the pore diameter of zirconia (Figure 76), are the main fraction seen by SAXS. This confirms the presence of a large fraction of AgNPs inside pores. The larger size measured by WAXS correspond to the large Ag particles grown outside the pores. Quantification of the two phases obtained with these techniques appears different: from SAXS, ratio between peaks area of volumetric distributions shows that the bigger particles are 10% of the total, while from WAXS are 66%. Another time appears the

difficulties on quantification with X-ray techniques: smaller nanoparticles are underestimated with WAXS, while bigger with SAXS.

Table 24: SAXS and WAXS dimensions of particles of silver fitted as sphere

Sample	SAXS $\langle D \rangle_{Vol}1$ (nm)	SAXS $\langle D \rangle_{Vol}2$ (nm)	WAXS $\langle D \rangle_{Vol}1$ (nm)	WAXS $\langle D \rangle_{Vol}2$ (nm)
MZN@Ag	3	11	1.6	35

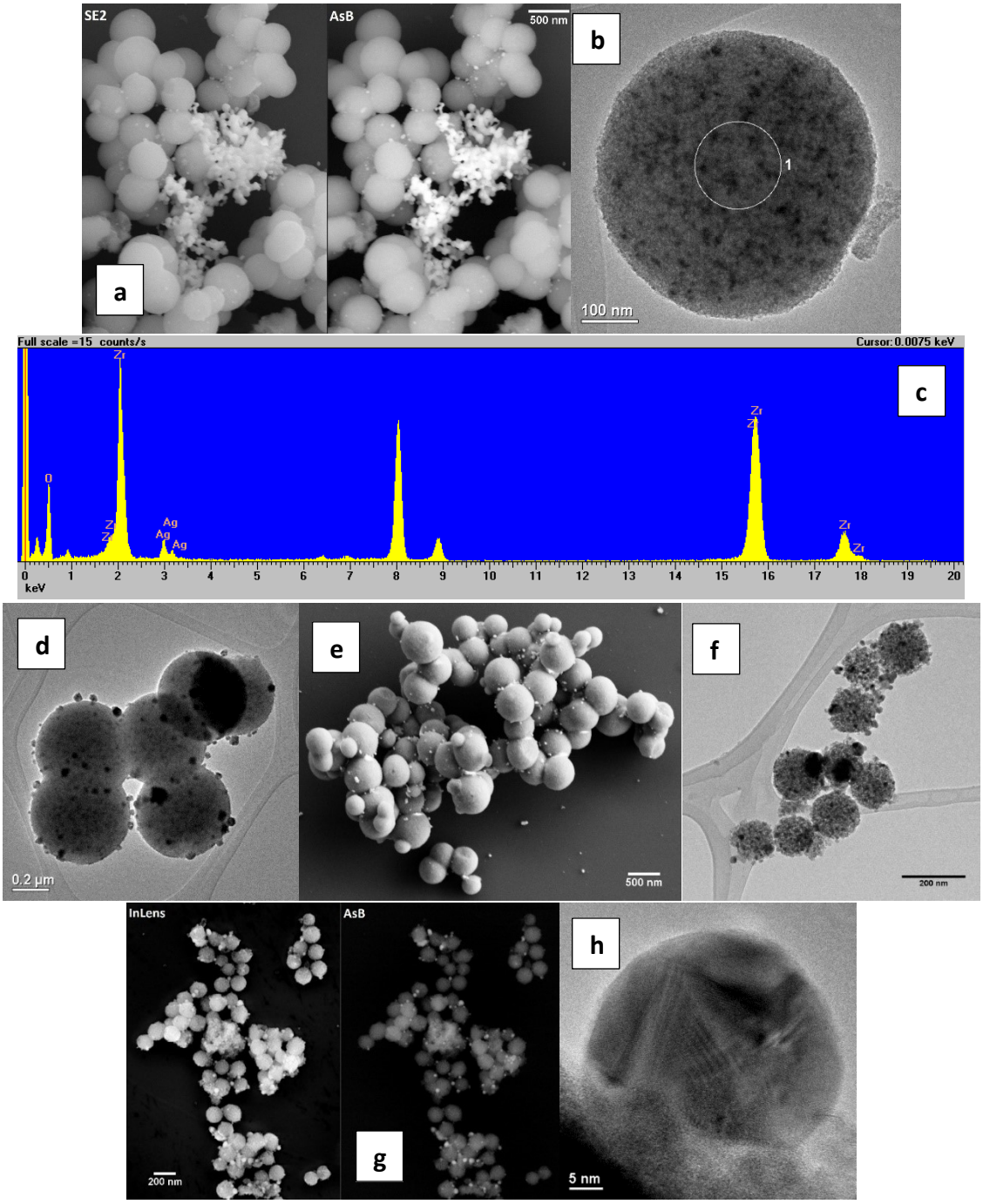

Figure 74: FEG-SEM (a, e, g) and TEM (b, d, f) images of different MZN@Ag samples obtained with the second protocol and HR-TEM (h) of single Ag nanoparticle on the surface of zirconia. Typical EDX spectrum is reported (c) on TEM specimens (b) in the underlined region.

Table 25: Quantification of elements from EDX spectrum recorded with TEM reported in Figure 74c

	Atomic (%)
O (K)	55.6
Zr (L)	39.7
Ag (L)	4.6

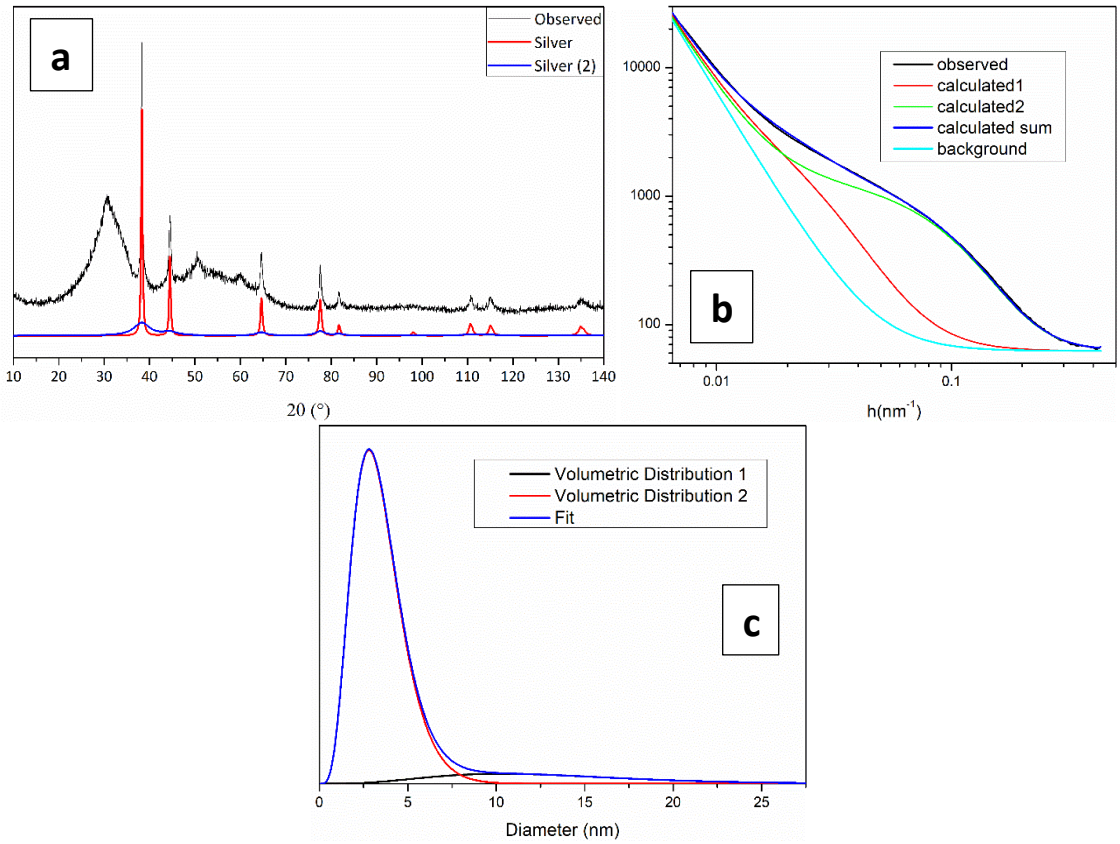

Figure 75:XRPD (a) and SAXS (b) measurements on MZN@Ag, with radii distributions obtained with SAXS (c), XRPD fitted with ICSD # 64706 for silver.

Nitrogen physisorption was also performed on the samples obtained in this way, before and after the introduction of Ag (Figure 76). As is visible from the graph, surface area and volume and diameter of pores decrease after the introduction of silver. Indeed, surface area decrease from 330 to 285 m^2/g, pore volume from 0.23 to 0.16 cm^3/g, while pore diameters from 3.14 to 2.87 nm.

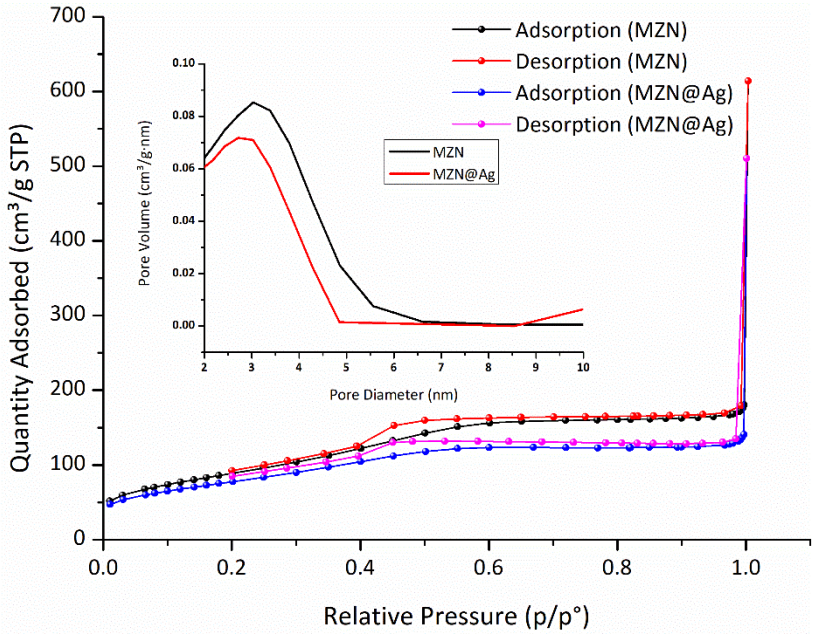

Figure 76: Nitrogen physisorption of MZN and MZN@Ag, compared. In the inlet pore distribution of samples.

These results confirm the presence of silver inside pores and the retained mesoporous structure of zirconia nanoparticles. Moreover, pore diameter obtained with this analysis, confirm the rightness of the dimension obtained with XRD measurements.

On this sample, first antibacterial tests were performed using *E. coli*. As one can see from Figure 77, nanoparticles start to have some action on bacteria around 300 µg/ml of concentration, at which they kill more than 50% of the bacteria during inhibition growth tests. This means that higher concentration of nanoparticles is required to completely inhibit the growth. Viability tests on bacteria, with higher concentration tested, show how completely inhibition growth is reached with concentration of MZN@Ag of 500 µg/ml.

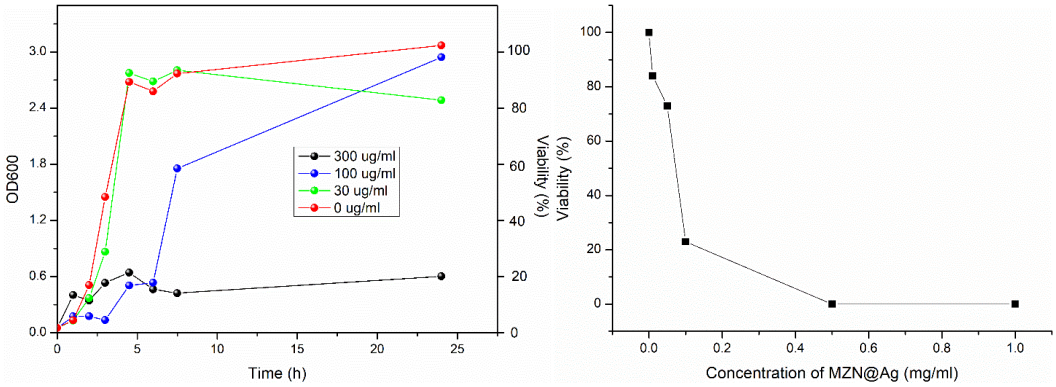

Figure 77: Preliminary biological tests results: on the left the growth of bacteria during time (OD600: Optical Density of 600 nm) and on the right the viability at the end of the experiment.

Although in parallel an oxidation way was performed, to see if improvement of the formation of AgNPs only inside pores can be obtained, thanks to the insolubility of the oxide. To do so, silver salt was oxidized with sodium hydroxide solution and then reduced with glucose solution, as previously reported. However, even the nanoparticles obtained

in this way present a lot of silver outside pores, as shown in Figure 78, that also in this case reacts under microscope beam.

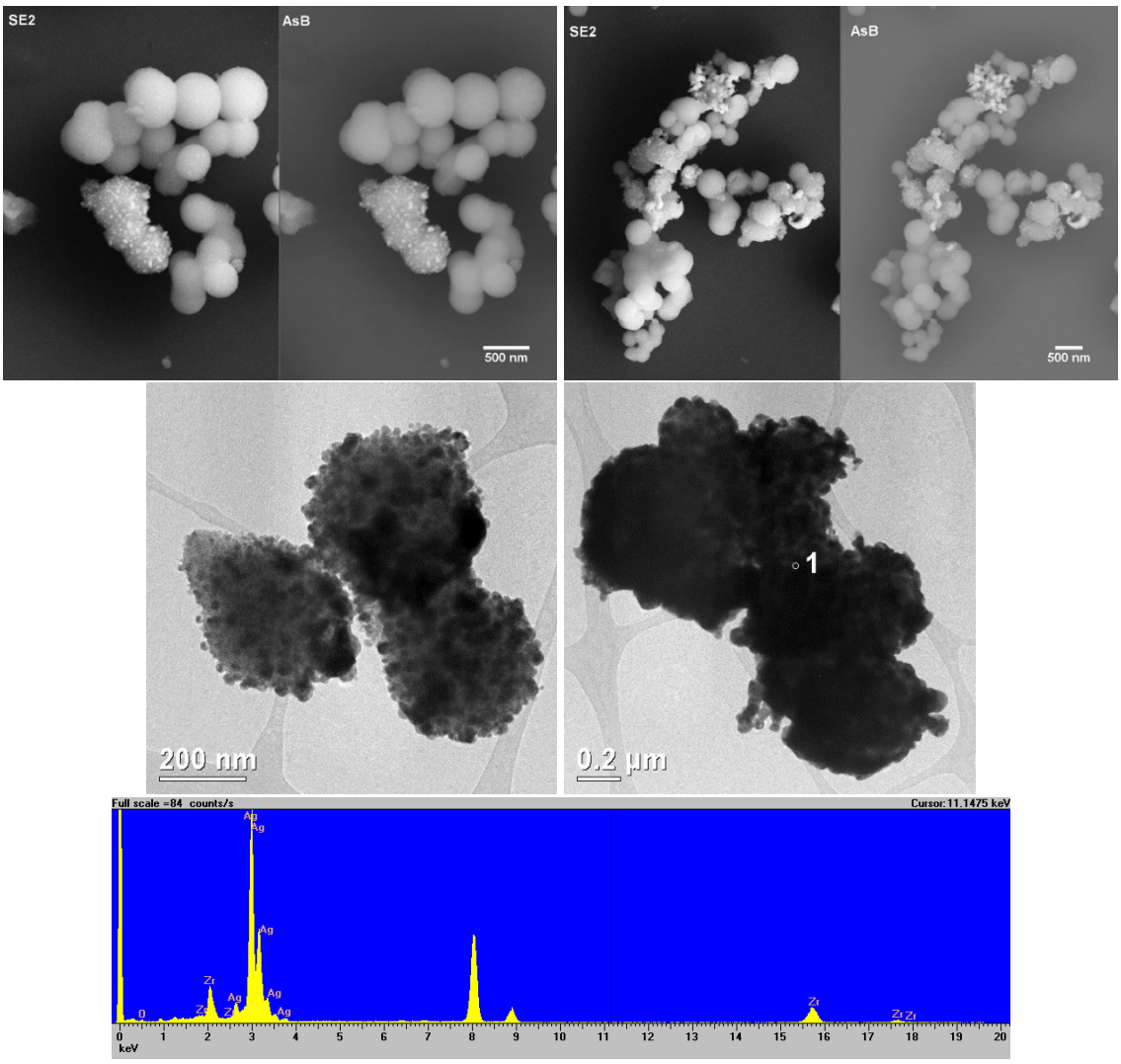

Figure 78: FEG-SEM (top) and TEM (middle) images of MZN@Ag obtained with oxidative protocol and EDX spectrum (bottom) obtained in the spot pointed with 1 in TEM image.

So, to try to produce silver deeper inside pores of zirconia, another approach was tested, always through the oxidation path. MZN synthesis was modified using Na_2HPO_4 salt solution instead of the one with NaF, to modify the surface of nanoparticles and bond Ag^+ ions, thanks to the affinity with PO_4^{3-} [150, 200]. Nanoparticles obtained (MZN-PO_4) show the same shape of the ones with the normal procedure (Figure 79).

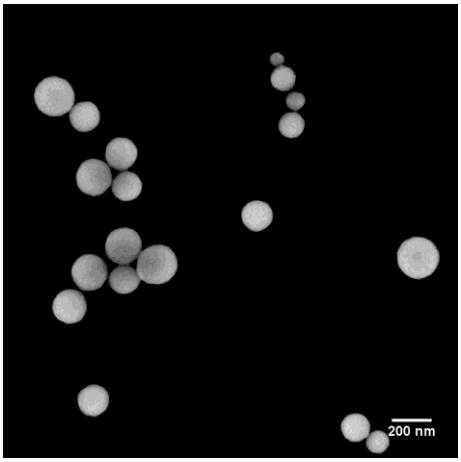

Figure 79: FEG-SEM image of MZN modified with phosphate salt during synthesis

Then, wet impregnation method of $AgNO_3$, oxidation (with NaOH) and reductions with glucose was used to produce AgNPs and the obtained nanocomposite is shown in Figure 80. In this case the amount of silver was decreased, to reduce silver outside of MZNs, fixing the amount for filling up the 25% of pore volume, but as one can see, also in this case silver is present outside and inside zirconia. Here, however, the AgNPs outside appear linked to MZN, probably via -Zr-O-P-O-Ag bonds.

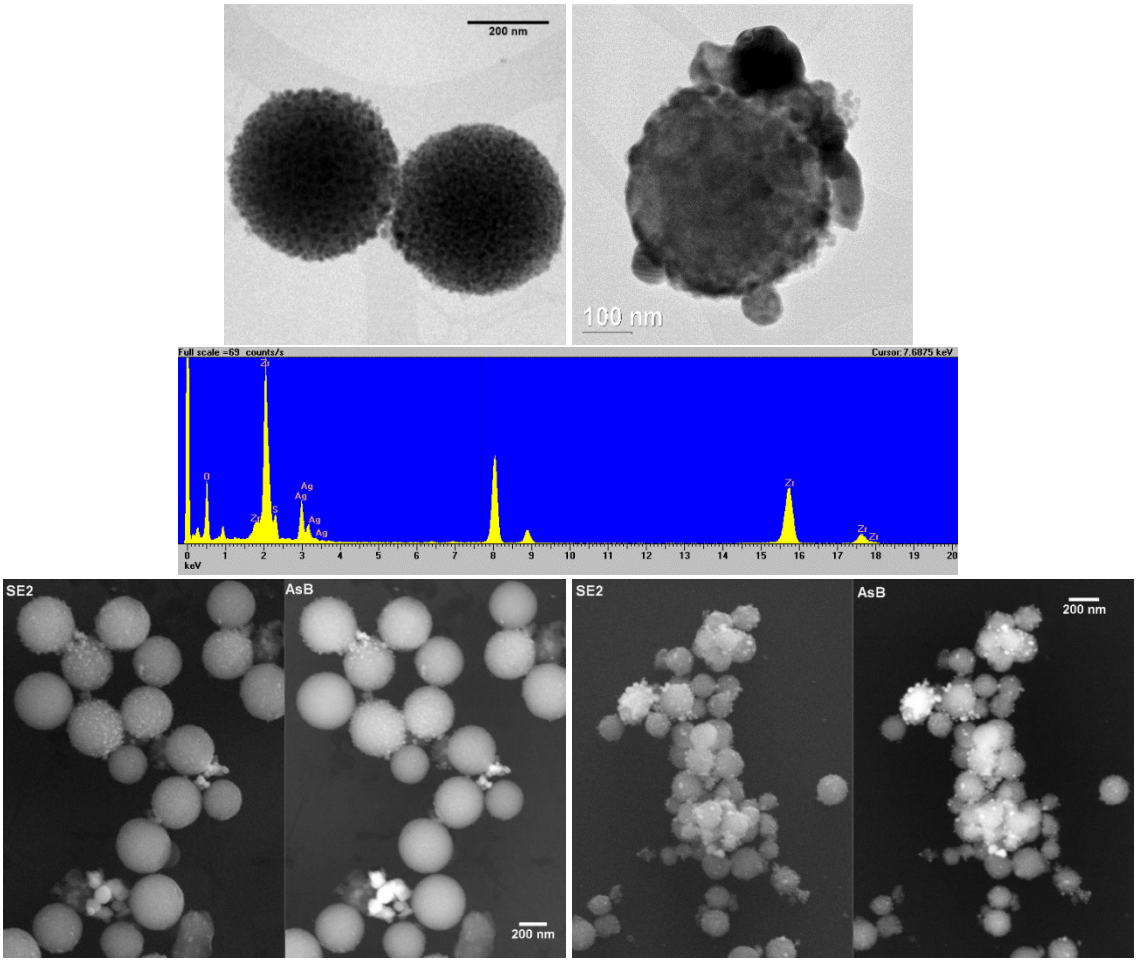

Figure 80: TEM (top) and FEG-SEM (bottom) images of MZN-PO4@Ag and EDX spectrum of a point in the middle of the particle in the TEM image in the right.

After the evidence of the presence of particles outside pores, not bonded to zirconia, other analyses were done to understand if it was possible to reduce Ag^+ with a thermal treatment in a reducing atmosphere, avoiding crystallization of zirconia and a reduction step in solution. First, a TPR test was performed on sample obtained with the deposition of AgCl inside pores, due to the impossibility to perform this test with nitrate salts. Indeed, with reduction steps and due to intrinsic characteristics of nitrate, it can produce ammonia with reducing atmosphere and decompose at lower temperature compared to chlorinated samples, affecting results and being harmful for the instrument. To do so, first of all, NaCl was impregnated on MZN, then it was left reacting with $AgNO_3$ and washed, to remove $NaNO_3$ and left the insoluble AgCl. The so obtained MZN@AgCl was then treated in TPR, with 4.84% H_2/Ar gas fluxed at 40 mL/min, with a temperature range from 30 to 850 °C (10 °C/min) and a thermo-conductivity detector at 100 °C. The results from TPR analysis are reported in Figure 81. As one can see from the graph, the reduction of silver happens between 200 and 350 °C, that make theoretically possible the reduction before the crystallization of zirconia, as previously reported. Electron microscope images of MZN@AgCl, recorded with secondary electrons (InLens detector) and back scattered secondary electrons detectors, before the TPR treatment (Figure 82) show how reduced silver is not visible in nanoparticles. Only few amounts of Ag can be seen outside MZNs, that has been reduced from microscope beam (Figure 82).

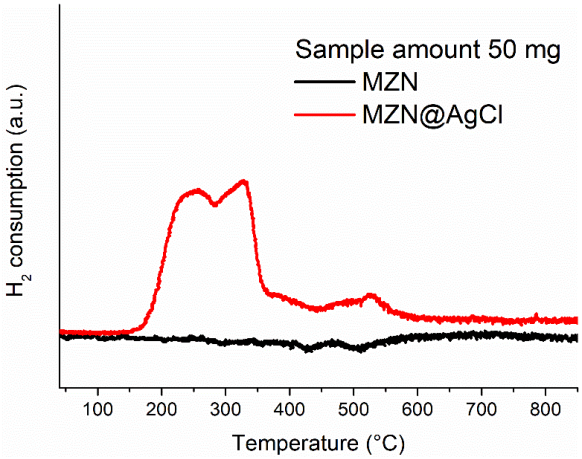

Figure 81: TPR of MZN compared to MZN@AgCl

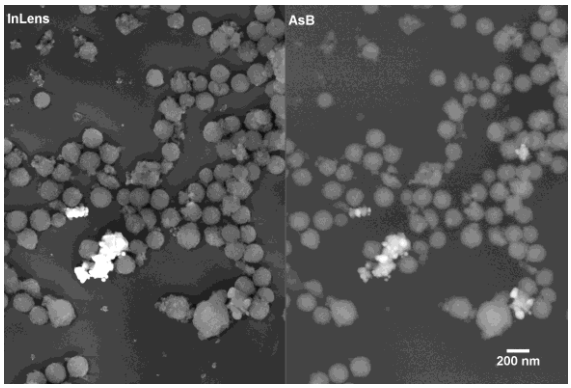

Figure 82: FEG-SEM images of MZN@AgCl

Moreover, to deeply understand the behaviour of zirconia and silver under thermal treatment and to see if it was applicable to our system, MCX line at Elettra Synchrotron was employed to study MZN@Ag with XRPD technique using a particular oven that the line is equipped with [181]. The screening of the temperature was done in the range from 25 to 600 °C, with steps of 10 °C/min, and diffraction patterns were recorded each 100 °C. Samples prepared with wet impregnation method of $AgNO_3$ with different molar % were tested: 3%, 25% and 50%. 5% H_2/Ar atmosphere was used as reducing agent. In Figure 83 diffraction patterns are reported, and peaks related to silver are pointed with a star. As one can see, only samples with 25 and 50% of silver present typical peaks related to the metal (pointed with stars in graphs).

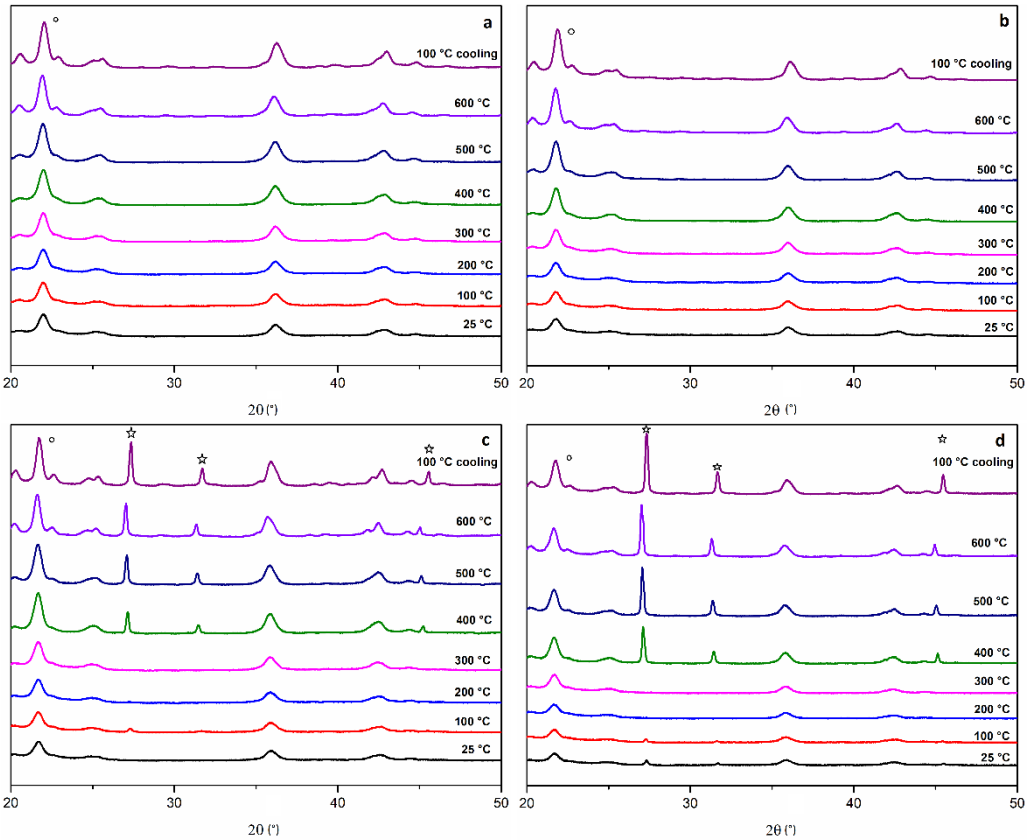

Figure 83: X-ray diffraction spectra of MZN (a), MZN@Ag3% (b), MZN@Ag25% (c), MZN@Ag50% (d), λ = 1.12576 Å, appearing of monoclinic phase (ICSD # 417639) pointed with dots and of silver phase (ICSD # 64706) with stars.

From these analyses, is possible to say that a thermal treatment under reducing atmosphere is allowed to produce silver particles without crystallization of zirconia, maintaining the temperature below 500 °C. Indeed, monoclinic crystal phase, the most thermodynamically stable, starts to appear around 500 °C (pointed with a dot in graphs), that means that a deeper crystallization process is occurring. Other peaks present in the patterns are related to small crystallites of tetragonal zirconia, also at room temperature, as previously reported in the description of the synthesis of MZNs, or in sample with 50%mol of Ag from the reduction of Ag^+ under light. Certainly, further investigations are needed to finally prove the possibility of this treatment without affecting porosity too much.

3.5. Preliminary tests of coupling with antibodies

In order to obtain a tool which is able to recover analytes, mMZN-8% has been superficially modified with targeting agents or probe. As previously reported, mMZN-8% has been chosen for applications thanks to the better properties that the system exploited during physical-chemical analyses. Initially, mMZN has been modified with phosphonic acids with carboxylic terminal group, to link it to antibodies via carbamide bonds. The successful of modifications has been proven with ζ-potential measurements (Figure 84). As usual, phosphonic acids increase the surface charge of nanoparticles, even if are loaded with the magnetic phase, probably also interacting with $CoFe_2O_4$, as previously reported with magnetic characterizations.

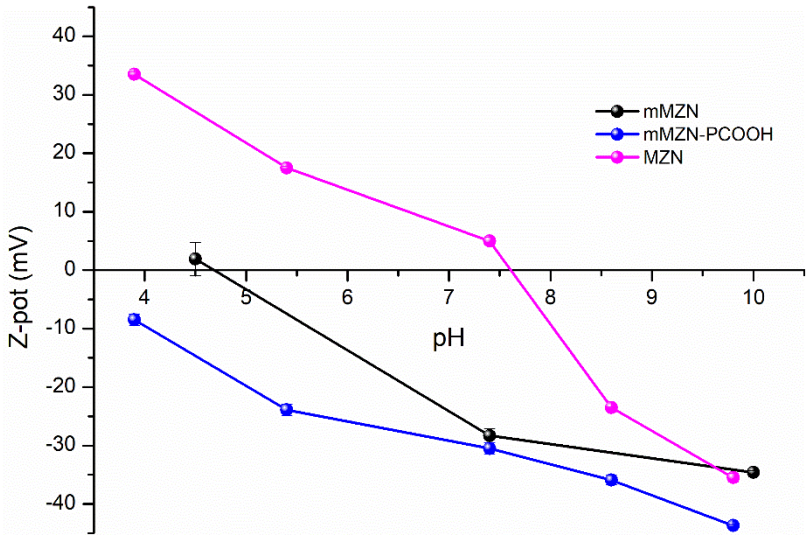

Figure 84: ζ-potential measurements on MZN, mMZN, and mMZN-PCOOH

The so modified system was employed for the linking with antibodies, for the early detection of the disease, which could be able to capture circulating proteins as biomarker of cancer [25, 52, 210-212].

Conjugation between nanoparticles and antibodies were performed employing the EDC/S-NHS protocol reported in Protocol for Ab conjugation in Materials and Methods. Here, nanoparticles were suspended in MES and EDC and sulfo-NHS were added to the suspension for the carboxylic groups activation. Then, the Abs were added, left reacting, and glycine or ethanol amine were used to stop the reaction. An antibody modified with HRP was used to see if the linking happens successfully and to quantify the amount of protein bonded to nanoparticles, because other common protocols for protein quantification result useless with our systems. The quantification of Ab-HRP on the NPs was performed with the TMB modification, classical for ELISA tests. These tests show also, as anticipated, how is crucial to avoid the use of PBS during reactions between proteins and MZNs modified with phosphonic acids.

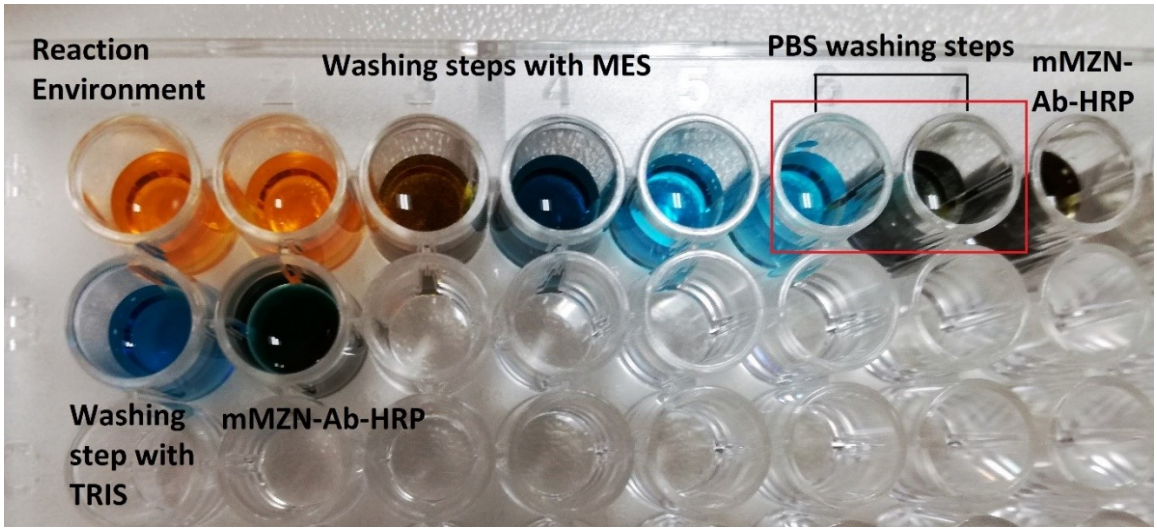

Figure 85: Analysis employing TMB reagent to follow the presence of antibodies during reaction, washing steps and on final system of mMZN-Ab-HRP

Figure 85 shows the development of the assay with TMB for reaction environment, washing steps with MES buffer, PBS buffer and TRIS buffer and mMZN-Ab-HRP. This image is taken before stopping of the TMB reaction with H_2SO_4, and shows how, with washing steps in MES, the concentration of Abs decreases (colour changes from orange to light blue means a decreasing in concentration), but if the system is washed with PBS the concentration increases again. This is a proof of the needs to avoid phosphate buffer if working with MZNs modified with phosphonic acids due to competition reactions between phosphor-containing molecules, as reported in "Results and Discussion, Functionalization of MZN" chapter. Indeed, if washed again with TRIS, a non-containing phosphor buffer solution, the amount of Abs released decrease again. As previously reported, these results were further investigated from Prof A. Scarso's research group, and they found that these behaviours with phosphate buffers decrease if bis-phosphonic acids were used. However, difficulties on synthesis make impossible the tests with bis-phosphonic acids with carboxylic ending group in our systems and the commercially available PCOOH was further used and PBS avoided.

Understood this point, conjugation avoiding PBS was performed and the Abs on nanoparticles were quantified reading at 450 nm using a plate reader with UV-Vis light.

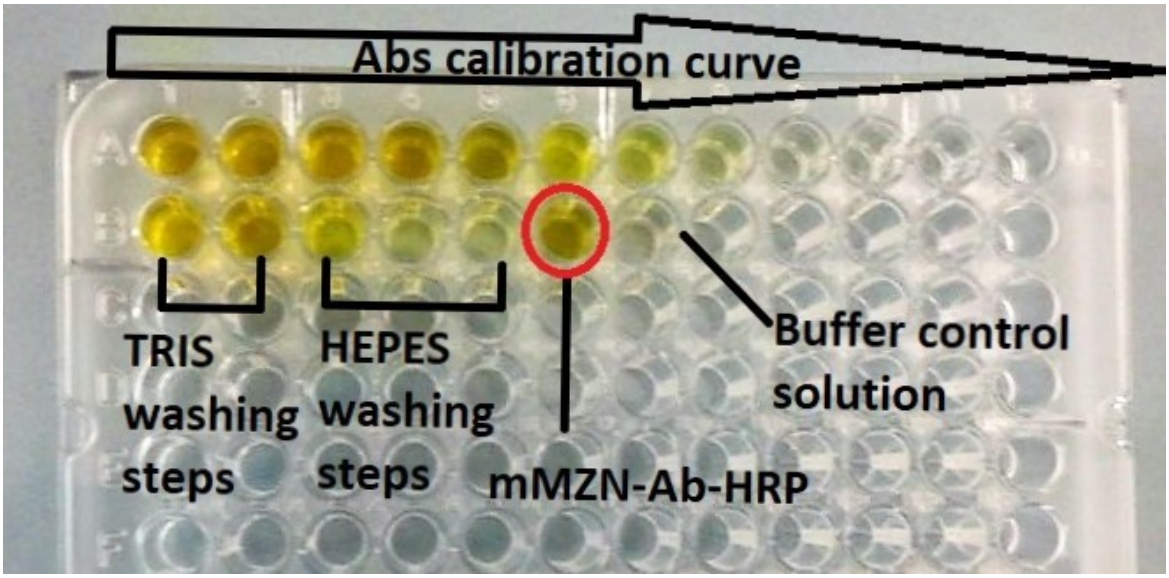

Figure 86: Calibration curve of Abs concentration and quantification of Abs in washing steps and on nanoparticles, after the blocking step with H_2SO_4

In Figure 86 is visible how in this case the concentration of Ab decreases with washing steps and now, in principle, is possible to quantify the antibodies linked to the nanoparticles. From calculations, it results that 23 µg of antibodies were linked per mg of nanoparticles, that correspond to 500 Abs for nanoparticle. This high value can be ascribed also to the possibility of the conversion of TMB from nanoparticles. The quantity of antibody linked with the washing steps in PBS, indeed, were quite high even if there was the detaching of big part of the proteins (0.2 µg/mg, 9 antibodies for nanoparticle), that can be ascribed to the catalysis of TMB by the nanoparticles. Indeed, it is known that commercially available ELISA kits with TMB suggest avoiding the presence of iron ions in the environment of the assay due to possible interaction. These trials show how this system is not the best one for the development of an ELISA performed in this way. Further tests could be performed to see if it is possible to use other dye that have no interaction with nanoparticles, as a deeper investigation of the coupling of phosphonic acids modified nanoparticles and protein.

4. CONCLUSIONS AND FUTURE PERSPECTIVES

During this work, several nanostructures have been developed for many biomedical applications. Zirconia was chosen as common denominator for all the made and investigated as valid alternative to systems made by silica [6-8]. Thus, we obtained theranostic, biosensing and orthopaedic devices, totally avoiding the employment of silica or organosilanes. To do so, phosphate and phosphonate molecules have been used to modify the surface of zirconia nanoparticles, thanks to the high affinity of Zr with P [17, 213-214]. The study shows how all the phosphor-containing molecules tested are able to link to zirconia nanoparticles, allowing also further modifications. Moreover, it has been seen that the best choice is the use of bis-phosphonate molecules, that strictly bond the nanoparticles, allowing a stronger way of functionalizations for other modifications and applications. However, the employment of these molecules was not ever easy or possible, due to the lack of products commercially available and difficulties on synthesis.

To obtain a theranostic device, cobalt ferrites have been introduced inside pores of zirconia, using wet impregnation and thermal treatments [135]. Different quantities of magnetic phase have been loaded and fully characterized. From these results it has been seen that cations deriving from $CoFe_2O_4$ can go in solid solution with zirconia, producing also soft magnetic phase, in addition to the hard one made of $CoFe_2O_4$, and affecting Mössbauer spectra, where a paramagnetic contribution is also visible [47, 170]. For deeper investigation, also the loading with only iron ions has been performed, and it has been seen that the stabilization of the tetragonal phase of zirconia is obtained, without the formation of any segregated iron oxides. Established that the best sample obtained, for shape and magnetic properties, was the one loaded with the 8 %mol/mol of $CoFe_2O_4$, it has been modified with bis-phosphonic acid with tio-ending group, for the linking of gold nanoparticles obtained with laser ablation protocols, provided us by the research group of Prof M. Meneghetti [35, 139-140]. In this way a system that could be recovered by magnetic sorting and exploiting plasmonic properties has been produced. The fast recovering was proved with magnetophoretic characterization and, after the modification with Raman reporters, the possibility of SERS analyses has been tested. Moreover, this system can potentially be applied in theranostic, taking advantage of the possibility to perform hyperthermia both with plasmonic and magnetic properties, and to use it as imaging probe. However, tests on hyperthermia and relaxations times (for the applications as contrast agents) are needed for practically apply it, as well as toxicity assays.

A further improve has been tried, to obtain a system which could be still porous but with good magnetic properties. First, a trial with decreased temperature of thermal treatment was performed, using also results obtained at MCX line at Elettra Synchrotron of Trieste. However, the so obtained system did not show a faster recovering with the magnet as the one previously obtained, and so, another way was investigated. $CoFe_2O_4$ seeds, obtained with polyol method, were used as nuclei for the growth of MZNs, to obtain a porous structure with superparamagnetic character at room temperature [87, 123, 173]. In this way, a porous structure, comparable to the normally obtained MZNs, with magnetic properties comparable to bulk cobalt ferrites was obtained. Furthermore, to increase and tune the magnetic properties, bi-magnetic core-shell structures of cobalt ferrites doped

with zinc or nickel were synthetized with thermal decomposition protocols at NTNU University of Trondheim, in collaboration with G. Singh and D. Peddis. In this way coupled magnetic phases were obtained, and tuning of coercivity and saturation, varying doping content, was possible. However, deeper investigation and characterizations of these systems are needed for a better optimization of the desired characteristics and to obtain a hydrophilic system. Preliminary study on coupling magnetic core and dielectric shell, made in this case of zirconia, was done employing thermal decomposition method, and a good starting point for the inclusion of magnetic seeds in zirconia matrix was achieved. In this way, it could be easier to couple single-domain magnetic seeds with the desired properties to our mesoporous zirconia nanoparticles, increasing the possibility to obtain porous structures and decreasing toxicity, avoiding also the possibility of metal ions leakages, of core-shell nanoparticles made of heavy metal oxides, which could be applied to biological systems. However, better characterizations are needed, to deeply understand the construction, such as also trials on reproducibility and coupling with MZN.

In parallel, investigations for the possible application of the system in orthopaedics were performed. Starting from the evidences of layer organizations of modified nanoparticles on several bulky surfaces, trials to obtain a homogeneous layer made of MZNs have been done. Solvents and surfaces were screened to find the better conditions for nanoparticles layers formations, as well as techniques of deposition (such as drop casting and dip coating protocols). Then, we studied the interaction between nanoparticles (MZN-PCOOH) suspended in buffers solutions (suitable for biological applications compared to organic solvents) and amino-modified medical grade titanium, for a practical application. The surface of titanium was firstly modified using atmospheric plasma device to introduce amino-group on it [198]. After some tests and the discovery that no primary amino-group were present, we move to the functionalization via sol-gel method, which provides primary amines necessaries for further modifications. The so modified surface, using APTES as amino and silane precursor, was linked to carboxylic-modified nanoparticles via EDC/S-NHS protocols, obtaining structures with nanoparticles strongly bonded to the surfaces. Indeed, trials employing dip coating coupled to chemical bond have been performed and were compared to depositions without covalent chemical bonds. Even in this case, trials for avoiding organosilanes were performed, employing phosphor-derivates. PNH2 was linked to titanium and EDC/S-NHS protocols were performed to attach MZN-PCOOH. The so obtained surface was tested for the growth of bacteria to follow biofouling formations, revealing the improve of modifications of surfaces due to lower growth of bacteria.

To further improve the system and obtain an antibacterial nanocomposite with long term activities, silver nanoparticles were synthetized inside pores of zirconia [150, 200-202, 208-209]. Several protocols have been performed, up to the definition of the best condition of synthesis, in terms of remain porosity, linking of silver to zirconia and antibacterial activity. The better results were obtained with two different protocols: one employing classical wet impregnation of silver nitrate inside pores of zirconia and subsequently reduced with formaldehyde solution, and a second one employing modified zirconia (MZN-PO_4), wet impregnation of silver nitrate, oxidation and reduction of silver.

With the first method, nanoparticles with silver both inside and outside pores are obtained, and good antibacterial activity was found (total inhibition growth at 0.5 mg/ml of MZN@Ag). With the second one, AgNPs appear stronger bonded to MZNs, probably thanks to the presence of phosphate moieties, even if also in this case silver appears also outside pores of zirconia. Preliminary data coming from thermal treatments with reducing atmosphere were obtained with TPR measurements and at MCX line at Elettra Synchrotron, showing that wet impregnation and low temperature thermal treatment could in principle be used to obtain silver inside zirconia without affecting porosity. However, these results are only a first approach and need further investigations for better understanding of the treatment and to see if particles grow only inside pores. The so obtained system, indeed, could be improved with the loading of antibacterial drugs, which can act in the short term, leaving silver ions to release in longer periods. Moreover, trials can be conducted to covalently link MZN@Ag to bulky surfaces, to obtain a nanostructured layer which can also exploit antibacterial activity in short and long times, for the application in prosthesis.

In addition, to improve the system and obtain a device with active targeting properties for applications in biosensing and theranostic, a preliminary study for the attachment of antibodies was performed. In this case, mMZN-8, modified with PCOOH, was employed to link Ab-HRP with EDC/S-NHS protocol. This modified protein was chosen for the possibility of quantification given by the HRP moiety, an enzyme which produces H_2O_2 and allow the reaction of TMB dye for quantification. However, this system shows the critical aspect in avoiding silica layer: the phosphonate moiety can be replaced by PBS, detaching the linked protein, making useless the system. This also shown the needs to use bis-phosphonate molecules, which appear more stable upon replacement, and highlights the necessities to improve the library of available molecules, decreasing also the difficulties on syntheses.

Practical trials on the applications of all the systems described above are actually needed to complete the study on these promising materials for the application in biomedicine. Indeed, the reactive character of zirconia could make difficult the loading of certain drugs/molecules, catalysing the broken of specific bond (as seen for phosphate molecules), making impossible the employment as DDS. Moreover, the coupling with other metal oxides could increase the catalytic activity of the system, making other reactive centres. Although this novel system requires extensive characterization and tests to be sure to apply it in the more appropriate and safe way, but the preliminary results obtained in this work are very encouraging.

5. REFERENCES

[1] Farka, Z.; Juřík, T.; Kovář, D.; Trnková, L.; Skládal, P., Nanoparticle-Based Immunochemical Biosensors and Assays: Recent Advances and Challenges. *Chemical Reviews* **2017,** *117* (15), 9973-10042.
[2] McKeating, K. S.; Aube, A.; Masson, J.-F., Biosensors and nanobiosensors for therapeutic drug and response monitoring. *Analyst* **2016,** *141* (2), 429-449.
[3] Sabale, S.; Kandesar, P.; Jadhav, V.; Komorek, R.; Motkuri, R. K.; Yu, X.-Y., Recent developments in the synthesis, properties, and biomedical applications of core/shell superparamagnetic iron oxide nanoparticles with gold. *Biomaterials Science* **2017,** *5* (11), 2212-2225.
[4] Zamora-Gálvez, A.; Morales-Narváez, E.; Mayorga-Martinez, C. C.; Merkoçi, A., Nanomaterials connected to antibodies and molecularly imprinted polymers as bio/receptors for bio/sensor applications. *Applied Materials Today* **2017,** *9*, 387-401.
[5] Ramos, A. P.; Cruz, M. A. E.; Tovani, C. B.; Ciancaglini, P., Biomedical applications of nanotechnology. *Biophysical Reviews* **2017,** *9* (2), 79-89.
[6] Sponchia, G.; Ambrosi, E.; Rizzolio, F.; Hadla, M.; Del Tedesco, A.; Russo Spena, C.; Toffoli, G.; Riello, P.; Benedetti, A., Biocompatible tailored zirconia mesoporous nanoparticles with high surface area for theranostic applications. *J Mater Chem B* **2015,** *3* (36), 7300-7306.
[7] Bagheri, E.; Ansari, L.; Abnous, K.; Taghdisi, S. M.; Charbgoo, F.; Ramezani, M.; Alibolandi, M., Silica based hybrid materials for drug delivery and bioimaging. *Journal of Controlled Release* **2018,** *277*, 57-76.
[8] Del Tedesco, A.; Ambrosi, E.; Borsacchi, S.; Benedetti, A., Functionalization of Mesoporous Silica Nanoparticles with Organosilanes: Experimental Evidence of the Interaction Between Organic Groups and Silica Surface. *Curr Org Chem* **2017,** *21* (24), 2434-2444.
[9] Chen, F.; Hableel, G.; Zhao, E. R.; Jokerst, J. V., Multifunctional nanomedicine with silica: Role of silica in nanoparticles for theranostic, imaging, and drug monitoring. *Journal of Colloid and Interface Science* **2018,** *521*, 261-279.
[10] Colilla, M.; Gonzalez, B.; Vallet-Regi, M., Mesoporous silica nanoparticles for the design of smart delivery nanodevices. *Biomaterials Science* **2013,** *1* (2), 114-134.
[11] de Juan, F.; Ruiz-Hitzky, E., Selective Functionalization of Mesoporous Silica. *Advanced Materials* **2000,** *12* (6), 430-432.
[12] Bagbi, Y.; Sharma, A.; Bohidar, H. B.; Solanki, P. R., Immunosensor based on nanocomposite of nanostructured zirconium oxide and gelatin-A. *International Journal of Biological Macromolecules* **2016,** *82*, 480-487.
[13] Gowri, S.; Gandhi, R. R.; Sundrarajan, M., Structural, optical, antibacterial and antifungal properties of zirconia nanoparticles by biobased protocol. *Journal of Materials Science & Technology* **2014,** *30* (8), 782-790.
[14] Jangra, S. L.; Stalin, K.; Dilbaghi, N.; Kumar, S.; Tawale, J.; Singh, S. P.; Pasricha, R., Antimicrobial activity of zirconia (ZrO2) nanoparticles and zirconium complexes. *Journal of nanoscience and nanotechnology* **2012,** *12* (9), 7105-7112.
[15] Kumar, S.; Kumar, S.; Tiwari, S.; Srivastava, S.; Srivastava, M.; Yadav, B. K.; Kumar, S.; Tran, T. T.; Dewan, A. K.; Mulchandani, A., Biofunctionalized nanostructured zirconia for biomedical application: a smart approach for oral cancer detection. *Advanced Science* **2015,** *2* (8).
[16] Tang, S.; Huang, X.; Chen, X.; Zheng, N., Hollow mesoporous zirconia nanocapsules for drug delivery. *Advanced Functional Materials* **2010,** *20* (15), 2442-2447.
[17] Scholz, S.; Kaskel, S., Surface functionalization of ZrO2 nanocrystallites for the integration into acrylate nanocomposite films. *Journal of Colloid and Interface Science* **2008,** *323* (1), 84-91.
[18] Tang, Y.; Zong, E.; Wan, H.; Xu, Z.; Zheng, S.; Zhu, D., Zirconia functionalized SBA-15 as effective adsorbent for phosphate removal. *Micropor Mesopor Mat* **2012,** *155*, 192-200.
[19] Forier, K.; Raemdonck, K.; De Smedt, S. C.; Demeester, J.; Coenye, T.; Braeckmans, K., Lipid and polymer nanoparticles for drug delivery to bacterial biofilms. *Journal of Controlled Release* **2014,** *190*, 607-623.

[20] Ambrogio, M. W.; Thomas, C. R.; Zhao, Y.-L.; Zink, J. I.; Stoddart, J. F., Mechanized Silica Nanoparticles: A New Frontier in Theranostic Nanomedicine. *Accounts Chem Res* **2011,** *44* (10), 903-913.
[21] Angelakeris, M., Magnetic nanoparticles: A multifunctional vehicle for modern theranostics. *Biochimica et Biophysica Acta (BBA) - General Subjects* **2017,** *1861* (6), 1642-1651.
[22] Huang, J.; Li, Y.; Orza, A.; Lu, Q.; Guo, P.; Wang, L.; Yang, L.; Mao, H., Magnetic Nanoparticle Facilitated Drug Delivery for Cancer Therapy with Targeted and Image-Guided Approaches. *Advanced Functional Materials* **2016,** *26* (22), 3818-3836.
[23] Li, Z.; Barnes, J. C.; Bosoy, A.; Stoddart, J. F.; Zink, J. I., Mesoporous silica nanoparticles in biomedical applications. *Chemical Society Reviews* **2012,** *41* (7), 2590-2605.
[24] Mamaeva, V.; Sahlgren, C.; Lindén, M., Mesoporous silica nanoparticles in medicine—Recent advances. *Advanced Drug Delivery Reviews* **2013,** *65* (5), 689-702.
[25] Rashid, Z.; Soleimani, M.; Ghahremanzadeh, R.; Vossoughi, M.; Esmaeili, E., Effective surface modification of MnFe2O4@SiO2@PMIDA magnetic nanoparticles for rapid and high-density antibody immobilization. *Appl Surf Sci* **2017,** *426*, 1023-1029.
[26] Laprise-Pelletier, M.; Bouchoucha, M.; Lagueux, J.; Chevallier, P.; Lecomte, R.; Gossuin, Y.; Kleitz, F.; Fortin, M.-A., Metal chelate grafting at the surface of mesoporous silica nanoparticles (MSNs): physico-chemical and biomedical imaging assessment. *J Mater Chem B* **2015,** *3* (5), 748-758.
[27] Wang, X.; Chen, D.; Cao, L.; Li, Y.; Boyd, B. J.; Caruso, R. A., Mesoporous Titanium Zirconium Oxide Nanospheres with Potential for Drug Delivery Applications. *Acs Appl Mater Inter* **2013,** *5* (21), 10926-10932.
[28] Amendola, V.; Scaramuzza, S.; Litti, L.; Meneghetti, M.; Zuccolotto, G.; Rosato, A.; Nicolato, E.; Marzola, P.; Fracasso, G.; Anselmi, C.; Pinto, M.; Colombatti, M., Magneto-Plasmonic Au-Fe Alloy Nanoparticles Designed for Multimodal SERS-MRI-CT Imaging. *Small* **2014,** *10* (12), 2476-2486.
[29] Araújo, J. E.; Lodeiro, C.; Capelo, J. L.; Rodríguez-González, B.; dos Santos, A. A.; Santos, H. M.; Fernández-Lodeiro, J., Novel nanocomposites based on a strawberry-like gold- coated magnetite (Fe@Au) for protein separation in multiple myeloma serum samples. *Nano Research* **2015,** *8* (4), 1189-1198.
[30] Bao, Y.; Wen, T.; Samia, A. C. S.; Khandhar, A.; Krishnan, K. M., Magnetic nanoparticles: material engineering and emerging applications in lithography and biomedicine. *Journal of Materials Science* **2016,** *51* (1), 513-553.
[31] Chen, C.; Wang, S.; Li, L.; Wang, P.; Chen, C.; Sun, Z.; Song, T., Bacterial magnetic nanoparticles for photothermal therapy of cancer under the guidance of MRI. *Biomaterials* **2016,** *104*, 352-360.
[32] Guo, T.; Lin, M.; Huang, J.; Zhou, C.; Tian, W.; Yu, H.; Jiang, X.; Ye, J.; Shi, Y.; Xiao, Y.; Bian, X.; Feng, X., The Recent Advances of Magnetic Nanoparticles in Medicine. *J Nanomater* **2018,** *2018*, 8.
[33] Lei, K.-M.; Mak, P.-I.; Law, M.-K.; Martins, R. P., A palm-size [small mu]NMR relaxometer using a digital microfluidic device and a semiconductor transceiver for chemical/biological diagnosis. *Analyst* **2015,** *140* (15), 5129-5137.
[34] Bedford, E. E.; Boujday, S.; Pradier, C.-M.; Gu, F. X., Spiky gold shells on magnetic particles for DNA biosensors. *Talanta* **2018,** *182*, 259-266.
[35] Bertorelle, F.; Pinto, M.; Zappon, R.; Pilot, R.; Litti, L.; Fiameni, S.; Conti, G.; Gobbo, M.; Toffoli, G.; Colombatti, M.; Fracasso, G.; Meneghetti, M., Safe core-satellite magneto-plasmonic nanostructures for efficient targeting and photothermal treatment of tumor cells. *Nanoscale* **2018,** *10* (3), 976-984.
[36] Marchesan, S.; Prato, M., Nanomaterials for (Nano)medicine. *ACS Medicinal Chemistry Letters* **2013,** *4* (2), 147-149.

[37] Fernandez de Grado, G.; Keller, L.; Idoux-Gillet, Y.; Wagner, Q.; Musset, A.-M.; Benkirane-Jessel, N.; Bornert, F.; Offner, D., Bone substitutes: a review of their characteristics, clinical use, and perspectives for large bone defects management. *Journal of Tissue Engineering* **2018,** *9*, 2041731418776819.
[38] Lian, X.; Liu, H.; Wang, X.; Xu, S.; Cui, F.; Bai, X., Antibacterial and biocompatible properties of vancomycin-loaded nano-hydroxyapatite/collagen/poly (lactic acid) bone substitute. *Progress in Natural Science: Materials International* **2013,** *23* (6), 549-556.
[39] Mazaheri, M.; Eslahi, N.; Ordikhani, F.; Tamjid, E.; Simchi, A., Nanomedicine applications in orthopedic medicine: state of the art. *International journal of nanomedicine* **2015,** *10*, 6039.
[40] Smith, W. R.; Hudson, P. W.; Ponce, B. A.; Rajaram Manoharan, S. R., Nanotechnology in orthopedics: a clinically oriented review. *BMC Musculoskeletal Disorders* **2018,** *19* (1), 67.
[41] Cauda, V.; Schlossbauer, A.; Kecht, J.; Zürner, A.; Bein, T., Multiple Core−Shell Functionalized Colloidal Mesoporous Silica Nanoparticles. *Journal of the American Chemical Society* **2009,** *131* (32), 11361-11370.
[42] Chan, M.-H.; Lin, H.-M., Preparation and identification of multifunctional mesoporous silica nanoparticles for in vitro and in vivo dual-mode imaging, theranostics, and targeted tracking. *Biomaterials* **2015,** *46*, 149-158.
[43] McCarthy, C. A.; Ahern, R. J.; Dontireddy, R.; Ryan, K. B.; Crean, A. M., Mesoporous silica formulation strategies for drug dissolution enhancement: a review. *Expert Opinion on Drug Delivery* **2016,** *13* (1), 93-108.
[44] Monaco, I.; Arena, F.; Biffi, S.; Locatelli, E.; Bortot, B.; La Cava, F.; Marini, G. M.; Severini, G. M.; Terreno, E.; Comes Franchini, M., Synthesis of Lipophilic Core–Shell Fe3O4@SiO2@Au Nanoparticles and Polymeric Entrapment into Nanomicelles: A Novel Nanosystem for in Vivo Active Targeting and Magnetic Resonance–Photoacoustic Dual Imaging. *Bioconjugate Chem* **2017,** *28* (5), 1382-1390.
[45] Roto, R.; Yusran, Y.; Kuncaka, A., Magnetic adsorbent of Fe3O4@SiO2 core-shell nanoparticles modified with thiol group for chloroauric ion adsorption. *Appl Surf Sci* **2016,** *377*, 30-36.
[46] Freris, I.; Riello, P.; Enrichi, F.; Cristofori, D.; Benedetti, A., Synthesis and optical properties of sub-micron sized rare earth-doped zirconia particles. *Optical materials* **2011,** *33* (11), 1745-1752.
[47] Navío; Hidalgo; Colón, G.; Botta, S. G.; Litter, M. I., Preparation and Physicochemical Properties of ZrO2 and Fe/ZrO2 Prepared by a Sol−Gel Technique. *Langmuir* **2001,** *17* (1), 202-210.
[48] Shi, C.-Y.; Wang, W.-Q.; Fang, J.-G.; Wu, J.-Z.; Wan, J.; Yuan, L., The Study of Preparation Conditions for Magnetic Iron-Zirconium Co-Oxide Microspheres. *Materials and Manufacturing Processes* **2012,** *27* (11), 1149-1153.
[49] Liu, M.-C.; Liu, B.; Sun, X.-Y.; Lin, H.-C.; Lu, J.-Z.; Jin, S.-F.; Yan, S.-Q.; Li, Y.-Y.; Zhao, P., Core/Shell Structured Fe3O4@TiO2-DNM Nanospheres as Multifunctional Anticancer Platform: Chemotherapy and Photodynamic Therapy Research. *Journal of Nanoscience and Nanotechnology* **2018,** *18* (7), 4445-4456.
[50] Chambre, L.; Degirmenci, A.; Sanyal, R.; Sanyal, A., Multi-Functional Nanogels as Theranostic Platforms: Exploiting Reversible and Nonreversible Linkages for Targeting, Imaging, and Drug Delivery. *Bioconjugate Chem* **2018,** *29* (6), 1885-1896.
[51] Justino, C. I. L.; Freitas, A. C.; Pereira, R.; Duarte, A. C.; Rocha Santos, T. A. P., Recent developments in recognition elements for chemical sensors and biosensors. *TrAC Trends in Analytical Chemistry* **2015,** *68* (0), 2-17.
[52] Wu, Y.; Zeng, L.; Xiong, Y.; Leng, Y.; Wang, H.; Xiong, Y., Fluorescence ELISA based on glucose oxidase-mediated fluorescence quenching of quantum dots for highly sensitive detection of Hepatitis B. *Talanta* **2018,** *181*, 258-264.

[53] Taebi, S.; Keyhanfar, M.; Noorbakhsh, A., A novel method for sensitive, low-cost and portable detection of hepatitis B surface antigen using a personal glucose meter. *Journal of Immunological Methods* **2018,** *458*, 26-32.
[54] Haun, J. B.; Yoon, T.-J.; Lee, H.; Weissleder, R., Magnetic nanoparticle biosensors. *Wiley Interdisciplinary Reviews: Nanomedicine and Nanobiotechnology* **2010,** *2* (3), 291-304.
[55] Kearns, H.; Goodacre, R.; Jamieson, L. E.; Graham, D.; Faulds, K., SERS Detection of Multiple Antimicrobial-Resistant Pathogens Using Nanosensors. *Analytical Chemistry* **2017,** *89* (23), 12666-12673.
[56] La Porta, A.; Sanchez-Iglesias, A.; Altantzis, T.; Bals, S.; Grzelczak, M.; Liz-Marzan, L. M., Multifunctional self-assembled composite colloids and their application to SERS detection. *Nanoscale* **2015,** *7* (23), 10377-10381.
[57] Lai, H.; Xu, F.; Wang, L., A review of the preparation and application of magnetic nanoparticles for surface-enhanced Raman scattering. *Journal of Materials Science* **2018,** *53* (12), 8677-8698.
[58] Pang, Y.; Wang, C.; Wang, J.; Sun, Z.; Xiao, R.; Wang, S., Fe3O4@Ag magnetic nanoparticles for microRNA capture and duplex-specific nuclease signal amplification based SERS detection in cancer cells. *Biosensors and Bioelectronics* **2016,** *79*, 574-580.
[59] Litti, L.; Amendola, V.; Toffoli, G.; Meneghetti, M., Detection of low-quantity anticancer drugs by surface-enhanced Raman scattering. *Analytical and Bioanalytical Chemistry* **2016,** *408* (8), 2123-2131.
[60] Litti, L.; Ramundo, A.; Biscaglia, F.; Toffoli, G.; Gobbo, M.; Meneghetti, M., A surface enhanced Raman scattering based colloid nanosensor for developing therapeutic drug monitoring. *Journal of Colloid and Interface Science* **2019,** *533*, 621-626.
[61] Baranowski, A.; Klein, A.; Ritz, U.; Ackermann, A.; Anthonissen, J.; Kaufmann, K. B.; Brendel, C.; Götz, H.; Rommens, P. M.; Hofmann, A., Surface Functionalization of Orthopedic Titanium Implants with Bone Sialoprotein. *PLOS ONE* **2016,** *11* (4), e0153978.
[62] Gu, J.; Wang, T.; Fan, G.; Ma, J.; Hu, W.; Cai, X., Biocompatibility of artificial bone based on vancomycin loaded mesoporous silica nanoparticles and calcium sulfate composites. *Journal of Materials Science: Materials in Medicine* **2016,** *27* (4), 1-11.
[63] Hsu, W. K.; Goldstein, C. L.; Shamji, M. F.; Cho, S. K.; Arnold, P. M.; Fehlings, M. G.; Mroz, T. E., Novel Osteobiologics and Biomaterials in the Treatment of Spinal Disorders. *Neurosurgery* **2017,** *80* (3S), S100-S107.
[64] Li, H.; Gu, J.; Shah, L. A.; Siddiq, M.; Hu, J.; Cai, X.; Yang, D., Bone cement based on vancomycin loaded mesoporous silica nanoparticle and calcium sulfate composites. *Materials Science and Engineering: C* **2015,** *49*, 210-216.
[65] Lu, H.; Liu, Y.; Guo, J.; Wu, H.; Wang, J.; Wu, G., Biomaterials with Antibacterial and Osteoinductive Properties to Repair Infected Bone Defects. *International journal of molecular sciences* **2016,** *17* (3), 334.
[66] Ryan, G.; Pandit, A.; Apatsidis, D. P., Fabrication methods of porous metals for use in orthopaedic applications. *Biomaterials* **2006,** *27* (13), 2651-2670.
[67] Fernandez-Moure, J. S.; Evangelopoulos, M.; Colvill, K.; Eps, J. L. V.; Tasciotti, E., Nanoantibiotics: a new paradigm for the treatment of surgical infection. *Nanomedicine* **2017,** *12* (11), 1319-1334.
[68] Kumar, T. S.; Madhumathi, K., Antibiotic delivery by nanobioceramics. *Therapeutic Delivery* **2016,** *7* (8), 573-588.
[69] Hench, L. L.; West, J. K., The sol-gel process. *Chemical Reviews* **1990,** *90* (1), 33-72.
[70] Brinker, C. J.; Scherer, G. W., *Sol-gel science: the physics and chemistry of sol-gel processing*. Academic press: 2013.
[71] Danks, A. E.; Hall, S. R.; Schnepp, Z., The evolution of 'sol–gel' chemistry as a technique for materials synthesis. *Materials Horizons* **2016,** *3* (2), 91-112.

[72] Gu, D.; Schüth, F., Synthesis of non-siliceous mesoporous oxides. *Chemical Society Reviews* **2014,** *43* (1), 313-344.
[73] Levy, D.; Zayat, M., *The Sol-Gel Handbook, 3 Volume Set: Synthesis, Characterization, and Applications*. John Wiley & Sons: 2015; Vol. 2.
[74] Lu, Y.; Ganguli, R.; Drewien, C. A.; Anderson, M. T.; Brinker, C. J.; Gong, W.; Guo, Y.; Soyez, H.; Dunn, B.; Huang, M. H.; Zink, J. I., Continuous formation of supported cubic and hexagonal mesoporous films by sol-gel dip-coating. *Nature* **1997,** *389* (6649), 364-368.
[75] Noureddine, A.; Lichon, L.; Maynadier, M.; Garcia, M.; Gary-Bobo, M.; Zink, J. I.; Cattoen, X.; Wong Chi Man, M., Controlled multiple functionalization of mesoporous silica nanoparticles: homogeneous implementation of pairs of functionalities communicating through energy or proton transfers. *Nanoscale* **2015**.
[76] Parida, K. M.; Mallick, S.; Sahoo, P. C.; Rana, S. K., A facile method for synthesis of amine-functionalized mesoporous zirconia and its catalytic evaluation in Knoevenagel condensation. *Applied Catalysis A: General* **2010,** *381* (1–2), 226-232.
[77] Singh, L. P.; Bhattacharyya, S. K.; Kumar, R.; Mishra, G.; Sharma, U.; Singh, G.; Ahalawat, S., Sol-Gel processing of silica nanoparticles and their applications. *Adv Colloid Interfac* **2014,** *214*, 17-37.
[78] Solanki, P. R.; Patel, M. K.; Kaushik, A.; Pandey, M. K.; Kotnala, R. K.; Malhotra, B. D., Sol-Gel Derived Nanostructured Metal Oxide Platform for Bacterial Detection. *Electroanalysis* **2011,** *23* (11), 2699-2708.
[79] Trewyn, B. G.; Slowing, I. I.; Giri, S.; Chen, H.-T.; Lin, V. S. Y., Synthesis and Functionalization of a Mesoporous Silica Nanoparticle Based on the Sol–Gel Process and Applications in Controlled Release. *Accounts Chem Res* **2007,** *40* (9), 846-853.
[80] Wu, S.-H.; Mou, C.-Y.; Lin, H.-P., Synthesis of mesoporous silica nanoparticles. *Chemical Society Reviews* **2013,** *42* (9), 3862-3875.
[81] Xie, Y.; Kocaefe, D.; Chen, C.; Kocaefe, Y., Review of Research on Template Methods in Preparation of Nanomaterials. *J. Nanomaterials* **2016,** *2016*, 11.
[82] Majidi, S.; Zeinali Sehrig, F.; Farkhani, S. M.; Soleymani Goloujeh, M.; Akbarzadeh, A., Current methods for synthesis of magnetic nanoparticles. *Artificial Cells, Nanomedicine, and Biotechnology* **2016,** *44* (2), 722-734.
[83] Yusoff, A. H.; Salimi, M. N.; Jamlos, M. F., A review: Synthetic strategy control of magnetite nanoparticles production. *ADVANCES IN NANO RESEARCH* **2018,** *6* (1), 1-19.
[84] Kandasamy, G.; Maity, D., Recent advances in superparamagnetic iron oxide nanoparticles (SPIONs) for in vitro and in vivo cancer nanotheranostics. *Int J Pharmaceut* **2015,** *496* (2), 191-218.
[85] Unsoy, G.; Gunduz, U.; Oprea, O.; Ficai, D.; Sonmez, M.; Radulescu, M.; Alexie, M.; Ficai, A., Magnetite: From Synthesis to Applications. *Current Topics in Medicinal Chemistry* **2015,** *15* (16), 1622-1640.
[86] Basly, B.; Popa, G.; Fleutot, S.; Pichon, B. P.; Garofalo, A.; Ghobril, C.; Billotey, C.; Berniard, A.; Bonazza, P.; Martinez, H.; Felder-Flesch, D.; Begin-Colin, S., Effect of the nanoparticle synthesis method on dendronized iron oxides as MRI contrast agents. *Dalton T* **2013,** *42* (6), 2146-2157.
[87] Cannas, C.; Musinu, A.; Ardu, A.; Orrù, F.; Peddis, D.; Casu, M.; Sanna, R.; Angius, F.; Diaz, G.; Piccaluga, G., CoFe2O4 and CoFe2O4/SiO2 Core/Shell Nanoparticles: Magnetic and Spectroscopic Study. *Chem Mater* **2010,** *22* (11), 3353-3361.
[88] Liang, W.-I.; Zhang, X.; Bustillo, K.; Chiu, C.-H.; Wu, W.-W.; Xu, J.; Chu, Y.-H.; Zheng, H., In Situ Study of Spinel Ferrite Nanocrystal Growth Using Liquid Cell Transmission Electron Microscopy. *Chem Mater* **2015,** *27* (23), 8146-8152.
[89] Muscas, G.; Singh, G.; Glomm, W. R.; Mathieu, R.; Kumar, P. A.; Concas, G.; Agostinelli, E.; Peddis, D., Tuning the Size and Shape of Oxide Nanoparticles by Controlling Oxygen Content in the Reaction Environment: Morphological Analysis by Aspect Maps. *Chem Mater* **2015,** *27* (6), 1982-1990.

[90] Singh, G.; McDonagh, B. H.; Hak, S.; Peddis, D.; Bandopadhyay, S.; Sandvig, I.; Sandvig, A.; Glomm, W. R., Synthesis of gadolinium oxide nanodisks and gadolinium doped iron oxide nanoparticles for MR contrast agents. *J Mater Chem B* **2017,** *5* (3), 418-422.
[91] Wang, C.; Yin, H.; Dai, S.; Sun, S., A General Approach to Noble Metal−Metal Oxide Dumbbell Nanoparticles and Their Catalytic Application for CO Oxidation. *Chem Mater* **2010,** *22* (10), 3277-3282.
[92] Alex, D.; Mathew, A.; Sukumaran, R. K., Esterases immobilized on aminosilane modified magnetic nanoparticles as a catalyst for biotransformation reactions. *Bioresource Technology* **2014,** *167*, 547-550.
[93] Amendola, V.; Scaramuzza, S.; Agnoli, S.; Granozzi, G.; Meneghetti, M.; Campo, G.; Bonanni, V.; Pineider, F.; Sangregorio, C.; Ghigna, P.; Polizzi, S.; Riello, P.; Fiameni, S.; Nodari, L., Laser generation of iron-doped silver nanotruffles with magnetic and plasmonic properties. *Nano Research* **2015,** *8* (12), 4007-4023.
[94] Amer, M. A.; Matsuda, A.; Kawamura, G.; El-Shater, R.; Meaz, T.; Fakhry, F., Characterization and structural and magnetic studies of as-synthesized Fe2+CrxFe(2−x)O4 nanoparticles. *Journal of Magnetism and Magnetic Materials* **2017,** *439* (Supplement C), 373-383.
[95] Arulmurugan, R.; Jeyadevan, B.; Vaidyanathan, G.; Sendhilnathan, S., Effect of zinc substitution on Co–Zn and Mn–Zn ferrite nanoparticles prepared by co-precipitation. *Journal of Magnetism and Magnetic Materials* **2005,** *288*, 470-477.
[96] Assar, S. T.; Abosheiasha, H. F.; Saafan, S. A.; El Nimr, M. K., Preparation, characterization and magnetization of nano and bulk Ni0.5Co0.5−2xLixFe2+xO4 samples. *Journal of Molecular Structure* **2015,** *1084* (Supplement C), 128-134.
[97] Atif, M.; Asghar, M. W.; Nadeem, M.; Khalid, W.; Ali, Z.; Badshah, S., Synthesis and investigation of structural, magnetic and dielectric properties of zinc substituted cobalt ferrites. *J Phys Chem Solids* **2018,** *123*, 36-42.
[98] Bakeer, D. E.-S.; Abou-Aly, A. I.; Mohammed, N. H.; Awad, R.; Hasebbo, M., Characterization and Magnetic Properties of Nanoferrite ZnFe2−x La x O 4 Prepared by Co-Precipitation Method. *Journal of Superconductivity and Novel Magnetism* **2017,** *30* (4), 893-902.
[99] Cardoso, V. F.; Francesko, A.; Ribeiro, C.; Bañobre-López, M.; Martins, P.; Lanceros-Mendez, S., Advances in Magnetic Nanoparticles for Biomedical Applications. *Advanced Healthcare Materials* **2018,** *7* (5), 1700845.
[100] Chandra, S.; Patel, M. D.; Lang, H.; Bahadur, D., Dendrimer-functionalized magnetic nanoparticles: A new electrode material for electrochemical energy storage devices. *J Power Sources* **2015,** *280*, 217-226.
[101] Feng, J.; Xiong, R.; Liu, Y.; Su, F.; Zhang, X., Preparation of cobalt substituted zinc ferrite nanopowders via auto-combustion route: an investigation to their structural and magnetic properties. *Journal of Materials Science: Materials in Electronics* **2018,** *29* (21), 18358-18371.
[102] Karimi, Z.; Karimi, L.; Shokrollahi, H., Nano-magnetic particles used in biomedicine: Core and coating materials. *Materials Science and Engineering: C* **2013,** *33* (5), 2465-2475.
[103] Lee, J.-H.; Huh, Y.-M.; Jun, Y.-w.; Seo, J.-w.; Jang, J.-t.; Song, H.-T.; Kim, S.; Cho, E.-J.; Yoon, H.-G.; Suh, J.-S.; Cheon, J., Artificially engineered magnetic nanoparticles for ultra-sensitive molecular imaging. *Nature Medicine* **2006,** *13*, 95.
[104] Li, Z.; Zheng, Y.; Gao, T.; Liu, Z.; Zhang, J.; Zhou, G., Fabrication of biosensor based on core–shell and large void structured magnetic mesoporous microspheres immobilized with laccase for dopamine detection. *Journal of Materials Science* **2018,** *53* (11), 7996-8008.
[105] Litti, L.; Rivato, N.; Fracasso, G.; Bontempi, P.; Nicolato, E.; Marzola, P.; Venzo, A.; Colombatti, M.; Gobbo, M.; Meneghetti, M., A SERRS/MRI multimodal contrast agent based on naked Au nanoparticles functionalized with a Gd(iii) loaded PEG polymer for tumor imaging and localized hyperthermia. *Nanoscale* **2018,** *10* (3), 1272-1278.

[106] Mahmed, N.; Heczko, O.; Söderberg, O.; Hannula, S. P., Room Temperature Synthesis of Magnetite (Fe 3−δ O 4) Nanoparticles by a Simple Reverse Co-Precipitation Method. *IOP Conference Series: Materials Science and Engineering* **2011,** *18* (3), 032020.
[107] Sun, S.; Zeng, H.; Robinson, D. B.; Raoux, S.; Rice, P. M.; Wang, S. X.; Li, G., Monodisperse MFe2O4 (M = Fe, Co, Mn) Nanoparticles. *Journal of the American Chemical Society* **2004,** *126* (1), 273-279.
[108] Suber, L.; Peddis, D., Approaches to Synthesis and Characterization of Spherical and Anisometric Metal Oxide Magnetic Nanomaterials. In *Nanotechnologies for the Life Sciences*, Kumar, C. S., Ed. 2011.
[109] Peddis, D.; Cannas, C.; Musinu, A.; Piccaluga, G., Magnetism in nanoparticles: beyond the effect of particle size. *Chem-Eur J* **2009,** *15* (32), 7822-7829.
[110] Papaefthymiou, G. C., Nanoparticle magnetism. *Nano Today* **2009,** *4* (5), 438-447.
[111] Peddis, D., Magnetic Properties of Spinel Ferrite Nanoparticles: Influence of the Magnetic Structure. In *Magnetic Nanoparticle Assemblies*, Pan Stanford: 2014; pp 159-198.
[112] Blundell, S., Magnetism in Condensed Matter. *American Journal of Physics* **2003,** *71* (1), 94-95.
[113] Luborsky, F. E., Development of Elongated Particle Magnets. *Journal of Applied Physics* **1961,** *32* (3), S171-S183.
[114] Peddis, D.; Jönsson, P. E.; Laureti, S.; Varvaro, G., Chapter 4 - Magnetic Interactions: A Tool to Modify the Magnetic Properties of Materials Based on Nanoparticles. In *Frontiers of Nanoscience*, Binns, C., Ed. Elsevier: 2014; Vol. 6, pp 129-188.
[115] Mathew, D. S.; Juang, R.-S., An overview of the structure and magnetism of spinel ferrite nanoparticles and their synthesis in microemulsions. *Chem Eng J* **2007,** *129* (1), 51-65.
[116] Schindelin, J.; Arganda-Carreras, I.; Frise, E.; Kaynig, V.; Longair, M.; Pietzsch, T.; Preibisch, S.; Rueden, C.; Saalfeld, S.; Schmid, B.; Tinevez, J.-Y.; White, D. J.; Hartenstein, V.; Eliceiri, K.; Tomancak, P.; Cardona, A., Fiji: an open-source platform for biological-image analysis. *Nat Methods* **2012,** *9*, 676.
[117] Schneider, C. A.; Rasband, W. S.; Eliceiri, K. W., NIH Image to ImageJ: 25 years of image analysis. *Nat Methods* **2012,** *9* (7), 671-675.
[118] Enzo, S.; Polizzi, S.; Benedetti, A., Applications of fitting techniques to the Warren-Averbach method for X-ray line broadening analysis. *Zeitschrift für Kristallographie-Crystalline Materials* **1985,** *170* (1-4), 275-288.
[119] Brunauer, S.; Emmett, P. H.; Teller, E., Adsorption of gases in multimolecular layers. *Journal of the American chemical society* **1938,** *60* (2), 309-319.
[120] Barrett, E. P.; Joyner, L. G.; Halenda, P. P., The determination of pore volume and area distributions in porous substances. I. Computations from nitrogen isotherms. *Journal of the American Chemical society* **1951,** *73* (1), 373-380.
[121] Naumkin, A. V.; Kraut-Vass, A.; Gaarenstroom, S. W.; Powell, C. J., NIST X-ray Photoelectron Spectroscopy Database, NIST Standard Reference Database Number 20, National Institute of Standards and Technology. Gaithersburg MD, 20899, 2000.
[122] Leung, K. C.-F.; Xuan, S.; Zhu, X.; Wang, D.; Chak, C.-P.; Lee, S.-F.; Ho, W. K. W.; Chung, B. C. T., Gold and iron oxide hybrid nanocomposite materials. *Chemical Society Reviews* **2012,** *41* (5), 1911-1928.
[123] Laureti, S.; Varvaro, G.; Testa, A.; Fiorani, D.; Agostinelli, E.; Piccaluga, G.; Musinu, A.; Ardu, A.; Peddis, D., Magnetic interactions in silica coated nanoporous assemblies of CoFe2O4 nanoparticles with cubic magnetic anisotropy. *Nanotechnology* **2010,** *21* (31), 315701.
[124] Sponchia, G.; Benedetti, A.; Riello, P. Totally-mesoporous zirconia nanoparticles, use and method for producing thereof 2015.
[125] Widoniak, J.; Eiden-Assmann, S.; Maret, G., Synthesis and Characterisation of Monodisperse Zirconia Particles. *Eur J Inorg Chem* **2005,** *2005* (15), 3149-3155.

[126] Cinier, M.; Petit, M.; Williams, M. N.; Fabre, R. M.; Pecorari, F.; Talham, D. R.; Bujoli, B.; Tellier, C., Bisphosphonate adaptors for specific protein binding on zirconium phosphonate-based microarrays. *Bioconjugate Chem* **2009,** *20* (12), 2270-2277.
[127] Liu, H.; Sun, X.; Yin, C.; Hu, C., Removal of phosphate by mesoporous ZrO2. *J Hazard Mater* **2008,** *151* (2–3), 616-622.
[128] Long, F.; Gong, J.-L.; Zeng, G.-M.; Chen, L.; Wang, X.-Y.; Deng, J.-H.; Niu, Q.-Y.; Zhang, H.-Y.; Zhang, X.-R., Removal of phosphate from aqueous solution by magnetic Fe–Zr binary oxide. *Chem Eng J* **2011,** *171* (2), 448-455.
[129] Ren, Z.; Shao, L.; Zhang, G., Adsorption of phosphate from aqueous solution using an iron–zirconium binary oxide sorbent. *Water, Air, & Soil Pollution* **2012,** *223* (7), 4221-4231.
[130] Song, J.; Zhou, B.; Zhou, H.; Wu, L.; Meng, Q.; Liu, Z.; Han, B., Porous Zirconium–Phytic Acid Hybrid: a Highly Efficient Catalyst for Meerwein–Ponndorf–Verley Reductions. *Angewandte Chemie International Edition* **2015,** *54* (32), 9399-9403.
[131] Zhang, J.; Lv, J.; Wang, X.; Li, D.; Wang, Z.; Li, G., A simple and visible colorimetric method through Zr4+-phosphate coordination for the assay of protein tyrosine phosphatase 1B and screening of its inhibitors. *Analyst* **2015,** *140* (16), 5716-5723.
[132] Guerrero, G.; Mutin, P. H.; Vioux, A., Anchoring of Phosphonate and Phosphinate Coupling Molecules on Titania Particles. *Chem Mater* **2001,** *13* (11), 4367-4373.
[133] Marcinko, S.; Fadeev, A. Y., Hydrolytic Stability of Organic Monolayers Supported on TiO2 and ZrO2. *Langmuir* **2004,** *20* (6), 2270-2273.
[134] Canepa, P.; Solano, I.; Uttiya, S.; Gemme, G.; Rolandi, R.; Canepa, M.; Cavalleri, O., Phosphonate molecular layers on TiO2 surfaces. *MATEC Web Conf.* **2017,** *98*, 03001.
[135] Parma, A.; Freris, I.; Riello, P.; Cristofori, D.; de Julian Fernandez, C.; Amendola, V.; Meneghetti, M.; Benedetti, A., Structural and magnetic properties of mesoporous SiO2 nanoparticles impregnated with iron oxide or cobalt-iron oxide nanocrystals. *J Mater Chem* **2012,** *22* (36), 19276-19288.
[136] Ma, S.; Wang, Y.; Zhu, Y., A simple room temperature synthesis of mesoporous silica nanoparticles for drug storage and pressure pulsed delivery. *J Porous Mat* **2011,** *18* (2), 233-239.
[137] Kumar, S.; Bhunia, S.; Singh, J.; Ojha, A. K., Absence of room temperature ferromagnetism in Fe stabilized ZrO2 nanostructures and effect of Fe doping on its structural, optical and luminescence properties. *Journal of Alloys and Compounds* **2015,** *649*, 348-356.
[138] Kuryliszyn-Kudelska, I.; Arciszewska, M.; Małolepszy, A.; Mazurkiewicz, M.; Stobinski, L.; Grabias, A.; Kopcewicz, M.; Paszkowicz, W.; Minikaev, R.; Domukhovski, V.; Nedelko, N.; Dobrowolski, W., Influence of Fe doping on magnetic properties of ZrO2 nanocrystals. *Journal of Alloys and Compounds* **2015,** *632*, 609-616.
[139] Amendola, V.; Meneghetti, M., Controlled size manipulation of free gold nanoparticles by laser irradiation and their facile bioconjugation. *J Mater Chem* **2007,** *17* (44), 4705-4710.
[140] Meneghetti, M.; Scarsi, A.; Litti, L.; Marcolongo, G.; Amendola, V.; Gobbo, M.; Di Chio, M.; Boscaini, A.; Fracasso, G.; Colombatti, M., Plasmonic Nanostructures for SERRS Multiplexed Identification of Tumor-Associated Antigens. *Small* **2012,** *8* (24), 3733-3738.
[141] Biscaglia, F.; Rajendran, S.; Conflitti, P.; Benna, C.; Sommaggio, R.; Litti, L.; Mocellin, S.; Bocchinfuso, G.; Rosato, A.; Palleschi, A.; Nitti, D.; Gobbo, M.; Meneghetti, M., Enhanced EGFR Targeting Activity of Plasmonic Nanostructures with Engineered GE11 Peptide. *Advanced Healthcare Materials* **2017,** *6* (23), 1700596-n/a.
[142] Wang, X.; Tilley, R. D.; Watkins, J. J., Simple Ligand Exchange Reactions Enabling Excellent Dispersibility and Stability of Magnetic Nanoparticles in Polar Organic, Aromatic, and Protic Solvents. *Langmuir* **2014,** *30* (6), 1514-1521.
[143] Borges, J.; Mano, J. F., Molecular Interactions Driving the Layer-by-Layer Assembly of Multilayers. *Chemical Reviews* **2014,** *114* (18), 8883-8942.

[144] Liu, Y.; Williams, M. G.; Miller, T. J.; Teplyakov, A. V., Nanoparticle layer deposition for highly controlled multilayer formation based on high-coverage monolayers of nanoparticles. *Thin Solid Films* **2016,** *598*, 16-24.
[145] Lee, H.; Dellatore, S. M.; Miller, W. M.; Messersmith, P. B., Mussel-Inspired Surface Chemistry for Multifunctional Coatings. *Science* **2007,** *318* (5849), 426-430.
[146] Chen, Z.; Qin, Y.; Amine, K.; Sun, Y. K., Role of surface coating on cathode materials for lithium-ion batteries. *J Mater Chem* **2010,** *20* (36), 7606-7612.
[147] Moreno, R., Colloidal processing of ceramics and composites. *Advances in Applied Ceramics* **2012,** *111* (5-6), 246-253.
[148] Hermanson, G. T., *Bioconjugate Techniques*. Elsevier Science: 2013.
[149] Tian, Y.; Qi, J.; Zhang, W.; Cai, Q.; Jiang, X., Facile, One-Pot Synthesis, and Antibacterial Activity of Mesoporous Silica Nanoparticles Decorated with Well-Dispersed Silver Nanoparticles. *Acs Appl Mater Inter* **2014,** *6* (15), 12038-12045.
[150] Wang, Q.; Yu, H.; Zhong, L.; Liu, J.; Sun, J.; Shen, J., Incorporation of Silver Ions into Ultrathin Titanium Phosphate Films: In Situ Reduction to Prepare Silver Nanoparticles and Their Antibacterial Activity. *Chem Mater* **2006,** *18* (7), 1988-1994.
[151] Yin, T.; Li, H.; Yang, N.; Gao, T.; Sun, L.; Li, G., Detection of CREB phosphorylation via Zr (IV) ion mediated signal amplification. *Biosensors and Bioelectronics* **2014,** *56*, 1-5.
[152] Chiminazzo, A.; Sperni, L.; Scarso, A.; Strukul, G., Organocatalytic Enantioselective Epoxidation of Some Aryl-Substituted Vinylidenebisphosphonate Esters: On the Way to Chiral Anti-Osteoporosis Drugs. *Catalysts* **2017,** *7* (3), 90.
[153] De Luca, L.; Chiminazzo, A.; Sperni, L.; Strukul, G.; Scarso, A., Pyrrolidine-Containing Bisphosphonates as Potential Anti-Resorption Bone Drugs. *Chemistry – A European Journal* **2017,** *23* (14), 3474-3478.
[154] De Luca, L.; Chiminazzo, A.; Sperni, L.; Strukul, G.; Scarso, A., Stereoselective Synthesis of Chiral Isatin Containing Bisphosphonates as Potential Anti-Resorption Bone Drugs. *ChemistrySelect* **2017,** *2* (11), 3262-3267.
[155] Gao, W.; Dickinson, L.; Grozinger, C.; Morin, F. G.; Reven, L., Self-Assembled Monolayers of Alkylphosphonic Acids on Metal Oxides. *Langmuir* **1996,** *12* (26), 6429-6435.
[156] Pawsey, S.; McCormick, M.; De Paul, S.; Graf, R.; Lee, Y. S.; Reven, L.; Spiess, H. W., 1H Fast MAS NMR Studies of Hydrogen-Bonding Interactions in Self-Assembled Monolayers. *Journal of the American Chemical Society* **2003,** *125* (14), 4174-4184.
[157] Pawsey, S.; Yach, K.; Reven, L., Self-Assembly of Carboxyalkylphosphonic Acids on Metal Oxide Powders. *Langmuir* **2002,** *18* (13), 5205-5212.
[158] Burwell, D. A.; Valentine, K. G.; Timmermans, J. H.; Thompson, M. E., Structural studies of oriented zirconium bis (phosphonoacetic acid) using solid-state phosphorus-31 and carbon-13 NMR. *Journal of the American Chemical Society* **1992,** *114* (11), 4144-4150.
[159] Veliscek-Carolan, J.; Rawal, A.; Luca, V.; Hanley, T. L., Zirconium phosphonate sorbents with tunable structure and function. *Micropor Mesopor Mat* **2017,** *252*, 90-104.
[160] Lin, X.-Z.; Ren, T.-Z.; Yuan, Z.-Y., Mesoporous zirconium phosphonate materials as efficient water-tolerable solid acid catalysts. *Catalysis Science & Technology* **2015,** *5* (3), 1485-1494.
[161] Griffith, C. S.; Reyes, M. D. L.; Scales, N.; Hanna, J. V.; Luca, V., Hybrid Inorganic–Organic Adsorbents Part 1: Synthesis and Characterization of Mesoporous Zirconium Titanate Frameworks Containing Coordinating Organic Functionalities. *Acs Appl Mater Inter* **2010,** *2* (12), 3436-3446.
[162] Harris, R. K.; Merwin, L. H.; Hägele, G., Solid-state nuclear magnetic resonance study of a series of phosphonic and phosphinic acids. *Journal of the Chemical Society, Faraday Transactions 1: Physical Chemistry in Condensed Phases* **1989,** *85* (6), 1409-1423.
[163] Cialla-May, D.; Zheng, X. S.; Weber, K.; Popp, J., Recent progress in surface-enhanced Raman spectroscopy for biological and biomedical applications: from cells to clinics. *Chemical Society Reviews* **2017,** *46* (13), 3945-3961.

[164] Rizvi, S. A. A.; Saleh, A. M., Applications of nanoparticle systems in drug delivery technology. *Saudi Pharmaceutical Journal* **2018,** *26* (1), 64-70.
[165] Yilong, W.; Shuyang, S.; Zhiyuan, Z.; Donglu, S., Nanomaterials for Cancer Precision Medicine. *Advanced Materials* **2018,** *30* (17), 1705660.
[166] Dapiaggi, M.; Maglia, F.; Tredici, I.; Maroni, B.; Borghini, G.; Tamburini, U. A., Complex thermal evolution of size-stabilized tetragonal zirconia. *J Phys Chem Solids* **2010,** *71* (8), 1038-1041.
[167] Choudhary, V. R.; Banerjee, S.; Pataskar, S. G., Combustion of dilute propane over transition metal-doped ZrO2 (cubic) catalysts. *Applied Catalysis A: General* **2003,** *253* (1), 65-74.
[168] Anku, W. W.; Oppong, S. O.-B.; Shukla, S. K.; Agorku, E. S.; Govender, P. P., Cobalt doped ZrO2 decorated multiwalled carbon nanotube: A promising nanocatalyst for photodegradation of indigo carmine and eosin Y dyes. *Progress in Natural Science: Materials International* **2016,** *26* (4), 354-361.
[169] Sangalli, D.; Cianci, E.; Lamperti, A.; Ciprian, R.; Albertini, F.; Casoli, F.; Lupo, P.; Nasi, L.; Campanini, M.; Debernardi, A., Exploiting magnetic properties of Fe doping in zirconia. *The European Physical Journal B* **2013,** *86* (5), 1-6.
[170] Garcia, F. L.; Resende, V. G. d.; De Grave, E.; Peigney, A.; Barnabé, A.; Laurent, C., Iron-stabilized nanocrystalline ZrO2 solid solutions: Synthesis by combustion and thermal stability. *Materials Research Bulletin* **2009,** *44* (6), 1301-1311.
[171] Grigorova, M.; Blythe, H. J.; Blaskov, V.; Rusanov, V.; Petkov, V.; Masheva, V.; Nihtianova, D.; Martinez, L. M.; Muñoz, J. S.; Mikhov, M., Magnetic properties and Mössbauer spectra of nanosized CoFe2O4 powders. *Journal of Magnetism and Magnetic Materials* **1998,** *183* (1), 163-172.
[172] Mameli, V.; Musinu, A.; Ardu, A.; Ennas, G.; Peddis, D.; Niznansky, D.; Sangregorio, C.; Innocenti, C.; Thanh, N. T. K.; Cannas, C., Studying the effect of Zn-substitution on the magnetic and hyperthermic properties of cobalt ferrite nanoparticles. *Nanoscale* **2016,** *8* (19), 10124-10137.
[173] Cannas, C.; Musinu, A.; Peddis, D.; Piccaluga, G., New Synthesis of Ferrite–Silica Nanocomposites by a Sol–Gel Auto-Combustion. *Journal of Nanoparticle Research* **2004,** *6* (2), 223-232.
[174] Peddis, D.; Mansilla, M. V.; Mørup, S.; Cannas, C.; Musinu, A.; Piccaluga, G.; D'Orazio, F.; Lucari, F.; Fiorani, D., Spin-Canting and Magnetic Anisotropy in Ultrasmall CoFe2O4 Nanoparticles. *The Journal of Physical Chemistry B* **2008,** *112* (29), 8507-8513.
[175] Kelly, P. E.; Grady, K. O.; Mayo, P. I.; Chantrell, R. W., Switching mechanisms in cobalt-phosphorus thin films. *IEEE Transactions on Magnetics* **1989,** *25* (5), 3881-3883.
[176] Peddis, D.; Orrù, F.; Ardu, A.; Cannas, C.; Musinu, A.; Piccaluga, G., Interparticle Interactions and Magnetic Anisotropy in Cobalt Ferrite Nanoparticles: Influence of Molecular Coating. *Chem Mater* **2012,** *24* (6), 1062-1071.
[177] Yeap, S. P.; Toh, P. Y.; Ahmad, A. L.; Low, S. C.; Majetich, S. A.; Lim, J., Colloidal Stability and Magnetophoresis of Gold-Coated Iron Oxide Nanorods in Biological Media. *The Journal of Physical Chemistry C* **2012,** *116* (42), 22561-22569.
[178] Nie, S.; Emory, S. R., Probing Single Molecules and Single Nanoparticles by Surface-Enhanced Raman Scattering. *Science* **1997,** *275* (5303), 1102-1106.
[179] Myroshnychenko, V.; Carbó-Argibay, E.; Pastoriza-Santos, I.; Pérez-Juste, J.; Liz-Marzán, L. M.; García de Abajo, F. J., Modeling the Optical Response of Highly Faceted Metal Nanoparticles with a Fully 3D Boundary Element Method. *Advanced Materials* **2008,** *20* (22), 4288-4293.
[180] Hohenester, U.; Trügler, A., MNPBEM – A Matlab toolbox for the simulation of plasmonic nanoparticles. *Computer Physics Communications* **2012,** *183* (2), 370-381.
[181] Riello, P.; Lausi, A.; Macleod, J.; Plaisier, J. R.; Zerauschek, G.; Fornasiero, P., In situ reaction furnace for real-time XRD studies. *Journal of Synchrotron Radiation* **2013,** *20* (1), 194-196.

[182] Santos, V.; Zeni, M.; Bergmann, C.; Hohemberger, J., Correlation between thermal treatment and tetragonal/monoclinic nanostructured zirconia powder obtained by sol–gel process. *Rev. Adv. Mater. Sci* **2008,** *17* (1/2), 62-70.
[183] TORAYA, H.; YOSHIMURA, M.; SŌMIYA, S., Quantitative Analysis of Monoclinic-Stabilized Cubic ZrO2 Systems by X-Ray Diffraction. *Journal of the American Ceramic Society* **1984,** *67* (9), C-183-C-184.
[184] Tirosh, E.; Shemer, G.; Markovich, G., Optimizing Cobalt Ferrite Nanocrystal Synthesis Using a Magneto-optical Probe. *Chem Mater* **2006,** *18* (2), 465-470.
[185] Mathieu, A.; Lotfi Ben, T.; Frédéric, H.; Leila, S.; Françoise, V.; Nader, Y.; Jean-Marc, G.; Souad, A.; Fernand, F., Size-dependent magnetic properties of CoFe 2 O 4 nanoparticles prepared in polyol. *Journal of Physics: Condensed Matter* **2011,** *23* (50), 506001.
[186] Coles, S. J.; Hursthouse, M. B.; Frey, J. G.; Milsted, A. J.; Carr, L. A.; Koch, T.; Lyon, E.; Duke, M., eCrystals: A Route for Open Access to Small Molecule Crystal Structure Data. In *ECM 23*, 2006.
[187] Nasrin, S.; Chowdhury, F.-U.-Z.; Hasan, M. M.; Hossen, M. M.; Ullah, S. M.; Hoque, S. M., Effect of zinc substitution on structural, morphological and magnetic properties of cobalt nanocrystalline ferrites prepared by co-precipitation method. *Journal of Materials Science: Materials in Electronics* **2018,** *29* (21), 18878-18889.
[188] Raut, A. V.; Barkule, R. S.; Shengule, D. R.; Jadhav, K. M., Synthesis, structural investigation and magnetic properties of Zn2+ substituted cobalt ferrite nanoparticles prepared by the sol–gel auto-combustion technique. *Journal of Magnetism and Magnetic Materials* **2014,** *358-359*, 87-92.
[189] Singh, C.; Jauhar, S.; Kumar, V.; Singh, J.; Singhal, S., Synthesis of zinc substituted cobalt ferrites via reverse micelle technique involving in situ template formation: A study on their structural, magnetic, optical and catalytic properties. *Materials Chemistry and Physics* **2015,** *156*, 188-197.
[190] Sundararajan, M.; Kennedy, L. J.; Aruldoss, U.; Pasha, S. K.; Vijaya, J. J.; Dunn, S., Microwave combustion synthesis of zinc substituted nanocrystalline spinel cobalt ferrite: Structural and magnetic studies. *Materials Science in Semiconductor Processing* **2015,** *40*, 1-10.
[191] Hossain, M. S.; Alam, M. B.; Shahjahan, M.; Begum, M. H. A.; Hossain, M. M.; Islam, S.; Khatun, N.; Hossain, M.; Alam, M. S.; Al-Mamun, M., Synthesis, structural investigation, dielectric and magnetic properties of Zn2+-doped cobalt ferrite by the sol–gel technique. *Journal of Advanced Dielectrics* **2018,** *08* (04), 1850030.
[192] Almeida Paz, Filipe A.; Shi, F.-N.; Klinowski, J.; Rocha, J.; Trindade, T., Synthesis and Characterisation of the First Three-Dimensional Mixed-Metal-Center Inorganic-Organic Hybrid Framework with N-(Phosphonomethyl)iminodiacetate. *Eur J Inorg Chem* **2004,** *2004* (13), 2759-2768.
[193] Bakhmutova, E. V.; Ouyang, X.; Medvedev, D. G.; Clearfield, A., Cobalt Phosphonates: An Unusual Polymeric Cobalt Phosphonate Containing a Clathrated Phosphonate Anion and a Layered Bisphosphonate. *Inorganic Chemistry* **2003,** *42* (22), 7046-7051.
[194] Chattopadhyay, S.; Dash, S. K.; Ghosh, T.; Das, D.; Pramanik, P.; Roy, S., Surface modification of cobalt oxide nanoparticles using phosphonomethyl iminodiacetic acid followed by folic acid: a biocompatible vehicle for targeted anticancer drug delivery. *Cancer nanotechnology* **2013,** *4* (4-5), 103-116.
[195] Manasmita, D.; Debasish, M.; Maiti, T. K.; Basak, A.; Pramanik, P., Bio-functionalization of magnetite nanoparticles using an aminophosphonic acid coupling agent: new, ultradispersed, iron-oxide folate nanoconjugates for cancer-specific targeting. *Nanotechnology* **2008,** *19* (41), 415101.
[196] Zhang, H.; He, H.-X.; Wang, J.; Mu, T.; Liu, Z.-F., Force titration of amino group-terminated self-assembled monolayers using chemical force microscopy. *Applied Physics A* **1998,** *66* (1), S269-S271.
[197] Heubel, P.-H. C.; Popov, A. I., Acid properties of some phosphonocarboxylic acids. *Journal of Solution Chemistry* **1979,** *8* (9), 615-625.

[198] Mussano, F.; Genova, T.; Verga Falzacappa, E.; Scopece, P.; Munaron, L.; Rivolo, P.; Mandracci, P.; Benedetti, A.; Carossa, S.; Patelli, A., In vitro characterization of two different atmospheric plasma jet chemical functionalizations of titanium surfaces. *Appl Surf Sci* **2017,** *409*, 314-324.
[199] Zhang, Y.; Chen, L.; Shi, M.; Zhai, D.; Zhu, H.; Chang, J.; Wu, C.; Zheng, X.; Yin, J., Mesoporous Bioactive Glass Nanolayer-Modified Zirconia Coatings on Ti-6Al-4V with Improved In Vitro Bioactivity. *International Journal of Applied Glass Science* **2016,** *7* (2), 216-228.
[200] Le Ouay, B.; Stellacci, F., Antibacterial activity of silver nanoparticles: A surface science insight. *Nano Today* **2015,** *10* (3), 339-354.
[201] Abou El-Nour, K. M. M.; Eftaiha, A. a.; Al-Warthan, A.; Ammar, R. A. A., Synthesis and applications of silver nanoparticles. *Arabian Journal of Chemistry* **2010,** *3* (3), 135-140.
[202] Chernousova, S.; Epple, M., Silver as Antibacterial Agent: Ion, Nanoparticle, and Metal. *Angewandte Chemie International Edition* **2013,** *52* (6), 1636-1653.
[203] Dakal, T. C.; Kumar, A.; Majumdar, R. S.; Yadav, V., Mechanistic Basis of Antimicrobial Actions of Silver Nanoparticles. *Frontiers in Microbiology* **2016,** *7* (1831).
[204] Guzman, M.; Dille, J.; Godet, S., Synthesis and antibacterial activity of silver nanoparticles against gram-positive and gram-negative bacteria. *Nanomedicine: Nanotechnology, Biology and Medicine* **2012,** *8* (1), 37-45.
[205] Klasen, H. J., Historical review of the use of silver in the treatment of burns. I. Early uses. *Burns* **2000,** *26* (2), 117-130.
[206] Klasen, H. J., A historical review of the use of silver in the treatment of burns. II. Renewed interest for silver. *Burns* **2000,** *26* (2), 131-138.
[207] Souza, L. R. R.; da Silva, V. S.; Franchi, L. P.; de Souza, T. A. J., Toxic and Beneficial Potential of Silver Nanoparticles: The Two Sides of the Same Coin. In *Cellular and Molecular Toxicology of Nanoparticles*, Springer: 2018; pp 251-262.
[208] Burdușel, A.-C.; Gherasim, O.; Grumezescu, A.; Mogoantă, L.; Ficai, A.; Andronescu, E., Biomedical Applications of Silver Nanoparticles: An Up-to-Date Overview. *Nanomaterials* **2018,** *8* (9), 681.
[209] Korani, M.; Ghazizadeh, E.; Korani, S.; Hami, Z.; Mohammadi-Bardbori, A., Effects of silver nanoparticles on human health. In *European Journal of Nanomedicine*, 2015; Vol. 7, p 51.
[210] Disis, M. L.; O'Meara, M. M., HER2/neu. In *Cancer Therapeutic Targets*, Marshall, J. L., Ed. Springer New York: New York, NY, 2017; pp 267-275.
[211] Perrier, A.; Gligorov, J.; Lefèvre, G.; Boissan, M., The extracellular domain of Her2 in serum as a biomarker of breast cancer. *Laboratory Investigation* **2018,** *98* (6), 696-707.
[212] Shi, H.-Z.; Wang, Y.-N.; Huang, X.-H.; Zhang, K.-C.; Xi, H.-Q.; Cui, J.-X.; Liu, G.-X.; Liang, W.-T.; Wei, B.; Chen, L., Serum HER2 as a predictive biomarker for tissue HER2 status and prognosis in patients with gastric cancer. *World Journal of Gastroenterology* **2017,** *23* (10), 1836-1842.
[213] Lo, C.-Y.; Chen, W.-Y.; Chen, C.-T.; Chen, Y.-C., Rapid Enrichment of Phosphopeptides from Tryptic Digests of Proteins Using Iron Oxide Nanocomposites of Magnetic Particles Coated with Zirconia as the Concentrating Probes. *Journal of Proteome Research* **2007,** *6* (2), 887-893.
[214] Yu, S.; Xiang, H.; Zhou, J.; Zhou, Z.; Zhu, M., The Synergistic Effect of Organic Phosphorous/α-Zirconium Phosphate on Flame-Retardant Poly(lactic acid) Fiber. *Fibers and Polymers* **2018,** *19* (4), 812-820.

Acknowledgement

First of all, I would like to thank my tutor, Prof Pietro Riello, for giving me the possibility to work with his research group, ever with useful tips. He teaches me how to work with people with the most different background of knowledge, ever with passion.

I want to acknowledge also Prof Alvise Benedetti for treating me as a daughter, ever with patience and good words, despite my stubbornness and pessimism. He tries to teach me how to deal with people, even if not ever with good results.

I would like to acknowledge Davide Peddis to introduce me on magnetism, a so difficult field, and let me appreciate it with ever constructive discussions. I thank also for the possibility that he gives me to work in Trondheim with Gurvinder Sing, ever brilliant and kind, in a great lab, and in Montelibretti with his research group, ever exiting.

I wish to thank Doc Giuseppe Toffoli for giving me the possibility of these years of research in deep contact with the biomedical field, in particular the oncological one, improving my knowledge with different skills.

I am grateful to Prof Elti Cattaruzza for the best advice on surface analyses and the treatment of data.

I would also thank the all other professors of the ETA building for giving me advices on the PhD work, good or bad they were.

I wish to acknowledge also all the people that helped me with all the measurements and other requests necessaries for my work: Prof Alessandro Scarso for the building of phosphonates, Prof Moreno Meneghetti and his research group for all the SERS applications of my particles, Prof Antonella Glisenti for the funny XPS sessions, Prof Michela Signoretto for TPR measurement, Prof Marco Geppi and PhD Silvia Borsacchi for SS-NMR measurements and for being ever helpful in a very short time, the MCX line at Elettra Synchrotron, and last but not least Nader Yaacoub for Mössbauer spectra.

I am grateful to all the technicians of ETA building (Tiziano, Davide and Martina) for being ever helpful during these years to all my sometimes insistent and stupid requests. But I am mostly grateful to them for the beautiful moments spends there, especially the ones which include foods (particularly the one cooked by Lele). I am glad to have met all the Via Torino Guys and spends there these years. In particular I wish to thank Emmanuele for the help in biological questions and Benedetta for all related to her babies bacteria, the X-ray guys Lele and Riccardo, and the plasma man Emanuele, also for the ever pleasure moments, and all the other (Ponty, Elisa, Nicolò, Vincenzo, Eleonora, Sara, Laura, Martina, Giulia, Francesca, Leonardo, Gloria, Michele).

I wish to thank also all the CRO's guys, which helps and create great moments in a so sad Aviano.

I am also glad to have met a lot of wonderful people from all around the world, from my period abroad and from other research groups. I wish to thank Sihai, for helping me to

survive in Norway, Maria, Alex, Sonja, Alessandro for the scientific help in difficult moments and for all the nice time together.

I thank all of my friends that encourage me during these years and support me in difficult moments. Thank Lisa, for all the strange moments and being friends for so many years, thank to BAM for all the difficulties for meeting but great moment when it happens, thank to my flatmate, for beautiful and difficult moments, for the dinners and beers.

Finally, I want to thank my family, to ever be a drive to improve myself, in bad and beautiful moments and for the sacrifices they did for me. Thank to my sister, who is so difficult to bear, but it can also be easy.

And thank Paolo, to be near me, to encourage me, even if it can be so difficult.